学 位 論 文

The Chemical Evolution and Ionization State of Star-Forming Galaxies

(星形成銀河の化学進化と電離状態)

平 成 2 5 年 1 2 月 博 士 （ 理 学 ）
申 請

東 京 大 学 大 学 院 理 学 系 研 究 科
天 文 学 専 攻

中 島　王 彦

学 位 論 文

The Chemical Evolution and Ionization State of Star-Forming Galaxies

星形成銀河の化学進化と電離状態

平 成 2 5 年 1 2 月 博 士 （ 理 学 ）
申 請

東 京 大 学 大 学 院 理 学 系 研 究 科
天 文 学 専 攻

中 島　王 彦

Acknowledgments

I would like to begin this thesis with my deepest gratitude to three advisors, Associate Prof. Kazuhiro Shimasaku, Associate Prof. Masami Ouchi, and Prof. Sadanori Okamura on my research over five years of the PhD course at the University of Tokyo. I am grateful to my supervisor, Associate Prof. Kazuhiro Shimasaku for his invaluable instructions, discussions, and supports. I was able to learn lots of *"how-to"*s needed for a scientist; how to read and write a paper, how to reduce data, how to write a proposal, how to give a talk in a conference, and so on. I really appreciate lots of his kind supports, without which I would not be able to accomplish my research as the thesis. I am grateful to Associate Prof. Masami Ouchi for his extensive instruction and support throughout my PhD studies. I was able to conduct and advance my research with his lots of useful advice and ideas. Discussions with him were really fruitful, raising me up as an astronomer. I was also able to improve my observational skills such as writing a proposal, preparing for and performing an observation, and reducing the data with his dedicated support. Without his strict but kind instructions, I could not acquire them. I am also thankful to him, who has invited me to the Kavli Institute for the Physics and Mathematics of the Universe (Kavli IPMU) in the last three years of the PhD course. The new environment at the institute has educated me a lot. I am also grateful to Prof. Sadanori Okamura for his kind instruction and support, especially for the first two years of the PhD course. He gave me an opportunity to reduce and analyze his imaging data, and this experience raised me to a higher level. I was also able to acquire presentation skills through his trainings.

For completing our work as the thesis, I feel especially thankful for researchers below. I am grateful to Dr. Yoshiaki Ono and Mr. Takuya Hashimoto who have assisted me not only as the same laboratory members but as essential research collaborators. Dr. Ono has kindly examined stellar populations of the $z = 2.2$ LAE sample we constructed. Mr. Hashimoto succeeded in NIR spectroscopy of $z = 2.2$ LAEs with Magellan/MMIRS, kindly providing me with the reduced data. Without their help, I could not have completed the work presented in this thesis. I would like to thank Dr. Janice C. Lee, Dr. Chun Ly, Dr. Daniel A. Dale, Dr. Samir Salim, Dr. Rose Finn, and the NewHα Survey team who kindly let us use their NB118, NB209, J, and K band imaging data, which are essential for our study. They also gave us lots of helpful comments on our work. I thank Dr. Sebastien Foucaud, Dr. Omar Almaini and those who are involved in the UKIDSS/UDS project who provided us with the UDS u^* band imaging data, which enable us to select $z = 2.2$ LAEs in the SXDS field. Their UDS NIR JHK imaging data are also helpful for estimating SEDs of the $z = 2.2$ LAEs. I thank Dr. Tohru Nagao and Dr. Roberto Maiolino who gave us their emission-line flux and metallicity measurements of local galaxies as well as many fruitful comments on metallicity indicators. I thank Dr. Michael Rauch who has kindly been carried out follow-up observations of the $z = 2.2$ LAEs with the Magellan Telescope. I thank Dr. Chris Simpson for providing the radio source catalog for the SXDS. I thank Dr. Lucia Guaita for providing us with the average SED of $z \sim 2$ BX galaxy. I thank Dr. Ikuru Iwata, Dr. Akio K. Inoue, and Dr. Yuichi Matsuda

for providing their catalogs of $z \sim 3$ LAEs, LBGs (including LyC leaking galaxies), and Lyα blobs for our Keck/MOSFIRE observation. I thank Dr. Tomoki Hayashino for providing the imaging data in the SSA22 field. I thank Dr. Tomohiro Yoshikawa and Dr. Masao Hayashi for their assistance with NIR spectroscopy data reduction. I thank Dr. Kiyoto Yabe, Dr. Masao Hayashi, and Dr. Naoyuki Tamura for their assistance with FMOS observation preparation and data reduction. I thank Dr. Masafumi Yagi for teaching me lots of techniques about data reductions, especially about Suprime-Cam data.

In addition to them, I am grateful to Dr. Steven L. Finkelstein, Dr. James E. Rhoads, Dr. Matthew Hayes, Dr. Lisa J. Kewley, Dr. Filippo Mannucci, Dr. Maritza Lara-Lopez, Associate Prof. Kentaro Motohara, Dr. Zhen-Ya Zheng, Dr. Eros Vanzella, Mr. Matthew Schenker, Dr. Lennox L. Cowie, Dr. Esther M. Hu, Dr. Anne Verhamme, Dr. Guillermo A. Blanc, Dr. Giovanni Cresci, Dr. Alessandro Marconi, Dr. Masato Onodera, Dr. Antonio Pipino, Dr. Alaine Henry, Dr. Maryam Shirazi, Dr. Jarle Brinchmann, Dr. Yuu Niino, Dr. Sally Oey, Dr. John D. Silverman, Dr. Kevin A. Bundy, Dr. Surhud More, and Dr. Naotaka Suzuki for their helpful comments and discussions.

I thank the referees, Associate Prof. Kentaro Motohara (chair), Associate Prof. Toshikazu Shigeyama, Prof. Yuzuru Yoshii, Prof. Hideyuki Kobayashi, and Associate Prof. Nobunari Kashikawa, for their helpful comments and suggestions, which greatly improved the thesis.

I thank the MPA/JHU teams which made their measured quantities on SDSS galaxies publicly available. Some of the data used in this thesis were collected at the Subaru Telescope, which is operated by the National Observatory of Japan. I sincerely thank the Subaru Telescope staff for their great help with our observations. In particular, I am grateful to Dr. Fumiaki Nakata for supporting our observations with Suprime-Cam, and Dr. Kentaro Aoki for his dedicated support with FMOS observation. Some of the data presented in this thesis were obtained at the W. M. Keck Observatory, which is operated as a scientific partnership among the California Institute of Technology, the University of California, and the National Aeronautics and Space Administration. The Observatory was made possible by the generous financial support by the W. M. Keck Foundation. Especially, I am grateful to Dr. Scott E. Dahm for supporting our NIRSPEC observation, and Dr. Gregory D. Wirth for assisting our MOSFIRE observation. I wish to extend special thanks to those of Hawaiian ancestry for allowing telescopes and astronomers on their sacred mountaintop. Their hospitality made our observations possible.

The optical images as well as near-infrared, UV, X-ray, and/or radio data used in conjunction with the NB387 data are obtained in some different projects; the Subaru/XMM-Newton Deep Survey (SXDS), the UKIRT Infrared Deep Sky Survey (UKIDSS) Ultra Deep Survey (UDS), the Cosmic Evolution Survey (COSMOS), the Great Observatories Origins Deep Survey (GOODS), the Multi-wavelength Survey by Yale-Chile (MUSYC), the Hawaii Hubble Deep Field North (Hawaii-HDFN), and the SSA22. I would like to thank all members who are associated with the projects. This thesis is based in part on observations made with Spitzer Space Telescope, which is operated by the Jet Propulsion Laboratory, California Institute of Technology under a contract with NASA. Support for this work was provided by NASA through an award issued by JPL/Caltech.

I am grateful to Dr. Tadayuki Kodama (and those who may concern) who gave me a chance to go abroad as a member of "Institutional Program for Young Researcher Oversea Visits" under the Japan Society for the Promotion of Science (JSPS) fund allocated to the National Astronomical Observatory of

Japan. I would like to sincerely thank Prof. Richard S. Ellis for accepting me to stay in the California Institute of Technology in January–March 2012 through the program. During the two-month stay, I was able to have meaningful discussions with him and the members of his laboratory in the institute, in particular Dr. Andrew B. Newman, Dr. Tucker Jones, Mr. Matthew Schenker, and Mr. Sirio Belli. I also thank Dr. Michael Rauch for valuable discussions at the Observatories of the Carnegie Institution for Science during the stay in Pasadena.

I feel thankful to Dr. Filippo Mannucci who allowed me to visit him and give a talk in the Arcetri Astrophysical Observatory, Istituto Nazionale di Astrofisica (INAF) in September 2013. Dr. Cresci, Dr. Marconi, and we were able to deepen our knowledge of the chemical evolution of galaxies through face-to-face discussion. I would like to thank Dr. Masato Onodera who gave me a chance to visit him and give a talk in Eidgenössische Technische Hochschule Zürich (ETH Zurich) in September 2013. I was able to have a fruitful discussion with him and the people in the ETH Zurich. I also thank him for presenting the City of Zurich, Switzerland. I really enjoyed the lives in Zurich.

I would like to thank the former and present members in my laboratory, Dr. Masao Hayashi, Dr. Yusei Koyama, Dr. Yoshiaki Ono, Mr. Takahiro Ohno, Mr. Shingo Shinogi, Mr. Takuya Hashimoto, Mr. Ryosuke Goto, Mr. Ryota Kawamata, and the secretary, Ms. Masumi Nakaya, as well as the members of the observational cosmology group in the Institute for Cosmic Ray Research, Dr. Rieko Momose, Dr. Suraphong Yuma, Dr. Takatoshi Shibuya, Mr. Akira Konno, Mr. Yoshiaki Naito, Mr. Masafumi Ishigaki, and Ms. Hiroko Tamazawa for productive discussions and extensive help with my work and my daily lives. I hope we will always keep in touch and continue our collaboration in future research.

Beyond our research group, I feel thankful to members of the Department of Astronomy, the University of Tokyo, especially my colleagues from the Bachelor course, Mr. Soh Ikarashi, Mr. Kohei Ueda, Mr. Ryou Ohsawa, Ms. Shiori Kyu, Ms. Mei Sasaki, Mr. Takafumi Sonoi, Mr. Yasuyuki Takahashi, Mr. Kohei Hattori, Mr. Takayuki Hayashi, and Dr. Takashi Moriya, who I share friendly rivalry. I thank Dr. Masayuki Tanaka, Dr. Masamune Oguri, Dr. Kiyoto Yabe, Dr. Ken-ichi Tadaki, and Dr. Masakazu A. R. Kobayashi for their helpful comments and kind encouragement. I also thank Dr. Takashi Moriya and Mr. Ayuki Kamada, with whom I really enjoyed the lives in the Kavli IPMU, including adventure activities such as cycling to the Ushiku Daibutsu and climbing Mt. Fuji. I sincerely acknowledge the secretaries of the Department, Ms. Keiko Sakurai, Ms. Mitsue Sasaki, Ms. Yuko Yamazaki, Ms. Yasuko Yoshino, Ms. Tomoko Ishikawa, Ms. Maki Noguchi, Ms. Mayumi Watanabe, Ms. Miho Yatabe, and Ms. Mari Oguro, as well as the secretaries of the Kavli IPMU for their kind help. My work in Kavli IPMU is supported by World Premier International Research Center Initiative (WPI Initiative), MEXT, Japan. I acknowledge the financial support from the Japan Student Services Organization (JASSO) for the second and third years of the PhD course, and the JSPS Research Fellowship for Young Scientists for the last two years of the PhD course.

Last but definitely not least, I would like to offer my sincere thanks and appreciation to my parents, Takeshi Nakajima and Tsuneko Nakajima, and my brother and sisters, Takenori Nakajima, Sonoko Miyao (Nakajima), and Sakiko Nakajima. I deeply appreciate their warm caring, kind understanding, and endless support throughout my life.

Abstract

For galaxy formation studies, it is essential to understand physical conditions of the interstellar medium (ISM) of galaxies. In particular, we focus on two important quantities, gas-phase metallicity and ionization parameter, that characterize the hot ISM of star-forming galaxies. Metallicity is the abundance of the elements heavier than hydrogen or helium, a record of the galaxy's star-formation history and gas infall+outflow. It is thus significant to understand the chemical evolution of galaxies and its dependence on galaxy global properties such as stellar mass ($M_\star$) and star-formation rate (SFR). Ionization parameter measures the ratio of the number density of ionizing photons to that of hydrogen atoms in an HII-region. It is sensitive to the degree of excitation of an HII-region, and largely governs the emergent emission-line spectrum from the HII-region as the metallicity does. However, previous high-redshift galaxy studies have mainly focused on metallicity to examine the chemical evolution of galaxies, and often lacked ionization parameter. In order to provide deeper insights into the evolution of galaxies, in this thesis, we investigate ionization parameter and metallicity of galaxies at $z = 0-3$ over wide ranges of $M_\star$ and SFR. We utilize line ratios of [O III]λ5007/[O II]λ3727 and ([O III]$\lambda\lambda$5007, 4959+[O II]λ3727)/Hβ (R23-index) with photoionization models.

First, we present a systematic study for ionization parameter, metallicity, $M_\star$, and SFR of galaxies at $z \sim 0$ with the $\sim 140,000$ SDSS galaxies. We also consider extreme populations of galaxies in the local universe, Green Pea galaxies (GPs), Lyman-break Analogs (LBAs), and galaxies emitting Ly-continuum radiation (LyC leakers). These local extreme populations are helpful to discuss local counterparts of high-z star-forming galaxies. We clarify that local galaxies typically have an ionization parameter of $\log(q_{\rm ion}/{\rm cm\,s^{-1}}) \sim 7.3$ and metallicity of $12+\log({\rm O/H}) \sim 9.0$ by using the [O III]/[O II] vs. R23-index diagram. In contrast, the local extreme populations exhibit significantly higher ionization parameters and lower metallicities. Among the SDSS sample, we find a relatively large scatter of galaxies on the [O III]/[O II] vs. R23-index diagram, inferring a trend that more metal-poor galaxies have a higher ionization parameter. Since metallicity is known to strongly correlate with galaxy global properties of $M_\star$ and SFR, we examine the relation between ionization parameter and metallicity with $M_\star$ and SFR. As a result, we clearly find a tendency that a high ionization parameter is found in less massive, more efficiently star-forming, and more metal-poor galaxies. We develop a four-dimensional relation of ionization parameter, SFR, $M_\star$, and metallicity, extending the fundamental metallicity relation (FMR; Mannucci et al. 2010; Lara-López et al. 2010) with ionization parameter. Interestingly, the local extreme populations follow the same relation.

Next, we extend our study of ionization parameter and metallicity of galaxies towards higher-redshift. Previous high-z observations, however, lack low-mass galaxies ($M_\star \lesssim 10^{9.5}\,M_\odot$) because most of them are based on continuum selected sample, such as Lyman-break galaxies (LBGs). In order to obtain detailed

emission-line properties of less massive galaxies at high-z and to study the diversity of high-z galaxies, we construct a large sample of Lyα emitters (LAEs) at $z \simeq 2.2$. We present the physical properties of the LAEs from near-infrared spectroscopy and narrowband imaging observations. From Keck/NIRSPEC and Magellan/MMIRS follow-up spectroscopy observations, we identify two LAEs, CDFS-3865 and COSMOS-30679, whose [O II], [O III], and Hydrogen Balmer lines are significantly detected. Their [O III]/[O II] ratios and $R23$-indices provide the first simultaneous determinations of ionization parameter and metallicity for LAEs. We find both of the LAEs have a high ionization parameter and low metallicity in contrast with local galaxies and LBGs at similar redshifts. We also present the average metallicity of the LAEs measured with two narrowband filters covering the [O II] and Hα+[N II] lines at $z \simeq 2.2$. By stacking the near-infrared images of the ~ 100 LAEs, we successfully obtain average nebular line fluxes of LAEs. The stacked object has a stellar mass of $5 \times 10^8 M_\odot$ and a SFR of $14 M_\odot\,\mathrm{yr}^{-1}$. We estimate, for the first time, the average metallicity of LAEs to be $Z \gtrsim 0.09 Z_\odot$ (2σ) based on the [O II]/(Hα+[N II]) index together with photoionization models and empirical relations. Although no estimation of ionization parameter is obtained by the narrowband survey, the estimated metallicity and SFR are useful to investigate average properties of low-mass LAEs.

Then, we present the extended study of ionization parameter and metallicity of galaxies at high-z. We use 69 intermediate-z ($z = 0.5$–1.5) and 39 high-z ($z \sim 2$–3) star-forming galaxies compiled from the literature. Notably, we include LAEs in the investigation, whose pilot estimations of ionization parameter and metallicity are given in our work. We confirm that $z \sim 2-3$ galaxies show an [O III]/[O II] ratio significantly higher than typical local galaxies by a factor of $\gtrsim 10$, and the photoionization models reveal that these high-z galaxies have an ionization parameter of $\log(q_{\mathrm{ion}}/\mathrm{cm\,s^{-1}}) \sim 7.6-9.0$, a factor of $\gtrsim 4-10$ higher than local galaxies. The intermediate-z galaxies appear to have an intermediately high ionization parameter. These trends indicate a redshift evolution of ionization parameter. Notably, the local extreme populations have an ionization parameter as high as high-z LBGs and LAEs. We also suggest that the intermediate- and high-z galaxies follow the same four-dimensional relation of ionization parameter, SFR, $M_\star$, and metallicity defined with the SDSS galaxies. The relation is thus considered to be fundamental over cosmic time, referred to as the fundamental ionization relation (FIR). We particularly find no significant differences between galaxies at $z \sim 2$ and 3 in the FIR.

Finally, we discuss the ionization parameter and metallicity of galaxies at $z = 0-3$. We confirm the trend that high-z galaxies have an ionization parameter significantly higher than local galaxies. This evolution of ionization parameter can be closely related to the evolution of SFR and $M_\star$, in the sense that higher-z galaxies are typically less massive and more highly star-forming (cf., evolution of the star-formation main-sequence; Daddi et al. 2007). In the local universe, a high ionization parameter and low metallicity comparable to high-z galaxies is found in the extreme populations of galaxies such as GPs. However, such populations occupy only $\sim 0.06\,\%$ of the SDSS sample with a number density ~ 100 times smaller than that of high-z galaxies. Galaxies with a high ionization parameter would emerge in a high redshift universe, and that these galaxies are more dominant in high-z than the local universe. We find the FIR looks universal over cosmic time up to $z \sim 3$. This is in contrast with the FMR whose possible evolution from $z \sim 2$ to 3 is reported. We find that the FMR evolution of $z \sim 2-3$ appears, if one omits ionization parameter differences, and that the FMR evolution does not exist for an average metallicity solution of $z \sim 3$ galaxies with a high-ionization parameter.

Interestingly, local LyC leakers have a high [O III]/[O II] ratio, indicating a positive correlation between [O III]/[O II] and ionizing photon escape fraction ($f_{\rm esc}$), which is successfully explained by our photoionization models. Because [O III]/[O II] ratios of $z \sim 2-3$ galaxies, especially LAEs, are comparable to, or higher than, those of the local LyC leakers, these high-z galaxies are candidates of Lyman-continuum emitting objects. A strong Lyα emission can coexist with a large $f_{\rm esc}$ of $\lesssim 0.8$, and the increasing fraction of LAEs towards high-z reconciles the picture of cosmic reionization whose major ionizing sources are faint galaxies having *intrinsically*-bright Lyα emission.

We also discuss the basic characteristics of LAEs at high-z that were poorly-understood so far. We find that $M_\star$–Z relation for LAEs is complicated compared with that for LBGs at similar redshifts. Metallicities of LAEs could be generally low regardless of their stellar masses (approximately sub-solar metallicity). With their high ionization parameters and low metallicities, LAEs would represent an early stage of galaxy evolution dominated by massive stars in compact HII-regions. The discrepancies between LAEs and LBGs on the $M_\star$–Z relation could be alleviated in the FMR plot, since we find that low-mass LAEs with $M_\star \lesssim 10^9\,M_\odot$ have star-formation efficiencies lower than expected from massive galaxies. By adopting a correct ionization parameter to estimate the metallicity, and by taking into account the differences of SFR between LAEs and LBGs, we find a better level of consistency between LAEs and other populations in the FMR plot. Alternatively, as discussed above, LAEs' high ionization parameters could be originated from high $f_{\rm esc}$ achieved by density-bounded HII-regions. Since the LAEs lying above the FIR tend to fall below the FMR, $f_{\rm esc}$ would be a key quantity to characterize these LAEs.

Contents

This thesis is mainly based on the following three papers:

Paper I Nakajima, K., Ouchi, M., Shimasaku, K., Ono, Y., Lee, J. C., Foucaud, S., Ly, C., Dale, D. A., Salim, S., Finn, R., Almaini, O., Okamura, S. *Average Metallicity and Star Formation Rate of Lyα Emitters Probed by a Triple Narrowband Survey*, The Astrophysical Journal, Volume 745, Issue 1, article id. 12, 19 pp., 2012
(Chapters 1, 3, 5, and Appendices A and C)

Paper II Nakajima, K., Ouchi, M., Shimasaku, K., Hashimoto, T., Ono, Y., Lee, J. C. *First Spectroscopic Evidence for High Ionization State and Low Oxygen Abundance in Lyα Emitters*, The Astrophysical Journal, Volume 769, Issue 1, article id. 3, 18 pp., 2013
(Chapters 1, 3, 5, and Appendices A and B)

Paper III Nakajima, K., Ouchi, M. *Ionization States of galaxies: Evolution, SFR-$M_\star$-Z Dependence, and Ionizing Photon Escape*, submitted to Monthly Notices of the Royal Astronomical Society, arXiv e-prints, arXiv:1309.0207, 18pp., 2013
(Chapters 1, 2, 4, 5)

1 Introduction

1.1. Galaxies and Their Evolution

When we look at the night sky, we can see thousands of stars. Almost all of the stars, including the Sun and much fainter $\sim 10^{11}$ stars, are gravitationally-bounded to form a galaxy, commonly called the Milky Way. Galaxy is a huge group of stars, stellar remnants, an interstellar medium (ISM) of gas and dust, and dark matter, the last of which we poorly-understand and know only by the pull of its gravity. After the establishment that the Andromeda nebula (M31) is not an element within the Milky Way but is a comparable stellar system in its own right (e.g., Hubble 1922), we have realized that there are innumerable galaxies in the universe beyond the Milky Way. Galaxies are now considered to be the fundamental building blocks of the universe.

Galaxies show a variety in their appearance, or morphology. According to the Hubble sequence (Hubble 1936), galaxies are historically classified into two groups; "early-type" and "late-type" galaxies. Elliptical and S0 galaxies are categorized as early-type, while spiral and irregular galaxies are as late-type galaxies. The Milky Way is a (barred) spiral galaxy, and thus a late-type galaxy.

Although the classification uses only morphology, the two types of galaxies show different properties in some respects. Early-type galaxies are in general bright and massive galaxies, showing red colors and almost no sign of current star-formation. On the other hand, late-type galaxies are less massive galaxies with blue colors, having a larger amount of gas that sustains the current star-formation. Therefore, late-type galaxies are in general composed of younger stars than early-type galaxies. A morphology-density relation has also been reported (e.g., Dressler 1980), where early-type galaxies tend to reside in the highest number density regions of galaxies such as cluster centers, while late-type galaxies are more frequently found in less-crowded, blank fields. It remains an open question, though, how these varieties of galaxy properties were formed in the past and evolved to be observed in the current universe. We would like to understand the evolution of galaxies.

The most direct way to study the galaxy properties in the past is to observe distant galaxies. The universe is expanding. This means that distant galaxies are moving away from us much faster than galaxies that are close by. As the distant galaxy moves away from us, the wavelength of light that it emits stretches and is moved to the red. The amount by which the wavelength of light from a receding object is lengthened is called the redshift (z). Due to the expansion of the universe, a more distant galaxy has a larger value of z. Since the speed of light is finite, distant galaxies at high-z are observed as they

appeared when the universe was much younger, with the smaller size by a factor of $(1+z)$. Therefore, distant galaxies at high-z provide us with opportunities to explore galaxy properties in the past universe, and to investigate how galaxies were formed and evolved to the current epoch.

Galaxy mass is thought to be a fundamental quantity which governs the evolution of galaxies. Theoretically, galaxy formation models based on ΛCDM cosmology predict that galaxies grow through subsequent mergings of lower-mass objects and that galaxy properties are largely determined by their masses through mass-dependent processes at work in the evolution of galaxies (e.g., Blumenthal et al. 1984; Davis et al. 1985; Bardeen et al. 1986). Therefore, observations of mass-dependence of galaxy properties back in cosmic time are crucial to understand how galaxies evolve to acquire present-day properties. Past observations have revealed that physical quantities like star formation rate (SFR) and gas-phase metallicity correlate with mass not only for present-day galaxies but also for high-z galaxies, with some evolutions (details are given in Section 1.3; e.g., Brinchmann et al. 2004; Tremonti et al. 2004; Ellison et al. 2008; Reddy et al. 2006; Erb et al. 2006a; Maiolino et al. 2008; Mannucci et al. 2009). This supports the importance of mass-dependent effects on galaxy evolution.

However, one of the crucial differences between studies of local and high-z galaxies is the explored mass range. For the local galaxies, the correlations between some physical properties and mass have been recognized over 3 orders of magnitude in stellar mass of $M_\star \simeq 10^{8.5}$–$10^{11.5}\,M_\odot$ (Brinchmann et al. 2004; Tremonti et al. 2004), by using the spectroscopic sample of the Sloan Digital Sky Survey (SDSS; e.g., York et al. 2000). For high-z galaxies, on the other hand, massive galaxies with $M_\star \gtrsim 10^{9.5}\,M_\odot$ have been mainly spectroscopically observed. To clarify the situation, we nextly explain how these high-redshift galaxies have been selected and studied in the following sections.

1.2. High-Redshift Galaxies

1.2.1. Continuum-selected Galaxies

Previous high-z observations lack low-mass galaxies ($\lesssim 10^{9.5}\,M_\odot$) because most of them are based on continuum-selected sample, such as Lyman-break galaxies (LBGs; e.g., Steidel & Hamilton 1992), BX/BM galaxies (e.g., Steidel et al. 2004), and BzK galaxies (e.g., Daddi et al. 2004):

- LBGs are star-forming galaxies that are selected based on a "break" in their spectral energy distributions (SEDs) at (912−) 1216 Å rest-frame that is termed Lyman-break. Since ionizing radiation with wavelengths shorter than 912 Å (Lyman-limit) is effectively absorbed by neutral hydrogen in stellar atmosphere and ISM, galaxy is virtually dark at wavelengths shorter than 912 Å. In addition, escaped radiation from the galaxy with wavelengths 912–1216 Å is absorbed by neutral hydrogen in the intergalactic medium (IGM) along the line of sight. This absorption in the IGM is especially effective for galaxies at $z > 4$, where the number density of an absorber of Lyman-limit system rapidly increases towards higher-z (e.g., Inoue & Iwata 2008). On the other-hand, UV-continuum radiation with wavelengths longer than 1216 Å remains unchanged. Accordingly, the Lyman-break appears in the galaxy's SED at $\simeq 1216$ Å. For the selection of LBGs at a redshift z, we perform an imaging observation with at least two broadband filters, which covers wavelength ranges shorter and longer than $1216(1+z)$ Å, respectively. Galaxies that are bright in the longer-wavelength broadband image but faint (or invisible) in the shorter-wavelength broadband image are selected

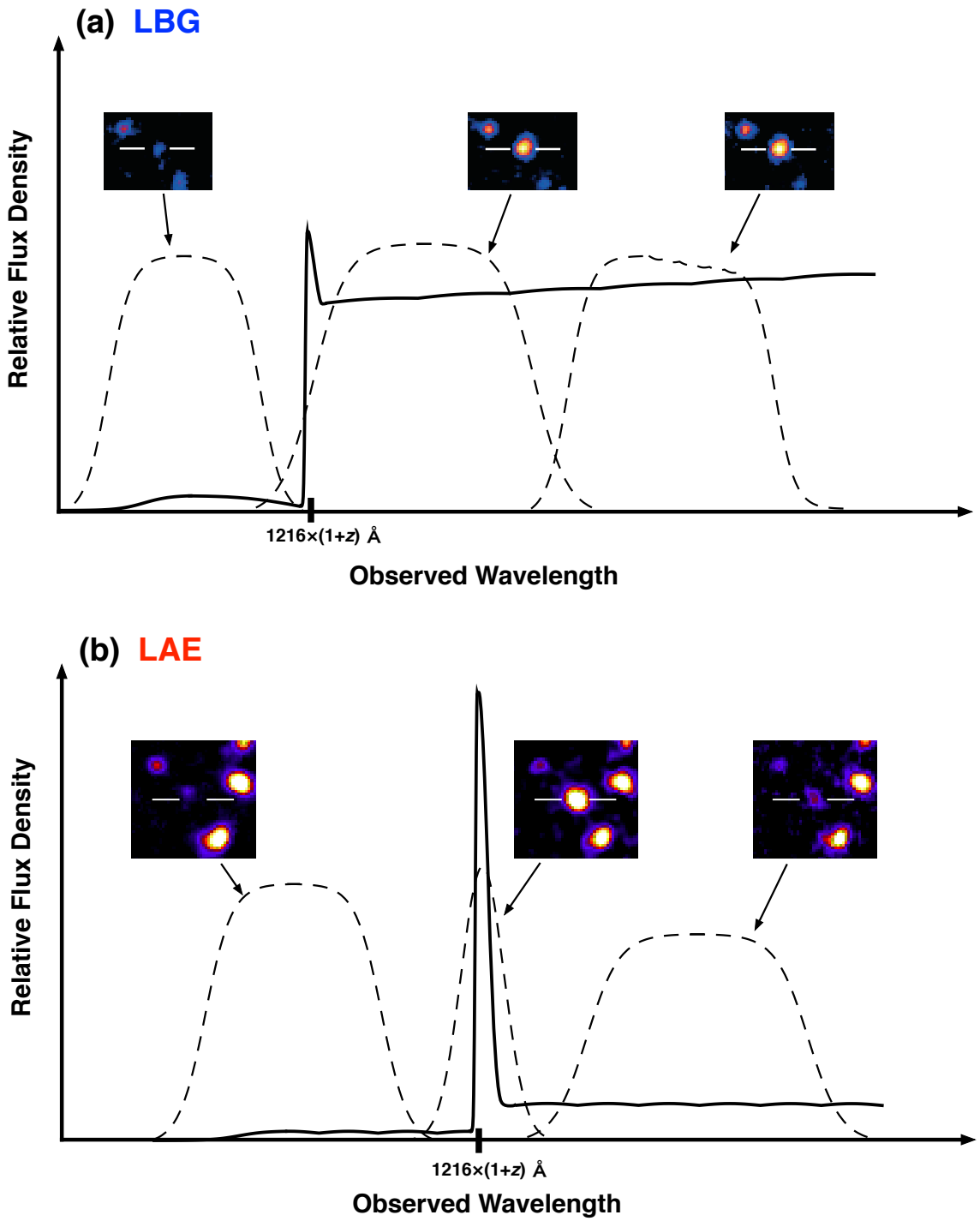

Figure 1.1. Schematic illustrations of how to select (a) LBGs and (b) LAEs. The thick curves show the simplified SEDs of LBGs and LAEs, and the dashed curves represent transmissions of broadband and narrowband filters. (a) Due to the absorption by neutral hydrogen in ISM and IGM, a gap termed Lyman-break appears at $\lambda = 1216 \times (1+z)$ Å for galaxies at redshift z. LBGs are very faint in a broadband image which covers wavelengths shorter than $1216 \times (1+z)$ Å, while bright in broadband images covering wavelengths longer than $1216 \times (1+z)$ Å, as illustrated in the inner-panels (these snapshots are obtained from a real LBG; Ouchi et al. 2004). (b) LAEs at redshift z show a very strong Lyα emission at $1216 \times (1+z)$ Å. These LAEs look very bright in the narrowband image, which covers $1216 \times (1+z)$ Å, in contrast to its adjacent broadband images located in shorter and longer wavelengths, as shown in the inner-panels (these snapshots are obtained from a real LAE; Kodaira et al. 2003).

as LBGs (Figure 1.1a). Thus, LBGs are sometimes called dropout galaxies. This technique is widely used to search for high redshift galaxies at $z \sim 3$ up to $z \gtrsim 10$ (e.g., Ellis et al. 2013).

- BX and BM galaxies are star-forming galaxies at $z \simeq 2.0$–2.5 and $z \simeq 1.5$–2.0, respectively. In the redshift range of $z \simeq 1.5$–2.5, no prominent features of SEDs are observable in optical wavelengths; the Lyman-break is in UV wavelengths, while another break in SEDs, 4000 Å-break, is redshifted into near infrared (NIR) wavelengths. BX/BM galaxies are selected by three broadband images of U, G, and R passbands, with the color selection criteria that galaxies does not show either Lyman- or 4000 Å-breaks in optical wavelengths. Properties of BX/BM galaxies are similar to those of LBGs at $z \sim 3$ (e.g., Steidel et al. 2004).

- BzK galaxies consist of star-forming and passive galaxies at $z \simeq 1.4$–2.5. The former and latter is commonly called sBzK and pBzK galaxies, respectively. BzK galaxies are selected by three broadband images of B, z, and K passbands, with the color selection criteria that galaxies does not show any break in optical (between B and z) but have a beak (i.e., 4000 Å-break) in NIR (between z and K) wavelengths. Among BzK galaxies, those with a blue color in UV-continuum are classified as sBzK, while those with a red color in UV-continuum and the prominent 4000 Å-break are classified as pBzK galaxies. For the purpose of studying evolution of star-forming galaxy in conjunction with LBGs and BX/BM galaxies, sBzK galaxies are more highlighted.

Although these continuum-selected galaxies are efficiently found based on broadband imaging observation, these galaxies are selectively massive galaxies. Now, low-mass galaxies at high redshift are especially interesting since they are likely to be building blocks of massive galaxies seen in later epochs.

1.2.2. Lyα Emitters

High redshift star-forming galaxies have been explored not only based on the UV-continuum but with the aid of strong emission lines. Hydrogen recombination lines such as Lyα and Hα, as well as ionized metal lines of oxygen, nitrogen, etc. are emitted from regions with a gas cloud photoionized by young massive stars (HII-regions). Star-forming galaxies thus show these emission lines intensely, and those selected by utilizing the emission lines are called emission-line galaxies, or emitters. Particularly, Lyα emitters (LAEs) have been commonly used to study high redshift galaxies, because Lyα emission at 1216 Å rest-frame is observable from galaxies at $z \simeq 2$ up to ~ 7 in the optical wavelengths. One can efficiently search for LAEs at a particular redshift of z using the narrowband filter centered on the wavelength of $\lambda = 1216 \times (1+z)$. By combining broadband filters located near the narrowband, one can find LAEs, which are particularly bright in the narrowband filter in comparison to the broadband images (Figure 1.1b). Since LAEs are not required to be detected in broadband images, they can be a useful probe to investigate low-mass galaxies in the early state of galaxy evolution.

Indeed, some previous studies have reported that LAEs are likely candidates for low-mass, young galaxies as suggested from their small sizes, faint continua, and low stellar masses inferred from SED fitting ($\lesssim 10^9 M_\odot$; Gawiser et al. 2006, 2007; Finkelstein et al. 2007, 2008, 2009a; Nilsson et al. 2007; Pirzkal et al. 2007; Lai et al. 2008; Ono et al. 2010a; Ono et el. 2010b; Yuma et al. 2010). More directly, Cowie et al. (2010, 2011) have studied LAEs at low redshifts ($z \sim 0.3$) searched by using *Galaxy Evolution Explorer (GALEX)*, and investigated their rest-frame optical nebular lines. The authors have found that a large portion of LAEs (75 %) have equivalent width (EW) of H$\alpha > 100$ Å, and that LAEs

on average have lower metallicities and younger ages than UV-continuum selected galaxies at similar redshifts. These findings are consistent with the idea that LAEs are galaxies in early stages of galaxy evolution.

At higher redshifts, however, direct evidences supporting the idea that LAEs are in an early evolutionary phase remain to be provided. Thanks to remarkable progress in observations of LAEs, our knowledge of properties of LAEs is rapidly accumulating (e.g., Cowie & Hu 1998; Steidel et al. 2000; Malhotra & Rhoads 2002; Ouchi et al. 2003; Kodaira et al. 2003; Malhotra & Rhoads 2004; Hayashino et al. 2004; Gawiser et al. 2006; Kashikawa et al. 2006; Shimasaku et al. 2006; Gronwall et al. 2007; Tapken et al. 2007; Ouchi et al. 2008; Overzier et al. 2008; Nilsson et al. 2009; Taniguchi et al. 2009; Guaita et al. 2010; Hayes et al. 2010; Ono et al. 2010a; Ono et el. 2010b; Ouchi et al. 2010; Blanc et al. 2011; Finkelstein et al. 2011; Guaita et al. 2011; Nilsson et al. 2011; Malhotra et al. 2012; Yamada et al. 2012). Nevertheless, in almost all observations physical quantities of LAEs have been estimated by SED fitting of broadband photometry. This is in contrast to massive galaxies at similar redshifts. In particular, while a large number of massive, continuum-selected galaxies have now direct measurements of SFR and metallicity from nebular lines, there are only a few LAEs with such direct measurements (McLinden et al. 2011; Finkelstein et al. 2011). One reason is that well-studied LAEs are located at very high redshift ($z \simeq 3$–7), where nebular lines redshifts into near infrared wavelengths and we cannot see them from the ground. Recently, surveys for LAEs at moderate redshift ($z = 2-3$) have began and bright LAEs among them are observed to measure nebular lines. It is known that SFRs derived from SED fitting are dependent on the star formation history assumed, and can vary by an order of magnitude among different histories (e.g., Ono et al. 2010a). It is also known that SED fitting cannot strongly constrain metallicities due to a degeneracy with age (e.g., Nilsson et al. 2011). Observations of nebular lines for a large number of LAEs are essential to extend our knowledge of galaxy properties towards low-mass galaxies below $M_\star \sim 10^9 M_\odot$, so that the mass-dependencies of galaxy properties be compared with those at present over the whole mass range.

1.3. Gas Metallicity and Ionization State of Galaxies

In addition to the fundamental stellar properties of stellar mass and SFR, it is essential to understand physical conditions of the ISM of galaxies for galaxy formation and evolution studies. In particular, we focus on two important quantities, gas-phase metallicity and ionization parameter, that characterize the hot ISM of star-forming galaxies. The study of these quantities over cosmic time provides a crucial information on the chemical evolution of galaxies and the physical state of HII-regions.

In astronomical terminology, we use the term "metal" to describe all the elements heavier than hydrogen or helium. The abundance of such heavy elements is termed "metallicity." Since most of metals are produced by nuclear reactions in stars and/or during explosions of stars, gas-phase metallicity is a record of galaxy's star formation history. In addition, metallicity is regulated by a complex interaction between infall of pristine gas and outflow of metal-enriched gas. Therefore, metallicity is an important parameter for understanding galaxy evolution processes. In this thesis, metallicity is defined by oxygen abundance, $12+\log(\mathrm{O/H})$, and the mentioned metallicity refers to gas-phase value in the ISM. The most reliable determination of metallicity is provided if the electron temperature can be measured directly, using auroral to nebular lines ratios such as [O III]$\lambda 4363/\lambda 5007$ ("direct T_e method"; e.g., Stasińska 1980; Kennicutt et al. 2003; Izotov et al. 2006). This is because a cooling efficiency of gas depends strongly on

its metallicity, in the sense that more metal-rich gas cools faster. Metal ions like O^+, O^{2+}, N^+, etc. are the most important coolants of an ionized gas, since collisional excitation energies in the ground state fine structure levels of these ions have typical excitation potentials of a few eV, which is comparable to the thermal energies of the electrons for typical ionized gas ($T_e \sim 10^4$ K). The information of the gas temperature enables us to estimate the amounts of O^+ and O^{2+} from the optical nebular lines of [O II]λ3727 and [O III]$\lambda\lambda$5007, 4959 alone, respectively. The oxygen abundance is then determined, such that O/H $= (O^+ + O^{2+})/H^+$. However, auroral lines are generally weak, and the measurement of the auroral lines is difficult even for galaxies in the local universe. The metallicity estimates using the direct T_e method are mainly reported for metal-poor galaxies in the local universe, whose gas temperature is high enough to excite O^{2+} species to emit [O III]λ4363. Therefore, we usually use some relations between metallicity and flux ratios of strong metal lines divided by a hydrogen recombination line to estimate the metallicity. One of the most frequently used indicator is the $R23$-index, defined as

$$R23 = \frac{[\mathrm{O\,III}]\lambda\lambda 5007, 4959 + [\mathrm{O\,II}]\lambda 3727}{\mathrm{H}\beta} \tag{1.1}$$

(e.g., Pagel et al. 1979; McGaugh 1991; Kewley & Dopita 2002). Another is the $N2$-index, defined as

$$N2 = \frac{[\mathrm{N\,II}]\lambda 6584}{\mathrm{H}\alpha} \tag{1.2}$$

(e.g., Storchi-Bergmann et al. 1994; Kewley & Dopita 2002; Pettini & Pagel 2004). These indicators have been calibrated by using the local galaxies with metallicity estimate from direct T_e method, in conjunction with photoionization models (see also Nagao et al. 2006; Maiolino et al. 2008).

An ionization parameter, q_{ion}, is sensitive to the degree of excitation of an HII-region, and governs the emission-line spectrum of the HII-region as the metallicity does. It is defined as the ratio of the mean ionizing photon flux to the mean hydrogen atom density in an HII-region, and its dimensionless form, $U = q_{\mathrm{ion}}/c$, is also used. Ionization parameters are estimated with emission lines of different ionization stages of the same element, such as [O III]λ5007/[O II]λ3727 ratio (e.g., Kewley & Dopita 2002).

Metallicities of galaxies have been well studied in the local and high-z universe in the diagram of stellar-mass vs. metallicity ($M_\star$–Z) relation. In the local universe, a tight $M_\star$–Z relation is recognized, where a metallicity increases with stellar mass (e.g., Tremonti et al. 2004). At high-z, similar $M_\star$–Z relations are reported at $z = 0.5 - 3.5$ (e.g. Savaglio et al. 2005; Erb et al. 2006a; Maiolino et al. 2008; Mannucci et al. 2009; Zahid et al. 2011; Yabe et al. 2012). These studies have found the evolution of $M_\star$–Z relation; metallicity decreases towards high-z at a given $M_\star$. Figure 1.2 shows the redshift evolution of $M_\star$–Z relation. Recently, Mannucci et al. (2010) and Lara-López et al. (2010) identify that the $M_\star$–Z relation depends on star formation rate (SFR), which is initially suggested by Ellison et al. (2008), and propose the fundamental metallicity relation (FMR) that forms a single plane in the stellar-mass, metallicity, and SFR space (see also Section 2.2). The FMR holds over $z \simeq 0 - 2.5$ with no evolution (Figure 1.3). This would indicate that there are physical processes commonly found in local and high-z galaxies. Many follow-up studies test the universality of the FMR over the wide range of stellar mass, SFR, and redshifts (e.g., Mannucci et al. 2011; Richard et al. 2011; Niino 2012; Yabe et al. 2012; Cresci et al. 2012; Wuyts et al. 2012; Christensen et al. 2012a; Belli et al. 2013; Lara-López et al. 2013). Although galaxies at $z \lesssim 2.5$ follow the FMR, galaxies at $z \gtrsim 3$ appear to fall below the FMR (Mannucci et al. 2010). Mannucci et al. (2010) claim that this disagreement suggests that there are physical mechanisms different from those of low-z galaxies at $z \sim 3$. However, this is still an open question.

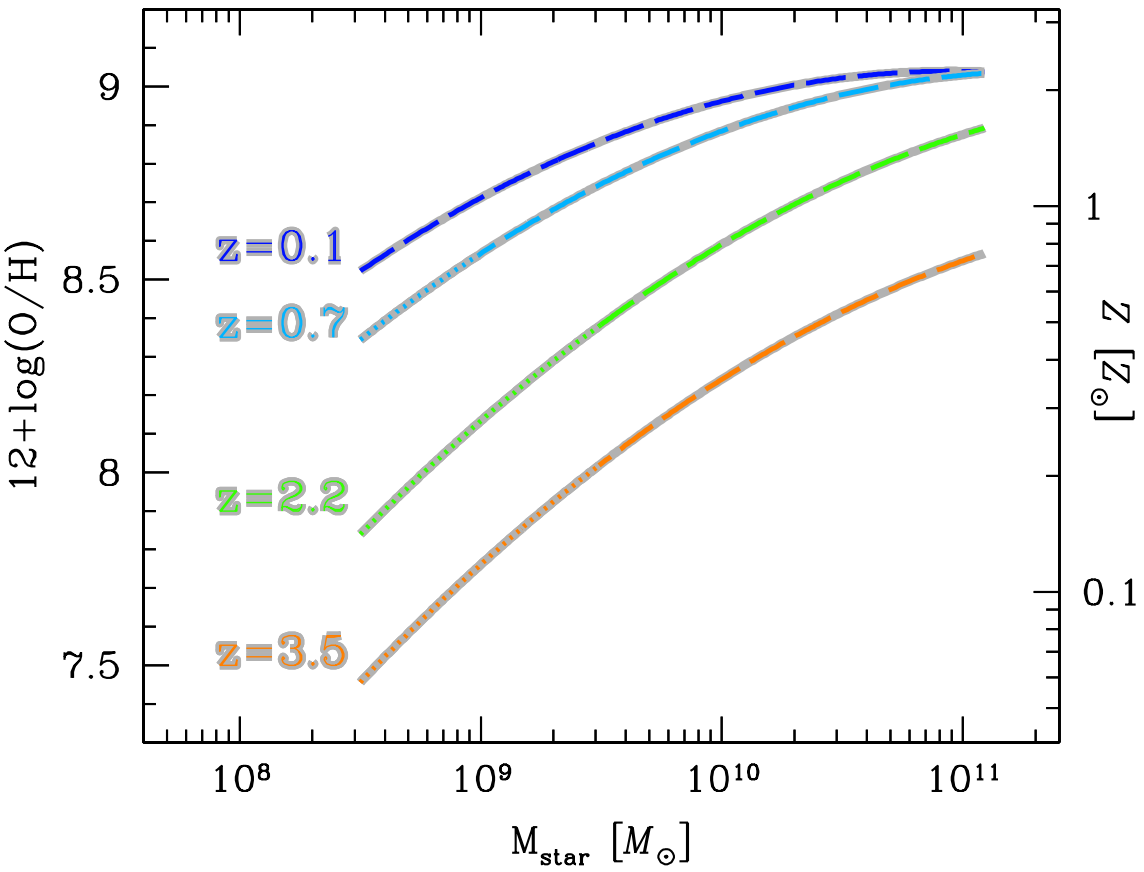

Figure 1.2. Previously claimed evolution of the $M_\star$–Z relation from $z = 0.1$ (blue; Tremonti et al. 2004; Kewley & Ellison 2008) to $z = 0.7$ (cyan; Savaglio et al. 2005), $z = 2.2$ (green; Erb et al. 2006a) and $z \sim 3$ (orange; Maiolino et al. 2008; Mannucci et al. 2009). These best-fit functions are given by Maiolino et al. (2008) for the $M_\star$–Z relation at $z \leq 2$, and by Mannucci et al. (2009) for the relation at $z \sim 3$. For each of the $M_\star$–Z relations, a mass range used to derive the $M_\star$–Z relation is indicated by dashed line, while the low-mass range whose $M_\star$–Z relation is a simple extrapolation of the best-fit function is displayed by dotted line. All data have been calibrated to the same metallicity scale of Maiolino et al. (2008).

In contrast to metallicities, ionization parameters of galaxies are poorly understood. An evolution of ionization parameter has been suggested, such that higher-z galaxies are found to have a higher ionization parameter (Lilly et al. 2003; Hainline et al. 2009; Richard et al. 2011) by using a diagram of [O III]/[O II] ratio and $R23$-index. However, the number of galaxies at $z > 2$ is small (~ 10), and the conclusive discussion of the evolution of ionization parameter remains to be obtained. In addition, until recently, statistical studies for ionization parameters do not cover (i) physical relations between ionization parameter and galaxy global properties, such as stellar mass and SFR, and (ii) evolution of the physical relations with ionization parameter. Dopita et al. (2006a) present that in the local universe an ionization parameter seems to gradually decrease with $M_\star$, but do not address the issue about evolution of this trend.

There is another diagnostics of ionization parameter, using a plot of [N II]/Hα and [O III]/Hβ ratios that is referred to as the BPT diagram (Baldwin et al. 1981). Local star-forming galaxies form a tight sequence on the BPT diagram (e.g., Kauffmann et al. 2003a). In contrast, high-z galaxies depart from the

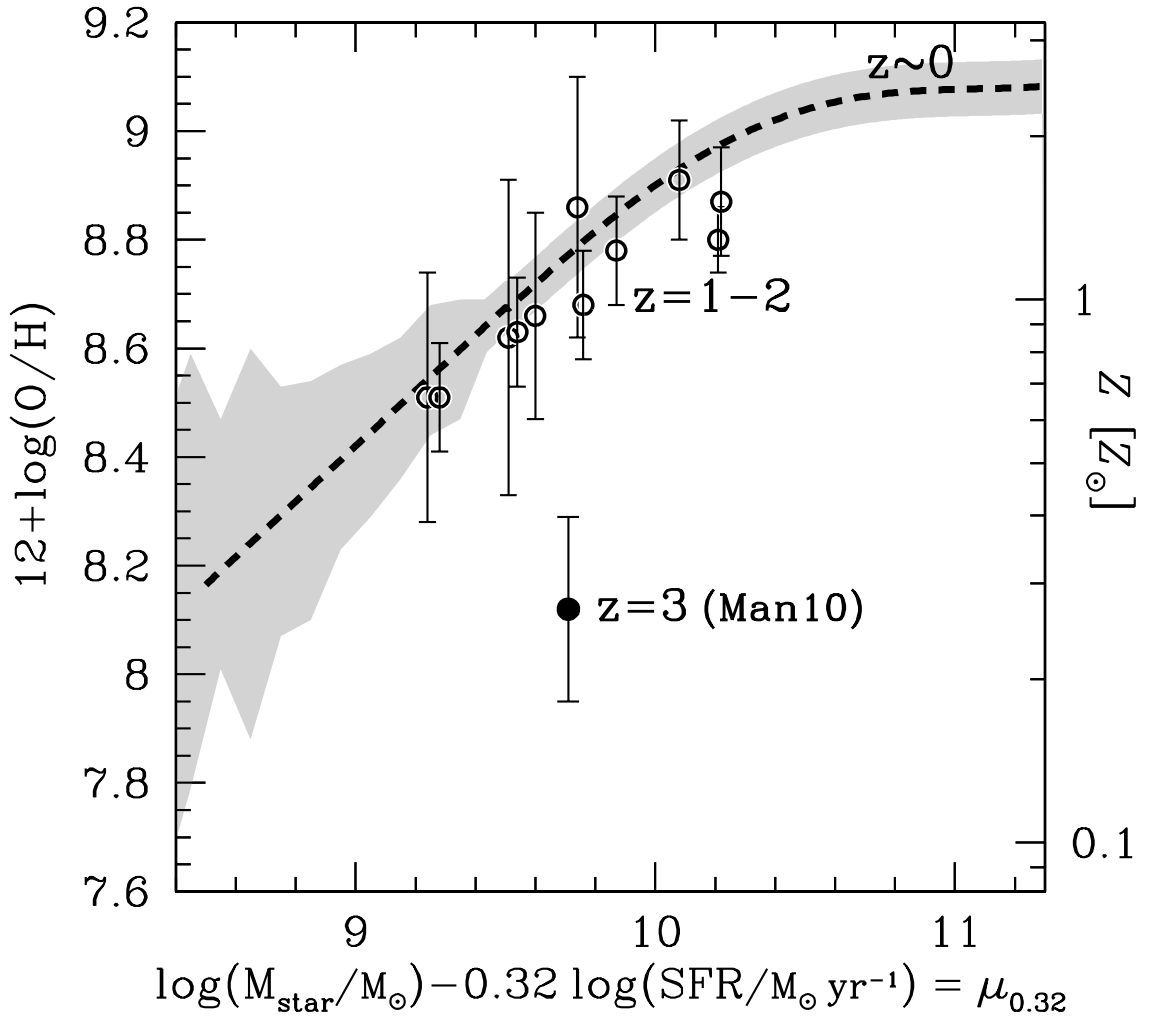

Figure 1.3. Local, intermediate-z, and high-z galaxies in the FMR plot. The black dashed curve and the gray shaded are indicate the FMR and its typical dispersion, respectively, defined with $z \sim 0$ galaxies (Mannucci et al. 2010, 2011). The black open and filled circles represent galaxies at $z = 1-2$ and $z \sim 3$, respectively, that are compiled by Mannucci et al. (2010). All data have been calibrated to the same metallicity scale of Maiolino et al. (2008).

local star-formation sequence towards higher [O III]/Hβ ratio (e.g., Shapley et al. 2005; Erb et al. 2006a; Liu et al. 2008; Hainline et al. 2009; Finkelstein et al. 2009b; Yabe et al. 2012). One interpretation of the departure is evolution of ionization parameter (e.g., Brinchmann et al. 2008; Kewley et al. 2013a,b). Kewley et al. (2013a) have compared high-z galaxy line ratios and theoretical predictions to investigate evolution of the star-forming sequence on the BPT diagram, and claimed that high-z galaxies would have a larger ionization parameter, a higher electron density, and/or a harder ionizing radiation field (see also Brinchmann et al. 2008; Kewley et al. 2013b).

Ionization parameters are also important for accurate estimates of metallicity from nebular emission lines. Since auroral lines for gas temperature determination are very faint, metallicity estimation methods based on local empirical relations (e.g., Equations 1.1 and 1.2; Maiolino et al. 2008) are often applied to high-z galaxies. These methods implicitly assume ionization parameters of typical local galaxies. Since various studies suggest that ionization parameter evolves with redshift, the estimated metallicities from

local empirical relations would be biased.

1.4. Cosmic Reionization

High redshift star-forming galaxies such as LAEs and LBGs are important to study the universe in the Epoch of Cosmic Reionization (EoR).

Today most hydrogen gas in the IGM of the universe is fully ionized, and we can see far into the universe. However, about 380,000 years after the Big Bang (at $z \sim 1100$), the temperature of the universe decreased below $\simeq 3,000$ K, allowing ions and electrons to combine into neutral hydrogen and helium. At that time, the IGM of the universe was completely neutral. Thus, there must have been an epoch, during which the IGM gas went from neutral to ionized, between $z = 0$–1100. This process is called cosmic reionization. For understanding the galaxy-, star-, quasar-, and structure-formations in the early universe, it is crucial to uncover the mysteries of the reionization, such that (i) when the reionization occurred, (ii) how it proceeded, and (iii) what the ionizing sources were.

The epoch of the end of the reionization has been constrained with the aid of so-called "Gunn-Peterson effect" (Gunn & Peterson 1965). Gunn & Peterson (1965) propose that if hydrogen gas with relatively high neutral fraction ($X_{\rm HI} > 10^{-4}$) is evenly distributed, radiation from a bright object (e.g., quasar) at that redshift is completely absorbed in the wavelengths below 1216 Å rest-frame. This absorption is called "Gunn-Peterson absorption trough." A complete Gunn-Peterson absorption tough would thus be detected for quasars in the EoR. By examining Gunn-Peterson absorption troughs of quasars at various redshifts in various directions, one can investigate the epoch of the end of the reionization, as well as the spatial distributions of how the reionization proceeded. By using the spectra of a sample of 19 quasars at $z = 5.74$–6.42 discovered by the SDSS, Fan et al. (2006) suggest that the Gunn-Peterson optical depths significantly increase at $z \sim 6$. This implies that $z \sim 6$ is the end of the overlapping stage of reionization.

Another useful way to study the EoR is to use statistical properties of LAEs at high-z. Since neutral hydrogen in the IGM absorbs Lyα photons from galaxies via the Lyα damping wing, the visibility of Lyα emission from high-z galaxies is sensitive to the neutral fraction of hydrogen in the IGM. We highlight two statistical properties used for the study of the reionization, Lyα luminosity function and fraction of LAEs among LBGs (Lyα fraction):

- The evolution of Lyα luminosity functions of high-z galaxies provides an useful insight to the reionization. Due to the increased fraction of neutral hydrogen in the IGM in the EoR, we expect a decreased number density of LAEs close to the EoR (e.g., Malhotra & Rhoads 2004; Kashikawa et al. 2006; Ouchi et al. 2010; Kashikawa et al. 2011). Malhotra & Rhoads (2004) find no significant change of Lyα luminosity functions between $z \sim 5.7$ and 6.6, while Kashikawa et al. (2006) suggest that Lyα luminosity function evolves from $z = 5.7$ to 6.6. By increasing the numbers of high-z LAEs, Ouchi et al. (2010) and Kashikawa et al. (2011) confirm the decrease of Lyα luminosity function from $z = 5.7$ to 6.6. This is in contrast to the UV luminosity functions of LAEs at $z = 5.7$ and 6.6, where no significant difference is found (e.g., Kashikawa et al. 2011). These recent studies of Lyα luminosity function have suggested that the neutral fraction in the IGM could be relatively high at $z \gtrsim 6$, consistent with the studies of Gunn-Peterson absorption troughs seen in high-z quasars. Ouchi et al. (2010) give a constraint of the neutral fraction $X_{\rm HI} \lesssim 0.2 \pm 0.2$ at $z = 6.6$, implying that the major reionization process took place at $z \gtrsim 7$.

- The fraction of galaxies showing strong Lyα emission among continuum-selected galaxies (i.e., LBGs), the Lyα fraction, can be another diagnostic to examine the ionization state of IGM at high-z (e.g., Stark et al. 2010). The Lyα fraction is suggested to be higher for less luminous LBGs, and to increase with redshift from $z \simeq 4$ to 6 (e.g., Ouchi et al. 2008; Vanzella et al. 2009; Stark et al. 2010, 2011). However, recent spectroscopic follow-up observations of $z \sim 7$ LBGs have found a sudden drop of the Lyα fraction from $z \sim 6$ to 7 (Vanzella et al. 2011; Pentericci et al. 2011; Ono et al. 2012; Schenker et al. 2012). This trend suggests that the neutral fraction of the IGM significantly increase from $z \sim 6$ to 7.

Not only as a tool, but also as the ionizing sources of the reionization, high redshift star-forming galaxies of LAEs and LBGs are important. Due to the steep decrease of number density of quasars with redshift at $z > 3$ (e.g., Fan et al. 2004), star-forming galaxies are likely to be a major ionizing source of the reionization in the early universe at $z > 6$–7. For understanding their role in the EoR, we need to know the escape fraction of ionizing photons, $f_{\rm esc}$, from the galaxies. Escaped ionizing photons are observed as Lyman-continuum (LyC) radiation, in the wavelengths shorter than $\lambda = 912$ Å rest-frame. Since the universe remains opaque to LyC photons at $z > 4$ (Inoue & Iwata 2008), direct measurements of $f_{\rm esc}$ for galaxies in the EoR are impossible. Alternatively, estimations of $f_{\rm esc}$ have been carried out for $z \sim 3$ galaxies, whose LyC radiation is observable in the shortest wavelength in optical, through spectroscopy (e.g., Steidel et al. 2001; Shapley et al. 2006) and narrowband imaging (e.g., Iwata et al. 2009; Vanzella et al. 2010; Nestor et al. 2011, 2013). As the latest result, Nestor et al. (2013) suggest that $z \sim 3$ galaxies have relatively high $f_{\rm esc}$ (~ 0.05–0.3). Since $f_{\rm esc}$ is known to be much smaller in the local universe (e.g., Leitherer et al. 1995), high-$f_{\rm esc}$ galaxies are likely to emerge at high-z (e.g., Inoue et al. 2006). Interestingly, among high-z star-forming galaxies, faint LAEs tend to have $f_{\rm esc}$ (~ 0.1–0.3) higher than bright LBGs ($f_{\rm esc} \sim 0.05$; e.g., Nestor et al. 2013). Studies of galaxies at $z \sim 6$–7 have identified a tension between the ionizing photon production rate and cosmic reionization (e.g., Ouchi et al. 2009; Robertson et al. 2010). A moderately high average $f_{\rm esc}$ of $\gtrsim 0.2$ would be required for galaxies in the early universe. Since LAEs are suggested to have a high $f_{\rm esc}$ and to be a more dominant population among star-forming galaxies at higher-z, more LAEs with a high $f_{\rm esc}$ would ease the tension of the deficit of ionizing photons at the early universe. However, the reason(s) why high-z galaxies, among which especially LAEs, tend to have a higher $f_{\rm esc}$ remains unclear.

Recently, a relationship between ionization parameter and $f_{\rm esc}$ and its importance for cosmic reionization are discussed. Theoretical studies have pointed out a possibility that $f_{\rm esc}$ positively correlates with ionization parameter, since an optically-thin nebula could show a high [O III]/[O II] ratio (e.g., Giammanco et al. 2005; Brinchmann et al. 2008; Kewley et al. 2013b; see also Section 5.1.5). If this correlation of ionization parameter and $f_{\rm esc}$ is established, ionization parameters allow us to investigate ionizing photon escapes that cannot be directly observed for galaxies at the EoR. Identifying ionization parameters for high-z star-forming galaxies of LAEs and LBGs is thus crucial, so that one can (i) confirm the trend that LAEs typically have an $f_{\rm esc}$ higher than LBGs with a different point of view, and (ii) understand the physical origin(s) of ionizing photon escape from galaxies.

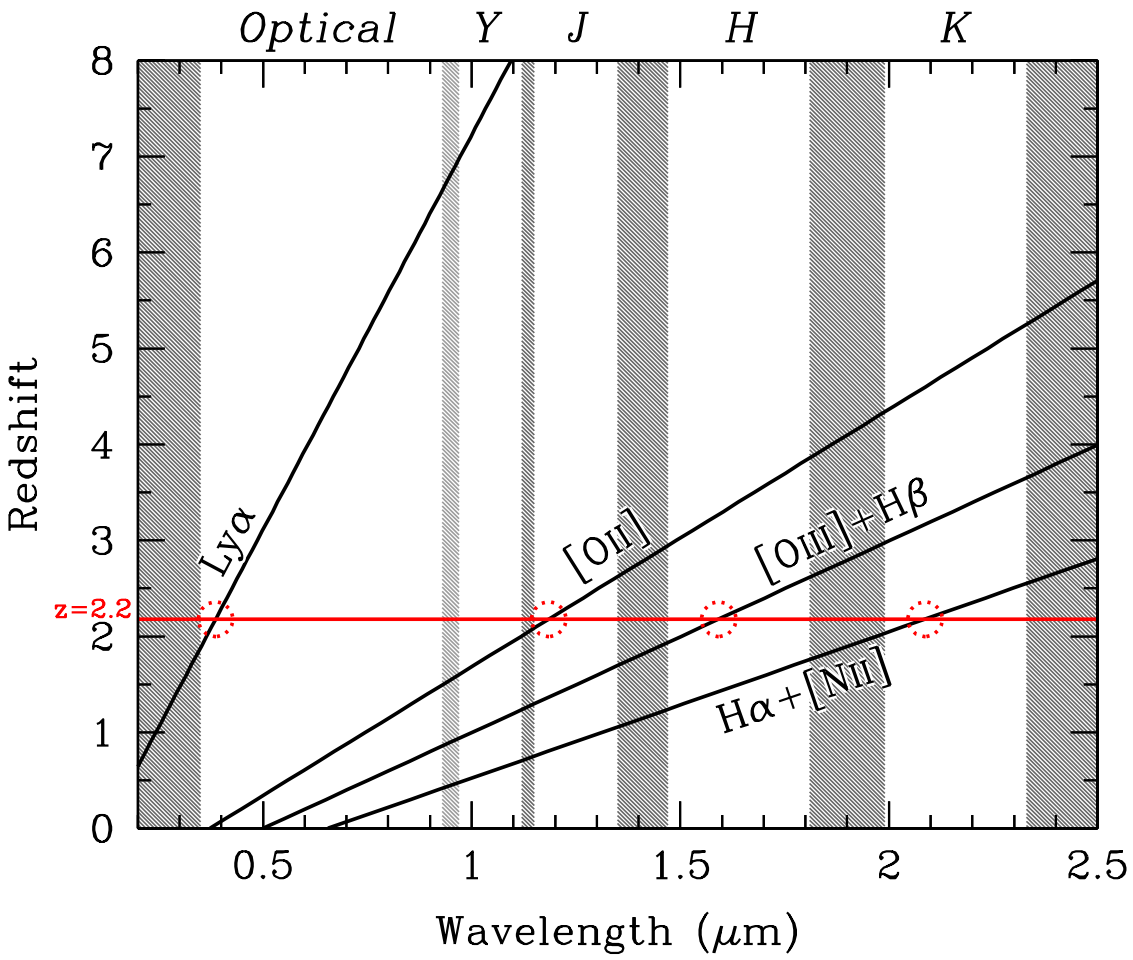

Figure 1.4. Visibility of Lyα, [O II]λ3727, [O III]$\lambda\lambda$5007,4959, Hβ, Hα, and [N II]$\lambda\lambda$6584,6548 emission lines along redshift. The thick lines trace the observed wavelength of the emission lines as a function of redshift. The unobservable wavelength ranges from the ground are shown in gray. At $z = 2.2$ (red line), Lyα emission line is observable in the bluest optical wavelength, and important rest-frame optical emission lines also fall into the *JHK* near-infrared wavelength ranges where we can observe from the ground.

1.5. Aims of This Thesis

In this thesis, we will investigate the evolution of galaxies traced by the essential gas properties of metallicity and ionization parameter. Especially, we direct a spotlight on ionization parameter, which has been frequently missed and/or implicitly assumed (fixed) to a certain value in many previous studies. We will demonstrate that ionization parameter is important to accurately estimate metallicities for star-forming galaxies especially at high-z, and to discuss the galaxy evolution appropriately.

We will make full use of the diagram of [O III]λ5007/[O II]λ3727 vs. R23-index to study ionization parameters and metallicities for galaxies at $z = 0$–3 with $\sim 140,000$ SDSS galaxies and ~ 100 galaxies at $z \gtrsim 1$ compiled from our data and from the literature. This diagram enables us to discuss the evolution of metallicity and ionization parameter with redshift. However, on the emission-line diagnostic diagrams like the [O III]/[O II] vs. R23-index diagram, dependencies of fundamental galaxy global properties of

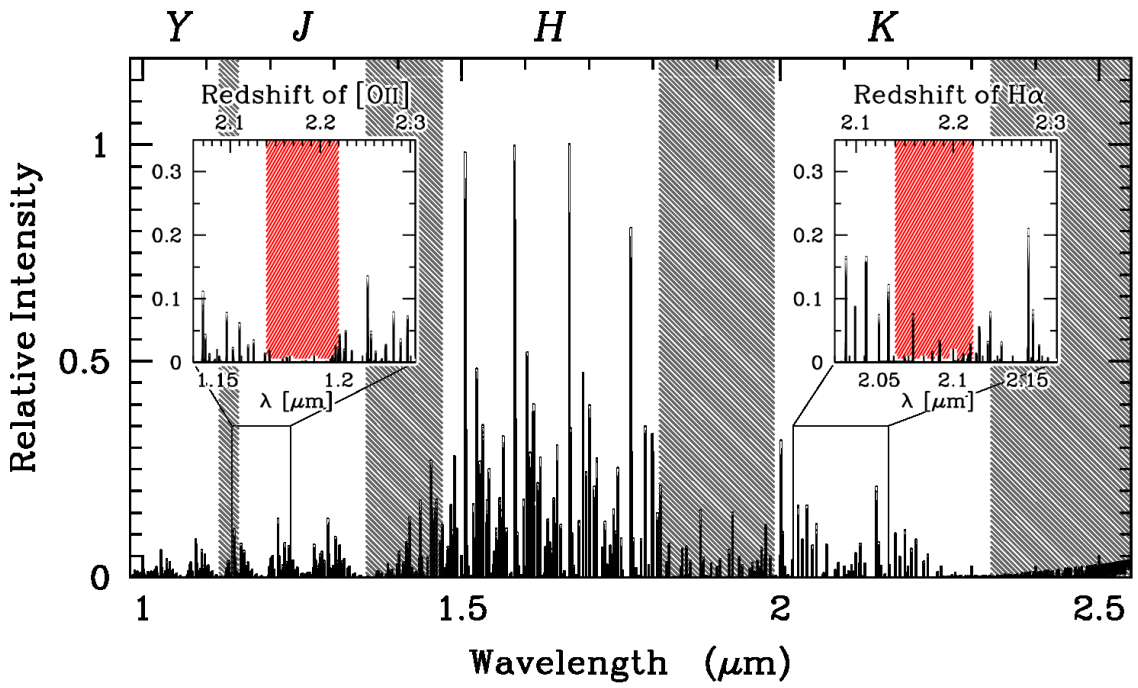

Figure 1.5. NIR spectrum of the sky background that is dominated by OH-lines. The wavelength ranges with low atmospheric transmission are shown in gray. The inner panels are a zoom-in around $\lambda \sim 1.2\,\mu$m and $2.1\,\mu$m, whose upper x-axis shows the redshift of [O II]λ3727 and Hα, respectively. In the two inner panels, the red shaded area displays the redshift range ($z = 2.14$–2.22), over which NB387 can select LAEs. At the redshifts, both [O II] and Hα fall in the wavelength ranges where OH-airglow is very weak.

stellar mass and SFR are invisible. Since metallicities are known to depend on stellar mass and SFR like the so-called fundamental metallicity relation (FMR; Mannucci et al. 2010; Lara-López et al. 2010), it is necessary to take into account the differences of stellar mass and SFR for a fair comparison between galaxies at different redshifts. We will thus extend the FMR with ionization parameter.

Previous high-z observations lack low-mass galaxies ($\lesssim 10^{9.5}\,M_\odot$) because most of them are based on continuum selected sample, such as LBGs. In order to obtain spectroscopic properties of less massive galaxies at high-z, we have carried out a large survey for $z \simeq 2.2$ LAEs, using our custom narrowband filter NB387 with Subaru/Suprime-Cam. The narrowband filter NB387 is newly developed by us, with a central wavelength and FWHM of 3870 Å and 94 Å, respectively, to select LAEs over $z = 2.14 - 2.22$. At this specific redshift range, important nebular lines such as [O II]λ3727, Hβ, [O III]$\lambda\lambda$5007, 4959, Hα, [N II]$\lambda\lambda$6584, 6548, are observable from the ground. Figure 1.4 clarifies the visibility of the nebular lines in the NIR JHK windows. The redshift $z \simeq 2.2$ is remarkably unique because [O II]λ3727 and Hα lines fall into a wavelength range where OH-airglow is very weak (Figure 1.5), thus enabling one to detect these lines not only by spectroscopy but also through NIR narrowband filters, which are developed to target the low OH-airglow wavelength ranges. We will present emission-line properties of the LAEs at $z \simeq 2.2$ by using both NIR spectroscopy and NIR narrowband imaging. Since LAEs are considered to be the least massive and the most efficiently star-forming galaxies (e.g., Ono et al. 2010a), LAEs provide us with the opportunity to explore parameter space in the relation between stellar mass, SFR, metallicity,

and ionization parameter, and to study the diversity of high-z galaxies.

Spectroscopic properties of LAEs are useful not only to study low-mass galaxies at high-z, but also to study the population of LAEs itself. Since their spectroscopic properties have been poorly understood, we will present a summary of LAEs' basic characteristics such as SFR, metallicity, EW(Lyα), etc., and compare them to those of LBGs to deepen our understanding of origin(s) of strong Lyα emission seen in LAEs. Furthermore, since LAEs are suggested to be an important population for the cosmic reionization (e.g., Iwata et al. 2009), identifying LAEs' properties is essential to evaluate roles of galaxies in the early universe. Especially, physical origins of how ionizing photons can escape from galaxies are of particular interest. We will present our photoionization model calculations to examine a relationship between $f_{\rm esc}$ and ionization parameter. By comparing LAEs with LBGs in terms of ionization parameter, we will provide an idea to explain a high $f_{\rm esc}$ for LAEs, which could have played an important role in supplying ionizing photons to the IGM in the early universe.

Layout of This Thesis

In Chapter 2, we present a systematic study for ionization parameter, metallicity, stellar mass ($M_\star$), and SFR of galaxies at $z \simeq 0$ with the $\sim 140,000$ SDSS galaxies. We also consider local galaxies whose characteristics are extreme and similar to those of high-z star-forming galaxies. We demonstrate that the diagnostic of [O III]/[O II] vs. R23-index diagram is useful to study the gas ionization state and metallicity in a galaxy with the aid of photoionization models. We then clarify the dependencies of ionization parameter on galaxy global properties of stellar mass, SFR, and metallicity for the local galaxies. We introduce a new relation that is described in the four-dimensional parameter space of [O III]/[O II] ratio, R23-index, stellar mass, and SFR.

In Chapters 3 and 4, we extend our studies of ionization parameter and metallicity of galaxies towards higher-z. Since previous high-z observations lack LAEs, we present in Chapter 3 physical properties of LAEs at $z \simeq 2.2$ identified in our own observations. Detailed description of the LAE sample is given in Appendix A. We first report results from our NIR follow-up spectroscopy of $z \simeq 2.2$ LAEs. We successfully detect Hα emission from seven LAEs, and perform a detailed analysis of six LAEs, free from active galactic nucleus activity, two out of which, CDFS-3865 and COSMOS-30679, have [O II] and [O III] line detections. They are the first [O II]-detected LAEs at high-z, and their [O III]/[O II] ratios and R23-index provide the first simultaneous determinations of ionization parameter and metallicity for LAEs. Full analysis is found in Appendix B. We then present the average metallicity and SFR of $z \simeq 2.2$ LAEs measured from [O II]λ3727, and Hα (+[N II]$\lambda\lambda$6584, 6548), which are obtained by the two NIR narrowband filters NB118 ($\lambda_c = 11866$Å, FWHM$= 111$Å) and NB209 ($\lambda_c = 20958$Å, FWHM$= 205$Å), respectively, developed by J. Lee et al. (Lee et al. in preparation; see also Ly et al. 2011; Lee et al. 2012). By using a stacking analysis of the NIR narrowband images of the LAEs, we will obtain average nebular-line fluxes of LAEs. Full description is provided in Appendix C. Although no estimation of ionization parameter is obtained by the NIR narrowband survey, the estimated metallicity and SFR are useful to investigate average properties of low-mass LAEs on the $M_\star$-SFR-metallicity plane.

In Chapter 4, we present the extended study of ionization state and metallicity of galaxies at higher-z. By using 69 intermediate-z ($z = 0.5 - 1.5$) and 39 high-z ($z \sim 2 - 3$) galaxies including both LBGs and LAEs, we show their ionization parameters and metallicities based on the relation between [O III]/[O II] ratio and R23-index. We then present the distribution of the intermediate- and high-z galaxies on the relation between [O III]/[O II] ratio, R23-index, stellar mass, and SFR derived with the SDSS sample.

We discuss the universality of the relation over cosmic time.

In Chapter 5, we discuss the observational results found in this work, addressing the issues of (i) the evolution of ionization parameter, (ii) its possible origins, (iii) the FMR evolution at $z \gtrsim 3$, (iv) the relations between [O III]/[O II] ratio, $R23$-index, stellar mass, and SFR, and (v) the correlation between ionization parameter and $f_{\rm esc}$. In the second half of the Chapter, we mainly focus on the basic characteristics of LAEs at high-z. Although the sample size is still small, we discuss the pilot results of LAEs' spectroscopic properties by comparing them to those of LBGs at similar redshifts.

In Chapter 6, we present our conclusions. Finally, in Chapter 7, we describe some future prospects. In order to advance the study presented in this thesis, we have been carrying out NIR multi-object spectroscopy of high-z galaxies of LAEs, LBGs, and LyC leaking galaxies with Subaru/FMOS and Keck/MOSFIRE. We briefly show the results of the observations, and finish this thesis by presenting goals of these on-going studies.

Throughout this paper, we use the AB magnitude system (Oke 1974), and assume an Asplund et al. (2009) solar metallicity, where $\log(Z/Z_\odot) = 12 + \log({\rm O/H}) - 8.69$. We estimate stellar masses and SFRs based on a Chabrier (2003) initial mass function (IMF) except for Chapter 3 and Appendices B and C, where we use a Salpeter (1955) IMF. The resulting stellar masses and SFRs are scaled to the Chabrier (2003) IMF by dividing them by a factor of 1.7 (e.g., Pozzetti et al. 2007) in the other chapters. We adopt a concordance ΛCDM cosmology with $(\Omega_m, \Omega_\Lambda, H_0) = (0.3, 0.7, 70\,{\rm km\,s^{-1}\,Mpc^{-1}})$.

2 Ionization State and Metallicity of Local Galaxies

In this chapter, we present a systematic study for ionization parameter, metallicity, stellar mass ($M_\star$), and SFR of galaxies at $z \simeq 0$ with the $\sim 140,000$ SDSS galaxies. We demonstrate that the diagnostic of [O III]/[O II] vs. $R23$-index diagram is useful to study the gas ionization state and metallicity in a galaxy.

We describe the local galaxy samples in Section 2.1, and test whether our SDSS sample reproduces the FMR in Section 2.2. In Section 2.3, We show the SDSS galaxies in the [O III]/[O II] vs. $R23$-index diagram, and investigate galaxy properties in the diagram with the aid of photoionization models. We then clarify the dependencies of ionization parameter on galaxy global properties of stellar mass, SFR, and metallicity.

2.1. Local Galaxy Samples

2.1.1. SDSS Galaxies

We make an SDSS sample from the SDSS Data Release 7 MPA/JHU catalog[2.1] including emission line properties and stellar masses (Kauffmann et al. 2003b; Brinchmann et al. 2004; Salim et al. 2007). We select galaxies with the criteria similar to those adopted by Mannucci et al. (2010); (1) $0.07 < z < 0.30$, (2) a signal-to-noise ratio (S/N) of H$\alpha > 25$, (3) $A_V < 2.5$, (4) Hα/H$\beta > 2.5$, (5) active galactic nuclei (AGN) are removed based on the BPT diagram (Baldwin et al. 1981) with the classification of Kauffmann et al. (2003a), (6) metallicities estimated from the $N2$- and $R23$-index (Maiolino et al. 2008) agree within 0.25 dex. We adopt the average value of the two metallicities[2.2], and use total stellar masses listed in the updated MPA/JHU stellar mass catalog[2.3]. All the emission line fluxes are corrected for extinction using Hα/Hβ and the extinction curve given by Cardelli et al. (1989). SFRs are estimated from the Hα luminosities by using the Kennicutt (1998)'s relation with the correction to the Chabrier (2003) IMF. We remove the same objects in the catalog that are found by the MPA/JHU group. We thus obtain 136,067 SDSS galaxies.

In this sample, we highlight two populations of galaxies shown below.

- Green Pea galaxies (GPs; Cardamone et al. 2009) that are local star-forming galaxies with a very strong [O III] emission line whose EW is ~ 1000 Å. They are found in the SDSS spectroscopic sample of galaxies with green colors in the SDSS *gri* composite images, where the strong [O III]

[2.1] http://www.mpa-garching.mpg.de/SDSS/DR7/

[2.2] These metallicities are only used for the consistency check of the FMR of Mannucci et al. (2010) (Section 2.2).

[2.3] http://home.strw.leidenuniv.nl/~jarle/SDSS/

emission fall in the *r* band. Because the strong [O III] emission has to be redshifted to the bandpass of *r*, the redshift of GPs ranges from 0.112 to 0.360. We use 80 GPs given by Cardamone et al. (2009) that are free from AGN contamination. We cross-match the 80 GPs to our SDSS galaxies, and identify 51 GPs. To include GPs at $z > 0.30$, we perform the same cross-matching to SDSS galaxies that do not meet the redshift criterion of (1), and obtain additional 15 GPs at $z > 0.3$. We use a total of $66 = (51 + 15)$ GPs in our analysis.

- Lyman-break Analogs (LBAs; Heckman et al. 2005; Hoopes et al. 2007; Basu-Zych et al. 2007; Overzier et al. 2008, 2009) that are super-compact UV-luminous local galaxies whose characteristics are similar to those of high-z LBGs. The UV imaging survey performed by the *Galaxy Evolution Explorer (GALEX)* is used to select star-forming galaxies at $0.1 < z < 0.3$ with a high luminosity of $L_{\rm FUV} > 10^{10.3}\,L_{\odot}$ and a high far UV surface brightness of $I_{\rm FUV} > 10^{9}\,L_{\odot}\,{\rm kpc}^{-2}$. We compile catalogs of Hoopes et al. (2007), Basu-Zych et al. (2007), and Overzier et al. (2009), and obtain 44 LBAs. Cross-matching them to our SDSS galaxies, we make an LBA sample composed of 33 LBAs.

We remove sources in our GP and LBA samples from our SDSS galaxies, and define a sample of SDSS galaxies with no GPs and LBAs as SDSS sample.

2.1.2. LyC Leakers

There are two local star-forming galaxies emitting Lyman-continuum (LyC) radiation, Haro 11 (Bergvall et al. 2006; Leitet et al. 2011) and Tol 1247-232 (Leitet et al. 2013). In order to study the relation between ionization parameter and ionizing photon escape, we investigate the two LyC leaking galaxies. Hereafter we refer to these two galaxies as LyC leakers. Emission line fluxes for Haro 11 and Tol 1247-232 are obtained from Bergvall & Östlin (2002) and Terlevich et al. (1993), respectively, and stellar masses from Leitet et al. (2013). Their SFRs are derived in the same manner as those of our SDSS galaxies (Section 2.1.1). Neither of them is contaminated by AGN (Leitet et al. 2013). We note that Haro 11 can be classified as an LBA (Heckman et al. 2011).

2.2. Testing FMR with Our SDSS Sample

Before we present our analysis results, we test whether our SDSS sample reproduces the FMR (Mannucci et al. 2010), in order to demonstrate that our SDSS sample is well-constructed and that we can handle the large sample appropriately. For this purpose, we derive metallicities based on the Maiolino et al.'s (2008) empirical relations, as adopted by Mannucci et al. (2010) (Section 2.1.1). It should be noted that our main discussion is based on metallicities derived with ionization parameter from the photoionization models of Kewley & Dopita (2002) (e.g., Section 2.3.3). In Figure 2.1, three panels show the $M_{\star}$-metallicity (top left), SFR-metallicity (top right), and $\mu_{0.32}$-metallicity (bottom) plots with our SDSS sample. The variable μ_{α} is defined as a combination of $M_{\star}$ and SFR,

$$\mu_{\alpha} = \log(M_{\star}) - \alpha \log({\rm SFR}), \tag{2.1}$$

where α is a free parameter. Mannucci et al. (2010) obtain $\alpha = 0.32$ that minimizes the scatter of their SDSS galaxies in the μ_{α}-metallicity plane. The colored lines in each panel represent a mean metallicity

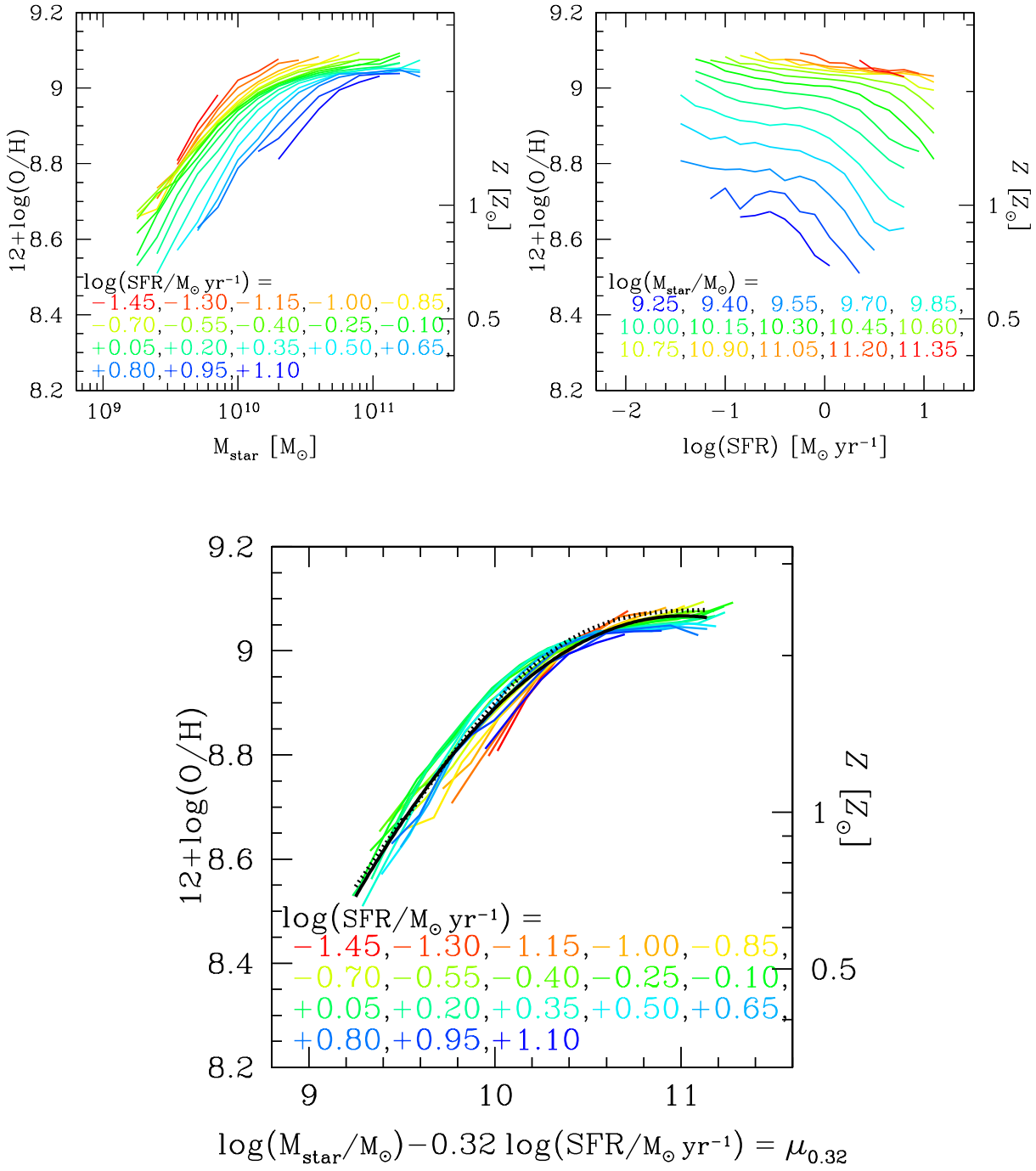

Figure 2.1. *Top Left:* The mass-metallicity relations of galaxies from our SDSS sample. Each line denotes a SFR subsample from our SDSS sample whose SFR is presented at the bottom of the panel. *Top Right:* The SFR-metallicity relation given by our SDSS sample. The lines represent the relations for subsamples with $M_\star$ values shown in the legend. *Bottom:* Same as the top left panel, but for the $\mu_{0.32}$-metallicity relation, a two-dimensional view of the FMR. The color code is the same as the one in the top left panel. The black solid curve is the quadratic best-fit of our SDSS sample, while the black dotted curve is the original FMR obtained by Mannucci et al. (2010) and Mannucci et al. (2011). The black solid and dotted lines are almost identical. Thus, our SDSS sample reproduces the original FMR.

of our SDSS galaxies for subsamples defined with SFR (top left and bottom panels) and $M_\star$ (top right panel) in a 0.15 dex range. We display subsamples containing > 50 galaxies.

In the bottom panel of Figure 2.1, the solid black curve indicates the quadratic best-fit of our SDSS sample, while the dotted curve presents the original FMR (Mannucci et al. 2010, 2011). The original FMR is expressed by a combination of a linear and a 4th-order polynomial functions, such that

$$\begin{aligned} 12+\log(\mathrm{O/H}) &= 8.90+0.37m-0.14s-0.19m^2 \\ &\quad +0.12ms-0.054s^2 \quad \text{for } \mu_{0.32}>9.5 \\ &= 8.93+0.51(\mu_{0.32}-10) \quad \text{for } \mu_{0.32}<9.5, \end{aligned} \tag{2.2}$$

where $m=\log(M_\star)-10$ and $s=\log(\mathrm{SFR})$ in solar units. From this plot, the FMR of our SDSS sample is almost identical to that of Mannucci et al. (2010, 2011). Therefore, we conclude that our SDSS sample successfully reproduces the original FMR of Mannucci et al. (2010)[2.4].

2.3. Ionization State of Galaxies at $z = 0$

2.3.1. [O III]/[O II] vs. $R23$-index Diagram

As briefly mentioned in Chapter 1, we utilize the [O III]/[O II] ratio versus $R23$-index diagram to discuss gas properties of ionization parameter and metallicity in galaxies (see also Kewley & Dopita 2002). Figure 2.2 is the diagram of [O III]/[O II] ratio and $R23$-index with our local galaxies. The underlying gray dots are the SDSS galaxies. Figure 2.2 indicates that galaxies with a higher $R23$-index have a higher [O III]/[O II] ratio. The two local galaxies of GPs and LBAs are shown with green and purple open circles, respectively. These galaxies, especially GPs, present the highest $R23$-index and [O III]/[O II] ratio among the local galaxies. Interestingly, the LyC leakers (orange pentagons) have values of [O III]/[O II] ratio and $R23$-index similar to those of GPs and LBAs.

2.3.2. Physical Origin of Large [O III]/[O II] Ratio

In Section 2.3.1, we have found the trend that galaxies with a higher $R23$-index have a higher [O III]/[O II] ratio in the local universe, covering over ~ 2 orders of magnitude in [O III]/[O II] ratio. In this section, we investigate the physical origin of large [O III]/[O II] ratios, using photoionization models. There are five physical parameters of nebulae that change the [O III]/[O II] ratio, a) spectral shape of ionizing source, b) gas temperature, c) metallicity, d) ionization parameter, and e) gas density. First, if the incident ionizing source includes an AGN whose spectrum is hard, high-ionization lines are stronger than low-ionization lines. However, since our samples are free from a significant AGN contamination (Section 2.1.1), the ionizing source difference does not significantly change the [O III]/[O II] ratio. Second, gas temperature changes the emissivity of [O III] and [O II] lines. Gas temperature is determined by the metal abundance, because coolings are dominated by collisionally excited metal ions such as O^+, O^{2+}, N^+ etc. We simply regard metallicity as a control parameter of temperature, and investigate the temperature dependence on the basis of gas metallicity. Thus, there are three key parameters, metallicity, ionization parameter, and gas density, that affect the [O III]/[O II] ratio.

[2.4] In our SDSS sample, we find a value of $\alpha = 0.30$ that minimizes the scatter in the μ_α-metallicity plane. However, the difference of residual dispersion of metallicity between $\alpha = 0.32$ and 0.30 is negligibly small, 0.0251 and 0.0255 dex, respectively.

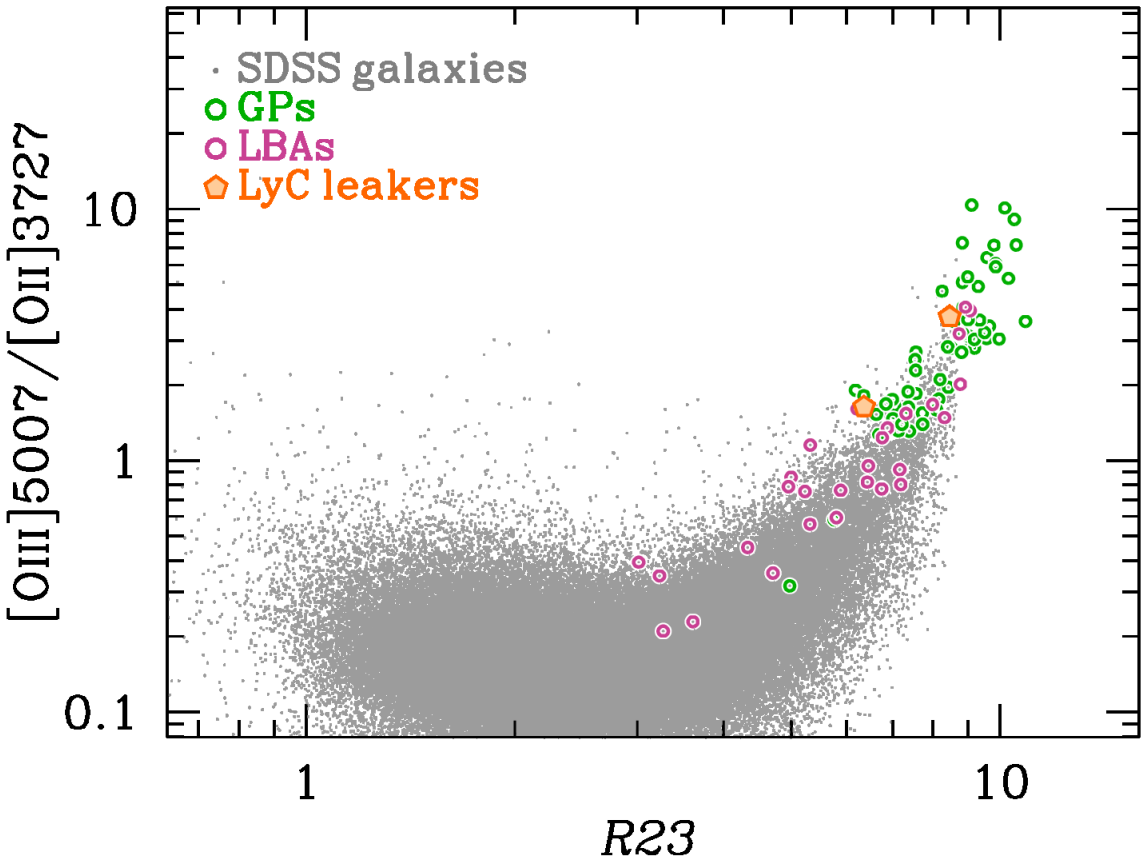

Figure 2.2. The relation between [O III]/[O II] and *R*23-index. The gray dots are the SDSS galaxies. The green and purple circles show GPs and LBAs, respectively, and the orange pentagons are LyC leakers in the local universe.

In Figure 2.3, we plot the photoionization models given by Kewley & Dopita (2002) with the black curves. The models predict line ratios at a given metallicity and ionization parameter with a fixed gas pressure of $P/k = 10^5\,\mathrm{cm^{-3}\,K}$[2.5] assuming isobaric conditions. The models in Figure 2.3 indicate that the [O III]/[O II] ratio and *R*23-index depend on metallicity and ionization parameter. In Figure 2.4, we show both the local galaxy samples and the photoionization models shown in Figure 2.2 and Figure 2.3, respectively, so that we can directly compare the data and models.

The models of Figure 2.3 present three important trends on the [O III]/[O II] vs. *R*23-index diagram;

1. [O III]/[O II] ratio increases with ionization parameter.

2. [O III]/[O II] ratio decreases with metallicity.

3. *R*23-index increases in a low-metallicity regime (low-*Z* branch) from $12 + \log(\mathrm{O/H}) = 7.5$ to ~ 8.5, and decreases in a high-metallicity regime (high-*Z* branch) from $12 + \log(\mathrm{O/H}) \sim 8.5$ towards a higher metallicity.

The trend of (1) is explained by the boost of high-energy ionizing photons as the ionization parameter increases. Such high-energy photons produce more abundant [O III]. The trend of (2) is caused by a

[2.5] For electron temperatures of 10^4 K. This pressure corresponds to a density of order $10\,\mathrm{cm^{-3}}$.

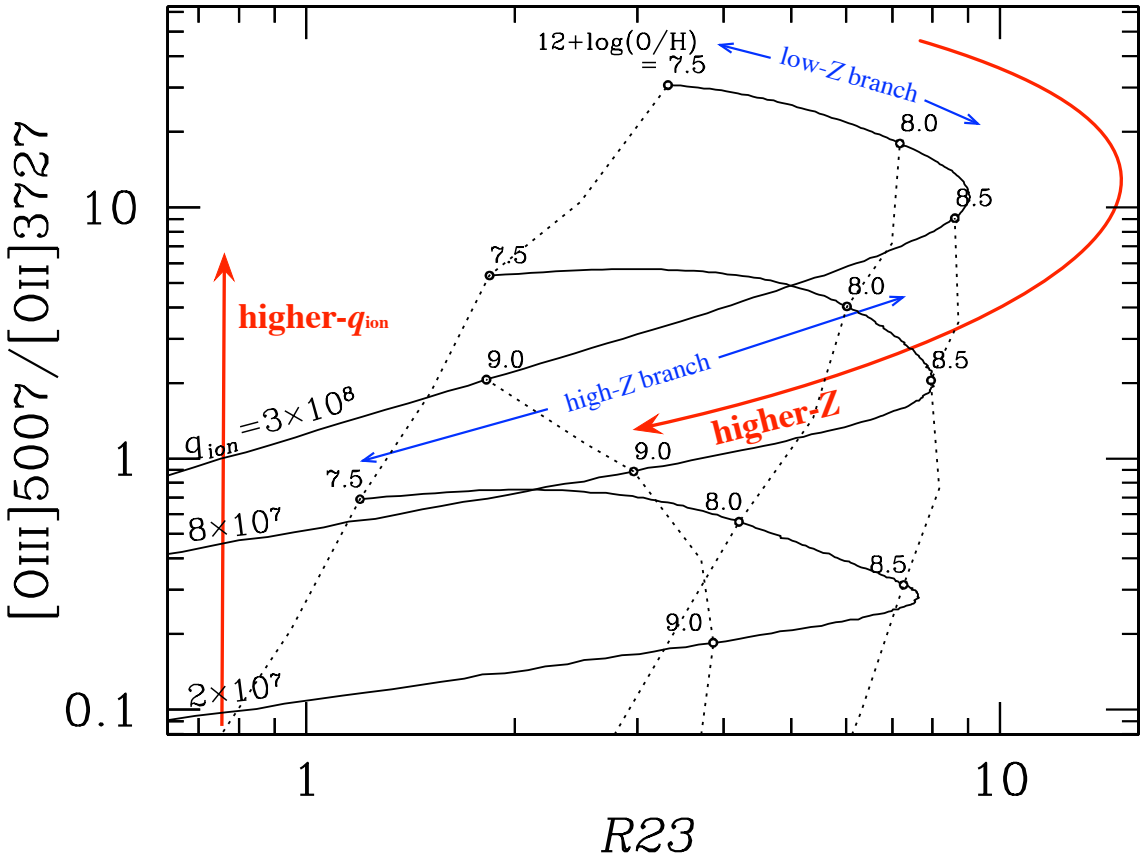

Figure 2.3. The relation between [O III]/[O II] and *R*23-index with photoionization models. The black solid curves present photoionization model tracks in the range of $12+\log(\mathrm{O/H})= 7.5-9.5$ for $q_{\rm ion}$ $=3\times10^8$, 8×10^7, and 2×10^7 cm s^{-1} (Kewley & Dopita 2002). The numbers with the small open circles on the model tracks denote metallicities in $12+\log(\mathrm{O/H})$. The dotted lines connect the photoionization model curves with the same metallicity value.

decrease of gas temperature in an HII-region. As gas metallicity increases, gas temperature drops due to cooling of metal lines. For gas clouds with high metallicity, the far-infrared fine-structure cooling of O^{2+} is more efficient than those in optical wavelength (e.g., Charlot & Longhetti 2001; Dopita et al. 2000). Thus, in optical wavelength, [O III] emission becomes faint, while [O II] emission does not change dramatically, which makes a decrease of [O III]/[O II] ratio to a higher metallicity. Similarly, the trend of (3) in the high-*Z* branch of $12+\log(\mathrm{O/H}) \gtrsim 8.5$ is explained by the weak optical [O III]+[O II] emission with more dominant far-infrared fine-structure cooling. Thus, the *R*23-index decreases with metallicity. On the other hand, in the low-*Z* branch of $12+\log(\mathrm{O/H}) \lesssim 8.5$, optical collisional excitation lines including [O III] and [O II] are the most efficient cooling radiation, *R*23-index increases as oxygen abundance, i.e., metallicity, increases. To summarize, the [O III]/[O II] ratio depends strongly on ionization parameter and moderately on metallicity. *R*23-index is mainly governed by metallicity, but also depends, albeit weakly, on ionization parameter.

In addition to metallicity and ionization parameter, emission line ratios would be changed by gas density. In fact, the recent study of Shirazi et al. (2013) argues that the large [O III]/[O II] ratio of high-*z*

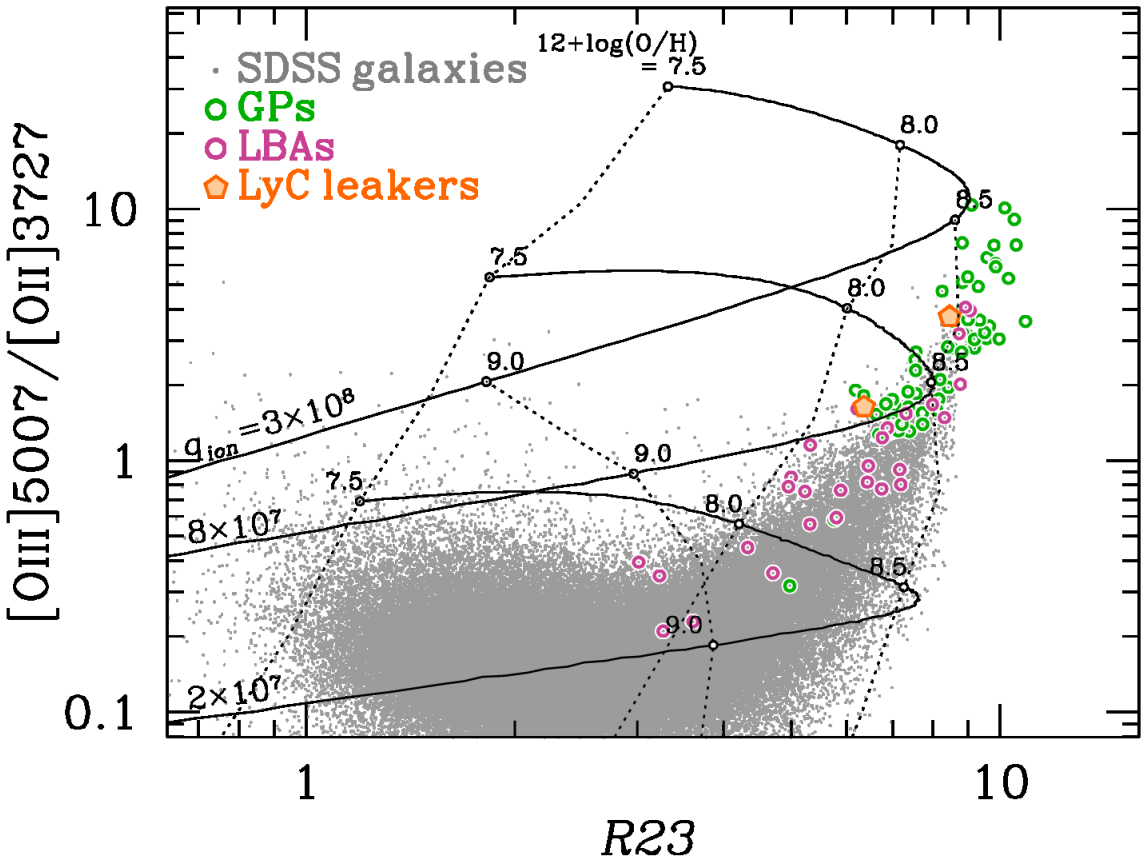

Figure 2.4. The relation between [O III]/[O II] and $R23$-index for the local galaxy samples (Figure 2.2) with photoionization models (Figure 2.3).

galaxies is explained by a high gas density. This argument is based on the following ideas. The ionization parameter is defined by

$$q_{\rm ion} = \frac{Q_{\rm H^0}}{4\pi R_{\rm s}^2 n_{\rm H}}, \tag{2.3}$$

where $Q_{\rm H^0}$ is the number of hydrogen ionizing photons per second, $R_{\rm s}$ is the Strömgren radius, and $n_{\rm H}$ is the total hydrogen density. The hydrogen ionizing photon production rate of $Q_{\rm H^0}$ is balanced by a recombination rate under the assumption of ionization equilibrium,

$$Q_{\rm H^0} = \frac{4}{3}\pi R_{\rm s}^3 n_{\rm H}^2 \alpha_B \varepsilon, \tag{2.4}$$

where α_B is a coefficient of the total hydrogen recombination to the $n > 1$ levels, and ε is the volume filling factor of the ionized gas. The combination of Equations (2.3) and (2.4) yields

$$q_{\rm ion}^3 \propto Q_{\rm H^0}\, n_{\rm H}\, \varepsilon^2. \tag{2.5}$$

By the comparison with low and high redshift galaxies with similar $M_\star$ and SFR, Shirazi et al. (2013) have found that the high-z galaxies show an [O III]/[O II] ratio higher than low-z counterparts by ~ 0.5 dex, indicating that high-z galaxies have a higher $q_{\rm ion}$ than the low-z counterparts by ~ 0.3 dex. Based on Equation (2.5), Shirazi et al. (2013) have argued that $n_{\rm H}$ increases by a factor of ~ 8 to high-z, assuming that high-z galaxies and their low-z counterparts have similar $Q_{\rm H^0}$ and ε values.

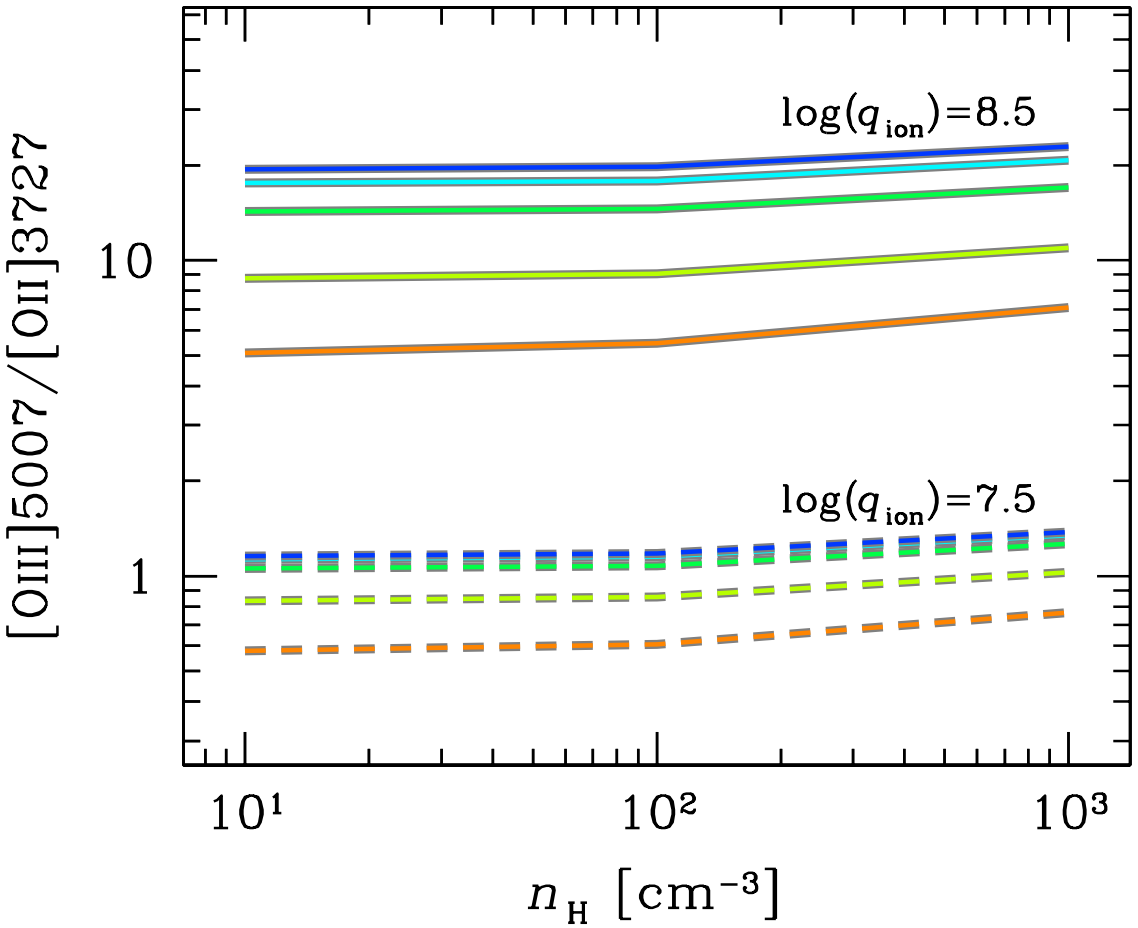

Figure 2.5. [O III]/[O II] vs. $n_{\rm H}$ predicted by CLOUDY for $\log(q_{\rm ion}) = 8.5$ (solid lines) and 7.5 (dashed lines). The blue, cyan, green, light green, and orange lines indicate a metallicity of $Z = 0.05$, 0.1, 0.2, 0.5, and $1.0\,Z_{\odot}$, respectively.

Motivated by the study of Shirazi et al. (2013), we investigate the dependence of [O III]/[O II] ratios on $n_{\rm H}$ as well as metallicity and ionization parameter. We perform photoionization model calculations with CLOUDY version 13.02 (Ferland et al. 1998, 2013). We assume a constant-density homogeneous cloud with a spherically closed geometry. A volume filling factor of the ionized gas is assumed to be unity for simplification. We include dust physics and the depletion factors of the various elements from the gaseous phase in the same manner as the analysis of Dopita et al. (2006b). Table 2.1 summarizes the adopted solar metallicities and gas-phase depletion factors. In non-solar metallicities, we assume that both the dust model and the depletion factors are unchanged, but the dust abundance is assumed to scale linearly with the gas metallicity, as adopted in Nagao et al. (2011). All elements except for nitrogen, carbon, and helium are taken to be primary nucleosynthesis elements. For nitrogen, we use a form given by López-Sánchez et al. (2012) to take account of its secondary nucleosynthesis component in a high metallicity range. For carbon and helium, we use forms in Dopita et al. (2006b). Photoionization models are calculated with the parameters of $Z = (0.05, 0.1, 0.2, 0.5, 1.0)\,Z_{\odot}$, $\log(q_{\rm ion}/{\rm cm\,s^{-1}}) = (7.5, 8.0, 8.5)$, and $n_{\rm H} = (10, 10^2, 10^3)\,{\rm cm^{-3}}$. The calculations are stopped at the depth where the electron density reaches 1 % of the total hydrogen density. The incident ionizing radiation fields are generated by STARBURST99 (Leitherer et al. 1999). We use instantaneous burst models at zero age with a Kroupa (2001)

IMF and lower and upper mass limits of 0.1 and $120\,M_{\odot}$, respectively. Stellar metallicities are matched to the gas-phase ones.

Figure 2.5 shows the CLOUDY calculation results on the [O III]/[O II] vs. $n_{\rm H}$ plane, and indicates that the [O III]/[O II] ratio increases only by $\lesssim 0.1$ dex from $n_{\rm H} = 10$ to $10^3\,{\rm cm}^{-3}$. This small change of [O III]/[O II] ratio is given by the density dependence of collisional deexcitation. Since both [O III] and [O II] are collisionally excited lines, their intensities are similarly enhanced in a high-density cloud. Thus, the [O III]/[O II] ratio is almost unchanged if the density is significantly smaller than their critical densities of $7 \times 10^5\,{\rm cm}^{-3}$ for [O III] and $(3\text{–}16) \times 10^3\,{\rm cm}^{-3}$ for [O II] (Osterbrock 1989). Figure 2.5 has confirmed that [O III]/[O II] ratio does not largely depend on the gas density (see also Fig. 1(f) in Charlot & Longhetti 2001). In contrast, ionization parameter and metallicity largely change the [O III]/[O II] ratio. Figure 2.5 presents that the [O III]/[O II] ratio is boosted by an order of magnitude from $\log(q_{\rm ion}) =$ 7.5 to 8.5. Similarly, the [O III]/[O II] ratio increases by a factor of $\sim 2-4$, if metallicity changes, by an order of magnitude, from $Z = 1.0$ to $0.1\,Z_{\odot}$.

Figure 2.5 suggests that the [O III]/[O II] ratio does not largely depend on $n_{\rm H}$, but ionization parameter and metallicity. Because Shirazi et al. (2013) argue the $n_{\rm H}$ evolution from the [O III]/[O II] ratios, our results of Figure 2.5 appear to be inconsistent with the argument of Shirazi et al. (2013). A key difference between the analyses of Shirazi et al. (2013) and ours is the treatment of $Q_{\rm H^0}$. Shirazi et al. (2013) assume that $Q_{\rm H^0}$ is the same in galaxies at high-z and their low-z counterparts, and conclude the increase of $n_{\rm H}$ from the increase of $q_{\rm ion}$ with Equation (2.5). It should be noted that, under the assumption of $Q_{\rm H^0}$ constant and the HII-region with a homogeneous density profile, the increase of $n_{\rm H}$ makes the radius of the HII-region small (Equation 2.4). This geometric effect could be implicitly associated with the conclusion of $n_{\rm H}$ increase under this assumption of constant $Q_{\rm H^0}$. On the other hand, our calculation varies $Q_{\rm H^0}$, and predicts [O III]/[O II] ratios at given ionization parameter and density. Although Shirazi et al. (2013) justify the same $Q_{\rm H^0}$ value for high and low-z galaxies with a similar SFR, it would not be the case, with different metallicity, stellar age, and IMF taken into account. For example, if high-z galaxies are metal poor, $Q_{\rm H^0}$ of high-z galaxies are higher than low-z galaxies with a given SFR. The evolution of IMF could also take place (e.g., van Dokkum & Conroy 2010). In this sense, there include uncertainties in the conclusion of $n_{\rm H}$ evolution that are raised from the assumption of constant $Q_{\rm H^0}$. It is true that the $n_{\rm H}$ evolution could be an origin of the evolution of ionization parameter as argued by Shirazi et al. (2013). Shirazi et al. (2013) have also confirmed that high-z galaxies tend to have a high electron density, which is measured directly from emission lines (see also Section 5.1.2). However, because ionization parameter is determined by $Q_{\rm H^0}$, $n_{\rm H}$, and gas filling factor (Equation 2.3), ionization parameter is more fundamental parameter of photoionization models, which allows the potential evolutions of $n_{\rm H}$, $Q_{\rm H^0}$, and gas filling factor.

To summarize, the gas density itself does not largely affect the [O III]/[O II] ratio, but ionization parameter and metallicity. Thus, one needs to understand the [O III]/[O II] ratio as a function of metallicities and ionization parameters. Hereafter, we study the relation between [O III]/[O II] ratio and $R23$-index with various ionization parameters and metallicities in the following analysis.

2.3.3. Interpretation of the [O III]/[O II] and $R23$-index Relation

In this section, we evaluate the average values of the local galaxies' ionization parameter and metallicity that are sensitive to [O III]/[O II] ratio and $R23$-index measurements, using the method given by Kobulnicky & Kewley (2004). Kobulnicky & Kewley (2004) use the photoionization model of Kewley

Table 2.1. Solar Metallicities ($Z_\odot$) and Depletion Factors (D) adopted for each element

Element	$\log(Z_\odot)$	$\log(D)$
H	0.00	0.00
He	−1.00	0.00
Li	−8.69	−0.80
Be.....	−10.58	−0.22
B.....	−9.21	−0.89
C.....	−3.61	−0.40
N	−4.07	−0.23
O	−3.31	−0.22
F.....	−7.52	−0.52
Ne	−4.00	0.00
Na	−5.67	−0.70
Mg	−4.46	−0.70
Al.....	−5.53	−2.00
Si	−4.46	−1.52
P.....	−6.50	−0.60
S.....	−4.74	0.00
Cl.....	−6.72	−0.40
Ar.....	−5.60	0.00
K	−6.88	−0.52
Ca.....	−5.64	−4.00
Sc.....	−8.83	−2.30
Ti	−6.98	−2.10
V	−8.00	−2.22
Cr.....	−6.33	−2.22
Mn	−6.54	−1.30
Fe.....	−4.55	−2.00
Co	−7.08	−2.00
Ni.....	−5.75	−2.00
Cu	−7.79	−1.00
Zn.....	−7.40	−0.60

Table 2.2. Average ionization parameter, $\log(q_{\rm ion})$, and metallicity, $12+\log({\rm O/H})$, ranges for the local galaxy samples estimated from the [O III]/[O II] ratio and $R23$-index.

Sample	$\log(q_{\rm ion})$	$12+\log({\rm O/H})$
SDSS	7.18–7.51	8.92–9.12
LyC leakers	7.69–8.28	8.13–8.75
LBAs	7.27–8.02	8.03–8.89
GPs	7.71–8.30	8.19–8.67

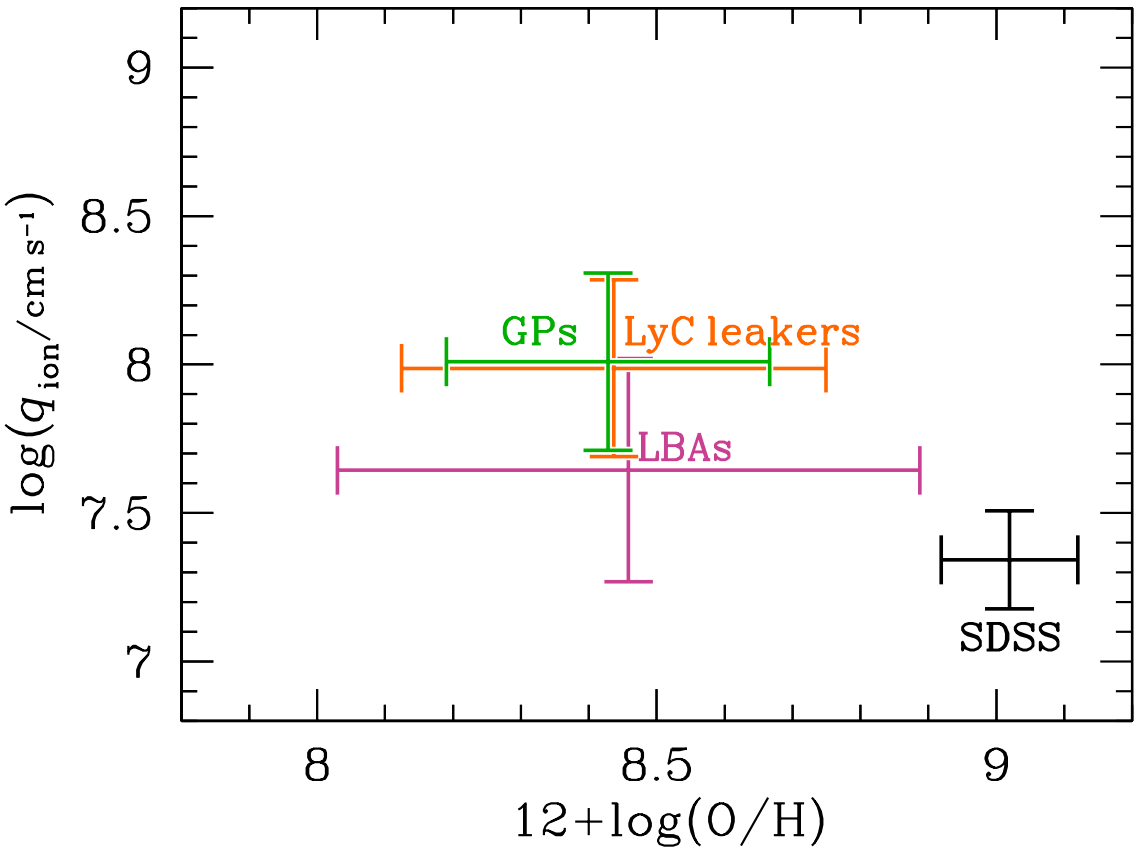

Figure 2.6. Average ionization parameter and metallicity for the local galaxy samples (Table 2.2).

& Dopita (2002), showing an equation of ionization parameter,

$$\begin{aligned}\log(q_{\rm ion}) = \{&32.81 - 1.153y^2\\ &+[12+\log({\rm O/H})](-3.396 - 0.025y + 0.1444y^2)\}\\ &\times\{4.603 - 0.3119y - 0.163y^2\\ &+[12+\log({\rm O/H})](-0.48 + 0.0271y + 0.02037y^2)\}^{-1},\end{aligned} \tag{2.6}$$

where $y = \log([{\rm O\,III}]\lambda\lambda 5007,4959/[{\rm O\,II}]\lambda 3727)$, and equations of metallicity,

$$\begin{aligned}12+\log({\rm O/H})_{\rm low} &= 9.40 + 4.65x - 3.17x^2\\ &\quad - \log(q_{\rm ion}) \times (0.272 + 0.547x - 0.513x^2),\end{aligned} \tag{2.7}$$

$$\begin{aligned}12+\log({\rm O/H})_{\rm high} &= 9.72 - 0.777x - 0.951x^2\\ &\quad - 0.072x^3 - 0.811x^4\\ &\quad - \log(q_{\rm ion}) \times (0.0737 - 0.0713x - 0.141x^2\\ &\quad + 0.0373x^3 - 0.058x^4),\end{aligned} \tag{2.8}$$

where $x = \log(R23)$ and the subscript low (high) corresponds to a metallicity value in the low-Z (high-Z) branch of metallicity. We use dust-corrected [O III]/[O II] ratio and $R23$-index. Note that, without other metallicity indicators, this method does not provide a single solution, but multiple solutions from

low-Z and high-Z branches. The demarcation metallicity between the two branches is $12+\log(\mathrm{O/H}) = 8.4$. We use Equations (2.6)–(2.8) to estimate a metallicity and ionization parameter iteratively until the metallicity converges[2.6]. We evaluate errors of metallicity and ionization parameter by Monte Carlo simulations. For each galaxy sample, we obtain the average values of $R23$-index, [O III]/[O II] ratio, and their uncertainties. We assume that for each of the flux ratios, the probability distribution of the true value is a Gaussian with its sigma equal to the observed uncertainty in the flux ratio. We randomly select a set of $R23$-index and [O III]/[O II] ratio following these Gaussian probability distributions, and calculate metallicity and ionization parameter with the set of $R23$-index and [O III]/[O II] ratio based on Equations (2.6)–(2.8). We repeat the process 500 times, and define one sigma errors of metallicity and ionization parameter by the 68 percentile of the distribution.

The estimated values are summarized in Table 2.2 and shown in Figure 2.6. We list the ranges of values in both the high-Z and low-Z branches for all of our samples except SDSS sample. For the SDSS sample, only the values in the high-Z branch are given, since the average metallicity for the low-Z branch, $12+\log(\mathrm{O/H}) = 7.7-8.1$, is significantly lower than that estimated with $R23$-index and $N2$-index (Figure 2.1). We have checked that the SDSS high-Z branch metallicity of $12+\log(\mathrm{O/H}) = 8.92-9.12$ (Table 2.2) is consistent with our estimate in Section 2.2, as well as those estimated in previous studies (e.g., Tremonti et al. 2004; Mannucci et al. 2010).

Although only weak constraints are placed on metallicity due to the degeneracy of the two branch solutions, the difference of ionization parameters between galaxy samples is clearly found in Figure 2.6. The SDSS galaxies have the average value of $\log(q_{\mathrm{ion}}/\mathrm{cm\,s^{-1}}) \sim 7.3$ (see also e.g., Dopita et al. 2006a). In contrast, GPs and the LyC leakers exhibit ionization parameters much higher than the SDSS galaxies. Similarly, the ionization parameter of LBAs is high. These extreme local populations of GPs, LyC leakers, and LBAs also have low metallicities. Such low metallicities and high ionization parameter of GPs are also inferred from previous studies (Amorín et al. 2010; Jaskot & Oey 2013).

Figure 2.4 suggests that there is a variation of ionization parameter in the SDSS sample. In fact, the SDSS galaxy distribution sequence departs from the model curve of $\sim 2\times10^7\,\mathrm{cm\,s^{-1}}$. In the large $R23$-index regime, we recognize the slope of the SDSS galaxy sequence steeper than that of the photoionization model predictions. This trend indicates that galaxies with a low metallicity of $12+\log(\mathrm{O/H}) \sim 8.5$ have a high ionization parameter (e.g., Dopita et al. 2006a; Nagao et al. 2006). If the $M_\star$–Z relation is in place (e.g., Tremonti et al. 2004), this would imply that low-$M_\star$ galaxies have a high ionization parameter. We examine the possible dependencies of $M_\star$ and other galaxy global properties on ionization parameters in Sections 2.3.4 and 2.3.5. Similarly, the important characteristics can be found in the small $R23$-index regime. The sequence of SDSS galaxies presents an upturn from high to low $R23$-index values. This trend is probably caused by the presence of a hidden AGN activity in a galaxy. In this regime, the SDSS galaxies departing from the model curve would be also dominated by objects with a low SFR and a high $M_\star$ (Section 2.3.5; see also Dopita et al. 2006a).

2.3.4. Dependence of [O III]/[O II] on $M_\star$ and SFR

In Section 2.3.3, we have estimated the typical ionization parameters for the local galaxy samples from the comparisons of the photoionization models with the measurements of [O III]/[O II] and $R23$-index, and compared them (Figure 2.6). However, these comparisons do not focus on possible depen-

[2.6] Three iterations are typically required to reach convergence (see also Kewley & Ellison 2008).

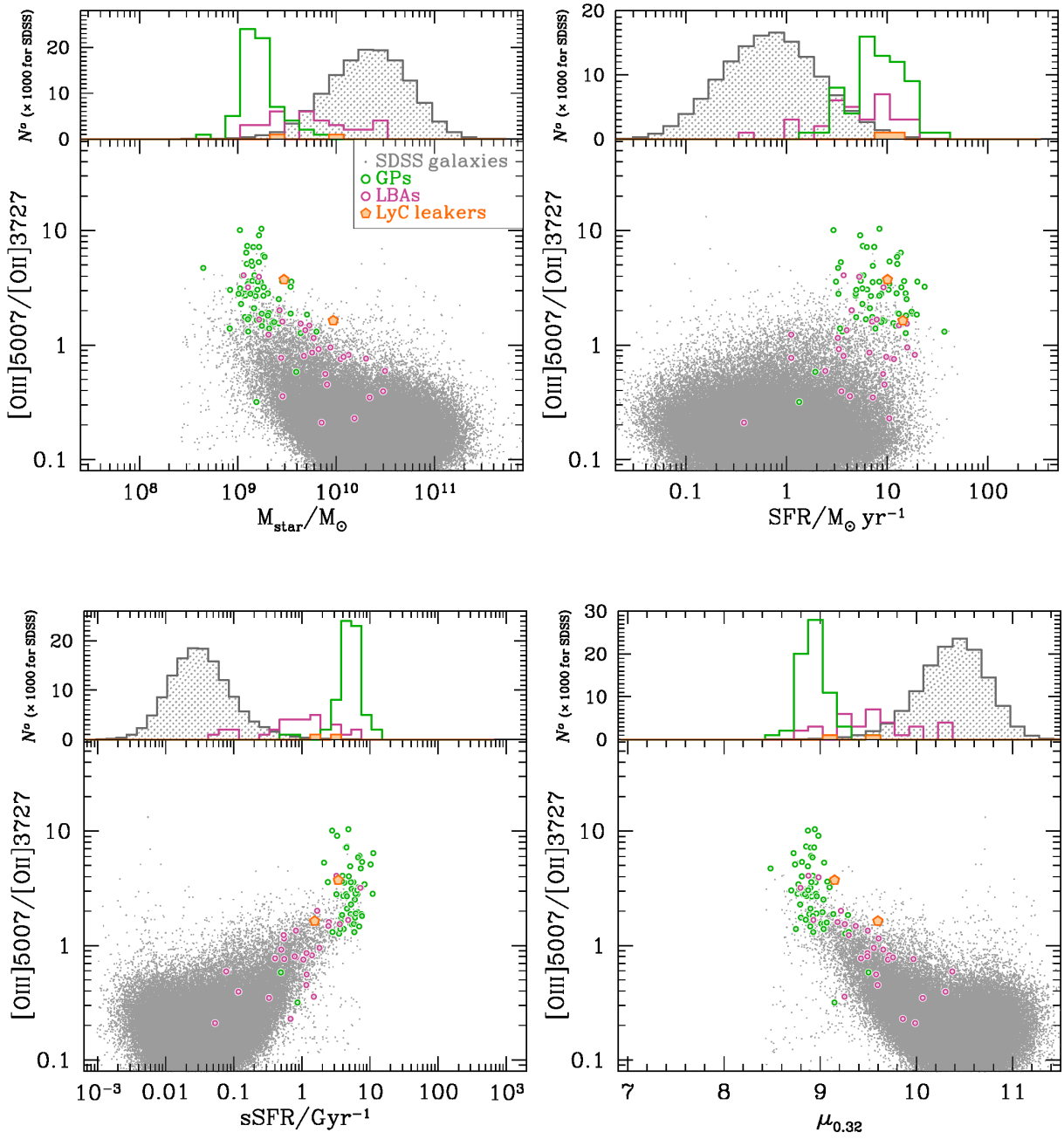

Figure 2.7. Dependence of [O III]/[O II] on $M_\star$ (top left), SFR (top right), sSFR (bottom left), and $\mu_{0.32}$ (bottom right). The symbols and colors are the same as those used in Figure 2.2. In each panel, the distribution of one of the galaxy global properties for the local galaxy samples is given in the top. The histogram for the SDSS sample (gray shaded) is divided by 1000.

dencies on galaxy global properties such as $M_\star$ and SFR. Figure 2.2 presents a relatively large scatter in [O III]/[O II] ratios at a given $R23$-index in one galaxy sample. This scatter could be originated from the galaxy global properties. To address the issue, we examine the dependencies of the [O III]/[O II] ratio on the galaxy global properties.

Figure 2.7 shows [O III]/[O II] ratios as a function of $M_\star$, SFR, specific SFR (sSFR; SFR divided by $M_\star$), and $\mu_{0.32}$ (Equation (2.1) with $\alpha = 0.32$). Figure 2.7 indicates that the [O III]/[O II] ratio correlates

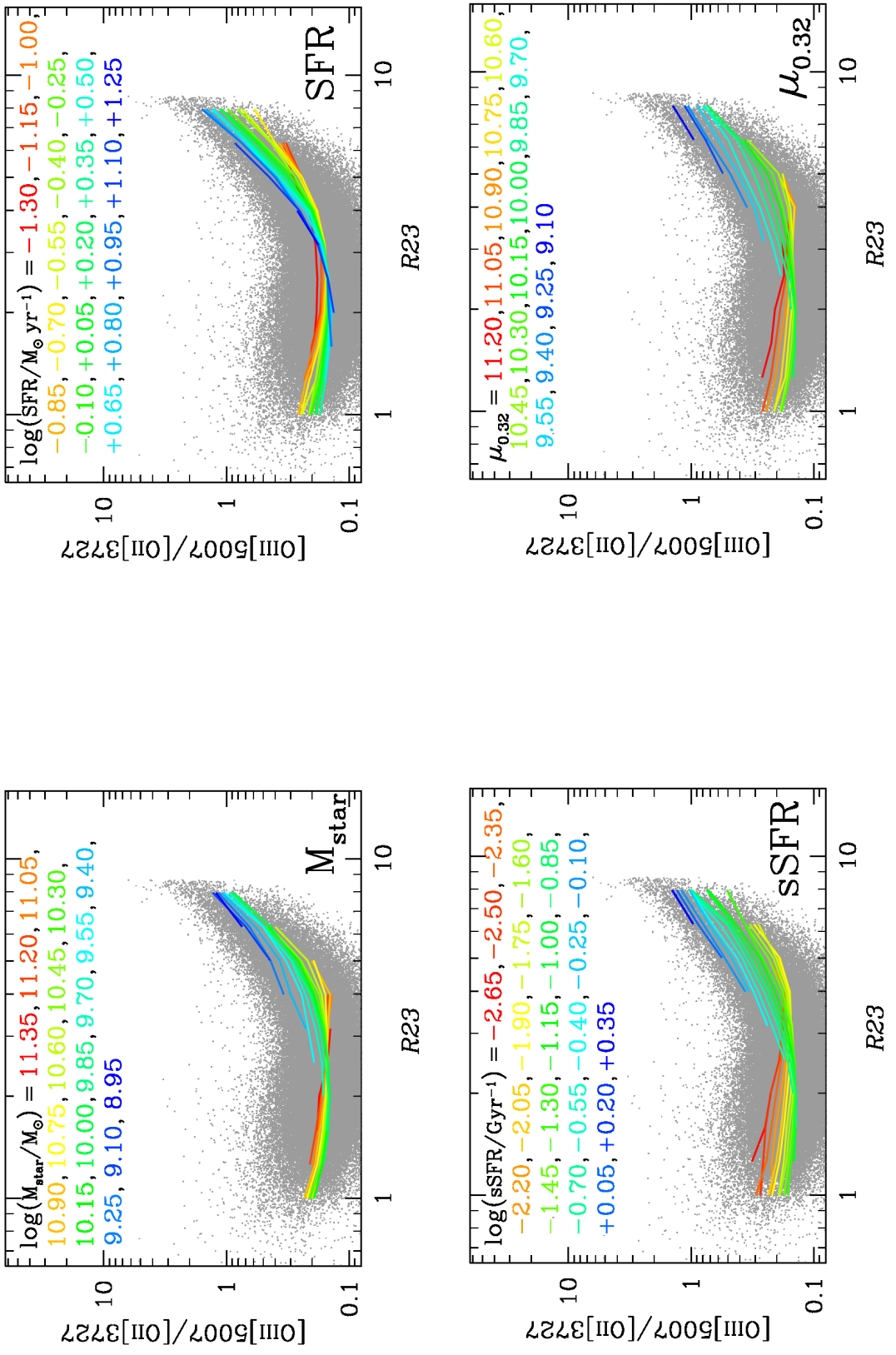

Figure 2.8. [O III]/[O II] vs. $R23$-index diagrams for the SDSS galaxies. The gray dots denote all of the SDSS galaxies. The colored lines represent the median [O III]/[O II] values for subsamples defined by a 3rd quantity of $M_\star$ (top left), SFR (top right), sSFR (bottom left), and $\mu_{0.32}$ (bottom right). The definition of the subsamples are indicated at the top of each panel. Subsamples including > 50 galaxies are presented.

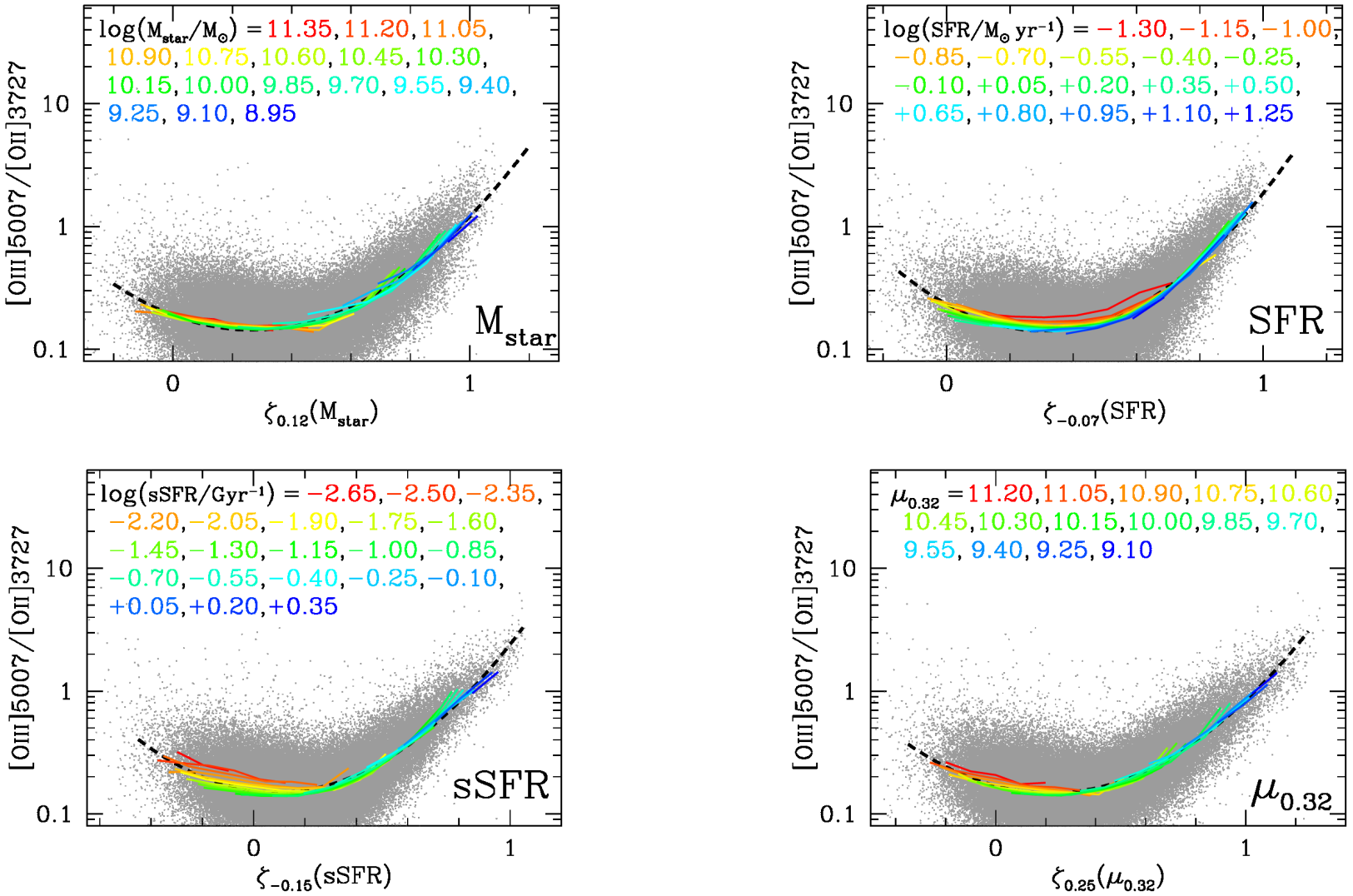

Figure 2.9. Same as Figure 2.8, but for [O III]/[O II] vs. ζ_β (Θ) diagrams. The black dashed-line shows the quadratic best-fit (Equation (2.10) with coefficients given in Table 2.3).

with the galaxy global properties of $M_\star$, SFR, sSFR, and $\mu_{0.32}$. A high [O III]/[O II] ratio is found in low $M_\star$, low $\mu_{0.32}$, and high sSFR galaxies. A similar trend is initially proposed by Brinchmann et al. (2008), but we find these trends in local extreme populations. There is an anti-correlation between [O III]/[O II] and metallicity (Section 2.3.2). Thus, the dependence of [O III]/[O II] ratio on $M_\star$ and $\mu_{0.32}$ is reasonable, because the $M_\star$–Z relation and the FMR are in place. In this way, the [O III]/[O II] ratio is tightly related to the galaxy global properties, while this ratio is an indicator of ionization parameter and metallicity. In the next section, we investigate dependencies of the galaxy global properties on ionization parameter and metallicity with the SDSS sample on the [O III]/[O II] vs. $R23$-index diagram.

Before moving to the next section, we comment here on the variations of global properties for the local galaxies shown in Figure 2.7. First, GPs are the least massive and the most actively star-forming galaxies in the local universe. Their low $\mu_{0.32}$ values are probably due to their low metallicities (e.g., Amorín et al. 2010). LBAs are the next extreme population. The LyC leakers have SFRs and stellar masses comparable to GPs and LBAs.

2.3.5. Fundamental Ionization Relation

As shown in Figures 2.2–2.4, the [O III]/[O II] vs. $R23$-index diagram allows us to study ionization state of galaxies. In Section 2.3.4, we discuss that the [O III]/[O II] ratio depends on four galaxy global properties of $M_\star$, SFR, sSFR, and $\mu_{0.32}$. The large scatter found in Figure 2.2 would be explained by the differences of the galaxy global properties.

In order to investigate the dependencies of $M_\star$, SFR, sSFR, and $\mu_{0.32}$ on the [O III]/[O II] vs. $R23$-index plane, we make subsamples of our SDSS sample. We choose one quantity from the four galaxy global properties. The chosen quantity is referred to as a '3rd quantity' hereafter. A bin size of a subsample is 0.15 dex in the 3rd quantity. We have checked that the bin size is large enough compared to the typical uncertainty of the the 3rd quantity. For a given subsample, we calculate a median [O III]/[O II] ratio of galaxies in a range of $\Delta\log R23 = 0.1$. We use subsamples with > 50 galaxies for our analysis. The four panels in Figure 2.8 show the subsamples of $M_\star$, SFR, sSFR, and $\mu_{0.32}$ on the [O III]/[O II] vs. $R23$-index plane. Figure 2.8 indicates that the relation between [O III]/[O II] and $R23$-index depends on the galaxy global properties. A high [O III]/[O II] ratio can be found in less massive, more efficiently star-forming, and probably more metal-poor galaxies (Dopita et al. 2006a). We introduce a parameter, $\zeta_\beta(\Theta)$, which combines $R23$-index and one of the 3rd quantities:

$$\zeta_\beta(\Theta) = \log(R23) - \beta \times \Theta, \tag{2.9}$$

where β is a free parameter and $\Theta = \log(M_\star/10^{10} M_\odot)$, $\log(\mathrm{SFR}/M_\odot\,\mathrm{yr}^{-1})$, $\log(\mathrm{sSFR}/\mathrm{Gyr}^{-1})$, and $(\mu_{0.32} - 10.0)$ for a 3rd quantity of $M_\star$, SFR, sSFR, and $\mu_{0.32}$, respectively. We calculate a scatter of the SDSS subsamples in the relation of [O III]/[O II] and $\zeta_\beta(\Theta)$ by varying β for each of the 3rd quantities, Θ. As a result, the scatter is minimized at $\beta = (0.12, -0.07, -0.15, 0.25)$ for Θ of ($M_\star$, SFR, sSFR, $\mu_{0.32}$). The four panels of Figure 2.9 present our SDSS galaxies on the [O III]/[O II] and $\zeta_\beta(\Theta)$ plane. The median values of the SDSS subsamples are fitted by a quadrature:

$$\log([\mathrm{O\,III}]/[\mathrm{O\,II}]) = a_0 + a_1 \zeta_\beta(\Theta) + a_2 \zeta_\beta^2(\Theta), \tag{2.10}$$

where a_0–a_2 are free parameters. The best-fit parameters are given in Table 2.3. We show the best-fit quadratures in Figure 2.9. These plots suggest that the 3rd quantity can reduce the systematic dispersions.

Table 2.3. Best-fit values for the quadrature of Equation (2.10).

3rd quantity	β	a_0	a_1	a_2
$M_\star$	$+0.12$	-0.722	-0.923	$+1.726$
SFR	-0.07	-0.634	-1.427	$+2.331$
sSFR	-0.15	-0.810	-0.267	$+1.458$
$\mu_{0.32}$	$+0.25$	-0.772	-0.536	$+1.232$

However, it is unclear whether the new parameter of β reduces the dispersion by a physical reason or a simple statistical reason. Here we use μ_α defined in Equation (2.1) as a 3rd quantity and search for an optimal combination of $M_\star$ and SFR by varying parameters of both α and β [2.7]. Note that the parameter α denotes the best combination of $M_\star$ and SFR for metallicity (Mannucci et al. 2010), while the parameter β defines the best combination of these quantities for both metallicity and ionization parameter. Based on Equation (2.9) with $\Theta = (\mu_\alpha - 10.0)$, we calculate χ^2 of the free parameters, α and β. Here we assume that 1σ [O III]/[O II] dispersions of our subsamples are originated from measurement errors. These 1σ dispersions are used to obtain the χ^2 values.

Figure 2.10 shows χ^2 values of α and β. The minimum χ^2 is provided by the parameters of $(\alpha, \beta) = (0.29, 0.25)$. The best-fit parameters are $\alpha = 0.29^{+0.04}_{-0.26}$ and $\beta = 0.25^{+0.06}_{-0.12}$. Interestingly, the best-fit value of $\alpha = 0.29^{+0.04}_{-0.26}$ is consistent with the one of the FMR ($\alpha = 0.32$). Thus, $\mu_{0.32}$ (μ_α for $\alpha = 0.32$) is the best 3rd quantity to describe the relation. Moreover, we have newly constrained the β parameter that is tightly related to ionization parameter. The best-fit β rules out $\beta = 0$ at the $> 95\,\%$ confidence level. The results of our analysis suggest that ionization parameters given with the [O III]/[O II] vs. $R23$-index diagram is important to characterize galaxies, and that ionization parameters are closely related to the galaxy global properties of $M_\star$ and SFR as well as metallicity.

We compare the local galaxy samples with the best-fit function of the SDSS galaxies in Figure 2.11. This figure is the same as the bottom right panel of Figure 2.9, but with local extreme populations of GPs, LBAs, and the LyC leakers. Although the best-fit function is derived with the SDSS sample alone, the local extreme populations appear to follow the same relation or fall on the extrapolation of the function. Some GPs having the highest [O III]/[O II] ratio and the two LyC leakers may lie above the relation, though. These rare, possible outliers are also interesting, and will be discussed in detail in Section 5.1.5.

To summarize, we have found the tight relation between [O III]/[O II] ratio and $\zeta_{0.25}\,(\mu_{0.32})$ for the local galaxies (Figure 2.11). The relation consists of four-dimensional parameter space defined by ionization parameter, metallicity, $M_\star$, and SFR. In the local universe, the relation is in general thought to be fundamental over wide ranges of stellar mass and SFR. Therefore, we hereafter refer to the relation as fundamental ionization relation (FIR). However, it is still unclear whether this relation is really fundamental over cosmic time. In the following chapters, we extend our study towards higher-redshift galaxies to examine the universality of the FIR.

[2.7] Although μ_α does not represent a function of SFR with no dependence of $M_\star$, we have found in our analysis that a ζ function with $\Theta = \Theta(\mathrm{SFR})$ provides the best-fit value of $\beta \simeq 0$ (Table 2.3), which indicates that a SFR alone does not reduce the scatter of the SDSS galaxy distribution.

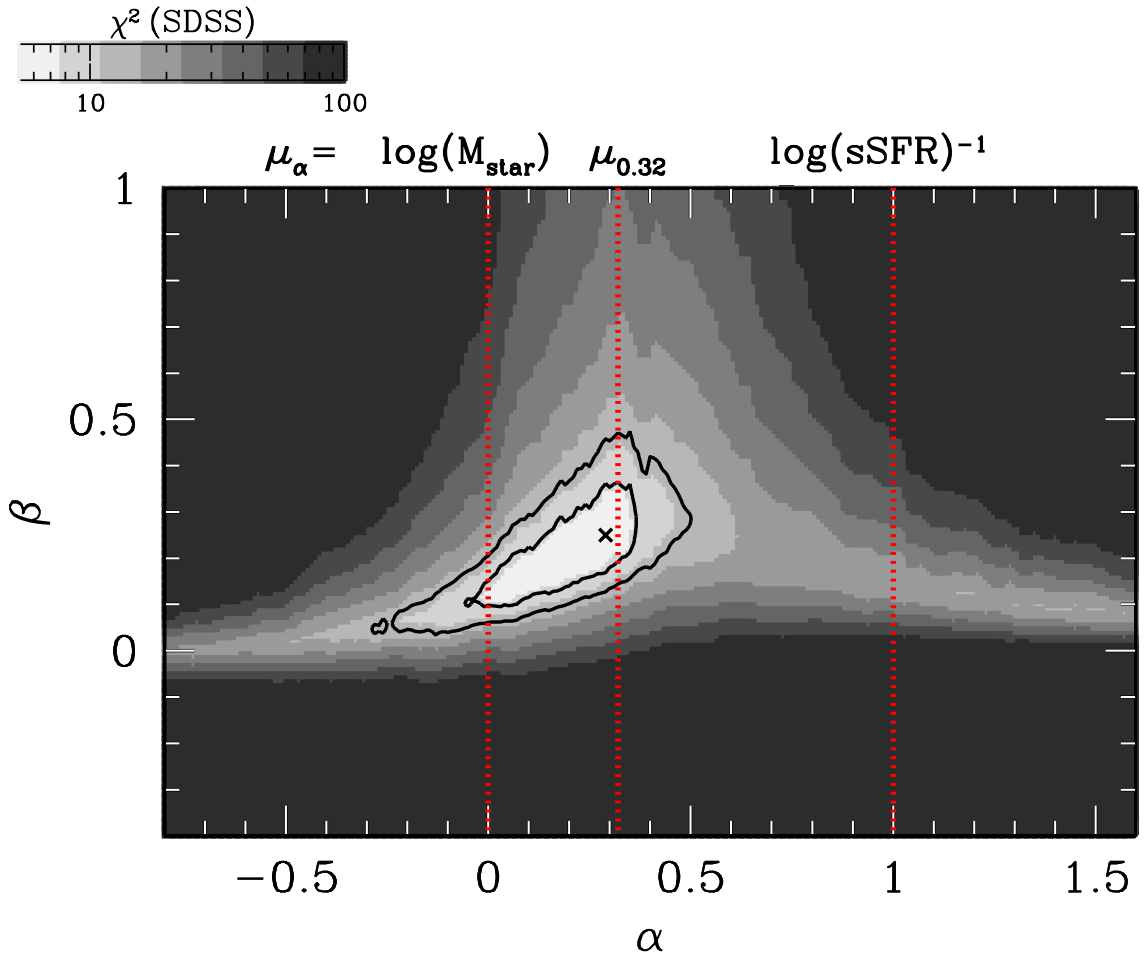

Figure 2.10. χ^2 contours of free parameters, α and β, that are used in the [O III]/[O II]-ζ_β (μ_α) relation of our SDSS sample. The gray scale represents a χ^2 value as shown in the gray bar at the top. A darker color indicates a larger χ^2 value. The black solid contours represent the 1σ (inner) and 2σ (outer) confidence levels, and the cross denotes the minimum χ^2 of 5.3 at (α, β)=(0.29, 0.25). The values of $\alpha = 0$ and 1 correspond to $\mu_\alpha = \log(M_\star)$ and $\log(\mathrm{sSFR})^{-1}$, respectively.

2.4. Summary of This Chapter

In this Chapter, we have presented a systematic study for ionization parameter, metallicity, $M_\star$, and SFR of galaxies at $z \sim 0$ with the $\sim 140,000$ SDSS galaxies. In addition, we have highlighted extreme populations of galaxies in the local universe, Green Pea galaxies (GPs), Lyman-break Analogs (LBAs), and galaxies emitting Ly-continuum radiation (LyC leakers). These local extreme populations are helpful to discuss local counterparts of high-z star-forming galaxies. We have made use of the line ratios of [O III]λ5007/[O II]λ3727 and ([O III]$\lambda\lambda$5007,4959+[O II]λ3727)/Hβ (R23-index). Main results in this chapter are summarized as follows.

- We have clarified that the [O III]/[O II] vs. R23-index diagram is useful to constrain ionization parameter and metallicity for a galaxy with the aid of photoionization models. Important trends on this diagram are: (i) [O III]/[O II] ratio increases with ionization parameter, (ii) [O III]/[O II] ratio decreases with metallicity, and (iii) R23-index increases in a low-metallicity regime (low-Z branch) from $12+\log(\mathrm{O/H}) = 7.5$ to ~ 8.5, and decreases in a high-metallicity regime (high-Z

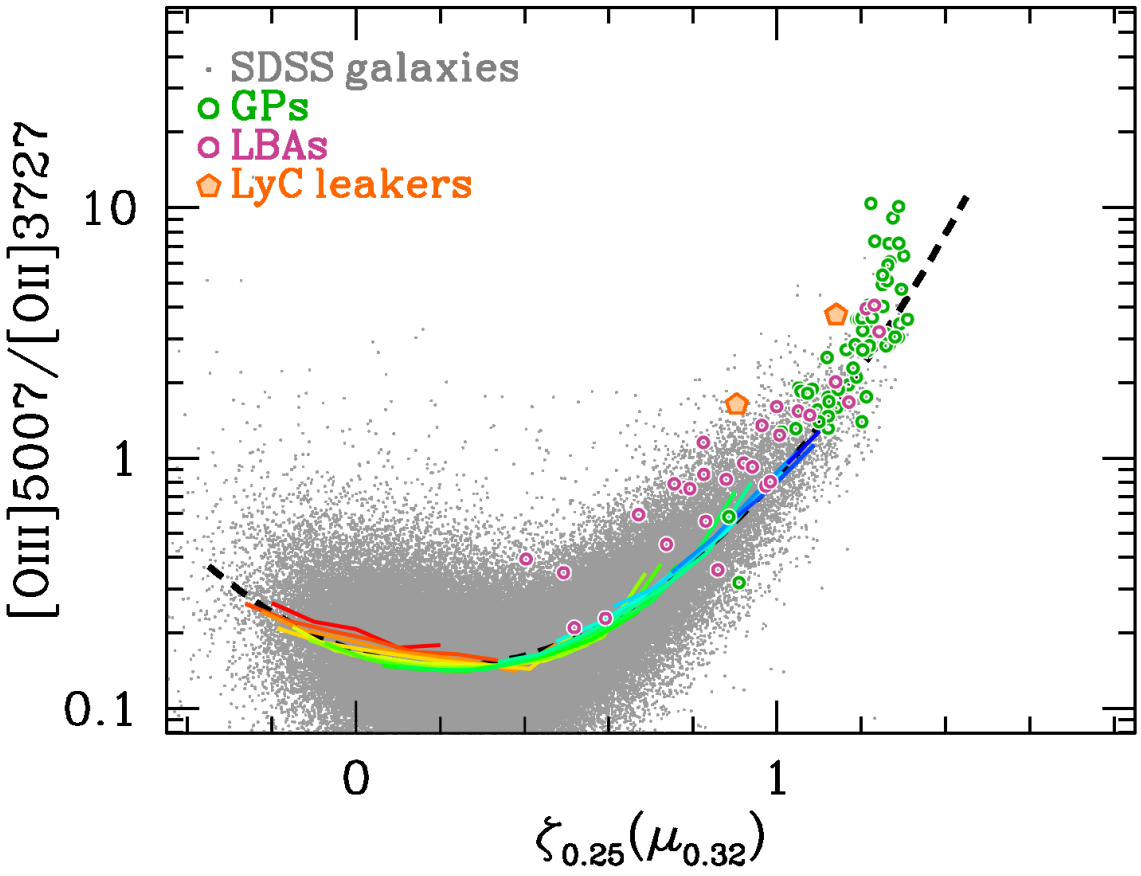

Figure 2.11. [O III]/[O II] vs. $\zeta_{0.25}(\mu_{0.32})$ relation for the local galaxy samples. The color code for the lines are the same as those at the bottom right panel of Figure 2.9.

branch) from $12+\log(\mathrm{O/H}) \sim 8.5$ towards a higher metallicity (Figure 2.3).

- We have found by using the SDSS sample that galaxies with a higher $R23$-index have a higher [O III]/[O II] ratio. The local extreme populations of galaxies, GPs, LyC leakers, and LBAs present the highest $R23$-index and [O III]/[O II] ratio among the local galaxies (Figure 2.4). We have interpreted the trends as indicating that galaxies with a low metallicity have a high ionization parameter. The local extreme populations thus have the highest ionization parameter and lowest metallicity in the local universe (Figure 2.6).

- We have identified a correlation between the [O III]/[O II] ratio and galaxy global properties of SFR, $M_\star$, and metallicity (Figure 2.7). A high [O III]/[O II] ratio is found in less massive, efficiently star-forming, and metal-poor galaxies (see also Figure 2.8).

- We have developed a four-dimensional relation of ionization parameter, SFR, $M_\star$, and metallicity (Figure 2.9), extending the fundamental metallicity relation (FMR; Mannucci et al. 2010; Lara-López et al. 2010) with ionization parameter. Interestingly, the local extreme populations follow the same relation (Figure 2.11).

3 Physical Properties of LAEs

In the previous chapter, we presented the physical properties and their relationships for galaxies in the local universe. In order to examine the evolution of such galaxy properties, we extend the study towards higher redshifts in this and the following chapters.

As mentioned in Section 1.2, high-z observations lack low-mass galaxies ($\lesssim 10^{9.5} M_{\odot}$) because most of them are based on continuum-selected sample, such as LBGs. In order to obtain detailed emission-line properties of less massive galaxies at high-z and to study the diversity of high-z galaxies, we focus on LAEs at $z \simeq 2.2$ in this chapter. As introduced in Section 1.5, at this redshift, important nebular lines such as [O II]λ3727, Hβ, [O III]$\lambda\lambda$5007, 4959, Hα, [N II]$\lambda\lambda$6584, 6548, are observable from the ground (Figure 1.4). The redshift $z \simeq 2.2$ is remarkably unique because [O II]λ3727 and Hα lines fall into a wavelength range where OH-airglow is very weak (Figure 1.5), thus enabling one to detect these lines not only by spectroscopy but also through NIR narrowband filters developed to target the low OH-airglow wavelength ranges.

We carried out NB387 ($\lambda_c = 3870$ Å and FWHM $= 94$ Å) imaging observation in five blank fields: the Subaru/XMM-Newton Deep Survey (SXDS) field (Furusawa et al. 2008), the COSMOS field (Scoville et al. 2007), the Chandra Deep Field South (CDFS; Giacconi et al. 2001), the Hubble Deep Field North (HDFN; Capak et al. 2004), and the SSA22 field (e.g., Steidel et al. 2000), covering a total of ~ 1.5 square degrees. The full description of the LAE sample construction is found in Appendix A. Briefly, objects which are bright in NB387 compared to the U and B bands are selected as LAE candidates. We select galaxies with emission line possessing EW$_{\rm obs} \gtrsim 90$ Å, which corresponds to EW ~ 30 Å of Lyα emission from galaxies at $z = 2.2$. Spurious objects, low-z interlopers, and AGNs are removed by using UV, X-ray, and/or radio data, as well as by visual inspection. The LAE sample contains in total 3,403 candidates under the constraint of $> 2\sigma$ excess of NB387 brightness over U.

In Section 3.1, we present results from Keck/NIRSPEC (McLean et al. 1998) and Magellan/MMIRS (McLeod et al. 2012) NIR follow-up spectroscopy of our LAEs. This study provides the first simultaneous estimations of ionization parameter and metallicity for high-z LAEs. We just report the physical properties of the followed-up LAEs in this section, and summarize the detailed analysis in Appendix B. In Section 3.2, we present results of the average metallicity and SFR of LAEs measured from our survey with two NIR narrowband filters covering the [O II]λ3727 and Hα (+[N II]$\lambda\lambda$6584, 6548) lines of LAEs at $z = 2.2$. By stacking NIR narrowband images of the LAEs, we successfully obtain average nebular-line fluxes of LAEs. We report in this section the physical properties of the stacked LAEs. The full description of the NIR narrowband study is summarized in Appendix C.

3.1. Ionization State and Metallicity of LAEs from NIR Spectroscopy

In this section, we present results from Keck/NIRSPEC and Magellan/MMIRS follow-up spectroscopy of LAEs at $z \simeq 2.2$. We describe the spectroscopic data in Section 3.1.1, briefly summarize the detection of emission lines from the LAEs in Section 3.1.2, and report the physical properties of the identified LAEs in Section 3.1.3. The detailed description of the study is summarized in Appendix B.

3.1.1. NIR Spectroscopic Data

3.1.1.1. Sample Construction

Of the $z \simeq 2.2$ LAE sample constructed by our Subaru narrowband survey (Appendix A), seven candidates were selected for Keck/NIRSPEC follow-up. We selected COSMOS-13636, COSMOS-30679, and COSMOS-43982, since their Lyα spectra had been obtained with Magellan/MagE (M. Rauch et al. in preparation; Section A.2.2.3). COSMOS-08501, HDFN-18325, and HDFN-18431 were selected because of their large Lyα equivalent widths and fluxes measured from the NB387 imaging data. CDFS-3865, whose rest-frame optical spectrum has in part already been taken with Magellan/MMIRS, was also observed with NIRSPEC for its [O II] detection. Table B.1 summarizes the details of the sample.

For the MMIRS observation, we observed CDFS and SSA22 fields with one mask each. Details of the observation and data reduction procedures are presented in Hashimoto et al. (2013). Briefly, we found three LAEs in which we identified Hα emission. In this thesis, we make use of the spectra of the three LAEs; CDFS-3865, CDFS-6482, and SSA22-8043 (Table B.1). We have checked that none of the LAEs selected for the follow-up observations has detections in GALEX, X-ray, and/or radio (i.e., they are not low-z interlopers such as [O II] emitters, CIV emitters, nor obvious AGNs; see also Appendix A).

3.1.1.2. NIRSPEC Observation

The observations were carried out on 9–10 February 2011. Both nights were photometric. We observed in low-resolution mode, with a slit width of $0\farcs76$ and a slit length of $42''$[3.1]. We observed all six candidate with Nirspec-6 filter (hereafter referred to as K band). In addition, we observed COSMOS-30679 with Nirspec-5 (H band) and Nirspec-3 (J band), and CDFS-3865 with J band. The wavelength ranges of K, H, and J bands are 1.88–2.31 μm, 1.47–1.76 μm, and 1.15–1.36 μm, respectively for our configurations. The resolution in the K band is $R \sim 1500$. Exposure times for each object are given in Table B.1.

Our science targets were acquired using the invisible object acquisition procedures. In this mode, an alignment star brighter than $K_{\rm Vega} \sim 18$ was placed in the slit simultaneously with a science target. We first acquired the star at the center of the slit, then we nodded the telescope so that both the science target and the star were on the slit with the same distance from the slit center. For CDFS-3865 and HDFN-18431, since we could not find any stars to place on the slit along with them, we first acquired the nearest star to the target (at distances of $68''$ for CDFS-3865 and $39''$ for HDFN-18431), then nodded the telescope with an offset, which was calculated from the WCS difference between the star and the science target. For HDFN-18325, although a star was found at a distance of $32''$, which is smaller than the slit length, half of the observation was done without the star in order to avoid the persistence caused by the

[3.1] The effective slit length is $\sim 38''$, since we did not place objects in $< 2''$ from the edges of the slit.

previous target alignment star. During an exposure, we manually guided the slit using the slit-viewing camera; if the star started to drift out of the slit, we manually moved the slit so that the star (and thus the invisible science target) stayed in the slit throughout each exposure.

Standard stars, which were selected from the Hipparcos catalog to have A0V spectral type and similar airmass to the science targets, were observed at the beginnings and the ends of the nights. The calibration data were taken in an ABBA position pattern, while the science data in AB position pattern.

3.1.1.3. NIRSPEC Data Reduction

We used the Keck IRAF-based WMKONSPEC package[3.2] to reduce the data. We also used IRAF scripts that were originally written for reducing near-infrared multi-object spectroscopic data from Subaru/MOIRCS (MCSMDP; Yoshikawa et al. 2010).

The data reduction process included bias subtraction, flat fielding, distortion correction, wavelength calibration, cosmic ray rejection, (A-B) sky subtraction, residual background subtraction, image shifting, and stacking. We used the bias and flat data that were obtained in the same night as the science data. We performed wavelength calibration using OH-lines by comparing them with an OH-line list (Rousselot et al. 2000). For cosmic ray rejection, we used LA.COSMIC (van Dokkum 2001). The sky and OH-lines of an A-position image were roughly removed by subtracting an average B-position image created from the previous and following images. We then removed the residual sky by subtracting a 9-th order polynomial fit in the spatial direction after masking columns of positive and negative parts caused by the alignment star and the object. Individual images were shifted in spatial direction so that the object is in the same position both in A-position and B-position images. The offset values were derived from the position differences of the alignment stars. When no star was observed simultaneously, we defined the offset values as the nod separation size. Finally, we stacked the position-matched individual images to create the two-dimensional (2D) spectra.

We obtained flux solutions by comparing spectra of the A0V standard stars and a model, which was created by a stellar spectral synthesis program (SPECTRUM; Gray & Corbally 1994) based on the Kurucz (1993)'s atmosphere models. The model spectra were then normalized so that their J, H, and K band magnitudes matched with those of standard stars, whose photometry was obtained from the Two Micron All Sky Survey (2MASS) All-Sky Point Source Catalog. The one-dimensional (1D) spectra were extracted by summing up 6–10 pixels in the spatial direction. The lengths of columns were determined based on the seeing conditions; about two times the seeing size was used. We also confirmed that the sizes were large enough to detect most of the signal, and maximize the signal-to-noise (S/N) ratio. The 1D and 2D spectra are shown in Figure B.2. We note in addition that the science targets and the standard stars used for the flux calibrations were observed and reduced with almost the same conditions, thus effects of slit losses were also corrected in the procedures, since the standard spectra extracted in the procedure were normalized to have the total magnitude of that star. LAEs typically have half-light radii $\lesssim 1.5$ kpc ($\lesssim 0\farcs18$ at $z \simeq 2.2$; Bond et al. 2009), which is much smaller than the seeing size. Therefore, we cannot resolve LAEs with our observations, and assuming the PSF profile for the LAEs is reasonable.

Emission line fluxes were measured by fitting a Gaussian profile to each line with the IRAF task `splot`. The sky noise level was estimated in the following manner; we prepared an aperture box, which had approximately twice the seeing size in spatial direction and twice the FWHM of the best fit Gaus-

[3.2] `http://www2.keck.hawaii.edu/inst/nirspec/wmkonspec.html`

sian to the emission line in wavelength direction. We spread more than 100 aperture boxes around the emission line after masking pixels heavily contaminated by OH-lines, and measured their photon counts. We then fit the histogram of the counts with a Gaussian, and regarded its σ as the 1σ fluctuation for the aperture used to measure the emission line. The line flues and their 1σ errors are summarized in Table B.2.

3.1.2. Emission Line Detections

We detect significant Hα emission in *K*-band 2D spectra for COSMOS-08501, COSMOS-13636, COSMOS-30679, COSMOS-43982, CDFS-3865, CDFS-6482, and SSA22-8043. Among the identified LAEs, CDFS-3865 also has detections of [O II]λ3727, Hβ, and [O III]$\lambda\lambda$5007, 4959, and COSMOS-30679 has detection of [O II] and [O III]. Our deep *J*-band spectroscopic observations provide the first [O II] detections for the two individual LAEs at high-z. More careful investigations of the spectra are given in Appendix B.

3.1.3. Physical Properties of LAEs

For the seven spectroscopically identified LAEs, we estimate their physical properties of ionization parameter, metallicity, and SFR from rest-frame optical emission lines, and stellar population such as stellar mass and dust extinction from SED fitting to broadband photometry. The detailed analysis is described in Appendix B. In this section, we briefly report the main results of the estimated physical properties, which are summarized in Table 3.1.

Our sample includes one possibly AGN-dominated galaxy, COSMOS-43982, and six star-forming galaxies judged from the BPT-diagram. Among the six star-forming galaxies, CDFS-3865 and COSMOS-30679 have a detection of [O II]+[O III], enabling us to estimate their ionization parameter and metallicity simultaneously (cf. Section 2.3.3). The [O III]/[O II] ratio and *R*23-index reveals that CDFS-3865 has a very high ionization parameter ($q_{\rm ion} = 2.5^{+1.7}_{-0.8} \times 10^8\,{\rm cm\,s^{-1}}$) and a low oxygen abundance (metallicity; $12 + \log({\rm O/H}) = 7.84^{+0.24}_{-0.25}$) in contrast with moderate values of other high-z galaxies such as LBGs. COSMOS-30679 also has a relatively high ionization parameter ($q_{\rm ion} = 8^{+10}_{-4} \times 10^7\,{\rm cm\,s^{-1}}$) and a low metallicity ($12 + \log({\rm O/H}) = 8.18^{+0.28}_{-0.28}$). For the other LAEs, we estimate their metallicities by using the empirical *N*2-index relation, and no constraint on ionization parameters is provided for them. Since only weak constrains on metallicity are derived for the LAEs without [O II], we also constrain an average metallicity from the *K*-band composite spectrum (Figure B.4) by using the empirical *N*2-index. The composite spectrum shows a prominent Hα but no [N II], which provides the 1σ (2σ) upper-limit of metallicity as $12 + \log({\rm O/H}) < 8.42$ (< 8.66). This upper-limit is useful to discuss basic characteristics of LAEs at high-z (Section 5.2).

Table 3.1. Physical Properties of the LAEs with NIR Spectroscopy

Object	$12+\log(\mathrm{O/H})$		$q_{\rm ion}$	$\mathrm{SFR}_{\rm cor}$	EW(Hα)	EW(Lyα)	L(Hα)	L(Lyα)	AGN	$\log(M_\star)$	$E(B-V)$
	$N2$	$R23$	(10^7 cm s^{-1})	($M_\odot$ yr^{-1})	(Å)	(Å)	(10^{42} erg s^{-1})	(10^{42} erg s^{-1})		($M_\odot$)	(mag)
	(1)	(2)	(3)	(4)	(5)	(6)	(7)	(8)	(9)	(10)	(11)
COSMOS-08501	<8.73	···	···	$6.7^{+1.6}_{-2.1}$	>280	255 ± 26	0.67 ± 0.13	8.41 ± 0.40	0	$7.84^{+1.21}_{-0.27}$	$0.08^{+0.04}_{-0.08}$
COSMOS-13636	<8.61	···	···	$13.2^{+1.9}_{-1.9}$	93^{+26}_{-32}	73 ± 5	0.95 ± 0.13	11.35 ± 0.50	0	$9.12^{+0.13}_{-0.14}$	$0.18^{+0.01}_{-0.01}$
COSMOS-30679	<8.46	$8.18^{+0.28}_{-0.28}$	8^{+10}_{-4}	$18.6^{+2.6}_{-2.6}$	93^{+25}_{-33}	87 ± 7	1.14 ± 0.10	8.47 ± 0.65	0	$9.74^{+0.26}_{-0.52}$	$0.24^{+0.04}_{-0.04}$
COSMOS-43982	···	···	···	$65.7^{+6.7}_{-6.0}$	41^{+4}_{-4}	105 ± 8	2.41 ± 0.21	11.00 ± 0.47	1	$10.80^{+0.01}_{-0.06}$	$0.40^{+0.02}_{-0.01}$
CDFS-3865	<8.35	$7.84^{+0.24}_{-0.25}$	25^{+17}_{-8}	$166.0^{+10.3}_{-10.3}$	813^{+175}_{-216}	64 ± 29	13.65 ± 0.85	29.79 ± 4.93	0	$9.50^{+0.01}_{-0.03}$	$0.14^{+0.00}_{-0.00}$
CDFS-6482	<8.72	···	···	$43.1^{+8.2}_{-8.2}$	261^{+103}_{-149}	75 ± 52	3.45 ± 0.63	15.40 ± 8.09	0	$9.80^{+0.06}_{-0.05}$	$0.15^{+0.02}_{-0.02}$
SSA22-8043	<8.90	···	···	$44.4^{+13.2}_{-13.1}$	120^{+53}_{-69}	28 ± 4	5.19 ± 1.52	2.22 ± 0.38	0	$10.07^{+0.06}_{-0.06}$	$0.03^{+0.02}_{-0.01}$

Note: (1) Oxygen abundance derived from $N2$-index. If [N II] is undetected, 1σ upper-limit is given. (2) Oxygen abundance derived from $R23$-index. Ionization parameter is derived simultaneously. (3) Ionization parameter (10^7 cm s^{-1}) estimated from the [O III]/[O II] ratio and $Z(R23)$. (4) Star formation rate ($M_\odot$ yr^{-1}) derived from Hα luminosity after correcting for extinction derived from SED fitting. (5) Rest-frame equivalent width of Hα (Å). (6) Rest-frame equivalent width of Lyα (Å). (7) Observed luminosity of Hα (10^{42} erg s^{-1}). (8) Observed luminosity of Lyα (10^{42} erg s^{-1}). (9) Flag of AGN: AGN candidates are flagged with "1". (10) Stellar mass from SED fitting. (11) Dust extinction from SED fitting.

3.2. Average Metallicity and SFR of LAEs from NIR Narrowband Imaging

In this section, we present the average metallicity and SFR of LAEs measured from our large area survey with three narrowband filters covering the Lyα, [O II]λ3727, and Hα (+[N II]$\lambda\lambda$6584, 6548) lines of LAEs at $z \simeq 2.2$. We briefly describe the triple narrowband survey in Section 3.2.1, show the stacking analysis to detect [O II] and Hα+[N II] emission in Section 3.2.2, and summarize the estimated physical quantities in Section 3.2.3. The detailed description of the study is summarized in Appendix C.

3.2.1. Triple Narrowband Survey

The redshift $z \simeq 2.2$ is particularly unique because [O II]λ3727 and Hydrogen Hα lines fall into wavelength ranges where OH airglow is very weak (Figure 1.5), thus enabling one to study SFRs and metallicities of LAEs using these lines from the ground. Over the redshift range of $z = 2.14$–2.22, where the NB387 filter can select LAEs, two emission lines of [O II] and Hα (+[N II]$\lambda\lambda$6584, 6548) are observed through NIR narrowband filters, NB118 ($\lambda_c = 11866$ Å and FWHM= 111 Å) and NB209 ($\lambda_c = 20958$ Å and FWHM= 205 Å), respectively, developed by the NewHα Survey (Lee et al. 2012; J. Lee et al. in preparation; Figure C.1). Details of the two narrowband filters data are found in Appendix C. We present the results from data of the Subaru/XMM-Newton Deep Survey (SXDS) field, which are the first results of this triple-narrowband survey.

We select LAEs in a $2,003$ arcmin^2 region which is covered by all the three passbands for selecting LAEs: NB387, u^*, and B (the region enclosed by both the blue and magenta lines in Figure C.2). We use only LAEs in a sub-region of $1,283$ arcmin^2 which is covered by NB118 (orange-shaded area in Figure C.2). In this "NB118 sub-region," a 353 arcmin^2 region is covered by NB209 as well ("NB209 sub-region"; red-shaded area in Figure C.2). Among the 919 LAE candidates found in the entire SXDS field (Appendix A.2.1), 561 are in the NB118 sub-region and 105 in the NB209 sub-region. Since Hα emission is necessary for estimating metallicity and SFR, we present results of the 105 LAEs in the NB209 sub-region in this section.

3.2.2. [O II] and Hα Emission Lines

Our NIR narrowband images are not deep enough to study [O II] and Hα properties of LAEs based on individual detections. Indeed, only 10 objects have detection of [O II] emission and only 3 have detection of Hα+[N II] emission, as described in Appendix C.2.2. We therefore carry out a stacking analysis of the whole LAE sample in the NB209 sub-region, and discuss average emission-line properties of $z \sim 2.2$ LAEs.

Stacking is done separately for the NB118 sub-region and the NB209 sub-region. For the NB209 sub-region, the NB118, J, NB209, and K images are stacked at the positions of the 105 LAE candidates. A signal is clearly visible in all the passbands including NB118 and NB209 (Figure C.3). We measure the magnitudes and colors of the stacked images, and convert them into line fluxes using Monte Carlo simulations.

From the simulations, which are fully described in Appendix C, we obtain EW$_{\rm rest}$ for [O II] and Hα+[N II], such that EW([O II]) $= 96^{+23}_{-19}$ and EW(Hα+[N II]) = 271^{+242}_{-104} Å. The errors in EW corre-

spond to 1σ. We calculate the [O II] and Hα+[N II] fluxes from the EWs obtained here combined with the total magnitudes, and convert them into luminosities, L([O II])$= 5.3^{+0.4}_{-0.4} \times 10^{41}$, and L(Hα+[N II]) = $8.0^{+1.2}_{-1.2} \times 10^{41}$ erg s^{-1}, respectively. After subtraction of [N II] emission, we obtain EW(Hα) = 256^{+229}_{-98} Å and L(Hα) = $7.6^{+1.1}_{-1.1} \times 10^{41}$ erg s^{-1} (see Appendix C.3.3). These EWs are larger than those obtained for other high-z galaxies (e.g., Cooper et al. 2006; Erb et al. 2006b), indicating that LAEs on average have intense emission lines. Recently, Cowie et al. (2011) have found that the bulk (~ 75 %) of the local LAEs have EW(Hα) > 100 Å. Thus, it seems that a large Hα EW is a common character of LAEs irrespective of redshift.

We estimate the average Lyα EW and luminosity in a similar manner. The Lyα EW$_{\rm rest}$ derived for the NB209 sub-region is 63^{+3}_{-5} Å, from which we obtain the observed Lyα luminosity to be $1.8^{+0.1}_{-0.1} \times 10^{42}$ erg s^{-1}. From previous narrowband surveys, LAEs with L(Lyα) $= 10^{42} - 10^{44}$ erg s^{-1} are referred to as typical LAEs (e.g., Gronwall et al. 2007; Ouchi et al. 2008). Therefore, the stacked LAE we obtain is expected to have average properties of LAEs with L(Lyα) $\gtrsim 10^{42}$ erg s^{-1}.

3.2.3. Physical Properties of the Stacked LAE

For the stacked LAE in the NB209 sub-region, we estimate its physical properties of metallicity and SFR from [O II] and Hα+[N II] emission lines, and its stellar population of stellar mass and dust extinction by using the SED fitting technique. The detailed analysis is completely described in Appendix C. In this section, we briefly report the main results of the estimated physical quantities, which are summarized in Table 3.2.

The stacked LAE has a stellar mass of $M_\star \sim 5 \times 10^8 M_\odot$, thus allowing us to investigate physical properties of low-mass galaxies at high-z. For the estimation of metallicity, since we have only [O II] and Hα+[N II] fluxes, we make use of the fact that [O II]/(Hα+[N II]) ratio can be expressed as a combination of two metallicity empirical indicators, $N2$-index and [O II]/Hβ, under some assumptions (Equation C.5). However, the new metallicity indicator of [O II]/(Hα+[N II]) ratio involves uncertainties of (i) two metallicity solutions (cf. $R23$-index; Section 2.3.2), (ii) ionization parameter, and (iii) dust extinction. Due to these uncertainties, we just adopt a conservative conclusion that the metallicity of the stacked LAE is no less than $0.17\,Z_\odot$ (1σ), or $0.09\,Z_\odot$ (2σ), which correspond to $12 + \log({\rm O/H}) = 7.93$ and 7.63, respectively. For the estimation of SFR, we use the Hα luminosity using the relation (Kennicutt 1998) after corrected for its dust extinction, which is estimated from SED fitting. Since we have only the Hα+[N II] luminosity for the stacked LAE, we subtract the contribution of [N II]$\lambda\lambda$6584, 6548 lines from the observed Hα+[N II] luminosity. We use the fact that [N II]/Hα ratio ($N2$-index) varies with metallicity. We estimate the [N II]/Hα ratio from the derived metallicity, inferring the ~ 6 % contribution of [N II] to the Hα+[N II] luminosity. Finally, we obtain SFR $= 14^{+2}_{-3} M_\odot$ yr^{-1}. This SFR is the first unbiased SFR estimate from Hα luminosity for typical $z \sim 2$ LAEs of L(Lyα) $> 1 \times 10^{42}$ erg s^{-1}.

Although no estimation of ionization parameter is obtained by the NIR narrowband survey, the estimated metallicity and SFR are useful to investigate average properties of low-mass LAEs on the $M_\star$-SFR-metallicity plane.

Table 3.2. Physical Properties of the stacked object

sample	$12+\log(\mathrm{O/H})$	$\mathrm{SFR_{cor}}$	EW(Hα)	EW(Lyα)	L(Hα)	L(Lyα)	$M_\star$	$E(B-V)$
		($M_\odot\,\mathrm{yr}^{-1}$)	(Å)	(Å)	($10^{42}\,\mathrm{erg\,s}^{-1}$)	($10^{42}\,\mathrm{erg\,s}^{-1}$)	($10^8 M_\odot$)	(mag)
	(1)	(2)	(3)	(4)	(5)	(6)	(7)	(8)
NB209 sub-region	>7.93 (1σ) >7.63 (2σ)	14^{+2}_{-3}	256^{+229}_{-98}	63^{+3}_{-5}	$0.76^{+0.12}_{-0.12}$	$1.80^{+0.05}_{-0.07}$	$4.79^{+0.22}_{-0.81}$	$0.27^{+0.01}_{-0.03}$

Note: (1) Oxygen abundance derived from [O II]/(Hα+[N II]) index. Firm lower limits of the metallicity are given. (2) Star formation rate ($M_\odot\,\mathrm{yr}^{-1}$) derived from H$\alpha$ luminosity after correcting for contribution of [N II] lines and extinction derived from SED fitting. (3) Rest-frame equivalent width of Hα (Å). (4) Rest-frame equivalent width of Lyα (Å). (5) Observed luminosity of Hα ($10^{42}\,\mathrm{erg\,s}^{-1}$). (6) Observed luminosity of Lyα ($10^{42}\,\mathrm{erg\,s}^{-1}$). (7) Stellar mass from SED fitting. (8) Dust extinction from SED fitting.

3.3. Summary of This Chapter

In this Chapter, we have presented physical properties of the LAEs at $z \simeq 2.2$ found by our Subaru/ Suprime-Cam survey (Appendix A). Near-infrared spectroscopy and narrowband imaging data are used, whose detailed descriptions are given in Appendices B and C, respectively. Main results are summarized as follows.

- From the near-infrared spectroscopy of Keck/NIRSPEC and Magellan/MMIRS, we have identified two LAEs, CDFS-3865 and COSMOS-30679, whose rest-frame optical multi-emission lines are detected including [O II]λ3727. This is the first report of [O II]-detection from narrowband-selected high-z LAEs individually. The [O III]/[O II] ratio and $R23$-index reveals that CDFS-3865 has a very high ionization parameter ($q_{\rm ion} = 2.5^{+1.7}_{-0.8} \times 10^8\,{\rm cm\,s^{-1}}$) and a low metallicity ($12 + \log({\rm O/H}) = 7.84^{+0.24}_{-0.25}$) in contrast with moderate values of other high-z galaxies such as LBGs. COSMOS-30679 also has a relatively high ionization parameter ($q_{\rm ion} = 8^{+10}_{-4} \times 10^7\,{\rm cm\,s^{-1}}$) and a low metallicity ($12 + \log({\rm O/H}) = 8.18^{+0.28}_{-0.28}$).

- From the two near-infrared narrowband filters covering [O II] and Hα+[N II] lines at $z \simeq 2.2$, we have obtained their average lines fluxes of LAEs by stacking analysis. By using the line ratio of [O II]/(Hα+[N II]) with photoionization models and empirical metallicity relations, we have found that the average metallicity of LAEs is no less than $0.09\,Z_\odot$ at the 2σ level (Figure C.6). This is the first constraint on the metallicity of a typical LAE at high-z. The average LAE has a stellar mass of $5 \times 10^8\,M_\odot$ and a SFR of $14\,M_\odot\,{\rm yr^{-1}}$. Although no estimation of ionization parameter is obtained by the narrowband analysis, the estimated metallicity and SFR are useful to investigate average properties of low-mass LAEs on the $M_\star$-SFR-metallicity plane.

4 Ionization State and Metallicity of Intermediate- and High-Redshift Galaxies

In Chapter 2, we have shown the SDSS galaxies have the average value of ionization parameter of $\log(q_{\rm ion}/{\rm cm\,s^{-1}}) \sim 7.3$ (see also Dopita et al. 2006a), and metallicity of $12+\log({\rm O/H}) \sim 9.0$ (see also e.g., Tremonti et al. 2004; Mannucci et al. 2010). In order to investigate the redshift evolution of ionization state and metallicity, we present physical properties of intermediate- ($z = 0.5-1.5$) and high-z ($z \sim 2-3$) star-forming galaxies in this chapter. Notably, we include LAEs in the investigation, whose pilot estimations of ionization parameter and metallicity are given by our study (Section 3.1). We treat LAEs and other continuum-selected galaxies such as LBGs differently, so that we can infer the relationship between ionization state and Lyα photon escape.

We describe the intermediate- and high-z galaxy samples in Section 4.1. In Section 4.2, we show their ionization parameters and metallicities based on the relation between [O III]/[O II] ratio and $R23$-index. We present the distribution of intermediate- and high-z galaxies on the [O III]/[O II] vs. $\zeta_\beta\,(\Theta)$ relation derived with the SDSS sample (Figure 2.11) in Section 4.3.

4.1. Intermediate- and High-Redshift Galaxy Samples

For the study of ionization parameter and metallicity, we make samples of intermediate- and high-z galaxies that have firm estimates of stellar mass and spectroscopic measurements of nebular emission lines (i.e., Hydrogen Balmer lines, [O II], [O III]). We particularly include strongly lensed galaxies, BX/BM galaxies, LBGs, and LAEs.

- Intermediate redshift galaxy sample ($z = 0.5-1.5$) is composed of 24 galaxies from the Gemini Deep Deep Survey (GDDS) and 15 galaxies from the Canada-France Redshift Survey (CFRS) (Savaglio et al. 2005; Maier et al. 2005). Moreover, we add 26 low-mass galaxies recently reported by Henry et al. (2013), and 4 strongly lensed galaxies (Christensen et al. 2012a; Queyrel et al. 2009) to the sample. In total, the intermediate-z sample contains 69 galaxies.

- High redshift galaxy sample ($z \sim 2-3$) consists of 39 galaxies in total, 21 strongly lensed galaxies (Pettini et al. 2001; Fosbury et al. 2003; Richard et al. 2011; Rigby et al. 2011; Christensen et al. 2012a; Wuyts et al. 2012; Belli et al. 2013), two LAEs (Section 3.1), one metal-poor BX galaxy (Erb et al. 2010), and 15 LBGs from the AMAZE and LSD projects (Maiolino et al. 2008; Mannucci et al. 2009).

We use a total of $108 = (69+39)$ intermediate- and high-z galaxies in our analysis.

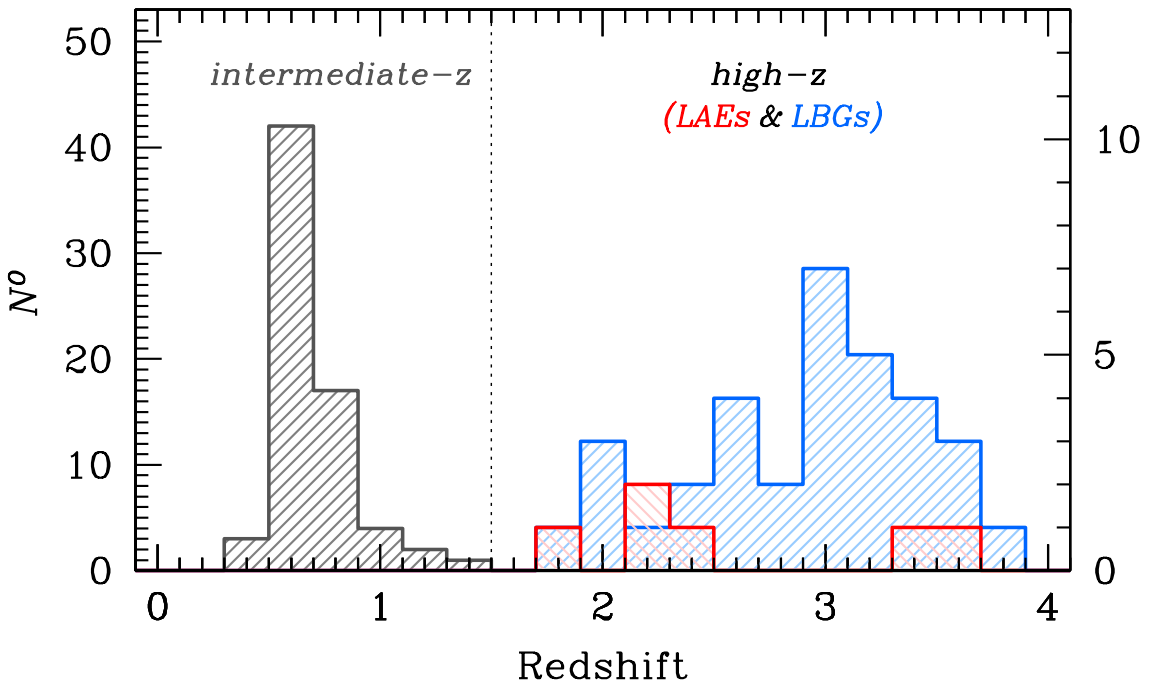

Figure 4.1. The redshift distribution of our samples of intermediate-z galaxies (gray), high-z LAEs (red), and LBGs (blue). The tick-size in the left y-axis corresponds to the intermediate-z galaxies, while the right y-axis shows the numbers for high-z galaxies.

We divide the high-z galaxy sample into two subsamples, LAE and LBG samples, to investigate the relationship between ionization state and Lyα photon escape. For high-z galaxies with a Lyα flux measurement, we classify galaxies with $\mathrm{EW_{rest}}$ (Lyα) > 20 Å as LAE; Lynx arc (Fosbury et al. 2003), BX418 (Erb et al. 2010), Abell 1689 31.1 arc, and SMACS J2031 arc (Christensen et al. 2012a,b). We include the two narrowband selected LAEs, CDFS-3865 and COSMOS-30679 (Section 3.1), to the LAE sample. For high-z galaxies with no Lyα flux measurement, we regard these galaxies as LBGs for simplification. Table 4.1 gives the details of our samples of intermediate-z galaxies, high-z LAEs and LBGs, and Figure 4.1 shows the redshift distribution of the samples.

We derive physical quantities for these intermediate- and high-z galaxies with the same procedures as those for our SDSS galaxies (Chapter 2). Emission line fluxes are corrected for extinction with Hα/Hβ and the extinction curve given by Calzetti et al. (2000). For galaxies with no Hα or Hβ measurement, we correct for extinction estimated from spectral energy distribution (SED) fitting, assuming that the amount of extinction is the same in continuum and emission lines. For galaxies neither with Hα/Hβ nor dust extinction from SED fitting[4.1], we adopt dust extinction inferred from stellar mass based on the empirical relation (Gilbank et al. 2010). SFRs are estimated from a hydrogen recombination line of Hα or Hβ corrected for dust extinction with the Kennicutt (1998)'s relation. If [O III]λ4959 fluxes are not available in the literature[4.2], we assume a value of 0.28 for the [O III]λ4959/5007 ratio (Richard et al. 2011). We have confirmed that this assumption does not affect our results significantly. We estimate intrinsic SFRs and stellar masses, using lens magnification factors for the strongly lensed galaxies. We

[4.1] These galaxies are $z \sim 1$ GDDS objects.
[4.2] There are 25, 10, and 9 galaxies at $z \sim 1$, 2, and 3, respectively.

Table 4.1. The Intermediate- and High-z Galaxy Samples

Reference	No.	Redshift
High-z LAE Sample (Total No = 6)		
This work (Section 3.1)	2	2.2, 2.2
Fosbury et al. (2003)	1	3.4
Erb et al. (2010)	1	2.3
Christensen et al. (2012a,b)	2	1.8, 3.5
High-z LBG Sample (Total No = 33)		
Pettini et al. (2001)	1	2.7
Maiolino et al. (2008)	9	3.2–3.8
Mannucci et al. (2009)	6	3.1–3.4
Richard et al. (2011)	8	2.2–3.1
Rigby et al. (2011)	1	1.7
Christensen et al. (2012a)	2	1.9, 2.0
Wuyts et al. (2012)	2	2.8, 2.9
Belli et al. (2013)	4	2.1–3.3
Intermediate-z Sample (Total No = 69)		
Savaglio et al. (2005)	24	0.5–1.0
Maier et al. (2005)	15	0.5–0.8
Queyrel et al. (2009)	1	1.4
Christensen et al. (2012a)	3	1.0–1.2
Henry et al. (2013)	26	0.6–0.7

Note: Summary of the intermediate- and high-z galaxy samples. For each of the samples, we list the references from which we collect the galaxies. The redshift range and the number of galaxies collected from the literature are also given for each of the references.

place the lower (upper) limits on the SFR and stellar mass of SGAS1527 (SGAS1226) that only has the upper (lower) limit of the magnification factor (Wuyts et al. 2012). We adopt the lower limit of stellar mass given by Villar-Martín et al. (2004) for Lynx arc (Fosbury et al. 2003). For high-z galaxies with no [O II] detections (Fosbury et al. 2003; Erb et al. 2010; Richard et al. 2011), we apply 3σ upper-limit fluxes of [O II] for the lower limits of [O III]/[O II] ratio, while we approximate their $R23$-indices under the assumption of no significant [O II] flux. Using the BPT diagram and/or the rest-frame UV spectroscopic properties, we have identified no obvious AGN activity in the high-z galaxies.

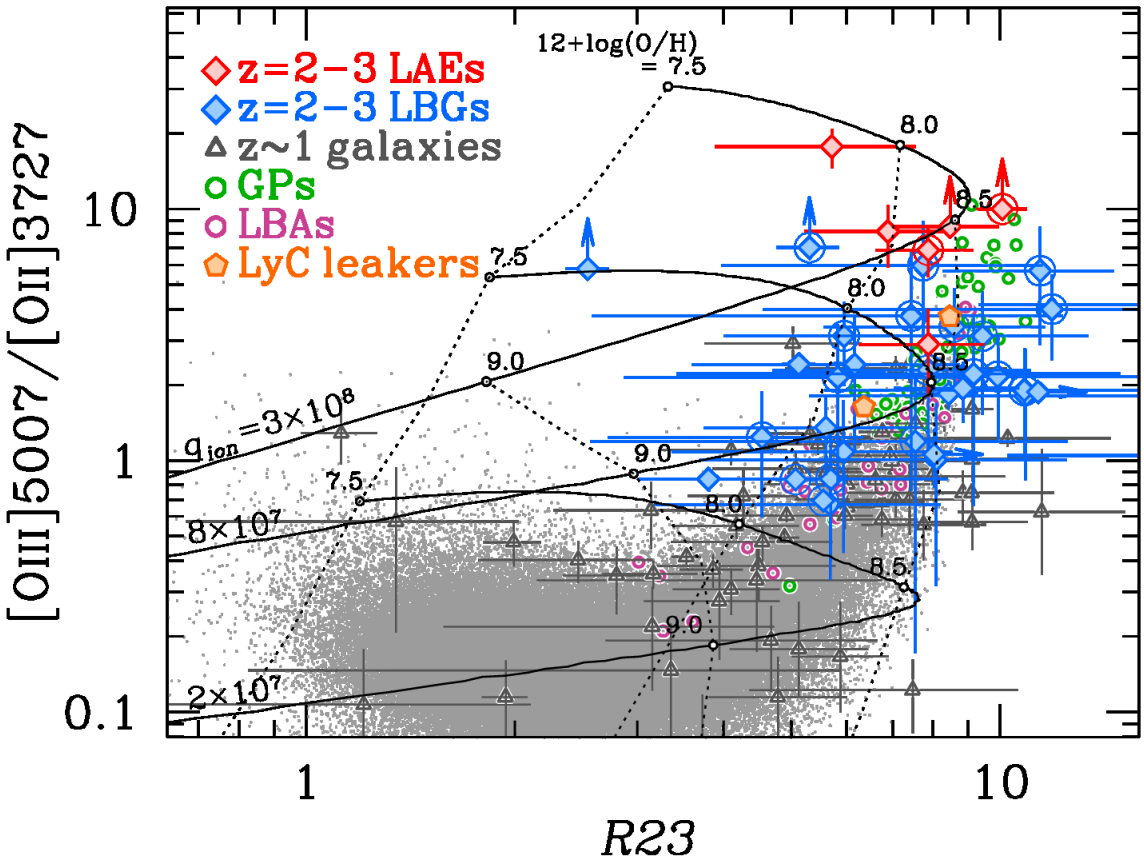

Figure 4.2. The relation between [O III]/[O II] and $R23$-index. The red and blue diamonds represent $z = 2-3$ LAEs and LBGs, respectively. Specifically, the diamonds with a circle denote galaxies at $z > 3$. The gray triangles are $z \sim 1$ star-forming galaxies. The other symbols and colors are the same as those used in Figure 2.2.

4.2. [O III]/[O II] vs. $R23$-index Diagram

In order to investigate ionization parameter and metallicity of the intermediate- and high-z galaxies, we plot them on the diagram of [O III]/[O II] ratio and $R23$-index in Figure 4.2. The red and blue diamonds denote $z \sim 2-3$ LAEs and LBGs, respectively. Compared to the SDSS galaxies, these high-z galaxies clearly present an [O III]/[O II] ratio higher than most of local galaxies by a factor of $\gtrsim 10$. The majority of $z \sim 1$ galaxies (the gray triangles) are placed at the middle between the SDSS galaxies and the $z \sim 2-3$ LBGs. LBGs at $z \gtrsim 3$ (blue diamonds with a circle) have an [O III]/[O II] ratio higher than those at $z \lesssim 3$ on average. In Figure 4.2, LAEs have the highest [O III]/[O II] ratio, which is higher than those of local galaxies by a factor of ~ 40, and even higher than those of the LBGs by a factor of ~ 4. The local galaxies of GPs (green open circles), LBAs (purple open circles), and LyC leakers (orange pentagons) are placed near the high-z galaxies. It should be noted that some LAEs have a remarkably high [O III]/[O II] ratio that cannot be found in the local galaxies.

We evaluate the average values of ionization parameter and metallicity of the intermediate- and high-z galaxy samples in the same manner as in Section 2.3.3. The estimated values are summarized in

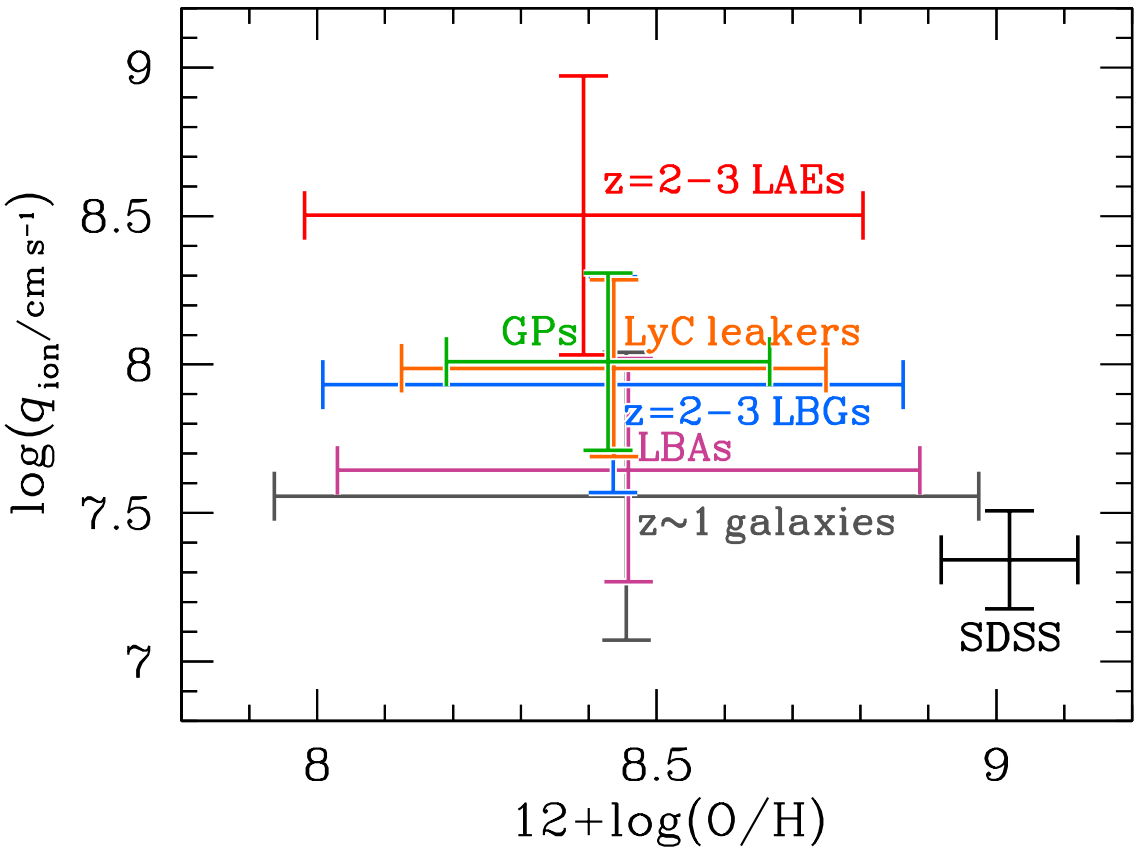

Figure 4.3. Average ionization parameter and metallicity for our galaxy samples (Table 4.2).

Table 4.2. Average ionization parameter, $\log(q_{\rm ion})$, and metallicity, $12+\log({\rm O/H})$, ranges for the intermediate- and high-z galaxy samples estimated from the [O III]/[O II] ratio and *R*23-index. The values for the local galaxy samples are also quoted from Table 2.2.

Sample	$\log(q_{\rm ion})$	$12+\log({\rm O/H})$
SDSS	7.18–7.51	8.92–9.12
$z\sim1$ galaxies	7.07–8.04	7.94–8.97
LyC leakers	7.69–8.28	8.13–8.75
LBAs	7.27–8.02	8.03–8.89
GPs	7.71–8.30	8.19–8.67
$z=2-3$ LBGs	7.57–8.29	8.01–8.87
$z=2-3$ LAEs	8.04–8.97	7.98–8.81

Table 4.2 and shown in Figure 4.3. The red, blue, and gray line show the average values of ionization parameter and metallicity for the high-z LAE, LBG, and intermediate-z samples, respectively. We again list the ranges of values in both the high-Z and low-Z branches for all of our samples except the SDSS sample.

A notable finding in Figure 4.3 is the evolution of ionization parameter with redshift. The SDSS galaxies have the average value of $\log(q_{\rm ion}/{\rm cm\,s^{-1}})\sim7.3$ (see also e.g., Dopita et al. 2006a). In contrast, high-z galaxies have an ionization parameter of $\log(q_{\rm ion}/{\rm cm\,s^{-1}})\sim7.6-9.0$. High-$z$ LBGs have an

ionization parameter higher than the SDSS galaxies by a factor of ~ 4, and LAEs show the highest ionization parameter among the galaxy samples, which is about an order of magnitude higher than the SDSS galaxies. The $z \sim 1$ galaxies are placed at the middle between the SDSS galaxies and the $z \sim 2-3$ LBGs, although the scatter is large. The redshift evolution of ionization parameter has been previously claimed (e.g., Lilly et al. 2003; Hainline et al. 2009; Richard et al. 2011). We confirm the evolution of the ionization state of galaxies with the high-z galaxy sample significantly larger than those used in the previous studies.

Another finding in Figure 4.3 is that the local extreme populations of GPs, LyC leakers, and LBAs are plotted in the similar area as high-z galaxies on the [O III]/[O II] vs. $R23$-index diagram. This suggests that these extreme populations have an ionization parameter as high as LBGs and LAEs at high redshifts. Moreover, the ionization parameter of GPs is comparable to that of LAEs. In this sense, GPs could be local counterparts of high-z LAEs.

4.3. Dependence of [O III]/[O II] and $R23$-index on $M_\star$ and SFR

Figure 4.4 is the same plot as Figure 2.7 but with intermediate- and high-z galaxy samples. From the histograms plotted in the top of each panel of Figure 4.4, we find that high-z galaxies have a $M_\star$ comparable with the SDSS galaxies, but a SFR higher than these local galaxies, in consistent with the tendency of the evolution of the star-formation main sequence (e.g., Daddi et al. 2007). The SFRs and $M_\star$ of high-z galaxies are little higher than those of GPs and LBAs, while the sSFR of high-z galaxies are comparable with those of GPs and LBAs. LAEs exhibit remarkable properties on average, having the least $M_\star$ and the highest SFR among galaxies at any redshift.

The bottom of each panel of Figure 4.4 shows the plot of [O III]/[O II] versus one of the galaxy global properties of $M_\star$, SFR, sSFR, and $\mu_{0.32}$. These panels indicate that the trend that a high [O III]/[O II] ratio is found in low $M_\star$, low $\mu_{0.32}$, and high sSFR galaxies found in the local universe seems to hold even at high-z.

We nextly compare the intermediate- and high-z galaxy samples with the best-fit function of the SDSS galaxies on the [O III]/[O II] vs. $\zeta_{0.25}(\mu_{0.32})$ diagram in Figure 4.5. This figure is the same as Figure 2.11, but with intermediate- and high-z galaxies. Although the best-fit function is derived with the SDSS sample alone, the local extreme populations and high-z galaxies appear to follow the same relation or fall on the extrapolation of the function. It should be noted that no significant differences are found between galaxies at $z \sim 2$ and 3. We note, however, that some galaxies including LAEs and LyC leakers are also found to depart significantly from the FIR towards higher [O III]/[O II]. We discuss a possible explanation of the deviations in Section 5.1.5.

To summarize, the relation of best-fit function between [O III]/[O II] and $\zeta_\beta(\Theta)$ (Figure 4.5) is thus in general thought to be a fundamental relation consisting of ionization parameter, metallicity, $M_\star$, and SFR over cosmic time. Therefore, as proposed in Section 2.3.5, we refer to the relation between [O III]/[O II] and $\zeta_{0.25}(\mu_{0.32})$ (Figure 4.5) as the Fundamental Ionization Relation (FIR). This universality indicates that ionization parameter is an essential property to describe star-forming galaxies at any redshift.

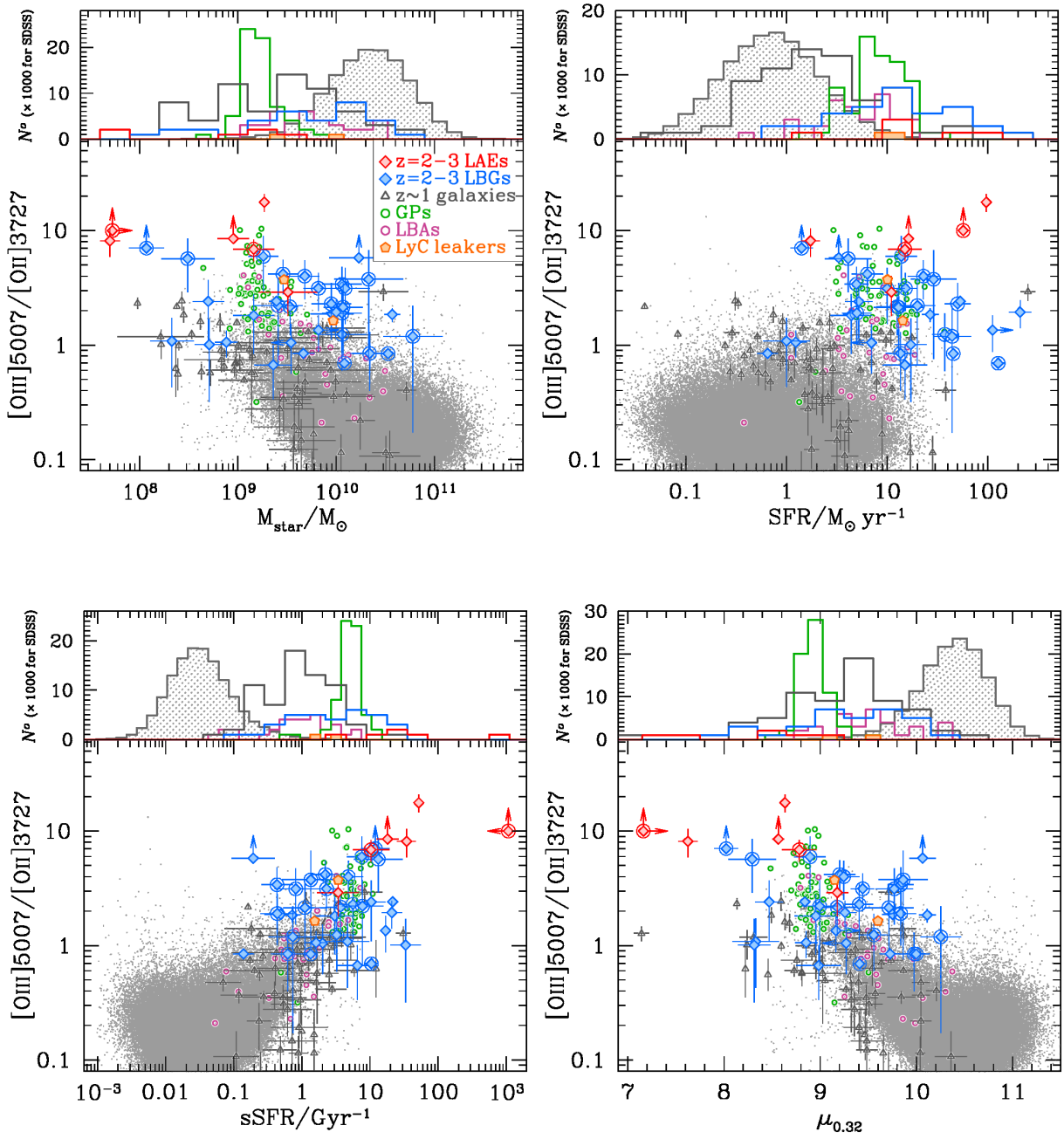

Figure 4.4. Dependence of [O III]/[O II] on $M_\star$ (top left), SFR (top right), sSFR (bottom left), and $\mu_{0.32}$ (bottom right). The symbols and colors are the same as those used in Figures 2.7 and 4.2. In each panel, the distribution of one of the galaxy global properties for the local galaxy samples is given in the top. If a galaxy global property is given only an upper- or lower- limit, the limit value is used for the histogram.

4.4. Summary of This Chapter

In this Chapter, we have presented the extended study of ionization state and metallicity in galaxies at high-z. We have used 69 intermediate-z ($z = 0.5$–1.5) and 39 high-z ($z \sim 2$–3) star-forming galaxies compiled from the literature. Notably, we include LAEs in the investigation, whose pilot estimations of ionization parameter and metallicity are given by our study (Section 3.1). We treat LAEs and other continuum-selected galaxies at high-z such as LBGs differently, so that we can infer the relationship

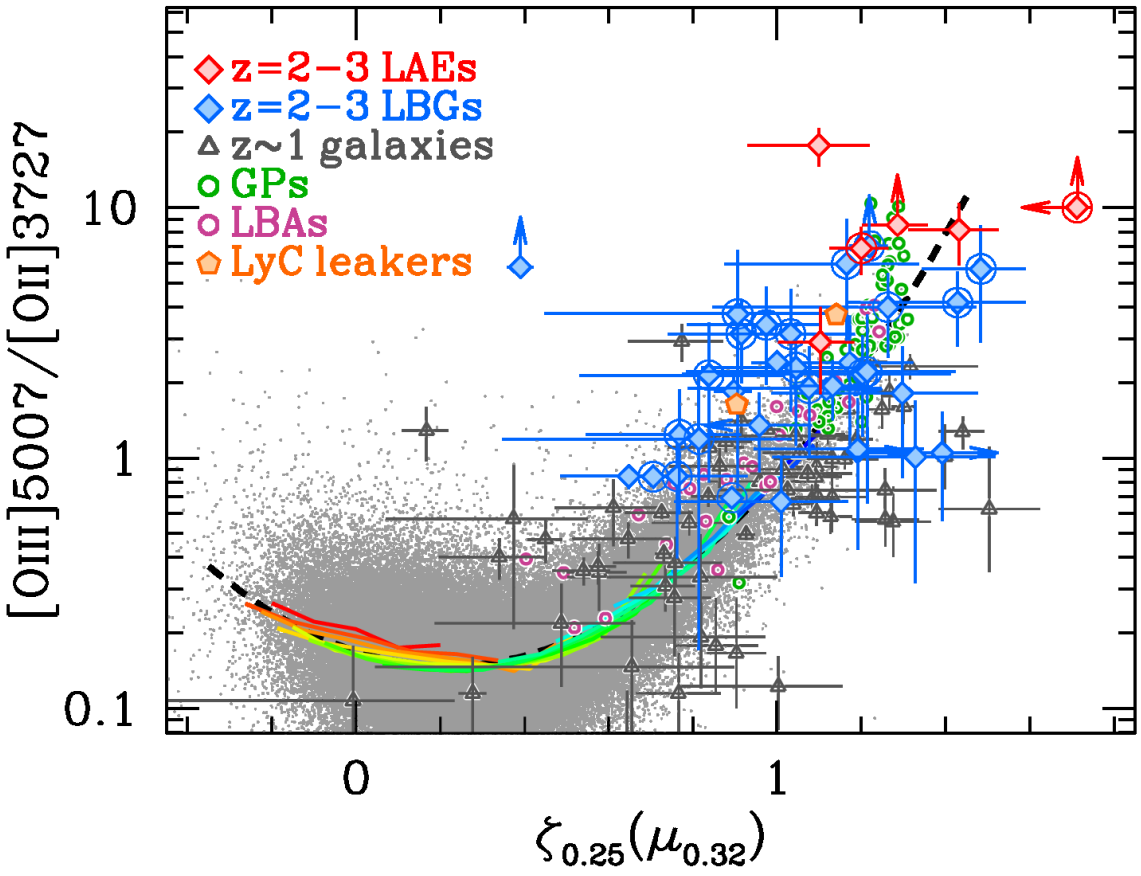

Figure 4.5. [O III]/[O II] vs. $\zeta_{0.25}(\mu_{0.32})$ relation for our galaxy samples. The symbols, lines, and colors are the same as those in Figures 2.11 and 4.2. In this plot, we compare the relation of the SDSS galaxies with our galaxy samples, high-z galaxies, GPs, LBA, and the LyC leakers.

between ionization state and Lyα photon escape. Main results in this chapter are summarized as follows.

- We have confirmed that $z \sim 2-3$ galaxies show an [O III]/[O II] ratio significantly higher than typical local galaxies by a factor of $\gtrsim 10$ (Figure 4.2). The photoionization models reveal that these high-z galaxies have an ionization parameter of $\log(q_{\rm ion}/{\rm cm\,s^{-1}}) \sim 7.6-9.0$, a factor of $\gtrsim 4-10$ higher than typical local galaxies (Figure 4.3).

- Among high-z galaxies, LAEs show the highest ionization parameter, which is about an order of magnitude higher than the SDSS galaxies and a factor of $\gtrsim 3$ higher than LBGs (Figure 4.3).

- We have found that the ionization parameters of the local extreme populations of GPs, LyC leakers, and LBAs are comparable with the ones of $z = 2-3$ galaxies (Figure 4.3). This trend supports the idea that these local extreme populations could be local counterparts of high-z star-forming galaxies. Moreover, the ionization parameter of GPs is comparable to that of LAEs. In this sense, GPs could be local counterparts of high-z LAEs.

- We have suggested that the intermediate- and high-z galaxies follow the same relation between [O III]/[O II], $R23$-index, $M_\star$, and SFR defined with the SDSS galaxies (Figure 4.5). The relation

is thus referred to as the fundamental ionization relation (FIR). We have particularly found no significant differences between galaxies at $z \sim 2$ and 3 in the FIR.

- We have found that LAEs exhibit remarkable properties on average, having the least $M_\star$, and the highest sSFR among galaxies at any redshift (Figure 4.4). Some LAEs follow the same FIR (or its simple extrapolation towards higher ζ) derived with the SDSS sample (Figure 4.5). We note, however, that the other LAEs are also found to depart significantly from the FIR towards higher [O III]/[O II] ratio. The two LyC leakers show a similar trend. The increased [O III]/[O II] ratios could be related to their low column densities of neutral hydrogen in HII-regions (see the discussion in Section 5.1.5).

5 Discussion

In this chapter, we discuss ionization state and metallicity of galaxies at $z = 0$–3 including LAEs. In Section 5.1, we address the issues of (i) the evolution of ionization parameter, (ii) its possible origins, (iii) the FMR evolution at $z \gtrsim 3$, (iv) the relations between [O III]/[O II] ratio, $R23$-index, stellar mass, and SFR, and (v) the correlation between ionization parameter and $f_{\rm esc}$. A bottom line is that taking into account the ionization parameter is important to accurately describe star-forming galaxies especially at high-z. In Section 5.2, we discuss what kind of galaxies LAEs are by presenting their basic characteristics such as stellar mass, SFR, metallicity, EW(Lyα), etc.

5.1. Ionization State of Galaxies

5.1.1. Evolution of Ionization State

We have confirmed the trend that high-z galaxies have ionization parameters significantly higher than local galaxies. The SDSS galaxies typically show $q_{\rm ion} \sim 2 \times 10^7$ cm s^{-1}, while the high-z LBGs exhibit an ionization parameter higher than the SDSS galaxies by a factor of ~ 4 (Table 4.2, Figure 4.2). This evolution of ionization parameter is consistent with the trend that high-z galaxies depart from the local star-forming sequence in the BPT diagram towards higher [O III]/Hβ ratio (e.g., Brinchmann et al. 2008; Kewley et al. 2013a,b), and with the recent spectroscopic surveys of high-z galaxies (Cullen et al. 2013; Holden et al. 2014).

This evolution can be closely related to the evolution of SFR and $M_\star$. As shown in Figure 2.8, a high [O III]/[O II] ratio, i.e., a high ionization parameter, is found in low $M_\star$, low $\mu_{0.32}$, and high sSFR galaxies. Since high-z galaxies tend to have a higher sSFR (or smaller $\mu_{0.32}$) than local galaxies (Figure 4.4; see also Daddi et al. 2007), they are supposed to show an ionization parameter typically higher than local galaxies. Note that ionization parameter is, by definition, the ratio of ionizing photon and hydrogen atom densities. Since the amount of ionizing photons and hydrogen atoms would be positively correlated with SFR and stellar mass, respectively, the evolution of ionization parameter would be explained by the increase of sSFR, i.e., the high SFR and low mass for high-z galaxies.

The local extreme populations of GPs, LyC leakers, and LBAs have an ionization parameter as high as $z \sim 2-3$ LBGs and LAEs. Moreover, the ionization parameter of GPs is comparable to that of LAEs. GPs' low metallicities (see also Amorín et al. 2010) and SFRs (Izotov et al. 2011) are also analogous to those observed in LAEs. In these senses, GPs could be local counterparts of $z \sim 2-3$ LAEs. However, GPs are quite rare objects in the local universe. In the SDSS Date Release 7 (DR7) spectroscopic galaxy

sample, 251 GPs are found (Cardamone et al. 2009). Searching the entire SDSS DR7 spectroscopic sample yields 418,429 objects which fall in the GPs redshift range ($z = 0.112$–0.360; Cardamone et al. 2009) and are classified as GALAXY. Therefore, the GPs occupy only $\sim 0.06\,\%$ of the SDSS galaxy sample. Based on the luminosity function determined for the SDSS galaxies (Blanton et al. 2003), the number density is $\sim 1.5 \times 10^{-2}\,\mathrm{Mpc}^{-3}$ above a detection limit $M_r = -17.63$, which corresponds to $0.037\,L^\star$. The limit is calculated from the apparent magnitude limit ($r < 17.77$; Tremonti et al. 2004) for the spectroscopic sample and the redshift threshold ($z > 0.028$; Nagao et al. 2006). The number density of the GPs is thus approximately $9 \times 10^{-6}\,\mathrm{Mpc}^{-3}$, which is almost consistent with the number density found by Cardamone et al. (2009) (~ 2 GPs per deg^2). On the other hand, the number density of LAEs at $z = 2.2$ is $\sim 1.7 \times 10^{-3}\,\mathrm{Mpc}^{-3}$ calculated by integrating the luminosity function provided by Hayes et al. (2010)[5.1] above $L = 0.037\,L^\star$. The number density of the GPs is thus almost two orders of magnitude smaller than that of LAEs. Interestingly, Heckman et al. (2005) report a similar difference of abundances between LBAs and $z \sim 3$ LBGs. These results indicate that galaxies with a high ionization parameter would emerge in a high redshift universe, and that these galaxies are more dominant in high-z than the local universe.

Recently, some studies have found galaxies with very strong nebular emission lines that are called extreme emission line galaxies (EELGs; e.g., van der Wel et al. 2011; Atek et al. 2011). van der Wel et al. (2011) investigate EELGs at $z \sim 1.7$ in the Cosmic Assembly Near-IR Deep Extragalactic Legacy Survey (CANDELS; Grogin et al. 2011; Koekemoer et al. 2011) deep imaging data of Hubble Space Telescope (HST)/WFC3. These EELGs present a very strong [O III] of EW $\gtrsim 1000$ Å that significantly boosts flux measurements in a NIR broadband, which are similar to the bright r-band fluxes of GPs. Although no estimates of ionization parameter are given for EELGs due to lacks of [O II] data, they could have a very high ionization parameter suggested from their very large EW([O III]), low $M_\star$ ($\sim 10^8\,M_\odot$), and high sSFR ($\sim 50\,\mathrm{Gyr}^{-1}$). Kakazu et al. (2007) study ultra-strong line galaxies (USELs) at $z \sim 1$ identified by narrowband imaging, and find that USELs have extremely low metallicities ($12 + \log(\mathrm{O/H}) \lesssim 8$) and very high [O III]/[O II] ratios ($\gtrsim 3 - 100$). They argue that USELs typically have ionization parameters as high as $q_{\mathrm{ion}} \gtrsim 10^8\,\mathrm{cm\,s}^{-1}$. Obviously, ionization parameter is a key quantity to characterize these extreme populations of galaxies.

5.1.2. What is the Origin of High Ionization State?

Equation (2.5) shows that ionization parameter is described by the ionizing photon production rate, hydrogen density, and volume filling factor of the ionized gas. If we assume volume filling factors are comparable between galaxies, ionizing photon production rate and hydrogen density are main factors that govern the ionization parameter. First, a high ionizing photon production rate would be a key to explain the high ionization parameter, since we have found the trend that highly star-forming galaxies have high ionization parameters (Sections 2.3.4 and 2.3.5). Such highly star-forming galaxies have many young stars, which produce ionizing photons and maintain the high ionizing photon production rates. High ionization parameters typically seen in high-z galaxies would be resulted from the fact that galaxies with high SFR for their $M_\star$ are more commonly found at high-z (Section 5.1.1). Possible origins of the high SFR for their $M_\star$ are their young stellar population, efficient star-formation, and/or top-heavy IMF. Such efficient star-formation would be driven by the accretion of cold gas (e.g., Dekel et al. 2009).

[5.1] The detection limit is $L = 2.8 \times 10^{41}\,\mathrm{erg\,s}^{-1}$ ($\sim 0.02\,L^\star$).

Alternatively, high ionized gas densities at high-z galaxies could be the origin of their high ionization parameters (Shirazi et al. 2013; Section 2.3.2). Indeed, such dense star-forming clumps are observed in massive high-z galaxies (e.g., Genzel et al. 2011). For less massive galaxies, outflows could play a role in the change of ionization parameter, since they efficiently remove the gas locally and reduce the gas density. However, the effect of outflows is complicated, since outflows also work as a star-formation feedback. We need more sophisticated theoretical models that incorporate these physics to fully understand the origins of high ionization parameters and the relationship between stellar mass, SFR, and metallicity (see also Section 5.1.4).

5.1.3. Revisiting the Issue of FMR Evolution from $z \sim 2$ to 3

Mannucci et al. (2010) have suggested that the FMR can describe properties of galaxies with no redshift evolution up to $z \sim 2.5$, and claimed that galaxies at $z \gtrsim 3$ fall significantly below the FMR by ~ 0.6 dex. The analysis of Mannucci et al. (2010) indicates the evolution of FMR from $z \sim 2$ to 3, but it is not clear why the FMR evolves only between $z \sim 2$ and $z \sim 3$. In contrast to the FMR evolution, we have argued in Section 4.3 that no significant differences are found between galaxies at $z \sim 2$ and 3 in the FIR (Figure 4.5). We address the question why the FMR shows the evolution but no evolution is found in the FIR.

Mannucci et al. (2010) use metallicities of $z \gtrsim 3$ galaxies given by Maiolino et al. (2008) and Mannucci et al. (2009) that are estimated with the local empirical relations of Maiolino et al. (2008). The local empirical relations of Maiolino et al. (2008) are obtained from two samples, (i) 259 local galaxies with $12+\log(\mathrm{O/H}) < 8.4$ whose metallicities are estimated by the electron temperature T_e method, and (ii) 22,482 star-forming SDSS galaxies with $12+\log(\mathrm{O/H}) > 8.2$ given with the photoionization model (Kewley & Dopita 2002; see also Nagao et al. 2006). Figure 5.1 presents $R23$-index and [O III]/[O II] ratio of the two samples. The red dashed curves denote the local empirical relations determined with these two samples (Maiolino et al. 2008). Figure 5.1 compares the photoionization models (black solid curves) with the local empirical relations, and indicates that the local empirical relations implicitly assume an ionization parameter. Given the fact that high-z galaxies have an ionization parameter higher than local galaxies (Section 5.1.1), the local empirical relations assuming a relatively low ionization parameter would provide biased metallicity estimates for high-z galaxies. At $z \lesssim 2.5$, the [N II]λ6584/Hα ratio can be used to estimate metallicities and/or to discriminate one from two metallicity solutions given by $R23$-index. However, at $z \gtrsim 2.5$ [N II]λ6584 and Hα lines cannot be detected from the ground. The [O III]/[O II] ratio is needed to determine one from two metallicity solutions of $R23$-index. The bottom panel of Figure 5.1 shows that the photoionization model predicts a lower metallicity if a lower ionization parameter is assumed. Thus, one may underestimate metallicities of $z \gtrsim 3$ galaxies with the local empirical relations, since the ionization parameter of $z \gtrsim 3$ galaxies is significantly higher than those of local galaxies (Section 5.1.1).

We evaluate the bias of $z \sim 3$ galaxy metallicity estimates, which is originated from the local empirical relation. We estimate metallicities of $z \sim 3$ galaxies with the Kobulnicky & Kewley (2004) method in the same manner as Section 2.3.3, allowing the ionization parameter evolution. We compile a total of 15 $z \sim 3$ galaxies from AMAZE (Maiolino et al. 2008) and LSD (Mannucci et al. 2009) projects. First, for a consistency check, we estimate metallicities of our 15 $z \sim 3$ galaxies with the local empirical relation used by Mannucci et al. (2010). We find that the average metallicity of the $z \sim 3$ galaxies is $12+\log(\mathrm{O/H})$ ~ 8.1 (left panel of Figure 5.2), which is consistent with that of Mannucci et al. (2010) ($12+\log(\mathrm{O/H})$

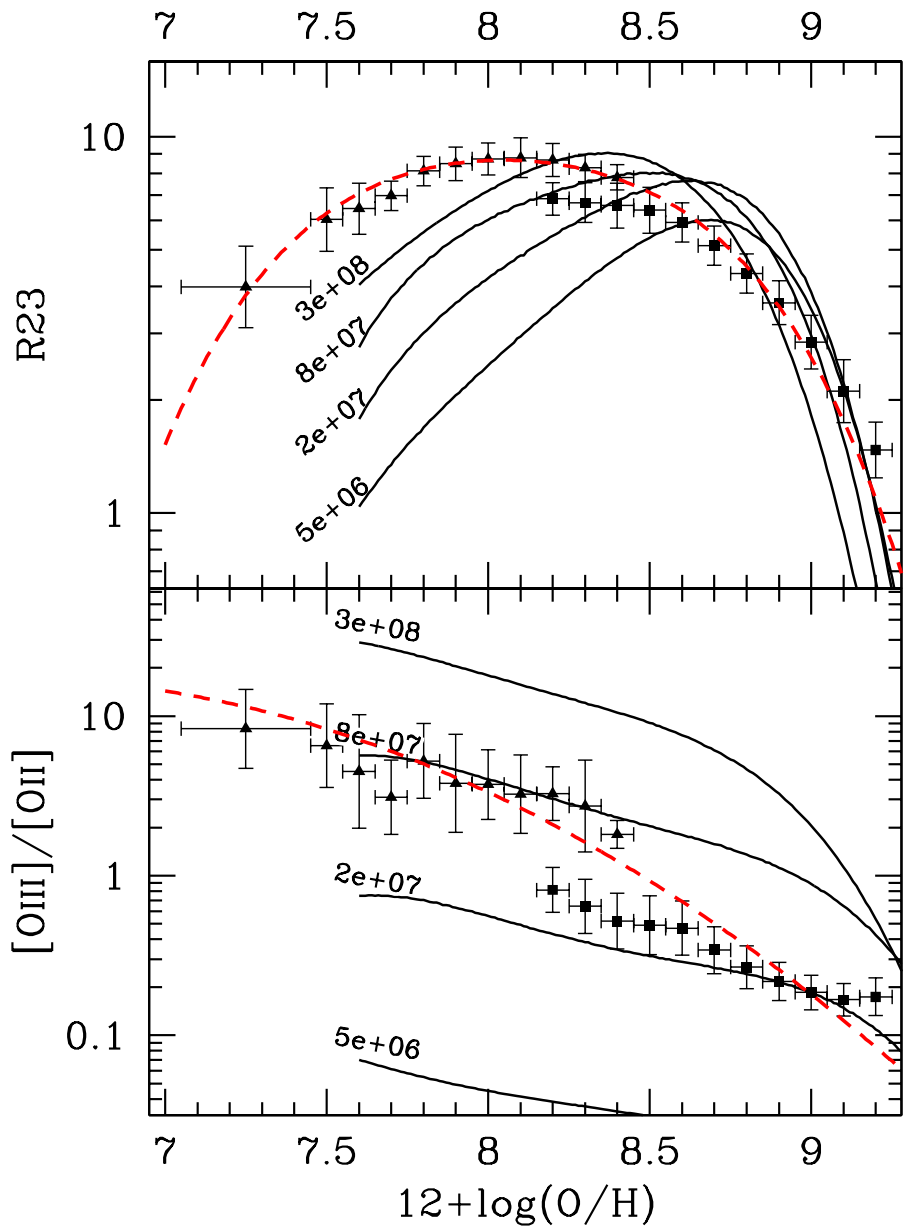

Figure 5.1. *R*23-index (top) and [O III]/[O II] ratio (bottom) as a function of metallicity. The triangles and squares show local galaxies in the samples (i) and (ii), respectively (see text), and the red dashed curve represents the local empirical relations (Maiolino et al. 2008). The black solid curves denote photoionization models (Kewley & Dopita 2002). The labels on the curves present values of $q_{\rm ion}$.

$\sim 8.0-8.2$). We confirm that our 15 galaxies and the local empirical relation can reproduce the results of Mannucci et al. (2010). Then, using the Kobulnicky & Kewley (2004) method, we obtain average metallicities of our 11 $z\sim 3$ galaxies for the low-Z and high-Z branches that are $12+\log({\rm O/H}) = 8.20$ and 8.65, with ionization parameters of $q_{\rm ion} \sim 6.6\times10^7$ and $1.1\times10^8\,{\rm cm\,s^{-1}}$, respectively. Typically $\sim 0.2-0.3$ dex errors are associated with the estimates of metallicity and ionization parameter for each of the galaxies. Note that four out of fifteen galaxies are omitted from these metallicity estimates, since their *R*23-index values fall out of the range covered by Equations (2.7) and (2.8). The right panel of Figure 5.2 compares the metallicity estimate of Mannucci et al. (2010) with ours allowing the ionization

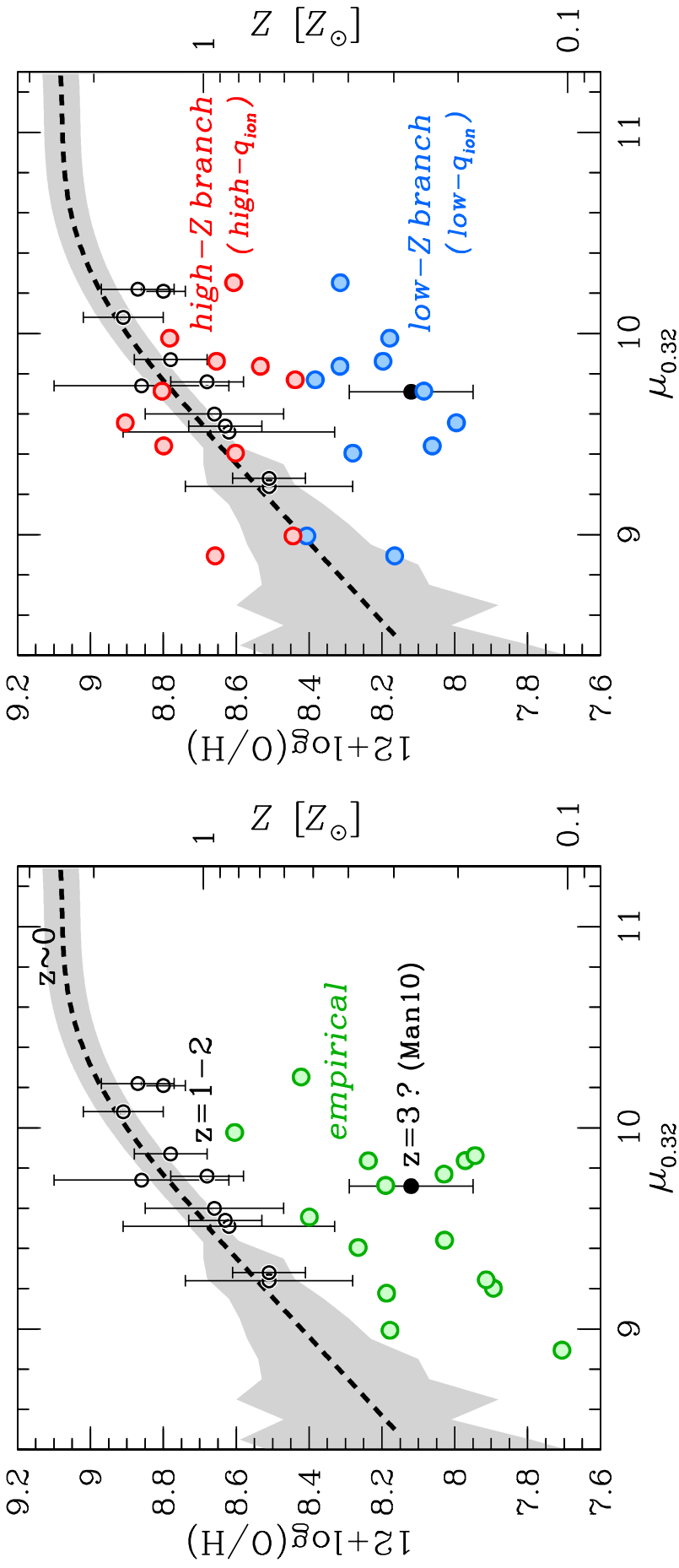

Figure 5.2. $z \sim 3$ galaxies in the FMR plot. *Left:* The black dashed curve and the gray shaded area indicate the FMR and its typical dispersion, respectively (Mannucci et al. 2010, 2011). The black open and filled circles represent galaxies at $z = 1$–2 and $z \sim 3$, respectively, that are compiled by Mannucci et al. (2010). The green circles denote $z \sim 3$ galaxies (Maiolino et al. 2008; Mannucci et al. 2009) whose metallicities are estimated with the local empirical relations in the same manner as Mannucci et al. (2010). These green circles are consistent with the average value shown in Mannucci et al. (2010). *Right:* Same as the left panel, but for metallicity estimates using the Kobulnicky & Kewley (2004) method that is free from the bias of ionization parameters. The red and blue circles denote metallicities of the $z \sim 3$ galaxies in the cases of high- and low-Z branches, respectively. Four $z \sim 3$ galaxies are omitted from the plot, since their $R23$-index values are out of the range where the Kobulnicky & Kewley (2004) method is available. The blue circles are consistent with the Mannucci et al. (2010)'s average

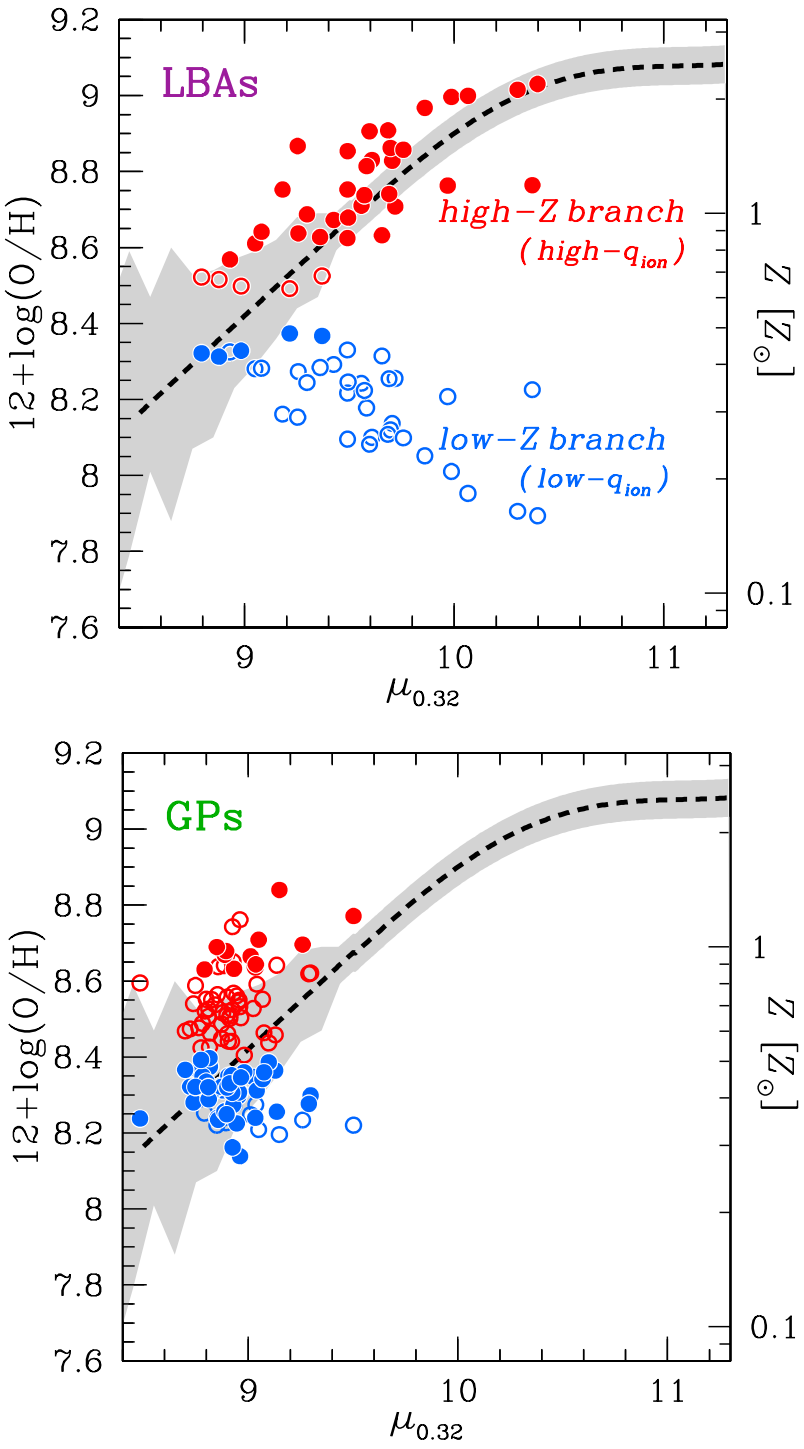

Figure 5.3. LBAs and GPs in the FMR plot. Metallicities are estimated by the Kobulnicky & Kewley (2004) method. *Top:* The red and blue circles denote metallicities of the LBAs in the cases of high- and low-Z branches, respectively. For each LBA, the two metallicity solutions are distinguished by the other metallicity indicators (see text). The filled circles present metallicities that agree better with the other metallicity estimates. The open circles show less likely solutions. *Bottom:* Same as the top panel, but for GPs. Four GPs are omitted from the plot, since their $R23$-index values are out of the range where the Kobulnicky & Kewley (2004) method is available. The two panels suggest that local galaxies follow the FMR (the dashed curve) over the wide ranges of $M_\star$ and SFR if their metallicities are estimated with ionization parameter.

parameter evolution. The high-Z branch metallicities appear to follow the FMR (black dashed curve; Mannucci et al. 2010, 2011). In contrast, the low-Z branch metallicities fall below the FMR, which is consistent with the result of Mannucci et al. (2010).

Because there is no useful line ratio, such as [N II]λ6584/Hα, that determines one from two metallicity solutions of low and high-Z branches, we cannot conclude which metallicities are correct and whether $z \sim 3$ galaxies follow the FMR. However, we find that the high ionization parameter of $\sim 1.1 \times 10^8$ cm s^{-1} for the high-Z branch solution agrees with the our findings of ionization parameter evolution from $z = 0$ to 3 (Section 5.1.1). Moreover, there are no physical reasons for the sudden departure from the FMR from $z = 2$ to 3, e.g., the smooth evolution of cosmic SFR/stellar mass densities at $z \gtrsim 2$ (Bouwens et al. 2011; Stark et al. 2013). Theoretical studies do not find the departure from the FMR at $z \sim 3$. Our metallicity estimates of high-Z branch of $z \sim 3$ galaxies are comparable with those predicted by Davé et al. (2011) who perform cosmological hydrodynamic simulations. Dayal et al. (2013) have explained the trend of the FMR with the redshift-independent simple analytic model. These pieces of evidence imply that the $z \sim 3$ galaxy metallicities of high-Z branch with the high-ionization parameter are correct, and that $z \sim 3$ galaxies follow the FMR.

As local counterparts of high-z galaxies, we also examine GPs and LBAs in the FMR plot in Figure 5.3. Their metallicities are estimated in the same manner as those for $z \sim 3$ galaxies. However, their two metallicity solutions can be distinguished, since other metallicity indicators of [N II]λ6584/Hα ratio and/or gas temperature are available for the local galaxies. The filled circles display metallicities that agree better with those estimated from the other metallicity indicators (see Izotov et al. 2011 for the metallicities of GPs measured from gas temperature). Figure 5.3 suggests that local extreme populations follow the FMR if their metallicities are estimated with ionization parameter. This finding confirms the validity of the FMR over the wide ranges of stellar mass and SFR in the local universe. Another notable trend seen in Figure 5.3 is that the LBAs metallicities of high-Z branch with the high-ionization parameter are generally correct. This is what we argue for the $z \sim 3$ galaxies. Since LBAs are local UV-selected galaxies whose characteristics are similar to those for high-z LBGs (e.g., Overzier et al. 2009), their trends in the FMR plot support our argument that $z \sim 3$ LBGs have metallicities of high-Z branch with high-ionization parameter and follow the FMR.

For more conclusive discussion, one needs deeper NIR spectroscopy to provide an ionization parameter indicator of [Ne III]λ3869/[O II]λ3727 (e.g., Nagao et al. 2006; Levesque & Richardson 2013; Richardson et al. 2013) or IR ($\lambda > 3\mu$m) spectroscopy from the space to obtain [N II]λ6584/Hα that determines one from two metallicity solutions for $z \sim 3$ galaxies. In particular, the [Ne III]/[O II] ratio is observable from the ground up to $z \sim 5$. We have confirmed the utility of the [Ne III]/[O II] ratio for LAEs, whose ionization parameters are very high (Fosbury et al. 2003; Christensen et al. 2012b).

5.1.4. Fundamental Ionization Relation

As demonstrated in Section 5.1.3, ionization parameter is important for metallicity estimates. Although the FMR reproduces properties of galaxies with no significant evolution, input metallicities to the FMR would be sometimes biased due to the evolution of ionization parameters. In this sense, the FIR is advantageous because the FIR allows the difference of ionization parameter. The FIR consisting of the fiducial $\mu_{0.32}$ parameter requires non-zero β, where $\beta = 0$ is ruled out at the > 95 % confidence level (Section 2.3.5). This indicates that the 4-dimensional relation of FIR between ionization parameter,

metallicity, SFR, and $M_\star$ is useful to characterize gas properties of galaxies.

Since metallicity and ionization parameter are influenced by star-formation, gas infall and outflow, it is helpful to examine the trend seen in the FIR to fully understand these complicated physics. For this purpose, we first review the interpretations of the FMR presented by Mannucci et al. (2010) and Dayal et al. (2013). Then, we try to extend their discussions toward the FIR. Hereafter, we assume that galaxies are in a quasi-steady-state situation, where metal enrichment, gas infall and outflow occur simultaneously (i.e., time-scales of metal enrichment are shorter than the other relevant time-scales).

In the discussion of Mannucci et al. (2010), the authors simply consider the metal enrichment by the star-formation, the metal dilution by the infalling gas, and the metal ejection by the outflowing gas. By introducing an infalling gas $M_{\rm gas}$ and an outflow proportional to $\mathrm{SFR}^s\, M_\star^{-m}$, the authors derive

$$12+\log(\mathrm{O/H}) \sim \log\left(\frac{\mathrm{SFR}}{M_{\rm gas}\,\mathrm{SFR}^s\, M_\star^{-m}}\right), \tag{5.1}$$

and by using the (integrated) Kennicutt-Schmidt law ($\mathrm{SFR} \sim M_{\rm gas}^n$, where $n \simeq 1.5$; e.g., Kennicutt 1998),

$$12+\log(\mathrm{O/H}) \sim m\log(M_\star) + \left(1-\frac{1}{n}-s\right)\log(\mathrm{SFR}). \tag{5.2}$$

By comparing this equation with the $\mu_{0.32}$ parameter of $\log(M_\star)-0.32\log(\mathrm{SFR})$, the authors obtain $m=1$ and $s=0.65$, i.e., outflows are inversely proportional to mass and increase with SFR.

A more careful investigation is made by Dayal et al. (2013). The authors assume that both infall and outflow rates are proportional to SFR. This assumption is reasonable, bearing in mind that infalls are expected to drive star-formation via fueling pristine gas into galaxies, and that outflows to be caused by energy and/or momentum injected by supernovae and/or radiation pressure from massive stars, both of which are resulted from star-formation. The authors further assume that the infalling gas is metal-free. Under these assumptions, a simple set of equations is derived, such that

$$\begin{aligned}
&\frac{\mathrm{d}M_\star}{\mathrm{d}t} \equiv \psi = \varepsilon_\star M_{\rm gas} \\
&\frac{\mathrm{d}M_{\rm gas}}{\mathrm{d}t} = -(1-R)\psi + (a-w)\psi, \\
&\frac{\mathrm{d}(ZM_{\rm gas})}{\mathrm{d}t} = y(1-R)(1-Z)\psi - (1-R)Z\psi - wZ\psi
\end{aligned} \tag{5.3}$$

where $\varepsilon_\star^{-1}$ the star-formation time-scale and the SFR is assumed to be proportional to the gas mass. The two constant, R and y, represent the returned fraction from stars and yield per stellar generation, respectively[5.2]. The outflow and infall rates are given as $w(M)\psi$ and $a(M)\psi$, respectively. For $Z \ll 1$, the following relation is obtained from Equation (5.3):

$$Z(\psi) = \frac{y(1-R)}{a}(1-\mu^{-\alpha}), \tag{5.4}$$

where $\mu = M_{\rm gas}/M_{\rm gas,0} = \psi/(\varepsilon_\star M_{\rm gas,0})$, $M_{\rm gas,0} \simeq M_\star(1-R+w-a)+M_{\rm gas}$, and $\alpha = a/(R-1+a-w)$. By fitting the $Z(\psi)$ curves for various $M_\star$ to the FMR, the authors derive

[5.2]The authors use (R, y)=(0.79, 0.0871) that is consistent with the Salpeter IMF for a lower and upper mass limit of 1 and $100\,M_\odot$, respectively.

$$\ln a = -0.43 - 0.05 \ln(M_\star / 10^{10.75} M_\odot),$$
$$\ln w = 1.76 - 0.33 \ln(M_\star / 10^{9.0} M_\odot). \quad (5.5)$$

The best-fit solutions suggest that (i) both infall and outflow are needed to explain the FMR, (ii) the infall efficiency is almost independent of the galaxy mass, and (iii) the outflow efficiency is small in massive galaxies and rapidly increases with decreasing $M_\star$. For massive galaxies ($> 10^{11} M_\odot$), a large amount of metal-poor gas is injected into the galaxies due to their high SFRs, but the dilution is compensated by the large amount of metals produced by star-formation. On the other hand, for less massive galaxies, their metal-enrichment by star-formation is modest due to their low SFR. Moreover, as a result of their smaller gravitational potential wells, outflows efficiently eject metal-rich gas out of the galaxies. This interplay between the star-formation, the infall of metal-poor gas, and the outflow of metal-rich gas would shape the FMR. Interestingly, this model predicts w (i.e., the mass loading factor) being proportional to $M_\star^{-1/3} \propto 1/V$, which is expected if the outflow is momentum-driven (e.g., Murray et al. 2005).

A similar analytic model could be useful to understand the FIR, or the FMR with ionization parameter. From Equation (2.5), ionization parameter is described by the ionizing photon production rate, hydrogen density, and volume filling factor of the ionized gas. If we assume the ionizing photon production rate is proportional to the SFR and the change of the volume filling factor is negligible, we obtain

$$\log(q_{\rm ion}) \sim \frac{1}{3}\log({\rm SFR}) + \frac{1}{3}\log(n_{\rm H}). \quad (5.6)$$

Although it is quantitatively unclear how the density is affected by gas infalls and outflows, we can predict the change of the ionization parameter due to the change of SFR in the same manner as shown in the model of Dayal et al. (2013), such that SFR $\simeq \varepsilon_\star(M_{\rm gas,0} - M_\star(1 - R + w - a))$. By comparing the prediction with the FIR, we would in return constrain the potential effect of density on the ionization parameter.

In the current form of the FIR, where pure observables of $R23$-index and [O III]/[O II] ratio are included with $M_\star$ and SFR, we cannot directly use the method. We plan to derive a four-dimensional relation of physical quantities of ionization parameter, metallicity, $M_\star$, and SFR, and to address a detailed interpretation of the FIR further in future work. Moreover, theoretical models that incorporate gas infalls and outflows would be helpful to interpret the FIR and the evolution of ionization parameter (Section 5.1.2), providing crucial constraints on how these physical mechanisms work together.

5.1.5. Relationship between Ionization State and Ionizing Photon Escape

We have found in Figure 2.2 that the $z \sim 0$ LyC leakers show [O III]/[O II] ratios significantly higher than typical low-z galaxies, which suggest that these LyC leakers have a high ionization parameter. The LyC leakers' [O III]/[O II] ratios are comparable to those of GPs, LBAs, and $z = 2-3$ galaxies (Figure 4.2). These results imply that galaxies with a high [O III]/[O II] ratio, GPs, LBAs, and $z = 2-3$ galaxies, may have a high $f_{\rm esc}$.

To examine the dependence of [O III]/[O II] ratio on $f_{\rm esc}$, we perform photoionization model calculations with CLOUDY. We assume a homogeneous inter-stellar gas cloud with the ionizing source which

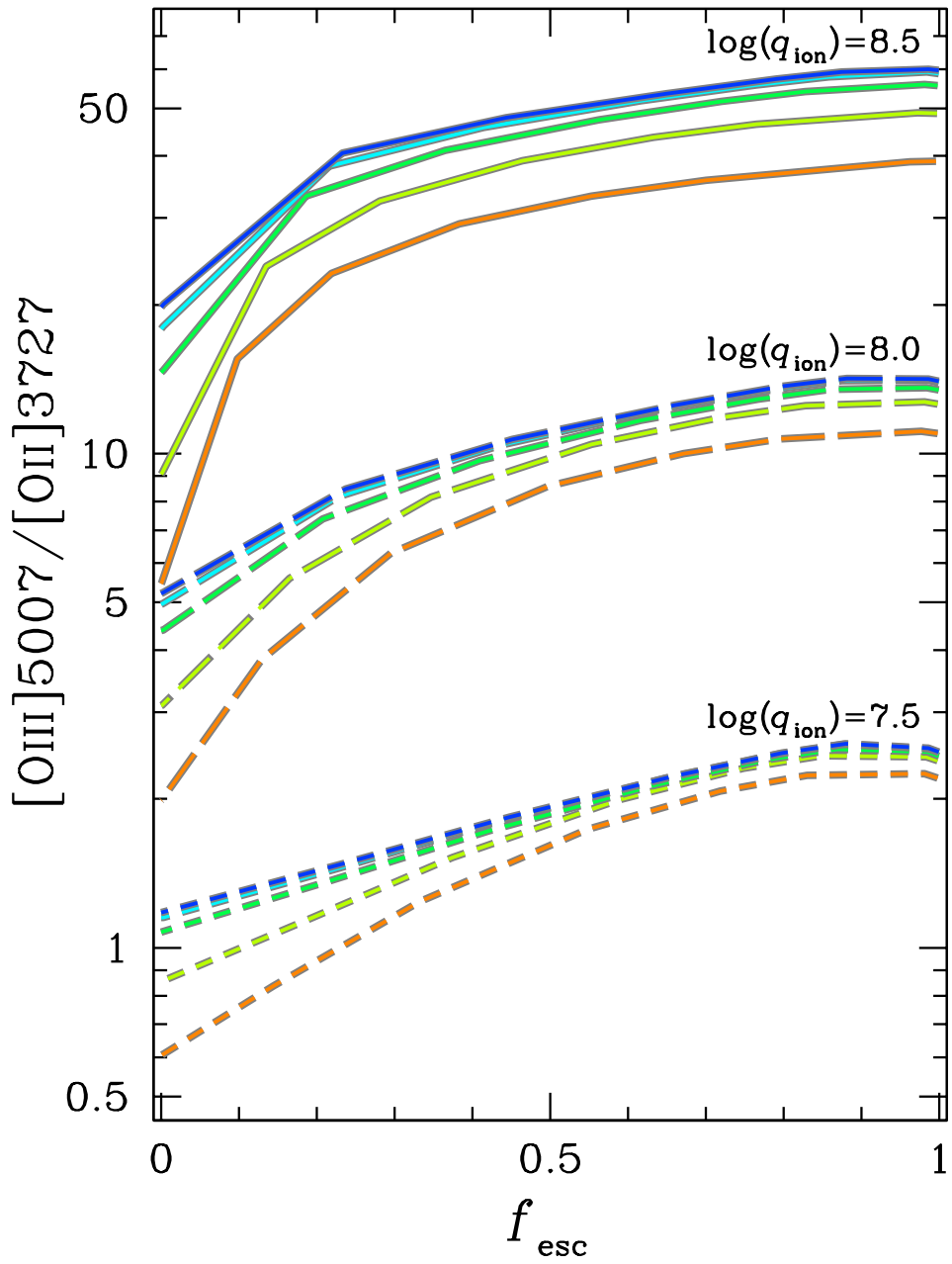

Figure 5.4. [O III]/[O II] vs. $f_{\rm esc}$ predicted by our CLOUDY models with $\log(q_{\rm ion}) = 8.5$ (solid lines), 8.0 (long-dashed lines), and 7.5 (dashed lines). The blue, cyan, green, light green, and orange lines denote [O III]/[O II]–$f_{\rm esc}$ relations for a metallicity of $Z = 0.05$, 0.1, 0.2, 0.5, and $1.0\,Z_{\odot}$, respectively.

is the same as that in Section 2.3.2. Under this assumption of homogeneous gas, we evaluate $f_{\rm esc}$ with the number of ionizing photons escaping from a thin cloud with a low column density. We adopt a neutral hydrogen (H^0) column density, $N_{\rm HI}$, as the stopping criterion of our calculations that ranges from $N_{\rm HI} = 10^{15}$ to $10^{20}\,{\rm cm}^{-2}$. The escape fraction is defined as the ratio of transmitted ionizing photons ($\lambda < 912$ Å) to input ionizing photons.

Figure 5.4 shows the CLOUDY calculation results on the [O III]/[O II] vs. $f_{\rm esc}$ plot[5.3]. Figure 5.4

[5.3]Figure 5.4 displays the models with the density of $n_{\rm H} = 10^2\,{\rm cm}^{-3}$. We have confirmed that our results do not change significantly with different densities of $n_{\rm H} = 10$ and 10^3, as discussed in Section 2.3.2.

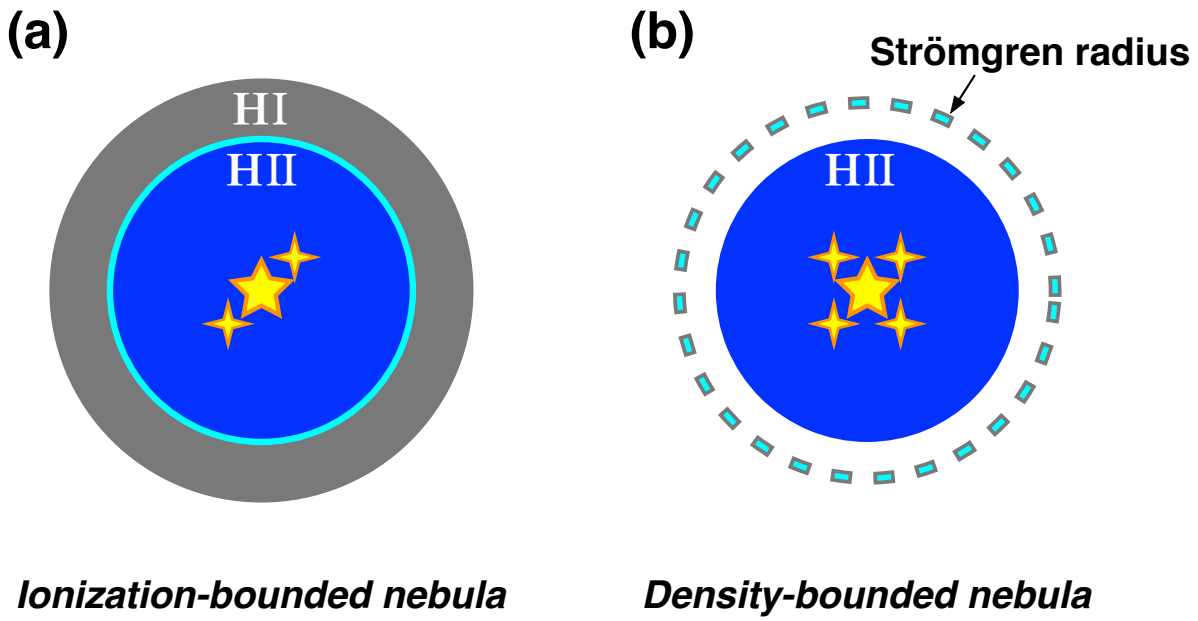

Figure 5.5. Schematic illustrations of two HII regions. A photoionized HII region is presented with blue, and an outer HI are is shown with gray. Yellow stars are central ionizing sources. (a) An ionization-bounded nebula whose radius is determined by the ionization equilibrium. The cyan shows the Strömgren radius. (b) A density-bounded nebula whose radius is determined by the distribution of gas cloud. The surrounding HI cloud is small enough that the central sources can ionized it completely. The nebula thus cannot form a complete Strömgren sphere.

indicates that the [O III]/[O II] ratio increases with $f_{\rm esc}$. This trend qualitatively explains the large [O III]/[O II] ratio of the LyC leakers in Figure 4.2. This relationship between [O III]/[O II] ratio and $f_{\rm esc}$ is understood by one of the two classifications of star-forming nebulae.

1. Ionization-bounded nebula whose radius is determined by the ionization equilibrium between the ionizing photon production rate and the recombination rate (Equation 2.4; Figure 5.5a). The radius of the ionized region is called the Strömgren radius.

2. Density-bounded nebula whose radius is determined by the distribution of gas cloud (Figure 5.5b). The density-bounded nebula does not expend all of ionizing photons, but leak ionizing photons that are not used for the ionization of the nebula.

The ionizing photon escape takes place in the density-bounded nebula under the assumption of homogeneous gas cloud. A density-bounded nebula with a less $N_{\rm HI}$ emits more ionizing photons, and has a higher $f_{\rm esc}$ (Giammanco et al. 2005). On the other hand, in the ionization-bounded nebula, lower ionization species of O^+ (producing [O II]) dominate in the outer region of the nebula, while an O^{2+} zone (producing [O III]) exists near the ionizing source (e.g., Shields 1990; Oey & Kennicutt 1997). Thus, the O^+ zone of density-bounded nebula is smaller than that of an ionization-bounded nebula, but the size of O^{2+} zone is similar in the density-bounded and ionization-bounded nebulae. As a result, the [O III]/[O II] ratio is large in density-bounded nebulae, and nebulae with a less $N_{\rm HI}$ have a higher [O III]/[O II] ratio. From the combination of $N_{\rm HI}$ vs. $f_{\rm esc}$ and $N_{\rm HI}$ vs. [O III]/[O II] relations, we understand the positive correlation between [O III]/[O II] and $f_{\rm esc}$.

In Figure 5.4, [O III]/[O II] ratios are determined not only by $f_{\rm esc}$, but also by ionization parameter and metallicity. For example, the [O III]/[O II] ratio increases by an order of magnitude from $\log(q_{\rm ion}) =$ 7.5 to 8.5. Similarly, the [O III]/[O II] ratio increases by a factor of $\sim 2-4$ from $Z = 1.0$ and $0.1\,Z_{\odot}$, although this dependence is small (Section 2.3.2). On the other hand, the [O III]/[O II] ratio increases by a factor of $\sim 2-3$ from $f_{\rm esc} = 0$ to 0.5. The [O III]/[O II] ratio is thus sensitive to $f_{\rm esc}$ as well as ionization parameter and metallicity. These results would suggest that a galaxy with a high [O III]/[O II] ratio can be a candidate of high $f_{\rm esc}$ object, but that not all of high [O III]/[O II] objects are LyC leakers.

It is worth noting that in Figure 4.5 the $z \sim 0$ LyC leakers lie above the FIR by a factor of $\sim 2-3$. The farther enhancement of [O III]/[O II] ratio may be caused by an ionizing photon escape. If it is true, some GPs and LAEs lying above the FIR would be good candidates of ionizing photon emitting objects. In Figure 4.5, LAEs particularly have a very high [O III]/[O II] ratio, some of which are departing from the FIR more significantly than LBGs over the sizes of error bars. This physical characteristics would be originated from a very large $f_{\rm esc}$ given by a low $N_{\rm HI}$ of LAE. The low $N_{\rm HI}$ of LAE is also supported by the gas-dynamics study of Hashimoto et al. (2013) who claim that LAEs typically have a $N_{\rm HI}$ lower than LBGs from the analysis of velocity offsets between a Lyα line and low-ionization interstellar absorption lines with respect to the systemic velocity. This tendency is confirmed with a larger number of LAEs by Shibuya et al. (2014a). In this companion paper, Shibuya et al. (2014b) examine LAE structures, suggesting that LAEs with a large Lyα EW tend to have a small ellipticity. This is consistent with the theoretical results that Lyα photons can more easily escape from face-on disks having a small ellipticity, due to a low $N_{\rm HI}$ (e.g., Verhamme et al. 2012; Yajima et al. 2012; Zheng & Wallace 2013). Moreover, recent deep narrowband imaging surveys have indicated diffuse Lyα emitting halos around high-z star-forming galaxies that are more prominent for LBGs (e.g., Steidel et al. 2011) than LAEs (Feldmeier et al. 2013). Since most of the observed Lyα emission in the diffuse halos probably originates from from the galaxy HII-regions and is scattered to the line of sight by extended HI gas in the galaxy's circum-galactic medium (CGM), LAEs could exhibit Lyα halos weaker than LBGs due to their smaller amounts of HI gas in the CGM. This scenario is consistent with our argument of low $N_{\rm HI}$ of LAE. Interestingly, that interpretation also consistently explains the results of direct LyC detections of $z \sim 3$ galaxies that reveal a high $f_{\rm esc}$ for LAEs ($\sim 0.1-0.3$) than LBGs (~ 0.05) (Iwata et al. 2009; Nestor et al. 2011, 2013). Thus, an origin of the high $f_{\rm esc}$ in LAEs would be their optically thin HI gas surrounding star-forming regions. A similar suggestion of the high $f_{\rm esc}$ is inferred for GPs (Jaskot & Oey 2013).

LAEs with a high $f_{\rm esc}$ would play a key role in supplying ionizing photons for cosmic reionization in the early universe. Previous $z \sim 6-7$ galaxy surveys have suggested that the universe could not be totally ionized by galaxies alone at $z \sim 6-7$ if one assumes similar properties of galaxies at $z \sim 3$ that include $f_{\rm esc} \sim 0.05$ (e.g., Ouchi et al. 2009; Robertson et al. 2010). Because the fraction of LAEs in star-forming galaxies increases with redshift (e.g., Ouchi et al. 2008; Stark et al. 2010), the average $f_{\rm esc}$ for $z \sim 6-7$ galaxies would be higher than that for $z \sim 3$ galaxies. The higher $f_{\rm esc}$ for $z \sim 6-7$ galaxies may resolve the problem of ionizing photon deficit in cosmic reionization. Note that the number of observed LAEs suddenly drops from $z \sim 6$ to 7 due to the Lyα damping absorption of partly neutral IGM (Vanzella et al. 2011; Pentericci et al. 2011; Ono et al. 2012; Schenker et al. 2012), but that galaxies with an intrinsically bright Lyα would not decrease from $z \sim 6$ to 7. A similar implication is provided by Schenker et al. (2013) on the basis of a small velocity offset of Lyα line with respect to the systemic velocity for $z = 3-4$ galaxies. We also note that this picture would be consistent with the observational fact that gas fraction of star-forming galaxies increases with redshift, or more properly, with sSFR (e.g.,

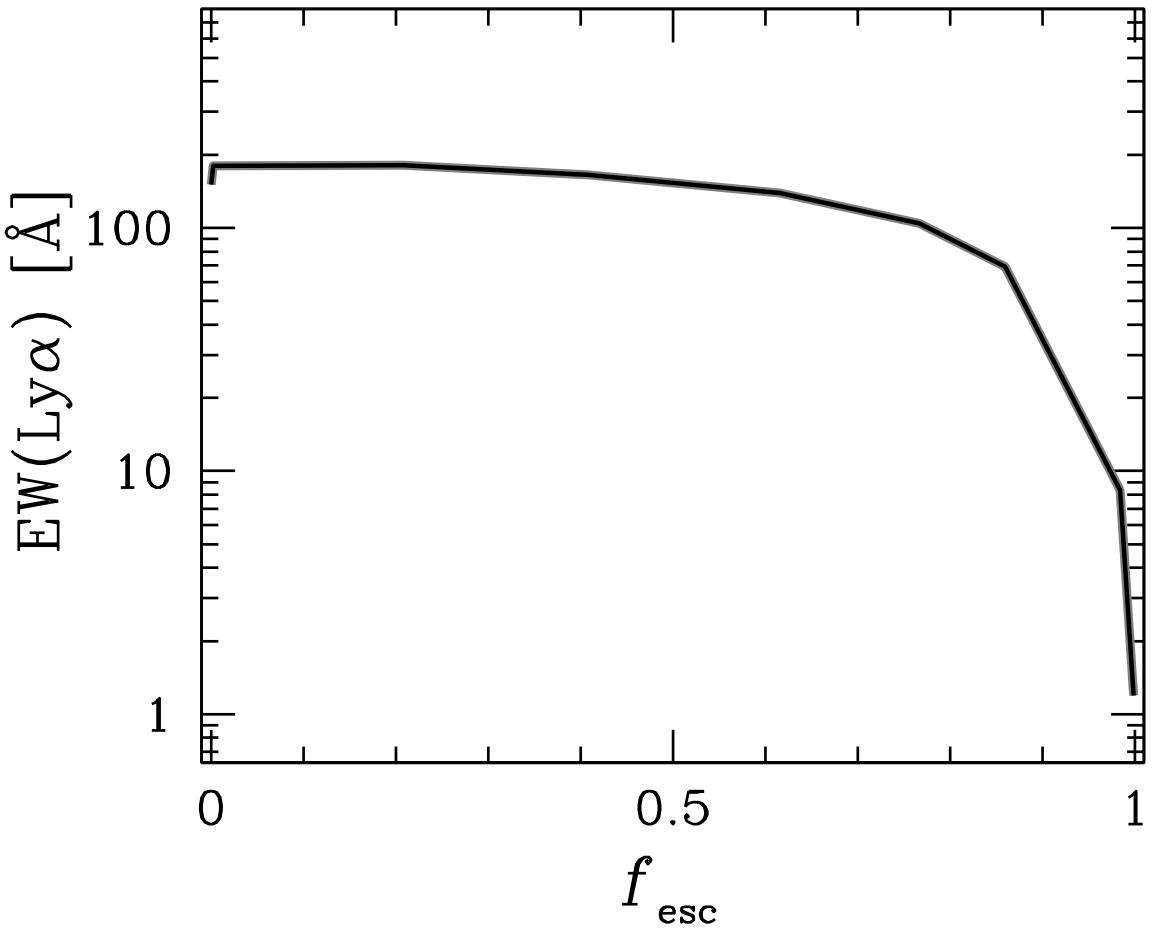

Figure 5.6. EW(Lyα) vs. $f_{\rm esc}$ predicted by our CLOUDY model for $Z = 0.2\,Z_{\odot}$ and $\log(q_{\rm ion}) = 8.0$.

Tacconi et al. 2010, 2013; Santini et al. 2014). If the molecular gas exists in dense cores of clumps embedded in density-bounded nebulae ionized by young stars, the galaxy could have high gas fraction and high $f_{\rm esc}$. A dense molecular gas clump could reside inside the HII-region, since the dense gas could be self-shielded from ionizing radiation. A good example is found in the Orion nebula (see, e.g., Genzel & Stutzki 1989 for a review). Such clumpy geometry of dense molecular gas could explain the high gas fraction, active star-formation, and high $f_{\rm esc}$ in high-z galaxies.

In the discussion of high $f_{\rm esc}$ for LAEs, there is one caveat that Lyα emission would become weaker in a high $f_{\rm esc}$, because less ionizing photons are spent for making ionized gas that emit Lyα. Therefore, LAEs may not be a population of high $f_{\rm esc}$. Figure 5.6 plots the relation between EW(Lyα) and $f_{\rm esc}$ predicted by our CLOUDY models. Here we assume $q_{\rm ion} = 10^8\,{\rm cm\,s^{-1}}$ and $Z = 0.2\,Z_{\odot}$, typical values observed in GPs (Amorín et al. 2010) and $z \sim 2$ LAEs (Sections C.3 and B.3). Figure 5.6 presents that the EW(Lyα) decreases sharply if its $f_{\rm esc}$ is over $\simeq 0.8$. However, in $f_{\rm esc} \simeq 0.0 - 0.8$, EW(Ly$\alpha$) remains unchanged within a factor of $\lesssim 2$. We have checked that the overall trends are the same, adopting other values of $q_{\rm ion}$ and Z. For example, EW(Lyα) increases (decreases) by a factor of $\sim 2-3$ for $Z = 0.05\,Z_{\odot}$ ($1\,Z_{\odot}$). LAEs are usually defined as galaxies with EW(Lyα) > 20 Å. If an escape fraction is very high, $f_{\rm esc} \gtrsim 0.9$, a galaxy cannot be observed as an LAE (Figure 5.6). However, LAEs, or galaxies with EW(Lyα) > 20 Å, can exist in the range of $f_{\rm esc} \lesssim 0.8$. Since a very high $f_{\rm esc}$ of $\gtrsim 0.8$ is not required for

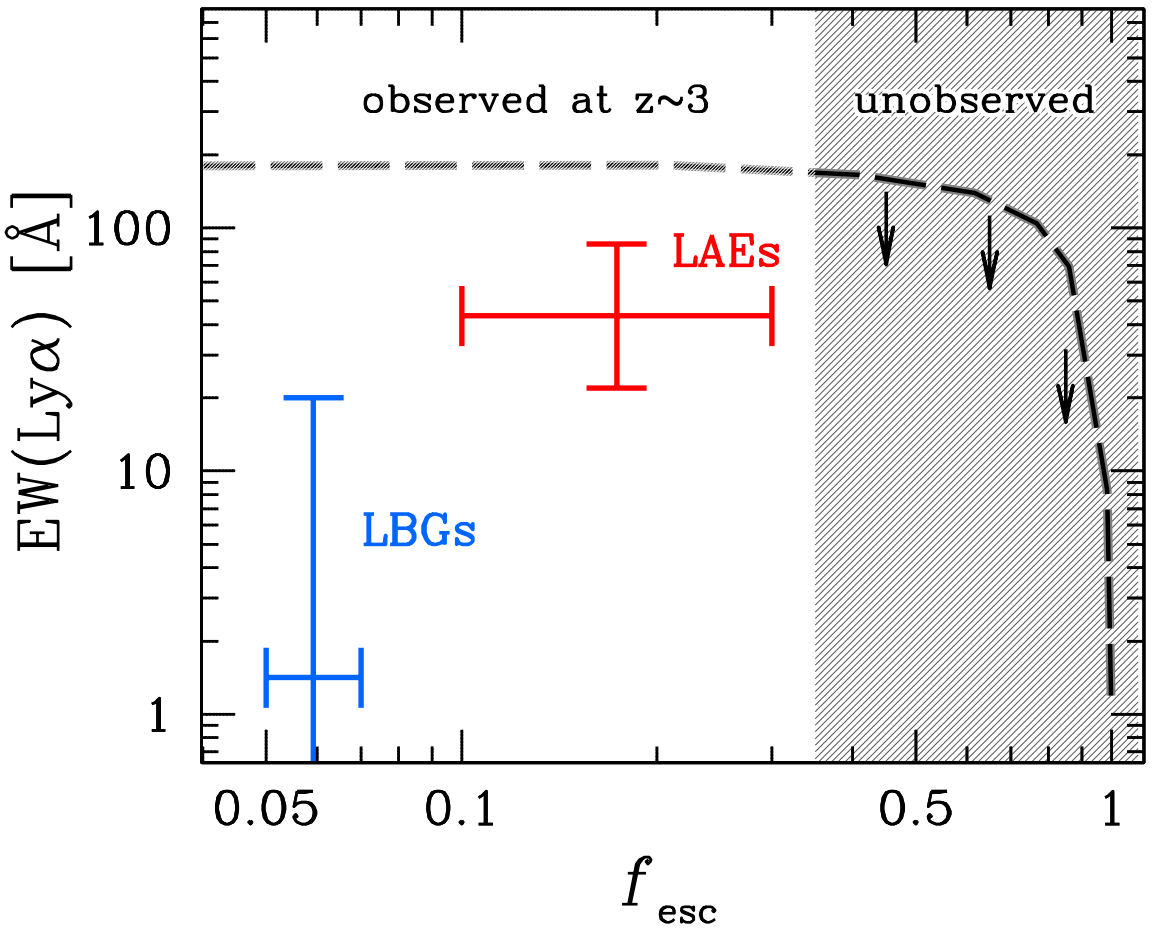

Figure 5.7. EW(Lyα) vs. $f_{\rm esc}$ plot. Observational results by Nestor et al. (2013) for $z \sim 3$ LAEs and LBGs are presented with red and blue colors, respectively. The dashed curve shows our model (Figure 5.6).

cosmic reionization but only $f_{\rm esc} \simeq 0.2$ (Robertson et al. 2013), the weakening of Lyα in density-bounded nebulae does not rule out the possibility that major ionizing sources are LAEs. Figure 5.7 compares our model and the recent observational results for $z \sim 3$ LAEs and LBGs whose $f_{\rm esc}$ are measured from LyC fluxes (Nestor et al. 2013)[5.4]. EW(Lyα) values of our model are regarded as upper limits, because EW(Lyα) decreases by dust extinction and hydrogen scattering. The observational results fall below our model, and are consistent with our model. The observations indicate a positive correlation between $f_{\rm esc}$ and EW(Lyα) in $f_{\rm esc} \lesssim 0.5$, while our model shows a nearly constant EW(Lyα) in this regime. This difference would infer that LAEs have a less dust extinction, a more homogeneous geometry for isotropic Lyα scattering, a less metallicity, and more ionizing photons than LBGs.

We note that our calculations assume a density-bounded nebula with a spherically closed geometry, and predict dependencies of $N_{\rm HI}$ on the emergent spectra. A volume filling factor of the ionized gas is assumed to be unity. Thus, we have presented this specific case of EW(Lyα) as a function of $f_{\rm esc}$. However, the EW(Lyα) and $f_{\rm esc}$ involve various complex physical effects. EW(Lyα) depends on gas and dust geometries (e.g., Neufeld 1991; Scarlata et al. 2009; cf. Duval et al. 2013) and galactic scale

[5.4] We refer to Nestor et al. (2011) and Shapley et al. (2003) for the ranges of EW(Lyα) of LAEs and LBGs, respectively.

outflow (e.g., Kunth et al. 1998; Verhamme et al. 2006). $f_{\rm esc}$ anti-correlates with a covering fraction of neutral gas. Recent spectroscopic studies suggest a low covering fraction of neutral gas in high-z star-forming galaxies (e.g., Shapley et al. 2003; Steidel et al. 2010; Jones et al. 2013). There exist the other complex physics of EW(Lyα) and $f_{\rm esc}$. Nevertheless, our analysis reveals the relation of EW(Lyα) and $f_{\rm esc}$ for the case that HII-regions are homogeneous density-bounded nebulae.

5.2. Basic Characteristics of LAEs

5.2.1. $M_\star$–Z Relation

Figure 5.8 shows the $M_\star$–Z relations for LAEs and LBGs. The red symbols represent LAEs at $z \sim 2$, while the blue symbols show the other galaxies such as LBGs at the similar redshifts. The same LAEs collected in Section 4.1 are plotted. We note that their metallicities are carefully estimated. For our LAEs of CDFS-3865 and COSMOS-30679, we estimate their metallicities with ionization parameter (Appendix B.3.3). For the other four LAEs of Lynx arc (Fosbury et al. 2003; Villar-Martín et al. 2004), BX418 (Erb et al. 2010), Abel 1689 31.3 arc (A31.1), and SMACS J2031 arc (M2031) (Christensen et al. 2012a,b), their metallicities are calibrated from gas temperature ("direct T_e method"). For Lynx arc, Villar-Martín et al. (2004) use the ratio of O III]$\lambda\lambda$1661, 1666/[O III]λ5007 to infer the gas temperature, from which the gas-phase metallicity of 10 ± 3 % of the solar value is estimated. Erb et al. (2010) follow the same calibration of Villar-Martín et al. (2004) to find $12 + \log({\rm O/H}) = 7.8 \pm 0.1$ from the gas temperature for BX418. The authors have checked that the metallicity is in excellent agreement with the metallicity estimated with ionization parameter (i.e., from R23-index and [O III]/[O II] ratio). Christensen et al. (2012b) determine the gas temperatures for A31.1 by using [O III]λ4363/λ5007 ratio, and for M2031 by using the O III]$\lambda\lambda$1661, 1666/[O III]λ5007 ratio. As a result, the authors obtain $12 + \log({\rm O/H}) = 7.69 \pm 0.13$ and 7.76 ± 0.03 for A31.1 and M2031, respectively. The authors have confirmed that these metallicities are consistent with those inferred from the Pilyugin & Thuan (2005)'s R23-index calibration, which takes the difference of ionization parameter into account. In addition, we include two LAEs discovered with the HETDEX pilot survey, HPS196 and HPS256 (Finkelstein et al. 2011). Since no measurement of [O II] is given for the two LAEs, their metallicities are estimated from N2-index by using the Maiolino et al. (2008)'s empirical relation. The non-detection of [N II] provides upper-limits of their metallicities.

From this plot, we find two interesting trends; (i) some LAEs fall below the conventional $M_\star$–Z relation of $z \sim 2$ LBGs, and (ii) the $M_\star$–Z relation is not so strong for LAEs as the relation for LBGs.

LAEs are found to have generally low metallicity of $12 + \log({\rm O/H}) \lesssim 8$. Since CDFS-3865, BX418, and HPS194 have stellar mass of $M > 10^9\,M_\odot$, they are less chemically enriched for their stellar masses. Although no constraint on ionization parameter is given for HPS194, the other metal-poor LAEs have very high ionization parameter. Since the high ionization parameter is suggestive of a galaxy having a very hard ionizing radiation field, the low-metallicities and high ionization parameters suggest that these LAEs would be very young galaxies dominated by massive stars in possibly small HII regions. The large EW(Hα) of ~ 800 Å for CDFS-3865 also support this idea (Table 3.1). Such young galaxies with high ionization parameters may not follow the $M_\star$–Z relation defined by more evolved galaxies. Alternatively, differences in star-formation activity may cause the scatter. We discuss this point later. Lynx arc and M2031 are at $z > 3$, and a direct comparison with the $z \sim 2$ LAEs may not be appropriate. However, no

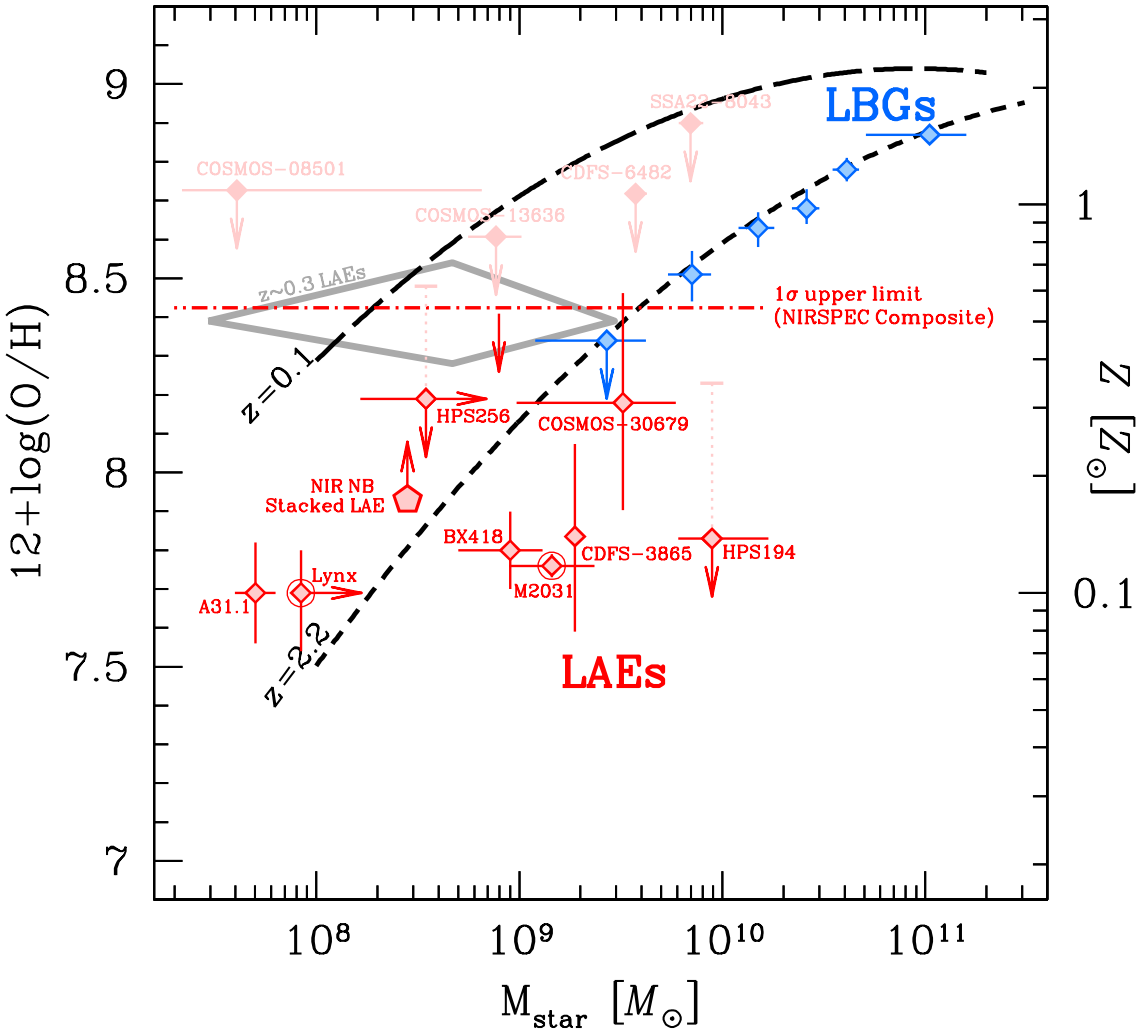

Figure 5.8. $M_\star$–Z relation for LAEs (red) and LBGs (blue; Erb et al. 2006a). The LAE sample includes two narrowband selected LAEs, CDFS-3865 and COSMOS-30679 (Section 3.1), Lynx arc (Fosbury et al. 2003; Villar-Martín et al. 2004), BX418 (Erb et al. 2010), Abel 1689 31.3 arc (A31.1), and SMACS J2031 arc (M2031) (Christensen et al. 2012a,b), the same of which are discussed in the ionization state section (Section 5.1). For the presentation purpose, we shift the red diamond for Lynx arc along the x-axis by $+0.2$ dex. The lower-limit of metallicity estimated from the stacked NIR narrowbands of LAEs is shown with the red pentagon (Section 3.2). Additionally, we include two LAEs at $z \sim 2.4$ discovered with the HETDEX pilot survey, HPS194 and HPS256 (Finkelstein et al. 2011). The upper-limits of metallicity (1σ) of the HETDEX LAEs are estimated from $N2$-index by using an empirical relation of Maiolino et al. (2008). The light red bars for the two LAEs show their upper-limits of metallicity estimated from $N2$-index by using the Kewley & Dopita (2002) relations assuming $q_{\rm ion} \sim 10^8\,{\rm cm\,s^{-1}}$. Our four LAEs without [O II], COSMOS-08501, COSMOS-13636, CDFS-6482, and SSA22-8043 are shown with the light red diamonds. The red dot-dashed line shows the 1σ upper-limit of metallicity ($N2$-index) for the composite spectrum in K band. Note that Lynx arc and M2031 (red diamonds with a circle) are LAEs at $z > 3$, and the other LAEs and LBGs are at $z \sim 2$. LAEs at $z = 0.195$–0.44 are also shown with the gray enclosed area (Cowie et al. 2011). The $M_\star$–Z relation compiled by Maiolino et al. (2008) at $z \sim 0$ and $z \sim 2$ are drawn as long-dashed and dashed curves, respectively. All data plotted here have been recalibrated to have the same metallicity scale (Maiolino et al. 2008) and IMF (Chabrier 2003) except for the LAEs with ionization parameter estimates. Metallicities of CDFS-3865 and COSMOS-30679 are estimated from $R23$-index by using Kewley & Dopita (2002)'s relations. Metallicities of Lynx arc, A31.1, M2031, and BX418 are calibrated from gas temperature.

significant differences of $M_\star$–Z relation between $z \sim 2$ and $z > 3$ is found for LAEs. It could be due to their comparable SFRs and ionization parameters. Although A31.1 fall above the simple extrapolation of the LBGs' $M_\star$–Z relation towards lower masses, its metallicity is still low. By contrast, the comparison with COSMOS-30679 is more unclear. Its large errors both in stellar mass and metallicity prevent us from telling if it is below/on the LBGs' relation. Since its ionization parameter is comparable to those for LBGs (Table 3.1), COSMOS-30679 may be an LBG-like galaxy.

The other interesting suggestion is that no significant $M_\star$–Z relation is found for $z = 2-3$ LAEs over the mass range of 10^8–$10^{10}\,M_\odot$. LAEs with $M \sim 10^{9-10}\,M_\odot$ (e.g., HPS194, CDFS-3865) seem less chemically-enriched for their stellar masses, while LAEs with $M \lesssim 10^9\,M_\odot$ (e.g., the NIR narrowband stacked LAE, A31.1) are not so metal-poor galaxies as expected from the massive LBGs. If this trend is true, it indicates that the evolution of LAEs may be more complex than that of LBGs. For the conclusive discussion, however, we need a larger LAE sample with accurate metallicity estimate.

We also constrain an average metallicity from the K band composite spectrum (Figure B.4) by using the empirical [N II]-index. The 1σ (2σ) upper-limit of metallicity is $12+\log(\mathrm{O/H}) < 8.42$ (8.66), which corresponds to $Z < 0.54\,(0.93)\,Z_\odot$. On the other hand, we independently obtain an average lower-limit of metallicity for LAEs to be $12+\log(\mathrm{O/H}) > 7.93$ (7.63), or $Z > 0.17\,(0.09)\,Z_\odot$ at the 1σ (2σ) level, based on the [O II]/(Hα+[N II]) ratio whose fluxes are obtained by stacking 1.18 and 2.09 μm narrowband images for more than 100 LAEs (Table 3.2; see also Appendix C.3.2). LAEs thus typically have a metallicity $12+\log(\mathrm{O/H}) = 7.93$–$8.42$ (7.63–8.66) at the 1σ (2σ) level. The range is robust in the sense that the upper-limit is constrained by bright, massive LAEs while the lower-limit by faint, low-mass LAEs. We note that the typical metallicity of LAEs is not very low. Scannapieco et al. (2003) proposed that LAEs may be extremely metal poor primordial galaxies, and Schaerer (2003) also found that large Lyα EWs can be observed from extremely metal poor galaxies ($Z/Z_\odot \lesssim 10^{-5}$). However, our firm lower limits, e.g., $Z > 2\times10^{-2}\,Z_\odot$ at the 4σ level (Appendix C.3.2), do not support this idea at least for $z \sim 2$ LAEs. More spectroscopic data are needed, however, to conclude that there are no exceptional LAEs that have nearly zero or super-solar metallicities. The metallicity range also suggests that LAEs at $z \sim 2$ are rather less chemically enriched than those at $z \sim 0.3$ ($12+\log(\mathrm{O/H}) \sim 8.4$[5.5]; Cowie et al. 2011).

We find the complicated $M_\star$–Z relation for LAEs. This may be due to the sampling of a large variety of evolutionary phases within the LAE population. Such variation has been indeed reported by other studies (e.g., Nilsson et al. 2011; Oteo et al. 2012). Alternatively, differences in star-formation activity may be a problem. To check the possibility, we plot the LAEs on the FMR in Figure 5.9. From this plot, we find that many LAEs appear to be consistent with the FMR, including A31.1 and the NIR NB stacked LAE. This indicates that their apparent high metallicities can be due to their relatively low SFR (Section 5.2.2). However, some LAEs such as HPS194, M2031, and possibly CDFS-3865 and BX418, still appear to fall below the FMR. Their low metallicities are not just likely due to their relatively high SFRs. The inconsistency for HPS194 is remarkable ($\gtrsim 5\sigma$ level). However, we note again that the metallicity for HPS194 is estimated from the empirical relation of $N2$-index. If we assume a generally high ionization parameter of $q_{\mathrm{ion}} \sim 10^8\,\mathrm{cm\,s^{-1}}$ for LAEs (Section 4.2), and assume the Kewley & Dopita (2002)'s models, the observed upper-limit of $N2$-index yields $12+\log(\mathrm{O/H}) \lesssim 8.2$ (1σ), which is ~ 0.4 dex higher than that estimated from the empirical relation. The difference of ionization condition in a galaxy may partly explain the inconsistency. Furthermore, Chonis et al. (2013) recently

[5.5] We recalculate the metallicity by using the Maiolino et al. (2008) indicator. The original estimate is ~ 0.15 dex lower.

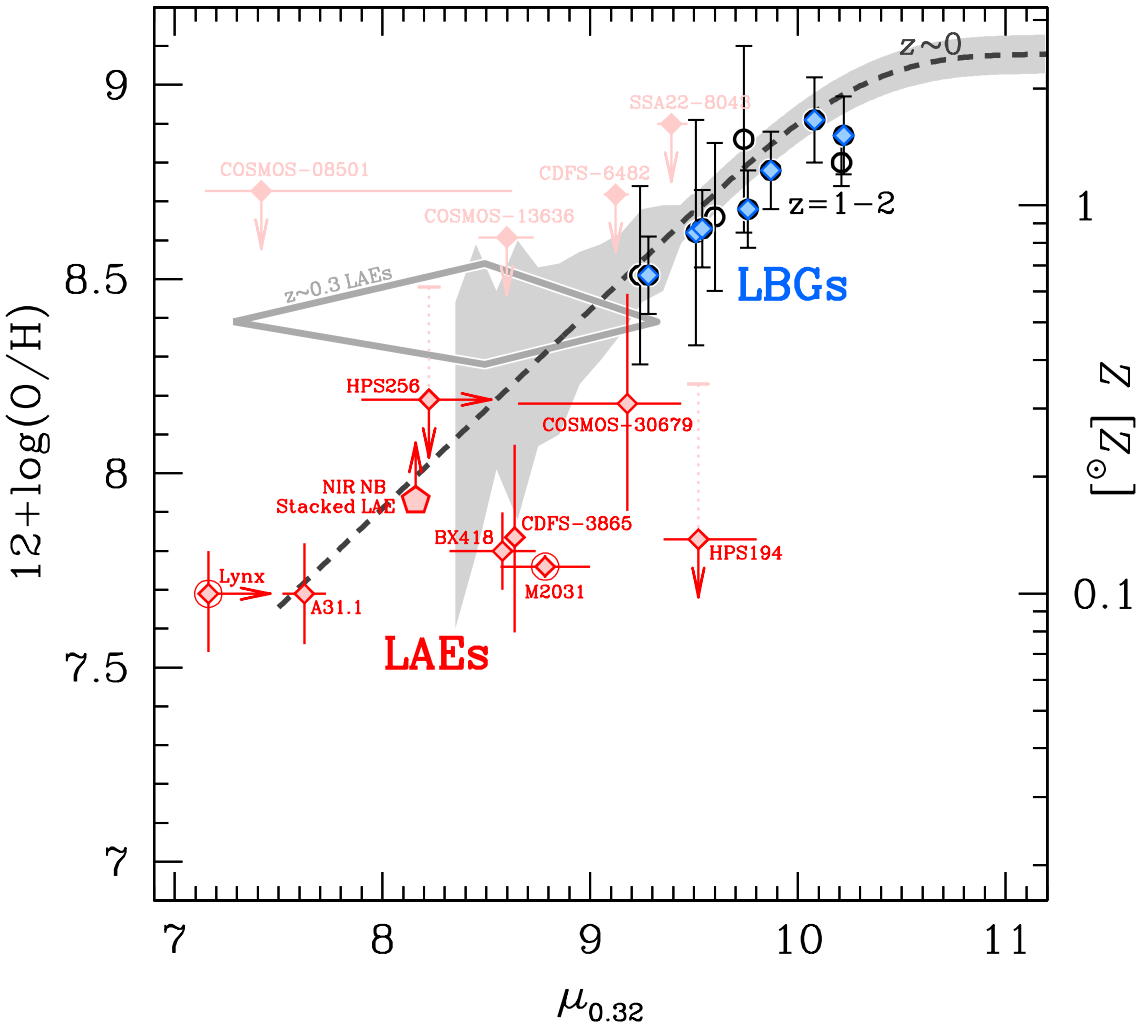

Figure 5.9. LAEs and LBGs in the FMR plot. The dashed curve and the shaded areas indicate the $z \sim 0$ relation and its typical dispersions respectively (Mannucci et al. 2010, 2011). The open squares show $z = 1-2$ star-forming galaxies collected/compiled by Mannucci et al. (2010) from Erb et al. (2006a) and so on. Galaxies at $z \sim 2$ are marked with the blue diamonds. Other symbols are the same as those in the M-Z relation. For the presentation purpose, we shift the red diamond for HPS256 along the x-axis by $+0.05$ dex.

report that HPS194 shows a companion continuum source at $< 1''$ distance by using the CANDELS image. No rest-frame optical emission lines from the companion source is detected (Chonis et al. 2013, G. Blanc et al. 2013, in preparation). Although it is still unclear whether the companion source lie at the same redshift, the stellar mass of HPS194 could be overestimated. This could also ease the large offset of HPS194 seen in the FMR plot.

Therefore, if we estimate metallicities with ionization parameters, even LAEs may follow the FMR. This trend is also suggested by the FIR. LAEs are then considered to be a young population with low metallicity, high specific SFR, and high ionization parameter, probably originated from young, massive stars dominated in small HII regions. Their large EW(Hα) also support the idea. However, as discussed in Section 5.1.5, if its $f_{\rm esc}$ is not negligible, a galaxy's metallicity and ionization parameter could be

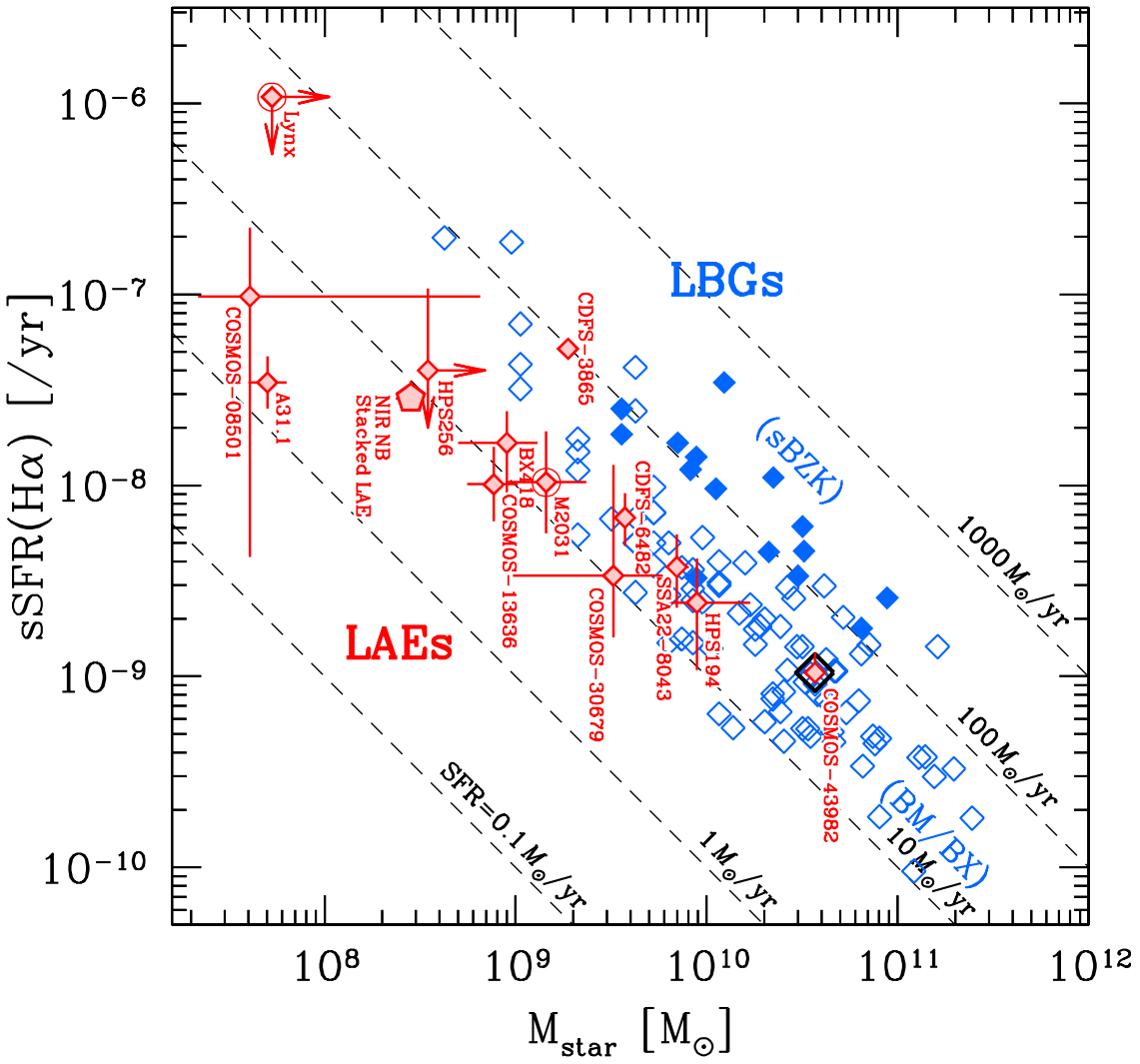

Figure 5.10. Relation between $M_\star$ and sSFR for $z \sim 2$ LAEs (red) and continuum selected galaxies (blue), except for two LAEs of Lynx arc and M2031 at $z \sim 3$ (marked with a circle). The same LAEs are plotted as in Figure 5.8. The open and solid blue triangles show BX/BM (Erb et al. 2006b) and sBzK galaxies (Hayashi et al. 2009), respectively. COSMOS-43982, a possible object with AGN activity, is marked with a black diamond. All sSFRs plotted here are derived from Hα luminosity with Chabrier (2003) IMF and corrected for dust extinction. The dashed lines correspond to constant SFRs of $0.1, 1.0, 10, 100$, and $1000\,M_\odot\,\mathrm{yr}^{-1}$.

incorrectly estimated. In fact, LAEs having an increased [O III]/[O II] ratio in the FIR (Figure 4.5), such as CDFS-3865, BX418, and M2031, still fall below the FMR. In addition to ionization parameter, metallicity, $M_\star$, and SFR, f_{esc} (or column density of neutral hydrogen) could be a key quantity to characterize these LAEs. More observational data with full suite of nebular emission lines will enable us to test the universality of the FMR (FIR) for both LBGs and LAEs over the wide range of properties.

5.2.2. $M_\star$–SFR Relation

In order to examine the star-formation activity of LAEs, we plot the LAEs on the sSFR versus stellar mass plane in Figure 5.10. We also plot BX/BM galaxies (Erb et al. 2006b) and sBzK galaxies (Hayashi et al. 2009). We note that this plot should be interpreted with cares since the spectroscopic data introduce limits in the sensitivity to low SFRs.

BX/BM and sBzK galaxies follow a simple scaling relation between sSFR and the stellar mass, whose tight relation is referred to as *the star formation main sequence* (e.g., Daddi et al. 2007). Note that BX/BM and sBzK galaxies appear to have slightly different sequences; BX/BMs show lower sSFRs at a given mass. Compared to them, LAEs appear to follow the BX/BMs' main sequence almost over the mass range of $M \gtrsim 10^{9.5}\,M_\odot$. LAEs which exhibit high ionization parameters and low metallicities (e.g., BX418, CDFS-3865), are not outliers on this diagram. This trend indicates that star-formation activities are determined by their stellar mass, irrespective of the presence of Lyα emission.

Another notable trend in Figure 5.10 is that LAEs with stellar mass of $M_\star < 10^{9.5}\,M_\odot$ have sSFRs lower than expected from a simple extrapolation of the BX/BM's star-formation main sequence towards lower masses. Remarkably, the NIR narrowband stacked LAE (red pentagon) appears to support the idea, representing an average SFR for LAEs with $M_\star \sim 5 \times 10^8\,M_\odot$ and being statistically more significant than individual galaxies. If this trend is true, it suggests that low-mass galaxies with $M_\star < 10^{9.5}\,M_\odot$ have lower star-formation efficiencies than extrapolated from more massive galaxies. This trend, if real, is qualitatively consistent with galaxy formation models which predict that less massive systems have low star-formation efficiencies owing to various mechanisms such as feedback from supernovae (see, e.g., Benson 2010 for a review).

5.2.3. Correlation between EW(Lyα) and EW(Hα)

Figure 5.11 shows equivalent widths of Lyα and Hα for LAEs (hereafter referred to as the "EWs diagram"). This plot may be useful to understand star-formation histories of LAEs, because the EWs' continuum fluxes evolve in different ways when different star-formation histories are assumed. Another advantage of using the EWs is that both are pure observables and to zeroth order independent of dust extinction (the effect of dust will be discussed at the end of this section). In this and the next sections, we use the same LAEs plotted in Figure 5.8 but without the three LAEs of Lynx arc, M2031, and A31.1, whose equivalent widths and fluxes of Hα are not given in the original papers.

The superposed curves on Figure 5.11 illustrate evolutions of the EWs for the two extreme star-formation histories, instantaneous burst (dashed) and constant star-formation (solid) at several metallicities (Schaerer 2003)[5.6]. For the instantaneous burst, since very massive stars ($M_\star \gtrsim 10\,M_\odot$) complete their evolution within $\lesssim 10$ Myr, both EWs decline rapidly. As a result, their curves evolve quickly to lower-left on the EWs diagram. For the constant star-formation, on the other hand, the EW(Lyα) stops declining around ~ 100 Myr because massive stars that are responsible for both Lyα emission and UV-continuum reach a steady mode. Since the EW(Hα) keeps declining as the older stars build up in the galaxy, their slopes of the evolutionary tracks become less steep on the EWs diagram. Although

[5.6]The models are collected from the Strasbourg astronomical Data Center (CDS). We present here the three metallicity cases assuming Salpeter IMF (Salpeter 1955) with upper (lower) mass cut-off to be $100\,M_\odot$ ($1\,M_\odot$). Case B recombination is assumed for an electron temperature of $T_e = 3 \times 10^4$ K at zero metallicity and $T_e = 10^4$ K otherwise, and an electron density of $n_e = 10^2$ cm^{-3}.

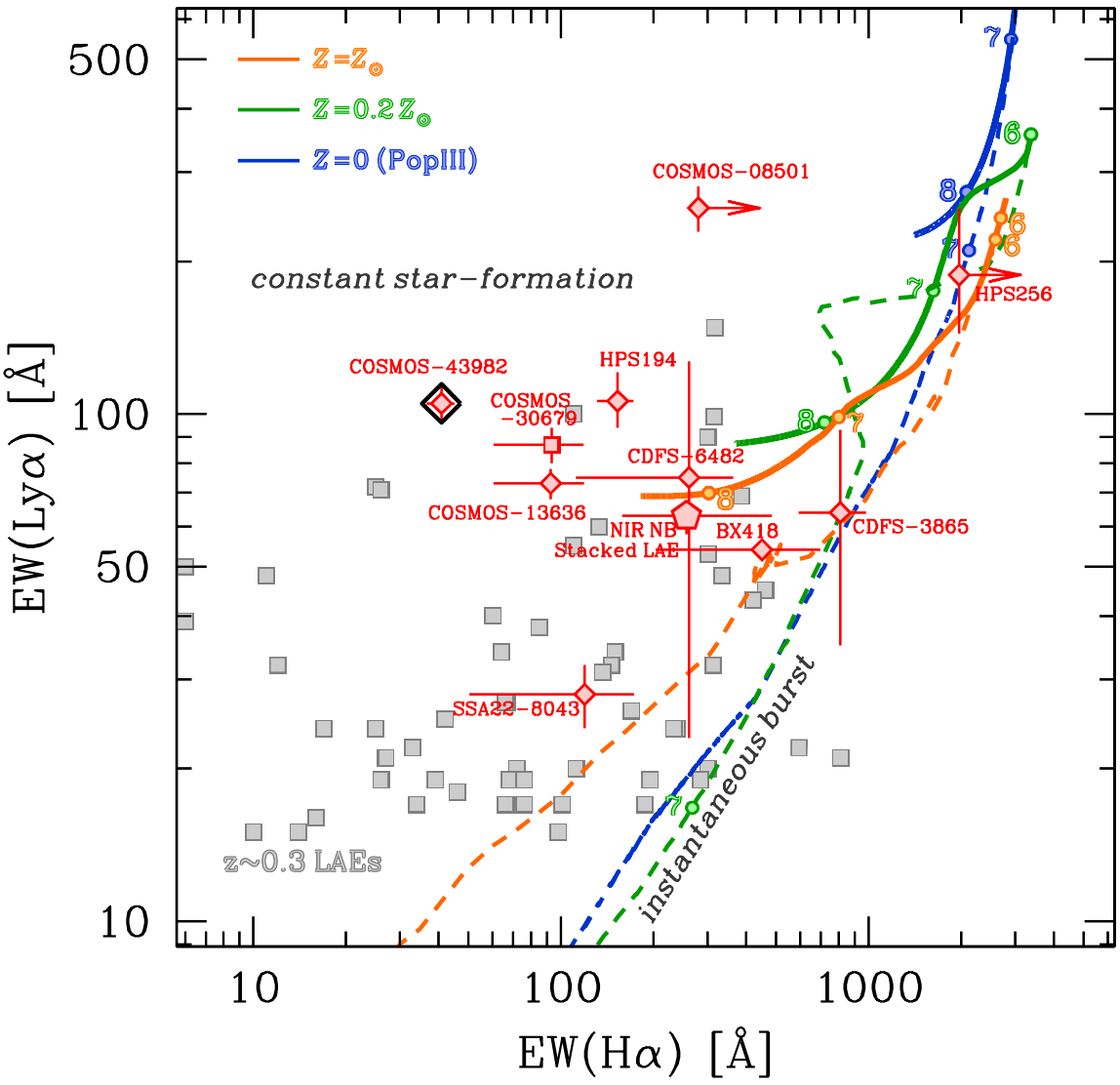

Figure 5.11. Relation between Lyα and Hα equivalent widths. The red symbols show $z \sim 2$ LAEs (same as in Figure 5.8), and the gray squares show LAEs at $z = 0.3$ (Cowie et al. 2011). Superposed lines are evolutions of the EWs for instantaneous burst (dashed) and constant star-formation (solid) at metallicities of solar (orange), sub-solar (green), and zero (blue) calculated by Schaerer (2003). Ages are denoted by the numbers 6, 7, and 8 near the dots on the lines which indicate 1 Myr, 10 Myr, and 100 Myr, respectively. For the solar-metallicity models, the lower point labeled "6" is for the instantaneous burst.

Schaerer's calculations stop at ~ 400 Myr for constant star-formation, the EW(Lyα) varies little after 100 Myr (Charlot & Fall 1993). Therefore, the tracks must extend to the left almost horizontally after the terminal points, reaching EW(Hα) ~ 100 Å for the solar-metallicity case when an age of ~ 3 Gyr (e.g., Leitherer et al. 1999)[5.7].

Compared with the model tracks, some LAEs with EW(Hα) ~ 1000 Å, CDFS-3865, HPS256 (Finkelstein et al. 2011), BX418 (Erb et al. 2010), and possibly COSMOS-08501, can be explained by the

[5.7] Although Leitherer et al. (1999) show the EW(Hα) evolution with age until 1 Gyr, we extend the evolution toward older age smoothly to obtain EW(Hα) ~ 100 Å at ~ 3 Gyr. We have confirmed the validity of the smooth extrapolation for constant star-formation by running GALAXEV (Bruzual & Charlot 2003).

instantaneous burst models with very young ages (a few Myr). The other LAEs whose EW(Hα) is modest appear to prefer the constant star-formation models with $\gtrsim 100$ Myr. Although the sample is small, we find more than half of the LAEs appear to need a continuous star-formation history rather than an instantaneous burst.

Note, however, that since the EWs are sensitive to recent starbursts, LAEs on instantaneous tracks are not necessarily very young, but can be experiencing a burst after a continuous star-formation. Such a combination of burst plus continuous star-formation is indeed needed to explain the EWs of Hα and optical colors observed in local dwarf galaxies (Lee 2006). An LAE with such a combined star-formation history will be on a track of instantaneous burst during starburst phases and on a track of constant star-formation for the remaining time.

Similarly, most of $z \sim 0.3$ LAEs appear to prefer continuous star-formation on the EWs diagram. Interestingly, $z \sim 2$ LAEs appear to have systematically higher EW(Lyα) and EW(Hα) than lower-z LAEs. Although our spectroscopic sample may be biased toward larger EW(Lyα), the difference may be a sign that higher-z LAEs are younger. This idea is supported by the inference of lower metallicities at higher-z (Section 5.2.1; see also e.g., Finkelstein et al. 2009a; Cowie et al. 2010, 2011).

However, one worry on the use of the EWs diagram is the effect of dust on Lyα. If the degree of dust extinction is different for Lyα and UV-continuum, EW(Lyα) is no longer independent of dust extinction. In order to examine this effect, we introduce a q parameter following Finkelstein et al. (2008). The q parameter is defined as $q = \tau(\mathrm{Ly}\alpha)/\tau_{1216}$, where $\tau(\mathrm{Ly}\alpha)$ and τ_{1216} are optical depth for Lyα and UV-continuum at $\lambda = 1216$ Å, respectively. Small q values (< 1) mean Lyα photons suffer less attenuation by dust than UV-continuum photons, while large values mean Lyα photons are more heavily attenuated. In the former (latter) case data points go down (up) on the EWs diagram after the corrections. From previous studies, LAEs at $z \sim 2$ have modest q values; e.g., from the values given in Hayes et al. (2010) we calculate $q \simeq 1$–1.5 for $z = 2.2$ LAEs whose Lyα and Hα luminosities are estimated from two narrowbands. Blanc et al. (2011) obtain $q = 0.99$ for $z = 2$–4 LAEs whose intrinsic Lyα luminosities are inferred from UV-continuum. Therefore, LAEs are on average likely to show $q \sim 1$, and whose observed EWs(Lyα) to be approximately intrinsic. However, we find a non-negligible scatter in q-values around unity (especially toward smaller values) for the individual LAEs with Hα measurement (Section 5.2.4; Figure 5.12 right). The LAEs with $q < 1$ go down on the EWs diagram and approach the instantaneous burst tracks. Unfortunately, with the current large errors in q-values, we cannot clearly tell which star-formation histories are likely for LAEs. Future radiative transfer calculations as well as higher S/N ratio spectra of Lyα and Hα (and probably Hβ) will enable full use of the EWs diagram.

5.2.4. Super Case B Objects?

Figure 5.12 (left) shows the Lyα/Hα ratio against EW(Lyα) for LAEs. The dark red symbols indicate the observed Lyα luminosity divided by the intrinsic Hα luminosity corrected using the attenuation inferred from the SED fitting (i.e., showing lower-limits of the intrinsic Lyα/Hα ratio on the y-axis) that correspond to the escape fraction of Lyα photons (see Equation 5.7 below), while the light red symbols show the observed Lyα/Hα ratios. We note that recent studies have shown that a fraction of Lyα is emitted from diffuse outer halos of galaxies (e.g., Steidel et al. 2011). We estimate the strength of Lyα from the color $U-$NB387 with a certain aperture (Appendix A), therefore the Lyα/Hα ratios we derive are the fraction of Lyα to Hα photons escaping from the central region of the LAEs.

From Figure 5.12 (left), a trend that LAEs with larger EW(Lyα) have larger Lyα/Hα ratio appears

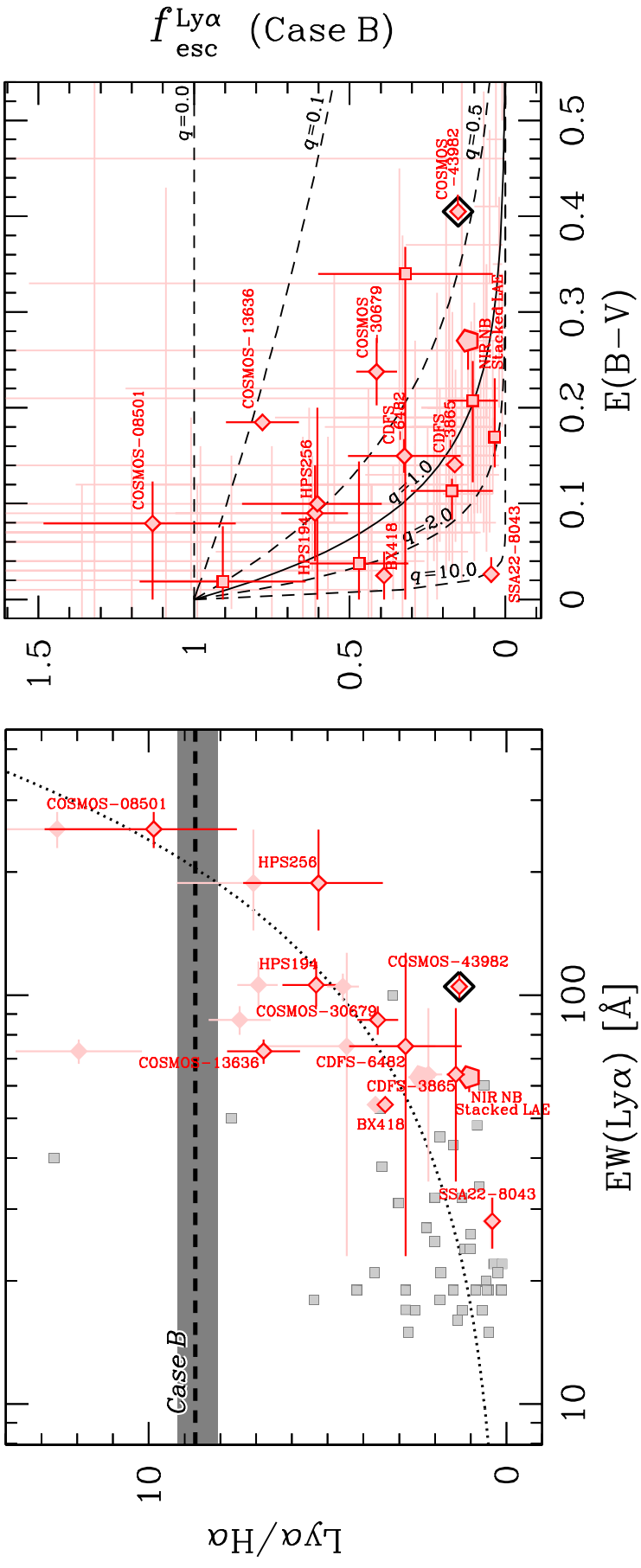

Figure 5.12. *Left:* Lyα/Hα flux ratio vs. EW(Lyα). Symbols are the same as in Figure 5.11. The darker symbols show the ratios calculated by the observed Lyα luminosity divided by the intrinsic Hα luminosity (i.e., lower-limit of the ratios), while the lighter show the ratios calculated by the observed Lyα and Hα luminosities. The ratios for $z \sim 0.3$ LAEs are based on observed luminosities. Dotted curve represents a single power-law fit given in Eq. (5.9). The dashed line and the gray shaded area show the Lyα/Hα flux ratio assuming the Case B recombination (8.7; Brocklehurst 1971) and its variation with electron density (8.1–9.2 with $n_e = 10^2$–10^{10} cm^{-3}; Hummer & Storey 1987) when $T_e = 10^4$ K, respectively. *Right:* Escape fraction of Lyα photons (assuming the Case B) vs. dust extinction. The red squares show $z = 2.2$ LAEs (Hayes et al. 2010), and the faint-colored red error bars show $z = 2$–4 LAEs (Blanc et al. 2011). Superposed curves show the relations at a given q parameter ($q = 0.0, 0.1, 0.5, 1.0, 2.0, 10.0$).

to be present. This trend itself is not so surprising, but interestingly some LAEs, COSMOS-08501, and possibly COSMOS-13636 and one LAE at $z \sim 0.3$, may have Lyα/Hα ratios exceeding the Case B recombination value ($\simeq 8.7$; Brocklehurst 1971), which we call "super Case B." Super Case B Lyα/Hα ratios have also been reported for some strong LAEs in the local universe (Hayes et al. 2007, Atek et al. 2008, Otí-Floranes et al. 2012, and references therein). The variation of the intrinsic Case B Lyα/Hα ratio (the gray shaded area) does not seem to be a significant issue. Although it is not obvious that super Case B objects are really included in our sample due to their large errors, it is worth discussing possible physical origins of them in case they really exist.

We consider the possible effect of geometry, and the kinematics of dust and gas in the ISM. Neufeld (1991) propose a clumpy, multi-phase ISM where gas and dust are gathered in clouds within a low-density medium (see also, e.g., Hansen & Oh 2006; Scarlata et al. 2009). With such circumstances, Lyα photons can be scattered at the surfaces of the clouds due to the resonant nature, while continuum photons would penetrate the clouds deeply. Since dust is contained in the clouds, Lyα photons would have a much smaller chance of encountering dust than other photons. In this scenario, a large EW(Lyα) and Lyα/Hα ratio can be observed. Alternatively, an outflow of the ISM can be a cause of strong Lyα emission (e.g., Kunth et al. 1998). However, Hashimoto et al. (2013) find an anti-correlation between EW(Lyα) and Lyα velocity offset for LAEs, the latter is considered to be positively correlated with outflow velocity. This anti-correlation is also supported by the observations of LBGs (Adelberger et al 2003; see also Shapley et al. 2003; Pettini et al. 2001). In addition, the authors measure the LAEs' outflow velocity directly from metal absorption lines, finding that outflow velocities for LAEs and LBGs are comparable. Therefore, outflows do not appear to be a major mechanism for producing large EW(Lyα) and Lyα/Hα ratio, though the sample size of LAEs is still small and much more data as well as theoretical works to interpret the properties are needed.

In order to clarify the effects of a potentially clumpy geometry of ISM on Lyα/Hα ratios, we plot in Figure 5.12 (right) the relation between $E(B-V)$ and the escape fraction of Lyα photons ($f_{\rm esc}^{\rm Ly\alpha}$) under the Case B recombination assumption. We estimate $f_{\rm esc}^{\rm Ly\alpha}$ as

$$f_{\rm esc}^{\rm Ly\alpha} \equiv \frac{L_{\rm obs}({\rm Ly}\alpha)}{L_{\rm int}({\rm Ly}\alpha)} = \frac{L_{\rm obs}({\rm Ly}\alpha)}{8.7 L_{\rm int}({\rm H}\alpha)}, \tag{5.7}$$

where subscripts 'int' and 'obs' refer to the intrinsic and observed quantities, respectively. The intrinsic Hα luminosities are derived from the observed Hα fluxes, corrected for dust extinctions. The superposed lines show the relations at a given q parameter (Section 5.2.3);

$$q = \frac{-\log\left(f_{\rm esc}^{\rm Ly\alpha}\right)}{0.4 k_{1216} E(B-V)}, \tag{5.8}$$

where k_{1216} is an extinction coefficient at $\lambda = 1216$ Å (11.98; Calzetti et al. 2000). The clumpy geometry of ISM (or outflow) is favored by objects with $q = 0$–1. From Figure 5.12 (right), most of the LAEs presented here are located in the range $q = 0$–1; e.g., COSMOS-13636 and COSMOS-30679 have large $f_{\rm esc}^{\rm Ly\alpha}$ in spite of their moderate amounts of dust. The NIR narrowband stacked LAE also suggests $q < 1$ ($q = 0.7 \pm 0.1$; see Section 3.2 and Appendix C). Although there are some exceptional objects (e.g., SSA22-8043), LAEs are suggested to have a q parameter of unity or less on average. This is in contrast to LBGs, whose q parameter is suggested to be higher ($q \sim 2$ for $z \sim 3$ LBGs with E$(B-V) = 0.1$–0.2; Kornei et al. 2010).

A notable object is COSMOS-08501. It appears to fall above the $q = 0$ line, where the clumpy ISM model does not work assuming Case B recombination, although the errors are relatively large. Moreover, since it is inferred to possess relatively small amount of dust, the large EW(Lyα) owing to the clumpy ISM is unlikely. In case the object is really super Case B, the only remaining explanation is the Lyα enhancement caused by collisional excitations. Due to the decreasing collisional strengths with increasing principle quantum number, collisional excitations can lead to Lyα/Hα ratios over the Case B value (see also Osterbrock 1989). Shocks caused by interactions with other sources, AGN activity, supernova explosions, strong outflows or infall are possible candidates for the collisional excitations.

Based on the HST images (Figure B.6), COSMOS-08501, a super Case B candidate, looks very compact and shows no sign of interactions. COSMOS-13636, which has a very small q parameter, shows two faint sources nearby within ~ 5 kpc (projected) from the object. Its strong Lyα emission can be (partly) due to shocks caused by interactions. Indeed, some fractions of LAEs are turned out to exhibit morphologies suggestive of mergers at higher redshift (e.g., Pirzkal et al. 2007; Bond et al. 2009) as well as lower redshift (Cowie et al. 2010). Theoretically, Tilvi et al. (2011) demonstrate that mergers play an important role in mass assembly and star-formation in majority of the LAEs especially at higher redshift. Unfortunately, the shock-induced Lyα emission due to mergings has not yet been taken into account in these theoretical works (see also Tilvi et al. 2009). Alternatively, as discussed by Mori et al. (2004), supernova explosions can cause strong shocks, resulting in strong Lyα emission. Although the authors intend to explain extended Lyα blobs (~ 100 kpc) with high Lyα luminosities ($\sim 10^{43}$ erg s^{-1}), their basic ideas can be applied to normal LAEs. AGN activity and outflows seem unlikely (see Appendix B.3.1 and Hashimoto et al. 2013).

When shocks (even partly) contribute to emission lines of LAEs, estimates of physical quantities such as ionization parameter (from [O III]/[O II] ratio), metallicity (from $N2$-index), SFR (from Hα), and dust extinction (from Balmer decrement) become less accurate. In particular, the intrinsic Hα/Hβ value becomes larger when shocks are present, resulting in an overestimate of the abundance of dust. This effect may also help explain the presence of super Case B objects (e.g., Otí-Floranes et al. 2012). Thus, the results presented in this paper may require some corrections for the presence of shocks. We plan to address this in future work, through the simultaneous application of photoionization and shock models, with deeper spectroscopy which will detect the weaker lines not fully detected in the observations presented here (e.g., Balmer lines, [O II], [O III], [N II], [S II]).

A final remark is that from our discussions so far it is evident that Lyα is not a robust indicator of SFR for LAEs. The observed data ($z = 0$–2) in Figure 5.12 (left) are relatively well represented by a single power-law fit

$$\begin{aligned} \log\left(\mathrm{Ly}\alpha/\mathrm{H}\alpha\right)_{\mathrm{obs}} = \quad & (-1.08 \pm 0.29) \\ & +(0.87 \pm 0.19) \times \log \mathrm{EW}(\mathrm{Ly}\alpha), \end{aligned} \tag{5.9}$$

which is shown by the dotted curve in Figure 5.12 (left). According to this simple relation, SFRs of LAEs with EW(Lyα) ~ 20 Å (a typical threshold in narrowband searches) can be underestimated by a factor of about 10. Thus, SFRs estimated from Lyα may involve a factor of ~ 10 uncertainties intrinsically.

5.3. Summary of This Chapter

In the first part of this Chapter, we have mainly discussed what we have found in the previous chapters regarding ionization state and metallicity of galaxies at $z = 0 - 3$. The discussions are summarized as follows.

- We have confirmed the trend that high-z galaxies have ionization parameters significantly higher than local galaxies. The local extreme populations of GPs, LyC leakers, and LBAs have an ionization parameter as high as $z \sim 2 - 3$ LBGs and LAEs. Moreover, the ionization parameter of GPs is comparable to that of LAEs. In this sense, GPs could be local counterparts of $z \sim 2 - 3$ LAEs. However, GPs are quite rare objects in the local universe, occupying only $\sim 0.06\,\%$ of the SDSS sample. The number density of GPs is approximately two orders of magnitude smaller than that of $z \sim 2$ LAEs. Interestingly, Heckman et al. (2005) report a similar difference of abundances between LBAs and $z \sim 3$ LBGs. These results indicate that galaxies with a high ionization parameter would emerge in a high redshift universe, and that these galaxies are more dominant in high-z than the local universe.

- We have particularly found no significant differences between galaxies at $z \sim 2$ and 3 in the FIR (Figure 4.5). This is in contrast with the FMR whose possible evolution from $z \sim 2$ to 3 is reported (Mannucci et al. 2010; see also Section 1.3). We have suggested that the FMR evolution can arise, if one omits ionization parameter differences and adopts local empirical metallicity relations for high-z galaxies. We have indicated that the FMR evolution does not exist for one out of two average metallicity solutions of $z \sim 3$ galaxies with a high ionization parameter of $\log(q_{\rm ion}/{\rm cm\,s^{-1}}) \gtrsim 8$ (right panel of Figure 5.2). This argument is supported by the local UV-selected galaxies of LBAs (top panel of Figure 5.3).

- According to the universality of the FIR over cosmic time, the evolution of ionization parameter could be interpreted as a result that galaxies with high SFR for their $M_\star$ are more commonly found at high-z, as suggested by the evolution of the star-formation main sequence (e.g., Daddi et al. 2007). Young stellar population, efficient star-formation, and/or top-heavy IMF are possible origins of the trend. Alternatively, clumpy star-forming regions with high ionized gas density could play a role in the high ionization state at high-z galaxies (Equation 2.5; e.g., Shirazi et al. 2013). In order to fully understand the origins of high ionization parameter, it is necessary to interpret the FIR with theoretical models. Since the FMR can be explained with the redshift-independent simple analytic model with the interplay between the star-formation, the infall of metal-poor gas, and the outflow of metal-rich gas (e.g., Mannucci et al. 2010; Dayal et al. 2013), the prescription could be extended toward the FIR (via Equation 5.6). Although it is still quantitatively unclear how the density is affected by gas infalls and outflows, comparing the model with the FMR and the FIR would allow us to infer the effect. With an updated FIR consisting of physical quantities of ionization parameter, $M_\star$, SFR, and metallicity (instead of $R23$-index and [O III]/[O II] ratio) and theoretical models, we will explore in detail the interpretation of the FIR as well as the high ionization state commonly observed at high-z in future work.

- We have found the $z \sim 0$ LyC leakers exhibit [O III]/[O II] ratios significantly higher than typical low-z galaxies. This trend suggests a positive correlation between [O III]/[O II] and ionizing

photon escape fraction ($f_{\rm esc}$). Our photoionization models of CLOUDY have reproduced the trend (Figure 5.4). The underlying physical condition is a density-bounded HII nebula with a low column density of neutral hydrogen gas (Figure 5.5). Since [O III]/[O II] ratios for $z = 2-3$ galaxies, especially LAEs, are comparable to, or higher than, those of the low-z LyC leakers, these high-z galaxies are candidates of high $f_{\rm esc}$ objects.

- Our CLOUDY photoionization models have revealed that EW(Lyα) remains almost unchanged if its $f_{\rm esc}$ is $\simeq 0-0.8$ (Figure 5.6), indicated that galaxies are identified as LAEs of a Lyα emitting population if their $f_{\rm esc}$ values are below $\simeq 0.8$. Note that clumpy geometry of dense neutral hydrogen gas could explain potentially high gas fraction in such high-z low-mass galaxies (e.g., Tacconi et al. 2010, 2013; Santini et al. 2014). Faint galaxies with intrinsically-bright Lyα having a high $f_{\rm esc}$ could significantly contribute to the ionizing photon production for cosmic reionization, since recent observations report that a fraction of LAEs in star-forming galaxies increases with redshift (e.g., Ouchi et al. 2008; Stark et al. 2010). If it is true, this would ease the tension of ionizing photon deficit problem (e.g., Ouchi et al. 2009; Robertson et al. 2010).

In the second part of this Chapter, we have focused on the basic characteristics of LAEs at high-z. Since previous high-z spectroscopic observations lacked LAEs, it is important to deepen our understandings of what kind of galaxies LAEs are from their detailed emission-line properties. Main discussions are summarized as follows.

- $M_\star$–Z relation for LAEs is complicated compared with that for LBGs at similar redshifts. LAEs with $M \gtrsim M^{9.5} M_\odot$ are less chemically-enriched for their stellar masses, while LAEs with $M \gtrsim M^{9.5} M_\odot$ tend to lie above the LBGs' relation (Figure 5.8). Metallicities of LAEs could be, on the whole, low (approximately sub-solar metallicity) regardless of their stellar masses. With their high ionization parameters and low metallicities, LAEs would represent an early stage of galaxy evolution dominated by massive stars in compact HII-regions. The discrepancies seen in LAEs on the $M_\star$–Z relation could be alleviated in the FMR plot (Figure 5.9). By adopting a correct ionization parameter to estimate a metallicity, and by taking into account the differences of SFR between LAEs and LBGs, we have found a better level of consistency between LAEs and other populations in the FMR plot. However, as found by our photoionization models, if its $f_{\rm esc}$ is not negligible, the metallicity could be incorrectly estimated, making its $M_\star$–Z relation and FMR more complex to be interpreted. In fact, LAEs lying above the FIR appear to fall below the FMR. $f_{\rm esc}$ (or column density of neutral hydrogen) would be a key quantity to characterize these galaxies.

- Combined with the upper- and lower-limits of metallicity derived for the composite K-band spectrum of LAEs (Section 3.1) and the stacked NIR narrowband images of LAEs (Section 3.2), respectively, LAEs typically have metallicities $12+\log({\rm O/H}) = 7.93$–$8.42$ (7.63–8.66) at the 1σ (2σ) level. Especially, this relatively high lower-limit does not support, at least at $z \sim 2$, the hypothesis that LAEs are extremely metal poor ($Z < 2\times10^{-2}\,Z_\odot$) galaxies at the 4σ level.

- We have found a trend that low mass LAEs with $M_\star \lesssim 10^{9.5} M_\odot$ fall below a simple extrapolation toward lower-masses of the observed sSFR–$M_\star$ relation of $z \sim 2$ LBGs (Figure 5.10). This indicates that low-mass galaxies with $M_\star \lesssim 10^{9.5} M_\odot$ have star formation efficiencies lower than expected from massive galaxies.

- The EW(Lyα) vs. EW(Hα) diagram interestingly suggests that more than half of the LAEs appear to need an extended star-formation such as a burst superimposed upon a continuous star-formation rather than the instantaneous burst alone. However, since EW(Lyα) may suffer from effects of dust and we do find a non-negligible scatter in q-values around unity (especially toward smaller values), we need to carefully interpret the result.

- LAEs with low q-values ($q = 0$–1) can be explained by the clumpy geometry of ISM. Interestingly, our sample may include objects with further enhanced Lyα, which we call super Case B. If they really exist, the only possible explanation is the collisional excitations of Lyα. Interactions with other sources and/or supernova explosions are possible key events that may cause shock-induced collisional excitation. If such shocks play a role in enhancement of the Lyα flux, physical quantities such as ionization parameter, metallicity, SFR, and dust extinction should be re-computed using a combination of photoionization and shock-excitation models.

6 Conclusions

In this thesis, we investigate ionization state and metallicity of galaxies at $z = 0-3$ over wide ranges of stellar mass ($M_\star$) and star formation rate (SFR). This thesis aims to provide deeper insights into the evolution of star-forming galaxies in terms of their physical state of HII-regions, and to understand roles of star-forming galaxies in the Epoch of Cosmic Reionization. We make use of line ratios of [O III]λ5007/[O II]λ3727 and ([O III]$\lambda\lambda$5007,4959+[O II]λ3727)/Hβ (R23-index) with photoionization models.

In the local universe, we find a trend that a high ionization parameter is found in less massive, efficiently star-forming, and metal-poor galaxies (Figure 2.8). A similar trend has been reported between $M_\star$, SFR, and metallicity as the fundamental metallicity relation (FMR; Mannucci et al. 2010; Lara-López et al. 2010), but we find the ionization parameter also varies as a function of $M_\star$, SFR, and metallicity. We develop a four-dimensional relation of ionization parameter, $M_\star$, SFR, and metallicity (Figure 2.11), extending the FMR with ionization parameter. The relation is valid over wide ranges of $M_\star$ and SFR for local galaxies, including local extreme populations of green pea galaxies (GPs) and Lyman-break analogs (LBAs).

At higher-z, we find that $z = 2-3$ galaxies show an ionization parameter of $\log(q_{\rm ion}/{\rm cm\,s^{-1}}) \sim 7.6-9.0$, a factor of $\gtrsim 4-10$ higher than typical local galaxies (Figure 4.3). When these high-z galaxies are compared to the four-dimensional relation of ionization parameter, $M_\star$, SFR, and metallicity, they follow the same relation defined with the local SDSS galaxies (Figure 4.5). The relation is thus referred to as the fundamental ionization relation (FIR). We particularly find no significant differences between galaxies at $z \sim 2$ and 3 in the FIR (Figure 4.5). This is in contrast with the FMR whose possible evolution from $z \sim 2$ to 3 is reported (Mannucci et al. 2010). We suggest that the FMR evolution can arise, if one omits ionization parameter differences and adopts local empirical metallicity relations for high-z galaxies. We indicate that the FMR evolution does not exist for one out of two average metallicity solutions of $z \sim 3$ galaxies with a high ionization parameter of $\log(q_{\rm ion}/{\rm cm\,s^{-1}}) \gtrsim 8$ (right panel of 5.2). This argument is supported by the local UV-selected galaxies of LBAs (top panel of 5.3). We argue that ionization parameter is essential to discuss the chemical evolution of galaxies appropriately.

According to the universality of the FIR over cosmic time, the evolution of ionization parameter could be interpreted as a result that galaxies with high SFR for their $M_\star$ are more commonly found at high-z, as

suggested by the evolution of the star-formation main sequence (e.g., Daddi et al. 2007). Young stellar population, efficient star-formation, and/or top-heavy IMF are possible origins of the trend. Alternatively, clumpy star-forming regions with high ionized gas density could play a role in the high ionization state at high-z galaxies (Equation 2.5; e.g., Shirazi et al. 2013). In order to fully understand the origins of high ionization parameter, it is necessary to interpret the FIR with theoretical models. Since the FMR can be explained with the redshift-independent simple analytic model with the interplay between the star-formation, the infall of metal-poor gas, and the outflow of metal-rich gas (e.g., Mannucci et al. 2010; Dayal et al. 2013), the prescription could be extended toward the FIR (via Equation 5.6). Although it is still quantitatively unclear how the density is affected by gas infalls and outflows, comparing the model with the FMR and the FIR would allow us to infer the effect. With an updated FIR consisting of physical quantities of ionization parameter, $M_\star$, SFR, and metallicity (instead of $R23$-index and [O III]/[O II] ratio) and theoretical models, we will explore in detail the interpretation of the FIR as well as the high ionization state commonly observed at high-z in future work.

We find the $z \sim 0$ LyC leakers exhibit [O III]/[O II] ratios significantly higher than typical low-z galaxies. This trend suggests a positive correlation between [O III]/[O II] and ionizing photon escape fraction ($f_{\rm esc}$). Our photoionization models of CLOUDY reproduce the trend (Figure 5.4). The underlying physical condition is a density-bounded HII nebula with a low column density of neutral hydrogen gas (Figure 5.5). Since [O III]/[O II] ratios for $z = 2-3$ galaxies, especially LAEs, are comparable to, or higher than, those of the low-z LyC leakers, these high-z galaxies are candidates of high $f_{\rm esc}$ objects. Our CLOUDY photoionization models reveal that EW(Lyα) remains almost unchanged if its $f_{\rm esc}$ is $\simeq 0-0.8$ (Figure 5.6), indicating that galaxies are identified as LAEs of a Lyα emitting population if their $f_{\rm esc}$ values are below $\simeq 0.8$. Note that clumpy geometry of dense neutral hydrogen gas could explain potentially high gas fraction in such high-z low-mass galaxies (e.g., Tacconi et al. 2010, 2013; Santini et al. 2014). Faint galaxies with intrinsically-bright Lyα having a high $f_{\rm esc}$ could significantly contribute to the ionizing photon production for cosmic reionization, since recent observations report that a fraction of LAEs in star-forming galaxies increases with redshift at the epoch with no IGM damping absorption (e.g., Ouchi et al. 2008; Stark et al. 2010). If it is true, this would ease the tension of ionizing photon deficit problem (e.g., Ouchi et al. 2009; Robertson et al. 2010).

7 Future Prospects

As have been summarized in this thesis, we have been able to examine the evolution of star-forming galaxies including LAEs carefully and accurately by incorporating ionization parameter. We have also shown that this study provides important insights into the ionizing sources responsible for the cosmic reionization.

However, there remain some unresolved issues. We have suggested that the FIR be universal over cosmic time, but the high-z galaxy sample is still relatively small, and we have not yet been able to test the fundamentality enough at high-z. Although LAEs on average show remarkably high ionization parameters, and some may lie off the FIR, it is still unclear whether this is due to their high $f_{\rm esc}$ achieved by their low column density of neutral hydrogen or other physical mechanisms. The weak $M_\star$–Z relation for high-z LAEs remains to be fully discussed with the current sample size of LAEs. We have suggested with photoionization models that galaxies with a high $f_{\rm esc}$ show a high [O III]/[O II] ratio, though it has not yet been tested observationally.

These problems that we have found in this study are the basic topics of my future work. We have been performing NIR multi-object spectroscopy observations of high-z galaxies including LAEs, LBGs, and LyC leaking galaxies with Subaru/FMOS (PI K. Nakajima) and Keck/MOSFIRE (PI K. Nakajima). Although these studies are still in the middle of their courses and not finished, we summarize their current status and primary goals below.

Definitive Identification for Properties of LAEs and LBGs at $z \sim 2$ with Subaru/FMOS

In order to obtain statistically reliable estimates of metallicity and ionization parameter of high-z galaxies over a wide range of stellar mass and to extend our knowledge of the $M_\star$–Z relation, the FMR, and the FIR toward higher-z, we carried out the Fiber Multi Object Spectrograph (FMOS; Kimura et al. 2010) spectroscopy of our $z = 2.2$ LAEs (Appendix A) as well as $z \sim 2$ continuum-selected galaxies such as BX/BM galaxies. FMOS is a NIR fiber-fed multi-object spectrograph, providing us with 400 fibers in a FoV of 30′ diameter. Two NIR spectrographs (IRS1 and IRS2) with an OH-airglow suppression system enable us to obtain spectra in the wavelength range of 0.9–1.8 μm. We select the instrument, because all nebular lines needed to estimate metallicity and ionization parameter simultaneously, i.e., [O III]$\lambda\lambda$,5007,4959, Hβ, and [O II]λ3727, are observable for $z \sim 2$ galaxies with FMOS. Furthermore, we can observe $\sim$ 200 objects at the same time with FMOS[7.1], enabling us to examine the average

[7.1] We adopted the cross beam switching mode, with which two fibers are allocated to one object, so that either of the two fibers observes the object and the other observes sky. Therefore, the number of targets is $\sim 400/2 = 200$.

Table 7.1. Summary of the FMOS Observation

Field	No. of LAEs (1)	No. of LBGs (2)	Exp. Time(3) (J-long)	Exp. Time(3) (H-short)	Date
SXDS	90	85	3.5	6.3	2012 Dec 21–23
COSMOS	94	80	2.0	7.0	2012 Dec 21–23

Note: (1) Number of LAEs observed with FMOS. (2) Number of LBGs observed with FMOS. We observed the same objects both with H-short and J-long bands with the same fibers. (3) Total Exposure time in J-long and H-short bands in units of hours. Data under the conditions of bad weather, poor seeing, etc. are not included.

emission-line properties via a stacking analysis.

The observation was carried out on 2012 December 21–23. All nights are basically photometric, except for the last two hours of the second night and the first two hours of the third night. These worse data are not used in the analysis. We observed in a high-resolution mode, which gives a wavelength resolution of $R \sim 2200$. We observed in two pointings, centered on the SXDS and the COSMOS fields, in the first and the second half of each night, respectively. We used the two spectrographs, IRS1 and IRS2, in the same mode and used only one band during a night; we observed with H-short band (1.40–1.60 μm) in the first and third nights, and with J-long band (1.11–1.35 μm) in the second night. The details of the observation are summarized in Table 7.1.

The obtained data were reduced with the FMOS pipeline FIBRE-pac (Iwamuro et al. 2012). Basic reduction processes were the same as those for the other NIR spectrographs, such as NIRSPEC (Section 3.1.1.3). Since the spectrum of an object is obtained by two fibers, we combine the two spectra to obtain the final spectrum for each of the objects. Since OH lines are invisible due to the OH-airglow suppression system, we used Th-Ar lamp frames for wavelength calibration. The relative flux calibration was obtained by using several G- and K-type stars observed simultaneously.

In total, we observed 349 $z \sim 2$ galaxies, among which 106 show the detection of [O III]λ5007 emission line[7.2], although the number is still preliminary. Notably, we obtained [O III]λ5007 lines from 65 LAEs. This is considered to be the largest high-z LAE sample with optical nebular lines. The detections of [O III] enable us to estimate their exact systemic redshifts, and to perform a stacking analysis of their spectra to increase the S/N ratios and provide average emission-line properties. Although we succeeded in obtaining emission lines from only ~ 30 % of the objects we observed, the detailed analysis of the success rate remains to be done. Briefly, possible factors that decreased the success rate are (i) the relatively low detection limit of FMOS for faint targets, (ii) emission lines (especially [O III]λ5007) are contaminated by strong OH lines in H-band, (iii) emission lines (especially [O III]λ5007) are out of the covered wavelength ranges (for continuum-selected galaxies), and/or (iv) mis-selections of the target as $z \sim 2$ galaxies.

In any case, we have constructed the large LAE and LBG samples with a firm detection of at least [O III]λ5007. Since deep multi-wavelength data exist in both the SXDS and COSMOS fields, we will obtain their stellar populations by SED fitting. By dividing the sample into some sub-samples in terms of various physical properties (e.g., $M_\star$, SFR, $\mu_{0.32}$, EW(Lyα)) and performing a stacking analysis, we

[7.2] The oxygen line is the strongest line we expect to see in their spectra.

are able to examine average metallicity and ionization parameter, and to discuss their dependencies on those physical properties at high-z more statistically reliably. First of all, we will test whether the FIR is really universal over cosmic time. Since the high-z LBG sample presented in this thesis is still small, we will address the issue with our larger sample of high-z LBGs. Next, we will investigate the difference between LAEs and LBGs. We have found in this thesis that LAEs may show the complex $M_\star$–Z relation, have a very high ionization parameter, and even deviate from the FIR towards higher [O III]/[O II] ratio. We will test whether these trends are real or not. Since LAEs are considered to be low mass and actively star-forming galaxies, they are helpful for us to explore parameter space in the $M_\star$–Z relation, FMR, and FIR. Remarkably, if the deviations of LAEs from the FIR are confirmed, our speculation is finally more likely, such that objects with high $f_{\rm esc}$ show an increased [O III]/[O II] ratio. Our FMOS data are thus very useful for extending the study described in this thesis.

Since we mainly focused on LAEs on the FMOS run, the number of continuum-selected galaxies whose emission lines are identified is not so large ($N = 41$). We will propose to carry out FMOS observation for continuum-selected galaxies at $z \sim 2$, so that we can further push the study and compare LAEs and LBGs more statistically. Moreover, in order to extend our study toward higher-z, we will propose to carry out NIR spectroscopy of $z \sim 3$ galaxies. We need both H-and K-band spectroscopy to study the FIR for $z \sim 3$ galaxies. Unfortunately however, FMOS is not capable of K-band spectroscopy. We will therefore propose to use other NIR multi-object spectrographs such as Subaru/MOIRCS (Suzuki et al. 2008; Ichikawa et al. 2006) and Keck/MOSFIRE.

Direct Confirmation of the Relationship between Ionization State and Ionizing Photon Escape

We have suggested with photoionization models that galaxies with high $f_{\rm esc}$ show a high [O III]/[O II] ratio (Figure 5.4). If this trend is real, the correlation is useful to investigate ionizing photon escapes that cannot be directly observed for galaxies at $z > 6$. Although both of the two local LyC leakers support the trend, they may not be statistically enough to convince one that galaxies showing an increased [O III]/[O II] ratio can have a high $f_{\rm esc}$. We need to test the trend observationally with a larger sample of galaxies with LyC radiation, and directly confirm (i) the positive correlation between [O III]/[O II] and $f_{\rm esc}$ and (ii) the trend that LyC leaking galaxies lie above the FIR.

For these purposes, we used the the Multi-Object Spectrograph for Infrared Exploration (MOSFIRE; McLean et al. 2012, 2010) on Keck I and carried out a NIR multi-object spectroscopy for $z \sim 3$ LAEs and LBGs in the SSA22 field whose $f_{\rm esc}$ have been already determined by I. Iwata, A. K. Inoue, et al. (in preparation) and Nestor et al. (2013). MOSFIRE is the newest and extremely powerful instrument at the Keck Observatory, providing with the highest quality NIR spectra covering 1.0–2.5 μm for < 46 objects with a FoV of $6' \times 3'$. Since our targets of $z \sim 3$ galaxies showing LyC radiation are generally very faint ($R \gtrsim 24$), MOSFIRE is the almost only multi-object NIR spectrograph that enables us to obtain their nebular emission lines individually.

The observation was carried out on 2013 October 7. Although we had originally planned to observe with K- and H-bands, which cover [O III]$\lambda\lambda$5007, 4959+Hβ and [O II]λ3727, respectively, we had only $\sim$ 1–2 hours on-source exposure times due to the thick cloud during the night and the reduced observation time. Accordingly, we observed only with K-band. We will propose to carry out an H-band and a deeper K-band spectroscopy for the same $z \sim 3$ galaxies with MOSFIRE to obtain the full suite of emission lines necessary to accomplish our study. We chose a slit width of $0\farcs7$, which gives a wavelength resolution of $R \sim 3600$ in K. We used one mask, which contains 16 objects with a constraint on $f_{\rm esc}$. Table 7.2 gives

Table 7.2. Summary of the MOSFIRE Observation

Field	No. of LBGs (1)	No. of LAEs (2)	Exp. Time[(3)] (H)	(K)	Date
SSA22	5, 0	6, 5	···	1–2	2013 Oct 7

Note: (1) The first quantity shows the number of LBGs whose $f_{\rm esc}$ is determined. The second indicates the number of LBGs whose upper-limit of $f_{\rm esc}$ is given. (2) The same as those in (1), but for LAEs. (3) Total Exposure time in K and H bands in units of hours. Due to the thick cloud, we only had time to observe with K band. According to a quick reduction during the observation, the on-source exposure time in K band is approximately 1–2 hours.

the summary of the observation. Briefly, 11 of them have an estimation of $f_{\rm esc}$, while the other 5 galaxies (all are classified as LAEs) have an upper-limit of $f_{\rm esc}$. Their $f_{\rm esc}$ are constrained by the LyC radiation observed through narrowband imaging observations. Six of the LyC leaking galaxies are provided by I. Iwata, A. K. Inoue, et al. (in preparation), and the other 10 are collected from the literature (Nestor et al. 2013). Possible foreground contaminants had been removed by a deep rest-frame UV and optical spectroscopy. We additionally include a star with $K < 19$ to use for flux calibration. Since the star is observed in exactly the manner as the science targets, we can use the star to estimate the slit loss and to check the variation of the weather condition.

Since the data have not yet been fully reduced and analyzed and the H-band data have not been taken yet, we summarize here the scientific goals we will address with the MOSFIRE data. The K- and H-bands spectroscopy for $z \sim 3$ galaxies provide both [O III]/[O II] ratio and $R23$-index. First of all, we are interested in the correlation between $f_{\rm esc}$ and [O III]/[O II] ratio, as theoretically suggested by our work (Figure 5.4). Combined with the typical $f_{\rm esc}$ inferred from Nestor et al. (2013) and the typical [O III]/[O II] ratio from our work (Section 4.2) for LAEs and LBGs, top of Figure 7.1 shows the rough trend between $f_{\rm esc}$ and [O III]/[O II] ratio. The 11 LAEs and LBGs with firm measurements of $f_{\rm esc}$ and the 5 LAEs whose upper-limit of $f_{\rm esc}$ is constrained will enable us to explore the trend in top of Figure 7.1, and to test directly whether the [O III]/[O II] ratio increases with $f_{\rm esc}$. We note, however, that we have also suggested that the [O III]/[O II] ratio depends not only on $f_{\rm esc}$, but largely on ionization parameter and metallicity. Therefore, we will nextly examine the distributions of the LyC leaking galaxies on the FIR. We have suggested a trend that both of the two local LyC leakers and some LAEs and GPs showing the highest [O III]/[O II] ratios may depart significantly from the FIR towards higher [O III]/[O II] ratio (bottom of Figure 7.1), and that the increased [O III]/[O II] ratio could be originated from their high $f_{\rm esc}$ achieved by a low column density of neutral hydrogen. By plotting the LyC objects on the FIR, we will confirm the trend statistically.

In these manners, we will address the unresolved issues we have found further with the larger number of emission-line properties of high-z galaxies and LyC leaking objects observed by ourselves, shedding bright light on the fundamental questions in Astronomy of the evolution of galaxies and the cosmic reionization.

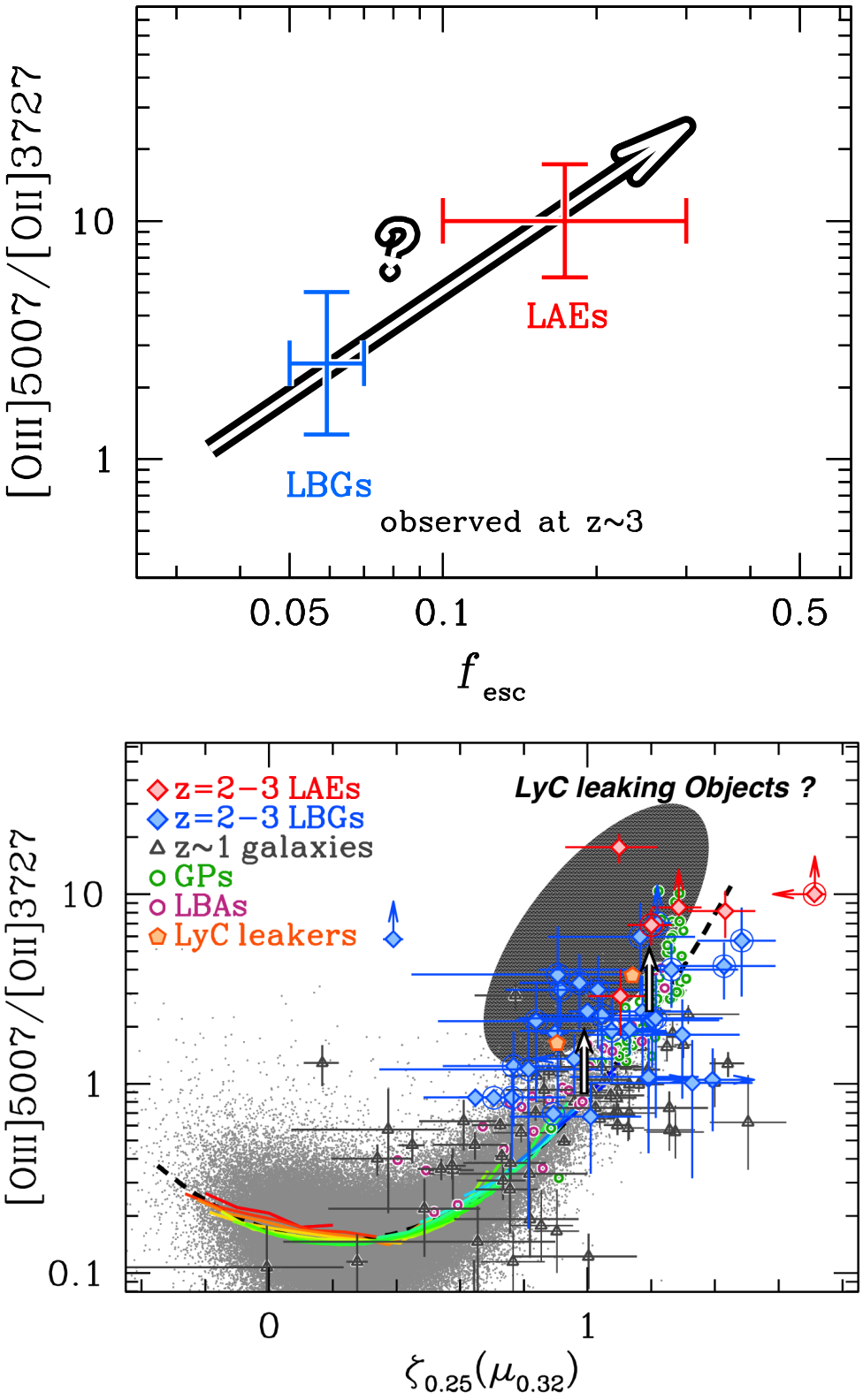

Figure 7.1. *Top:* [O III]/[O II] vs. f_{esc} plot for LAEs (red) and LBGs (blue). Their typical f_{esc} are observationally inferred from Nestor et al. (2013), and [O III]/[O II] ratios from our compilation presented in this thesis. The black arrow indicates the expected trend, which we have been proposing to confirm. *Bottom:* The FIR plot (Figure 4.5). Galaxies lying above the FIR (shaded area with gray) could be LyC leaking objects. The trend is supported by the two local LyC leakers, but has not yet been fully examined observationally.

References

Adelberger, K., Steidel, C. C., Shapley, A. E., & Pettini, M., 2003, ApJ, 584, 45

Amorín, R. O., Pérez-Montero, E., Vílchez, J. M., 2010, 715, L128

Asplund, M., Grevesse, N., Sauval, A. J., Scott, P., 2009, ARA&A, 47, 481

Atek, H., Kunth, D., Hayes, M., Östlin, G., & Mas-Hesse, L. M., 2008, A&A, 488, 491

Atek, H.,et al., 2011, ApJ, 743, 121

Baldwin, J. A., Phillips, M. M., Terlevich, R., 1981, PASP, 93, 5

Bardeen, J. M., Bond, J. R., Kaiser, N., & Szalay, A. S. 1986, ApJ, 304, 15

Basu-Zych, A. R., et al., 2007, ApJS, 173, 457

Belli, S., Jones, T., Ellis, R. S., Richard, J., 2013, ApJ, 772, 141

Benson, A. J., 2010, Phys. Rep., 495, 33

Bergvall, N., Östlin, G., 2002, A&A, 390, 891

Bergvall, N., Zackrisson, E., Andersson, B. -G., Arnberg, D., Masegosa, J., Östlin, G., 2006, A&A, 448, 513

Bertin, E., & Arnouts, S., 1996, A&AS, 117, 393

Blanc, G. A., et al., 2011, ApJ, 736, 31

Blanton, M. R., et al., 2003, ApJ, 592, 819

Blumenthal, G. R., Faber, S. M., Primack, J. R. & Rees, M. J., 1984, Nature, 311, 517

Bond, N. A., Gawiser, E., Gronwall, C., Ciardullo, R., Altmann, M., & Schawinski, K., 2009, ApJ, 705, 639

Bouwens, R. J., et al., 2011, ApJ, 737, 90

Brinchmann, J., Charlot, S., White, S. D. M., Tremonti, C., Kauffmann, G., Heckman, T., Brinkmann, J., 2004, MNRAS, 351, 1151

Brinchmann, J., Pettini, M., Charlot, S., 2008, MNRAS, 385, 769

Brocklehurst, M., 1971, MNRAS, 153, 471

Bruzual, G., & Charlot, S., 2003, MNRAS, 344, 1000

Calzetti, D., Armus, L., Bohlin, R. C., Kinney, A. L., Koornneef, J., Storchi-Bergmann, T., 2000, ApJ, 533, 682

Capak, P., et al., 2004, AJ, 127, 180

Cardamone, C., et al., 2009, MNRAS, 399, 1191

Cardamone, C., et al., 2010, ApJS, 189, 270

Cardelli, J. A., Clayton, C., Mathis, J. S., 1989, ApJ, 345, 245

Chabrier, G., 2003, PASP, 115, 763

Charlot, S., & Fall, S. M., 1993, ApJ, 415, 580

Charlot, S., Longhetti, M., 2001, MNRAS, 323, 887

Charlot, S., Kauffmann, G., Longhetti, M., Tresse, L., White, S. D. M., Maddox, S. J., & Fall, S. M., 2002, MNRAS, 330, 876

Chonis, T. S., et al., 2013, ApJ, 775, 99

Christensen, L., et al., 2012a, MNRAS, 427, 1953

Christensen, L., et al., 2012b, MNRAS, 427, 1973

Cooper, M. C., et al., 2006, MNRAS, 370, 198

Cowie, L. L., & Hu, E. M., 1998, AJ, 115, 1319

Cowie, L. L., Barger, A. J., & Hu, E. M., 2010, ApJ, 711, 928

Cowie, L. L., Barger, A. J., & Hu, E. M., 2011, ApJ, 738, 136

Cresci, G., Mannucci, F., Sommariva, V., Maiolino, R., Marconi, A., Brusa, M., 2012, MNRAS, 421, 262

Cullen, F., Cirasuolo, M., McLure, R. J., Dunlop, J. S., 2013, arXiv e-prints, arXiv:1310.0816

Daddi, E., et al., 2004, ApJ, 617, 746

Daddi, E., et al., 2007, ApJ, 670, 156

Davé, R., Finlator, K., Oppenheimer, B. D., 2011, MNRAS, 416, 1354

Davis, M., Efstathiou, G., Frenk, C. S., & White, S. D. M., 1985, ApJ, 292, 371

Dayal, P., Ferrara, A., Dunlop, J. S., 2013, MNRAS, 430, 2891

Dekel, A., et al., 2009, Nature, 457, 451

Dickinson, M., Giavalisco, M., & GOODS Team, 2003, in The Mass of Galaxies at Low and High Redshift, ed. R. Bender & A. Renzini (Berlin: Springer), 324

Dopita, M. A., Kewley, L. J., Heisler, C. A., Sutherland, R. S., 2000, ApJ, 542, 224

Dopita, M. A., et al., 2006a, ApJ, 647, 244

Dopita, M. A., et al., 2006b, ApJS, 167, 177

Dressler, A., 1980, ApJ, 236, 351

Dressler, A., Hare, T., Bigelow, B. C., & Osip, D. J., 2006, SPIE, 6269, 13

Duval, F., Schaerer, D., Östlin, G., Laursen, P., 2013, arXiv e-prints, arXiv:1302.7042

Ellis, R. S., et al. 2013, ApJ, 763, L7

Ellison, S. L., Patton, D. R., Simard, L., McConnachie, A. W., 2008, ApJ, 672, L107

Erb, D. K., Shapley, A. E., Pettini, M., Steidel, C. C., Reddy, N. A., & Adelberger, K. L., 2006a, ApJ, 644, 813

Erb, D. K., Steidel, C. C., Shapley, A. E., Pettini, M., Reddy, N. A., & Adelberger, K. L., 2006b, ApJ, 647, 128

Erb, D. K., Pettini, M., Shapley, A. E., Steidel, C. C., Law, D. R., Reddy, N. A., 2010, ApJ, 719, 1168

Fan, X., et al., 2004, AJ, 128, 515

Fan, X., et al., 2006, AJ, 132, 117

Feldmeier, J. J., et al., 2013, ApJ, 776, 75

Ferland, G. J., et al., 1998, PASP, 110, 761

Ferland, G. J., et al., 2013, RMxAA, 49, 137

Finkelstein, S. L., Rhoads, J. E., Malhotra, S., Pirzkal, N., & Wang, J., 2007, ApJ, 660, 1023

Finkelstein, S. L., Rhoads, J. E., Malhotra, S., Grogin, N., & Wang, J., 2008, ApJ, 678, 655

Finkelstein, S. L., Rhoads, J. E., Malhotra, S., & Grogin, N., 2009a, ApJ, 691, 465

Finkelstein, S. L., et al., 2009b, ApJ, 700, 376

Finkelstein, S. L., et al., 2011, ApJ, 729, 140

Förster Schreiber, N. M., et al., 2009, ApJ, 706, 1364

Fosbury, R. A. E., et al., 2003, ApJ, 596, 797

Furusawa, H., et al., 2008, ApJS, 176, 1

Gallagher, J. S., Hunter, D. A., & Bushouse, H., 1989, AJ, 97, 700

Gawiser, E., et al., 2006, ApJ, 642, L13

Gawiser, E., et al., 2007, ApJ, 671, 278

Genzel, R., Stutzki, J., 1989, ARA&A, 27, 41

Genzel, R., et al., 2011, ApJ, 733 101

Giacconi, R., Rosati, P., Tozzi, P., et al., 2001, ApJ, 551, 624

Giammanco, C., Beckman, J. E., Cedrés, B, 2005, A&A, 438, 599

Gilbank, D. G., Baldry, I. K., Balogh, M. L., Glazebrook, K., Bower, R. G., 2010, MNRAS, 405, 2594

Gray, R. O., & Corbally, C. J., 1994, AJ, 107, 742

Grogin, N. A., et al., 2011, ApJS, 197, 35

Gronwall, C., et al., 2007, ApJ, 667, 79

Guaita, L., et al., 2010, ApJ, 714, 255

Guaita, L., et al., 2011, ApJ, 733, 114

Gunn, J. E., & Peterson, B. A., 1965, ApJ, 142, 1633

Gunn, J. E., & Stryker, L. L., 1983, ApJS, 52, 121

Hainline, K. N., Shapley, A. E., Kornei, K. A., Pettini, M., Buckley-Geer, E., Allam, S. S., Tucker, D. L., 2009, ApJ, 701, 52

Hansen, M., & Oh, S. P., 2006, MNRAS, 367, 979

Hashimoto, T., et al., 2013, ApJ, 765, 70

Hayashi, M., et al., 2009, ApJ, 691, 140

Hayashino, T., et al., 2004, AJ, 128, 2073

Hayes, M., et al., 2007, MNRAS, 382, 1465

Hayes, M., et al., 2010, Nature, 464, 562

Heckman, T. M., et al., 2005, ApJ, 619, L35

Heckman, T. M., et al., 2011, ApJ, 730, 5

Henry, A., Kartin, C. L., Finlator, K., Dressler, A., 2013, ApJ, 769, 148

Holden, B. P., et al., 2014, arXiv e-prints, arXiv:1401.5490

Hoopes, C. G., et al., 2007, ApJS, 173, 441

Hopkins, A. M., 2004, ApJ, 615, 209

Hubble, E. P., 1922, ApJ, 56, 162

Hubble, E. P., 1936, Realm of the Nebulae. Yale Univ. Press, New Haven

Hummer, D. G., & Storey, P. J., 1987, MNRAS, 224, 801

Ichikawa, T., et al. 2006, SPIE, 6269, 38

Inoue, A. K., Iwata, I., Deharveng, J. -M., 2006, MNRAS, 371, L1

Inoue, A. K., Iwata, I., 2008, MNRAS, 387, 1681

Iwamuro, F., et al. 2012, PASJ, 64, 59

Iwata, I., et al., 2009, ApJ, 692, 1287

Izotov, Y. I., Stasińska, G., Meynet, G., Guseva, N. G., & Thuan, T. X., 2006, A&A, 448, 955

Izotov, Y. I., Guseva, N. G., & Thuan, T. X., 2011, ApJ, 728, 161

Jansen, R. A., Franx, M., & Fabricant, D., 2001, ApJ, 551, 825

Jaskot, A. E., Oey, M. S., 2013, ApJ, 766, 91

Jones, T. A., Ellis, R. S., Schenker, M. A., Stark, D. P., 2013, ApJ, 779, 52

Kakazu, Y., Cowie, L. L., Hu, E. M., 2007, ApJ, 668, 853

Kashikawa, N., et al., 2006, ApJ, 648, 7

Kashikawa, N., et al., 2011, ApJ, 734, 119

Kauffmann, et al., 2003a, MNRAS, 346, 1055

Kauffmann, G., et al., 2003b, MNRAS, 341, 33

Kennicutt, R. C., Jr., 1992, ApJ, 388, 310

Kennicutt, R. C., Jr., 1998, ARA&A, 36, 189

Kennicutt, R. C., Jr., Bresolin, F., & Garnett, D. R., 2003, ApJ, 591, 801

Kewley, L. J., Dopita, M. A., Sutherland, R. S., Heisler, C. A., & Trevena, J., 2001, ApJ, 556, 121

Kewley, L. J., Dopita, M. A., 2002, ApJS, 142, 35

Kewley, L. J., Geller, M. J., & Jansen, R. A., 2004, AJ, 127, 2002

Kewley, L. J., & Ellison, S. L., 2008, ApJ, 681, 1183

Kewley, L. J., Maier, C., Yabe, K., Ohta, K., Akiyama, M., Dopita, M. A., Yuan, T., 2013a, ApJ, 774L, 10

Kewley, L. J., et al., 2013b, ApJ, 774, 100

Kimura, M., et al., 2010, PASJ, 62, 1135

Kobulnicky, H. A., Kewley, L. J., 2004, ApJ, 617, 240

Kodaira, K., et al., 2003, PASJ, 55, L17

Koekemoer, A. M., et al., 2011, ApJS, 197, 36

Kroupa, P., 2001, MNRAS, 322, 231

Kornei, K. A., Shapley, A. E., Erb, D. K., Steidel, C. C., Reddy, N. A., Pettini, M., & Bogosavljevic, M., 2010, ApJ, 711, 693

Kunth, D., Mas-Hesse, J. M., Terlevich, E., Terlevich, R., Lequeux, J., Fall, S. M., 1998, A&A, 334, 11

Kurucz, R., 1993, Kurucz CD-ROM 13 (Cambridge, MA: SAO)

Lai, K., et al., 2008, ApJ, 674, 70

Lara-López, M. A., et al., 2010, A&A, 521, L53

Lara-López, M. A., et al., 2013, MNRAS, 434, 451

Lawrence, A., et al., 2007, MNRAS, 379, 1599

Lee, J. C., 2006, PhD thesis, Univ. Arizona

Lee, J. C., et al., 2012, PASP, 124, 782

Leitet, E., Bergvall, N., Piskunov, N. Andersson, B. -G., 2011, A&A, 532, A107

Leitet, E., Bergvall, N., Hayes, M., Linné, S., Zackrisson, E., 2013, A&A, 553, A106

Leitherer, C., Ferguson, H. C., Heckman, T. M., Lowenthal, J. D., 1995, ApJ, 454, L19

Leitherer, C., et al., 1999, ApJS, 123, 3

Levesque, E. M., & Richardson, M. L. A., 2013, ApJ accepted, arXiv:1309.0513

Lilly, S. J., Carollo, C. M., Stockton, A. N., 2003, ApJ, 597, 730

Liu, X., Shapley, A. E., Coil, A. L., Brinchmann, J., Ma, C. -P., 2008, ApJ, 678, 758

López-Sánchez, Á. R., Dopita, M. A., Kewley, L. J., Zahid, H. J., Nicholls, D. C., Scharwächter, J., 2012, MNRAS, 426, 2630

Ly, C., et al. 2011, ApJ, 726, 109

Ly, C., Malkan, M. A., Kashikawa, N., Ota, K., Shimasaku, K., Iye, M., & Currie, T., 2012, ApJ, 747, L16

Madau, P., 1995, ApJ, 441, 18

Maier, C., Lilly, S. J., Carollo, C. M., Stockton, A., Brodwin, M., 2005, ApJ, 634, 849

Maiolino, R., et al., 2008, A&A, 488, 463

Malhotra, S., & Rhoads, J. E., 2002, ApJ, 565, 71

Malhotra, S., & Rhoads, J. E., 2004, ApJ, 617, 5

Malhotra, S., Rhoads, J. E., Finkelstein, S. L., Hathi, N., Nilsson, K., McLinden, E., & Pirzkal, N., 2012, ApJ, 750, L36

Mannucci, F., et al., 2009, MNRAS, 398, 1915

Mannucci, F., Cresci, G., Maiolino, R., Marconi, A., Gnerucci, A., 2010, MNRAS, 408, 2115

Mannucci, F., Salvaterra, R., Campisi, M. A., 2011, MNRAS, 414, 1263

Marshall, J. L., et al. 2008, SPIE, 7014, 169

McGaugh, S. S., 1991, ApJ, 380, 140

McLean, I. S., et al., 1998, SPIE, 3354, 566

McLean, I. S., et al., 2010, SPIE, 7735, 47

McLean, I. S., et al., 2012, SPIE, 8446, 17

McLeod, B., et al., 2012, PASP, 124, 1318

McLinden, E. M., et al., 2011, ApJ, 730, 136

Miyazaki, S., et al., 2002, PASJ, 54, 833

Mori, M., Umemura, M., & Ferrara, A., 2004, ApJ, 613, L97

Moustakas, J., Kennicutt, R. C., Jr., & Tremonti, C. A., 2006, ApJ, 642, 775

Murray, N., Quataert, E., Thompson, T. A., 2005, ApJ, 618, 569

Nagao, T., Maiolino, R., Marconi, A., 2006, A&A, 459, 85

Nagao, T., Maiolino, R., Marconi, A., Matsuhara, H., 2011, A&A, 526, 149

Nestor, D. B., Shapley, A. E., Steidel, C. C., Siana, B., 2011, ApJ, 736, 18

Nestor, D. B., Shapley, A. E., Kornei, K. A., Steidel, C. C., Siana, B., 2013, ApJ, 765, 47

Neufeld, D. A., 1991, ApJ, 370, L85

Niino, Y., 2012, ApJ, 761, 126

Nilsson, K. K., et al., 2007, A&A, 471, 71

Nilsson, K. K., et al., 2009, A&A, 498, 13

Nilsson, K. K., Östlin, G., Møller, P.,Möller-Nilsson, O., Tapken, C., Freudling, W., & Fynbo, J. P. U., 2011, A&A, 529, 9

Oey, M. S., Kennicutt, R. C., Jr., 1997, MNRAS, 291, 827

Oke, J. B., 1974, ApJS, 27, 21

Oke, J. B., 1990, AJ, 99, 1621

Oke, J. B., et al., 1995, PASP, 107, 375

Ono, Y., et al., 2010a, MNRAS, 402, 1580

Ono, Y., Ouchi, M., Shimasaku, K., Dunlop, J., Farrah, D., McLure, R., & Okamura, S., 2010b, ApJ, 724, 1524

Ono Y., et al., 2012, ApJ, 744, 83

Osterbrock, D. E., 1989, Astrophysics of Gaseous Nebulae and Active Galactic Nuclei (Suasalito, CA: University Science Books)

Oteo, I., et al., 2012, A&A, 541, 65

Otí-Floranes, H., et al., 2012, A&A, 546, 65

Ouchi, M., et al., 2003, ApJ, 582, 60

Ouchi, M., et al., 2004, ApJ, 611, 660

Ouchi, M., et al., 2008, ApJS, 176, 301

Ouchi, M., et al., 2009, ApJ, 706, 1136

Ouchi, M., et al., 2010, ApJ, 723, 869

Overzier, R. A., et al., 2008, ApJ, 677, 37

Overzier, R. A., et al., 2009, ApJ, 706, 203

Pagel, B. E. J., Edmunds, M. G., Blackwell, D. E., Chun, M. S., Smith, G., 1979, MNRAS, 189, 95

Peng, C. Y., Ho, L. C., Impey, C. D., & Rix, H., 2010, AJ, 139, 2097

Pentericci, L., et al., 2011, ApJ, 743, 132

Pettini, M., et al., 2001, ApJ, 554, 981

Pettini, M., Pagel, B. E. J., 2004, MNRAS, 348, L59

Pilyugin, L. S., Thuan, T. X., 2005, ApJ, 631, 231

Pirzkal, N., Malhotra, S., Rhoads, J. E., & Xu, C., 2007, ApJ, 667, 49

Polletta, M., et al., 2007, ApJ, 663, 81

Pozzetti, L., et al., 2007, A&A, 474, 443

Queyrel, J., et al., 2009, A&A, 506, 681

Reddy, N. A., et al., 2006, ApJ, 644, 792

Richard, J., Jones, T., Ellis, R., Stark, D. P., Livermore, R., Swinbank, M., 2011, MNRAS, 413, 643

Richardson, M. L. A., Levesque, E. M., McLinden, E. M., Malhotra, S., Rhoads, J. E., Xia, L., 2013, arXiv e-prints, arXiv:1309.1169

Rigby, J. R., Wuyts, E., Gladders, M. D., Sharon, K., Becker, G. D., 2011, ApJ, 732, 59

Robertson, B. E., Ellis, R. S., Dunlop, J. S., McLure, R. J., Stark, D. P., 2010, Nature, 468, 55

Robertson, B. E., et al., 2013, ApJ, 768, 71

Rousselot, P., Lidman, C., Cuby, J. G., Moreels, G., & Monnet, G., 2000, A&A, 354, 1134

Salim, S., et al., 2007, ApJS, 173, 267

Salpeter, E. E., 1955, ApJ, 121, 161

Santini, P., et al., 2014, A&A, 562, 30

Savaglio, S., et al., 2005, ApJ, 635, 260

Scannapieco, E., Schneider, R., & Ferrara, A., 2003, ApJ, 589, 35

Scarlata, C., et al., 2009, ApJ, 704, L98

Schaerer, D., 2003, A&A, 397, 527

Schaerer, D. & de Barros, S., 2009, A&A, 502, 423

Schenker, M. A., et al., 2012, ApJ, 744, 179

Schenker, M. A., Ellis, R. S., Konidaris, N. P., Stark, D. P., 2013, ApJ, 777, 67

Schlegel, D. J., Finkbeiner, D. P., & Davis, M., 1998, ApJ, 500, 525

Scoville, N., et al., 2007, ApJS, 172, 1

Shapley, A. E., Steidel, C. C., Pettini, M., Adelberger, K. L., 2003, ApJ, 588, 65

Shapley, A. E., Coil, A. L., Ma, C. -P., Bundy, K., 2005, ApJ, 635, 1006

Shapley, A. E., Steidel, C. C., Pettini, M., Adelberger, K. L., & Erb, D. K., 2006, ApJ, 651, 688

Shibuya, T., et al., 2014a, arXiv e-prints, arXiv:1402.1168

Shibuya, T., et al., 2014b, arXiv e-prints, arXiv:1401.1209

Shields, G. A., 1990, ARA&A, 28, 525

Shimasaku, K., et al., 2006, PASJ, 58, 313

Shirazi, M., Brinchmann, J., Rahmati, A., 2013, arXiv e-prints, arXiv:1307.4758

Simpson, C., et al., 2006, MNRAS, 372, 741

Stark, D. P., Ellis, R. S., Chiu, K., Ouchi, M., Bunker, A., 2010, MNRAS, 408, 1628

Stark, D. P., Ellis, R. S., Ouchi, M., 2011, ApJ, 728, L2

Stark, D. P., Schenker, M. A., Ellis, R. S., Robertson, B. E., McLure, R., Dunlop, J., 2013, ApJ, 763, 129

Stasińska, G., 1980, A&A, 84, 320

Steidel, C. C., & Hamilton, D., 1992, AJ, 104, 941

Steidel, C. C., Adelberger, K. L., Shapley, A. E., Pettini, M., Dickinson, M., Giavalisco, M., 2000, ApJ, 532, 170

Steidel, C. C., Pettini, M., Adelberger, 2001, ApJ, 546, 665

Steidel, C. C., Shapley, A. E., Pettini, M., Adelberger, K. L., Erb, D. K., Reddy, N. A., Hunt, M. P., 2004, ApJ, 604, 534

Steidel, C. C., et al., 2010, ApJ, 717, 289

Steidel, C. C., Bogosavljevic, M., Shapley, A. E., Kollmeier, J. A., Reddy, N. A., Erb, D. K., Pettini, M., 2011, ApJ, 736, 160

Storchi-Bergmann, T., Calzetti, D., Kinney, A. L., 1994, ApJ, 429, 572

Suzuki, R., et al., 2008, PASJ, 60, 6

Tacconi, L. J., et al., 2010, Nature, 463, 781

Tacconi, L. J., et al., 2013, ApJ, 768, 74

Takahashi, M. I., et al., 2007, ApJS, 172, 456

Tanaka, I., et al., 2011, PASJ, 63, 415

Taniguchi, Y., et al., 2009, ApJ, 701, 915

Tapken, C., Appenzeller, I., Noll, S., Richling, S., Heidt, J., Meinköhn, E., Mehlert, D., 2007, A&A, 467, 63

Taylor, E. N., et al., 2009, ApJS, 183, 295

Teplitz, H. I., Collins, N. R., Gardner, J. P., Hill, R. S., & Rhodes, J., 2003, ApJ, 589, 704

Terlevich, E., Díaz, A. I., Terlevich, R., Vargas, M. L. G., 1993, MNRAS, 260, 3

Tilvi, V., Malhotra, S., Rhoads, J. E., Scannapieco, E., Thacker, R. J., Ilev, I. T., & Mellema, G., 2009, ApJ, 704, 724

Tilvi, V., Scannapieco, E., Malhotra, S., & Rhoads, J. E., 2011, MNRAS, 418, 2196

Tremonti, C. A., Heckman, T. M., Kauffmann, G., et al., 2004, ApJ, 613, 898

Tresse, L., Maddox, S. J., Le Fèvre, O., & Cuby, J. -G., 2002, MNRAS, 337, 369

Ueda, Y., et al., 2008, ApJS, 179, 124

van der Wel, A., et al., 2011, ApJ, 742, 111

van Dokkum, P. G., 2001, PASP, 113, 1420

van Dokkum, P. G., Conroy, C., 2010, Nature, 468, 940

Vanzella, E., et al., 2009, ApJ, 695, 1163

Vanzella, E., et al., 2010, ApJ, 725, 1011

Vanzella, E., et al., 2011, ApJ, 730, L35

Verhamme, A., Schaerer, D., Maselli, A., 2006, A&A, 460, 397

Verhamme, A., et al., 2012, A&A, 546, A111

Viilar-Martín, M., Cerviño, M., Delgado, G., 2004, MNRAS, 355, 1132

Wuyts, E., Rigby, J. R., Sharon, K., Gladders, M. D., 2012, ApJ, 755, 73

Yabe, K., et al., 2012, PASJ, 64, 60

Yagi, M., Kashikawa, N., Sekiguchi, M., Doi, M., Yasuda, N., Shimasaku, K., & Okamura, S., 2002, AJ, 123, 66

Yajima, H., Li, Y., Zhu, Q., Abel, T., Gronwall, C., Ciardullo, R., 2012, ApJ, 754, 118

Yajima, H., & Li, Y., 2013, MNRAS accepted, arXiv:1211.0088

Yamada, T., Nakamura, Y., Matsuda, Y., Hayashino, Y., Yamauchi, R., Morimoto, N., Kousai, K., Umemura, M., 2012, ApJ, 143, 79

Yan, H., et al., 2005, ApJ, 634, 109

York, D. G., et al., 2000, AJ, 120, 157

Yoshikawa, T., et al., 2010, ApJ, 718, 112

Yuma, S., et al., 2010, ApJ, 720, 1016

Zahid, H. J., Kewley, L. J., & Bresolin, F., 2011, ApJ, 730, 137

Zheng, Z., Wallace, J., 2013, arXiv e-prints, arXiv:1308.1405

A The $z = 2.2$ LAE Sample

In this chapter, we summarize the $z = 2.2$ LAE sample provided by our custom narrowband NB387 survey with Subaru/Suprime-Cam (Miyazaki et al. 2002). LAEs are thought to be low-mass, young galaxies with a moderate SFR as suggested from their small size, faint continua, and so on (e.g., Bond et al. 2009; Ono et al. 2010a; Finkelstein et al. 2011) compared with other high-z populations. Therefore, LAEs provide us with the opportunity to explore parameter space in the $M_\star$–Z relation and the FMR, and to study the diversity of high-z galaxies. We conducted NB387 imaging observation with five blank fields: the Subaru/XMM-Newton Deep Survey (SXDS) field (Furusawa et al. 2008), the COSMOS field (Scoville et al. 2007), the Chandra Deep Field South (CDFS; Giacconi et al. 2001), the Hubble Deep Field North (HDFN; Capak et al. 2004), and the SSA22 field (e.g., Steidel et al. 2000). The Great Observatories Origins Deep Survey (GOODS; e.g., Dickinson et al. 2003) South and North, named GOODS-S and GOODS-N, are included and centered on the CDFS and HDFN, respectively.

We summarize the NB387 survey in Section A.1, and show the details of the selection methods, the constructed sample of the $z = 2.2$ LAEs, and spectroscopic follow-up observations (if available) in each field in Sections A.2. Estimations of physical properties of the LAEs are presented in the following two Appendices.

A.1. NB387 Data Summary

A.1.1. Observation

We carried out NB387 imaging observations with Subaru/Suprime-Cam of the SXDS, COSMOS, CDFS, HDFN, and SSA22 on 2009 July 20, December 14–16 and 19–20 (HST). The SXDS field is covered by deep Suprime-Cam broadband data in five pointings with small overlaps; these five "sub-fields" are named SXDS-C, -N, -S, -E, and -W, respectively, after their relative positions on the sky (Furusawa et al. 2008). We thus have NB387 imaging for in total nine pointings of Suprime-Cam. Table A.1 summarizes details of the observations. For photometric calibration, we observed spectrophotometric standard stars Feige34, LDS749B, and G93-48 (Oke 1990). Each standard star was observed twice or more under photometric condition with airmasses of 1.1–1.3.

A.1.2. Data Reduction

We used the Suprime-Cam Deep Field Reduction package (Yagi et al. 2002; Ouchi et al. 2004) to reduce the NB387 data. The data reduction process included bias subtraction, flat fielding, distortion

Table A.1. Summary of NB387 Imaging Data in the SXDS field

Field	Exp. Time (1)	PSF (2)	Area (3)	Limit Mag (4)	Date
SXDS-C	3.2 [9]	0.88	587 [41]	25.7	2009 Dec 14–16
SXDS-N	2.5 [5]	0.70	409 [159]	25.6	2009 Dec 16
SXDS-S	2.5 [5]	0.85	775 [344]	25.7	2009 Dec 16
SXDS-E(5)	3.3 [10]	1.95	···	···	2009 Dec 19, 20
SXDS-W	1.8 [5]	1.23	232 [122]	25.1	2009 Dec 16, 19
COSMOS	4.5 [9]	0.97	845 [109]	26.1	2009 Dec 14–16
CDFS (GOODS-S)	8.0 [16]	0.85	882 [50]	26.4	2009 Dec 14–15
HDFN (GOODS-N)	9.3 [20]	0.90	913 [134]	26.5	2009 Dec 14–16
SSA22	1.0 [3]	0.91	800 [239]	24.9	2009 Jul 20

Note: (1) Total exposure times (hour). The value in square brackets shows the numbers of exposures that are combined. (2) FWHM of PSFs of the stacked image that are registered with broadband images (arcsec). (3) Effective area that is used for the selection (arcmin^2). The value in square brackets shows the area with low-S/N, where the limiting magnitudes are 0.4–0.5 mag shallower than the values listed in the next column. (4) Limiting magnitude derived from 5σ sky noise in a $2''$ diameter aperture. Note that the limiting magnitude in the SXDS-W is defined in a $2''.5$ diameter aperture. (5) The SXDS-E has large PSF size and is not included in the following analysis. So, we do not report the limiting magnitude and covered area in this field.

correction, cosmic-ray rejection, sky subtraction, bad pixel/satellite trail masking, image shifting, and stacking. For cosmic-ray rejection, we used LA.COSMIC (van Dokkum 2001). After the stacking process, our image were registered with the broadband images in each field. using bright stellar objects commonly detected in the NB387 and the broadband images. The reduced and registered NB387 images are shown in Figures A.1–A.5.

A.1.3. Data Quality

The point-spread-function(PSF) sizes of the registered images are $0''.70 - 1''.2$, except for the SXDS-E data. The SXDS-E has large PSF size of $\sim 2''$ and is not included in the following analysis. The 5σ detection limits in a $2''$ diameter aperture[A.1] are $25.1 - 25.7$ mag in SXDS, 26.1 in COSMOS, 26.4 in GOODS-S, 26.5 in GOODS-N, and 24.9 in SSA22 fields. These values are estimated without using the edges of the images, where signal-to-noise (S/N) ratios are significantly low due to dithering. However, we include those low-S/N regions to increase the number of LAEs, setting brighter limiting magnitudes (0.4–0.5 mag) according to the S/N ratios. The limiting magnitudes are estimated in the same manner as in Furusawa et al. (2008); we spread 5,000 $2''.0$ diameter apertures over the entire image randomly after masking detected objects, and measure their photon counts. We then fit the negative part of the histogram of the counts with Gaussian, and regard its σ as the 1σ sky fluctuations of the image for $2''.0$ diameter apertures. The limiting magnitudes which appear in the following sections are also estimated in the same manner.

[A.1] We use a $2''.5$ diameter aperture in the SXDS-W due to the bad PSF size.

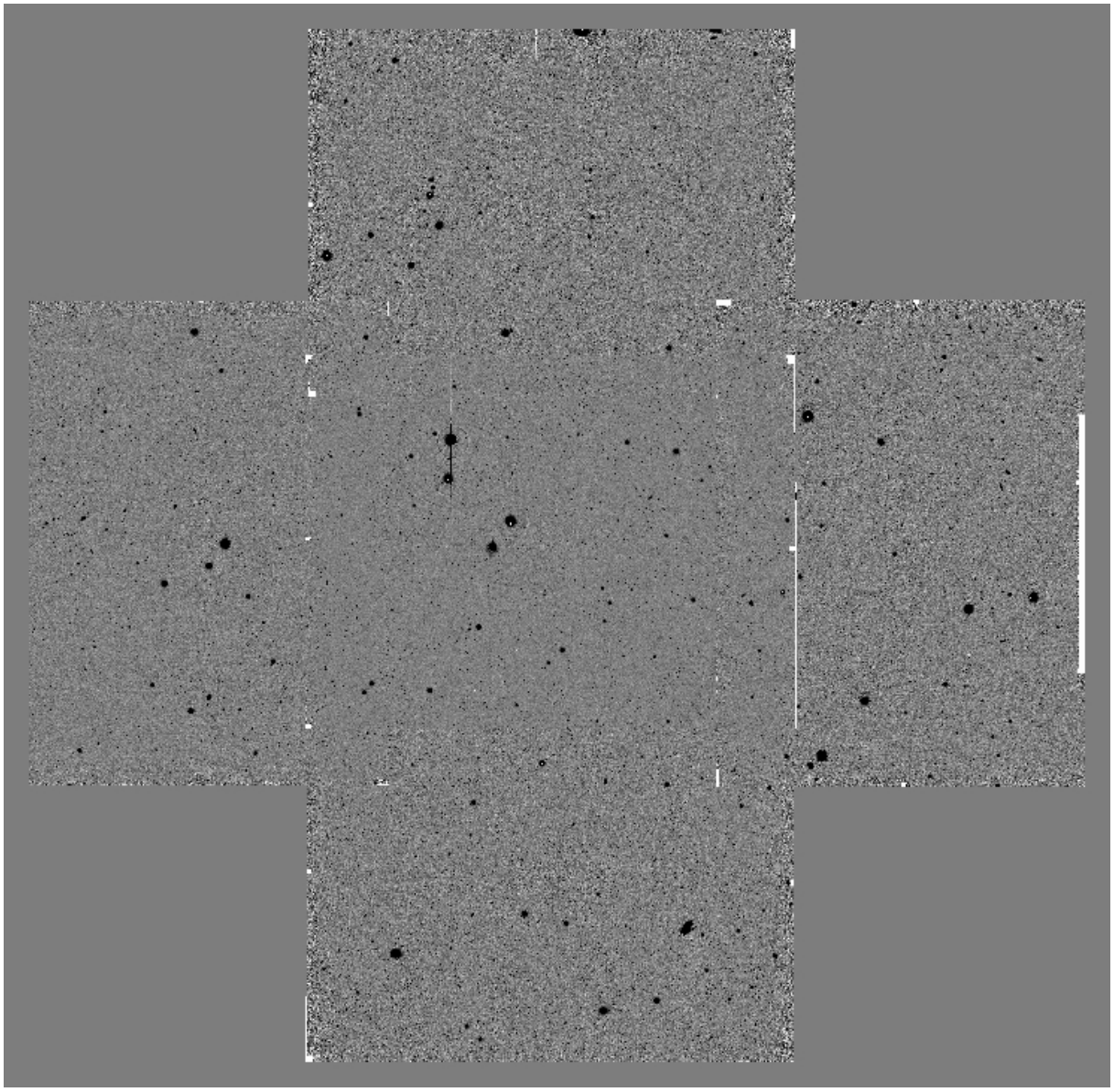

Figure A.1. The reduced NB387 image of the SXDS field. The five sub-fields are co-added according to their registered WCS. North is up and east is to the left.

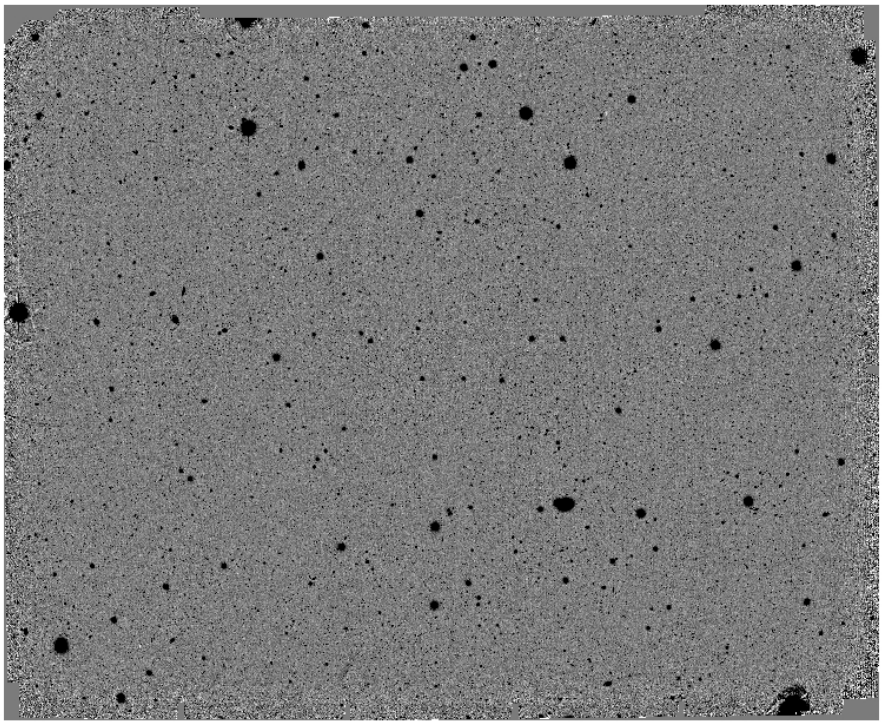

Figure A.2. The reduced NB387 image of the COSMOS field. North is up and east is to the left.

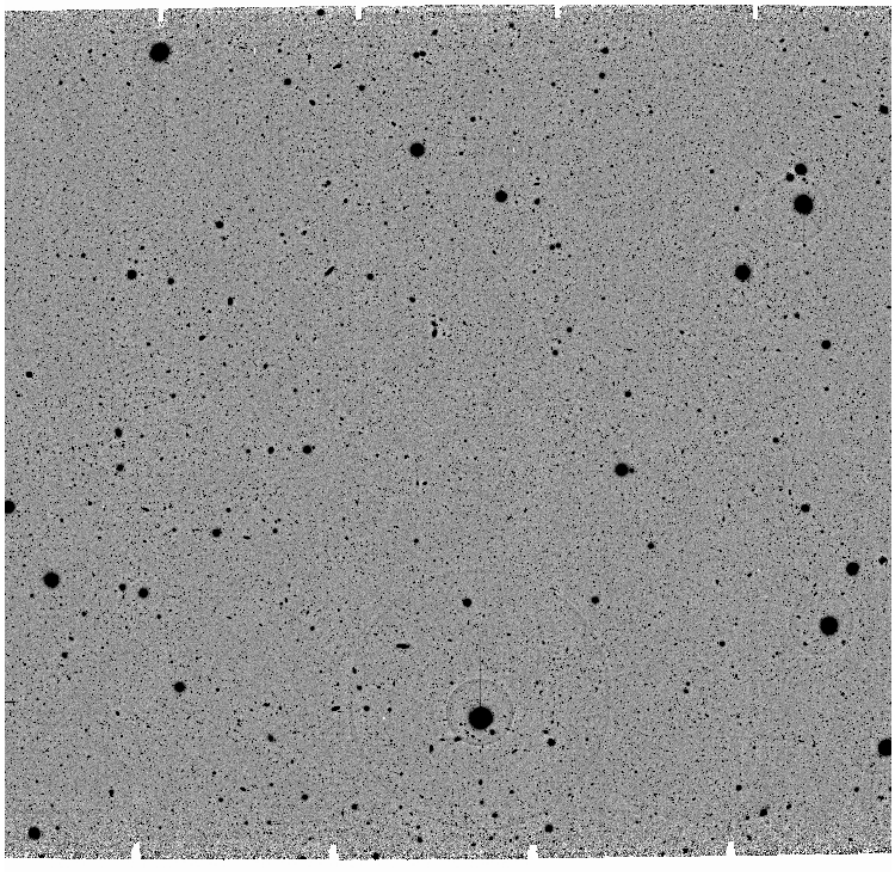

Figure A.3. The reduced NB387 image of the CDFS field. North is up and east is to the left.

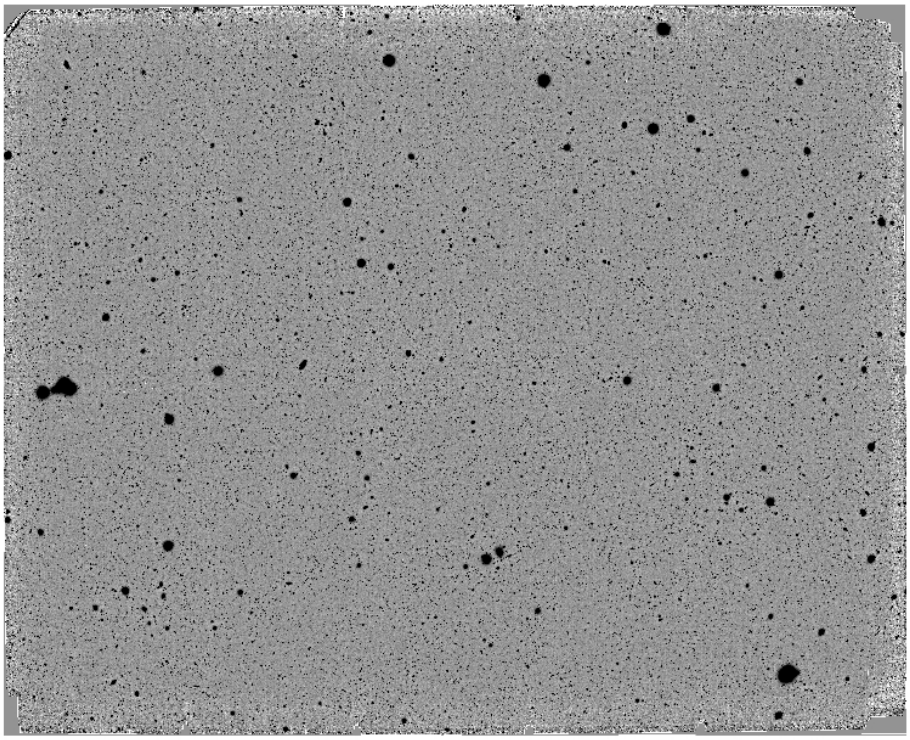

Figure A.4. The reduced NB387 image of the HDFN field. North is up and east is to the left.

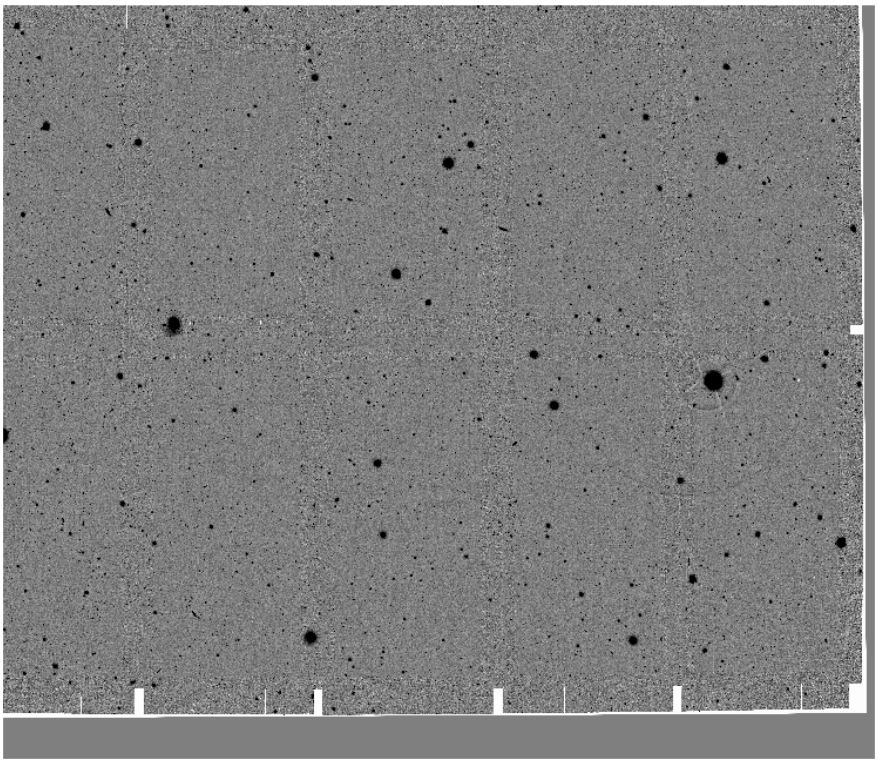

Figure A.5. The reduced NB387 image of the SSA22 field. North is up and east is to the left.

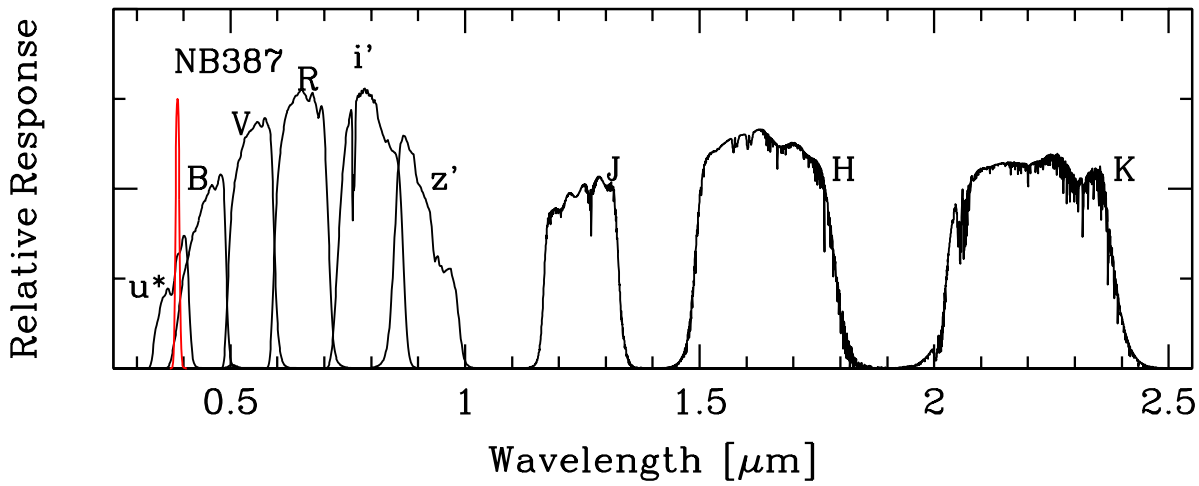

Figure A.6. Relative response curves of the optical and NIR broadband filters of CFHT *, Subaru B, V, R, i', z' and UKIRT/WFCAM J, H, K (black). The red curve shows the NB387 response curve. The responses include the throughputs of the instrument and the telescope as well as atmospheric absorption.

We infer the errors in photometric zero points of our NB387 images from a comparison of colors (e.g., u^*-NB387 and $B-$NB387 in SXDS) of stellar objects in the images with those of 175 Galactic stars calculated from Gunn & Stryker (1983)'s spectrophotometric atlas. The estimated errors are less than 0.05 mag, which are small enough for our study.

A.2. Photometric Samples of LAEs at $z = 2.2$

We describe the photometric samples of $z = 2.2$ LAEs in each field below. First we show the broadband data used in the field. We then describe how to select $z = 2.2$ LAEs. As an example, we show the procedure in the SXDS field in detail.

A.2.1. SXDS

We select LAEs in a $2,003$ $(= 587 + 409 + 775 + 232)$ arcmin^2 region which is covered by all the three passbands for selecting LAEs: NB387, u^*, and B.

A.2.1.1. Broadband Images

The optical broadband data are required not only for selecting LAEs but also for performing SED fitting to infer the LAEs' stellar populations. We use the publicly available B, V, R, i', and z' data taken with Subaru/Suprime-Cam by the SXDS project (Furusawa et al. 2008), and the u^* data taken with CFHT/MegaCam as part of the UKIDSS/UDS project (Foucaud et al. in preparation). As for the NIR broadband data, the UKIDSS/UDS project provides deep J, H, and K images of UKIRT/WFCAM (Lawrence et al. 2007). In this thesis, we use the data release 8 (DR8) images. We also use Spitzer/IRAC 3.6, 4.5, 5.8, and 8.0 μm photometry from the Spitzer legacy survey of the UDS field (SpUDS) so that stellar population parameters be well constrained.

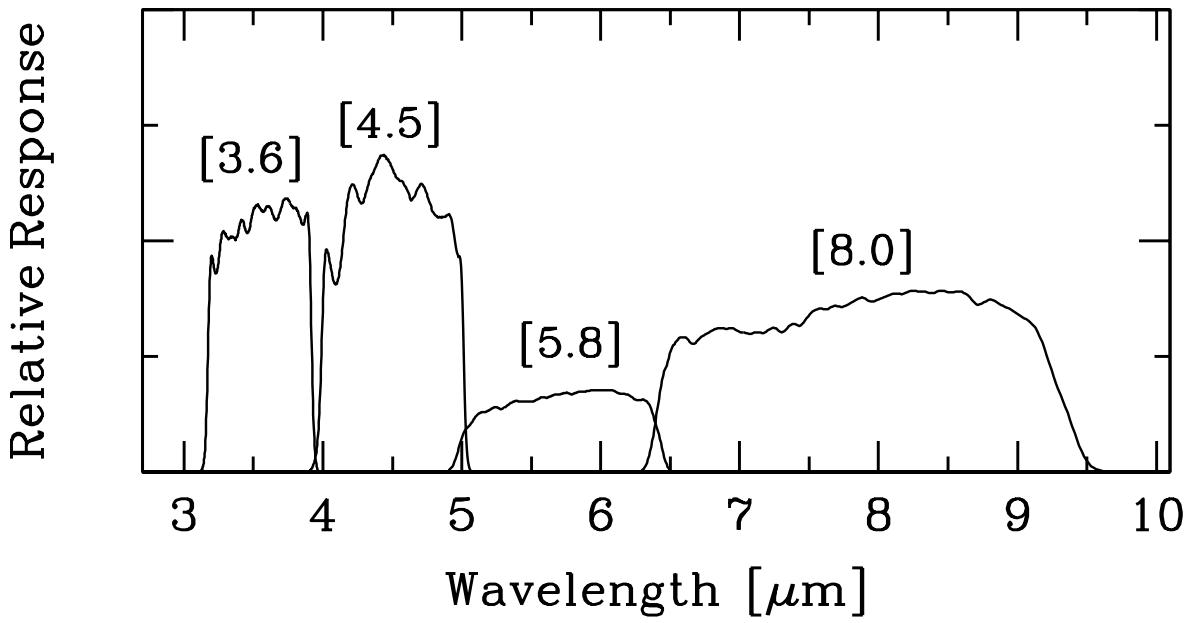

Figure A.7. Relative response curves of the 4 channels of Spitzer/IRAC.

Table A.2. Summary of Optical and NIR Broadband Imaging Data in the SXDS Field

Band	Observatory	PSF (1)	Limit Mag (2)	Reference (3)
$u^{*(4)}$	CFHT	0.85	26.9	(a)
B	Subaru	0.78–0.84	27.5–27.8	(b)
V	Subaru	0.72–0.82	27.1–27.2	(b)
R	Subaru	0.74–0.82	27.0–27.2	(b)
i'	Subaru	0.68–0.82	26.9–27.1	(b)
z'	Subaru	0.70–0.76	25.8–26.1	(b)
$J^{(4)}$	UKIRT	0.81	24.8	(c)
$H^{(4)}$	UKIRT	0.81	24.1	(c)
$K^{(4)}$	UKIRT	0.81	24.6	(c)

Note: (1) PSF size is defined as an FWHM of point sources (arcsec). (2) The limiting magnitude (5σ) estimated by $2''$ diameter random aperture photometry. (3) (a) S. Foucaud et al. (in preparation); (b) Furusawa et al. (2008); (c) Lawrence et al. (2007); see also `http://www.ukidss.org/`. (4) The u^* image covers the same area of the UKIDSS/UDS project which corresponds to about 77 % of the SXDS-C, -N, -S, -E, and -W.

Table A.2 summarizes the details of the broadband data. The passbands of optical and NIR broadband images are shown in Figure A.6, and IRAC 4 channels in Figure A.7.

A.2.1.2. Object Detection and Candidate Selection

We use the SExtractor software (Bertin & Arnouts 1996) to perform source detection and photometry. We run SExtractor in double-image mode, with the NB387 image used as the detection image. We identify sources with 5 adjoining pixels and brightness above $> 2\sigma$ of the sky background. The diameter to define aperture magnitudes is set to $2\farcs5$ for the SXDS-W and $2\farcs0$ for the other sub-fields. We use aperture magnitudes to calculate colors, and adopt `MAG_AUTO` for the total magnitude. All magnitudes are corrected for Galactic extinction of $E(B-V) = 0.020$ (Schlegel et al. 1998). The NB387-detection catalog contains 42,995 objects with aperture magnitudes brighter than the 5σ sky noise.

We select LAE candidates on the u^*-NB387 vs. $B-$NB387 color plane (top panel in Figure A.8). In this figure, colors of model galaxies and Galactic stars are plotted in order to define the selection criteria for LAEs. The tracks indicate the colors of model galaxies redshifted from 0.00 to 3.50 with a step of $\Delta z = 0.01$. We assume the intergalactic medium (IGM) attenuation model of Madau (1995). Base on Figures A.8, we define the color criteria of $z \sim 2.2$ LAEs as:

$$u^* - \mathrm{NB387} > 0.5 \;\&\&\; B - \mathrm{NB387} > 0.2, \tag{A.1}$$

which select LAEs with $\mathrm{EW_{rest}} \gtrsim 30$ Å. The 2σ photometric errors in u^*-NB387 for the faintest objects (NB387=25.7) in our NB387-detected catalog are $\simeq 0.5$ mag. Thus, the criterion of u^*-NB387> 0.5 ensures that the contamination fraction in our LAE sample due to photometric errors is sufficiently low. We use 2σ limiting magnitudes instead when an object is not detected in u^* or B at 2σ level. The selection criteria require NB387 magnitude significantly brighter than both u^* and B magnitudes, which results in small number of non-emitters in the sample.

Using Equation (A.1), we identify 1,044 LAE candidates in the NB387 detected catalog. These candidates are contaminated by spurious objects and foreground and background interlopers. We remove those contaminants by the procedures described in the next two subsections.

A.2.1.3. Rejection of Spurious Objects

Given the limited number of ditherings in our NB387 imaging ($\sim 4-5$), a clipped-mean stacking fails to completely remove the remaining cosmic rays which survived LA.COSMIC rejection on individual dithered images. Since cosmic rays have steeper light profiles than the PSF, we removed 21 sources with FWHMs significantly smaller than the PSF. We then perform visual inspection on all the remaining objects, and eliminate 90 obvious spurious sources such as ghosts due to bright stars and bad pixels.

A.2.1.4. Identification of Interlopers

In addition to LAEs, other emission line objects, such as [O II] emitters at $z \simeq 0.04$, Mg IIλ2798 emitters at $z \simeq 0.4$, and CIVλ1550 emitters at $z \simeq 1.5$, may be included in our sample. Our survey area, 2,003 arcmin^2, corresponds to 400 Mpc^3 for [O II] emitters, which is two orders of magnitude smaller than the volume sampled by Lyα emitters (48,100 Mpc^3). The number of [O II] emitters is therefore expected to be small.

To remove [O II] emitters from our sample, we use the Galaxy Evolution Explorer (GALEX) NUV ($\lambda_c = 2267$ Å, FWHM = 616 Å) and FUV ($\lambda_c = 1516$ Å, FWHM = 269 Å) data. Real LAEs in our sample will be invisible in these data, since these two passbands are located shortward of the Lyman break at $z \sim 2.2$. Thus, objects visible in either of the two GALEX band data are likely to be [O II]

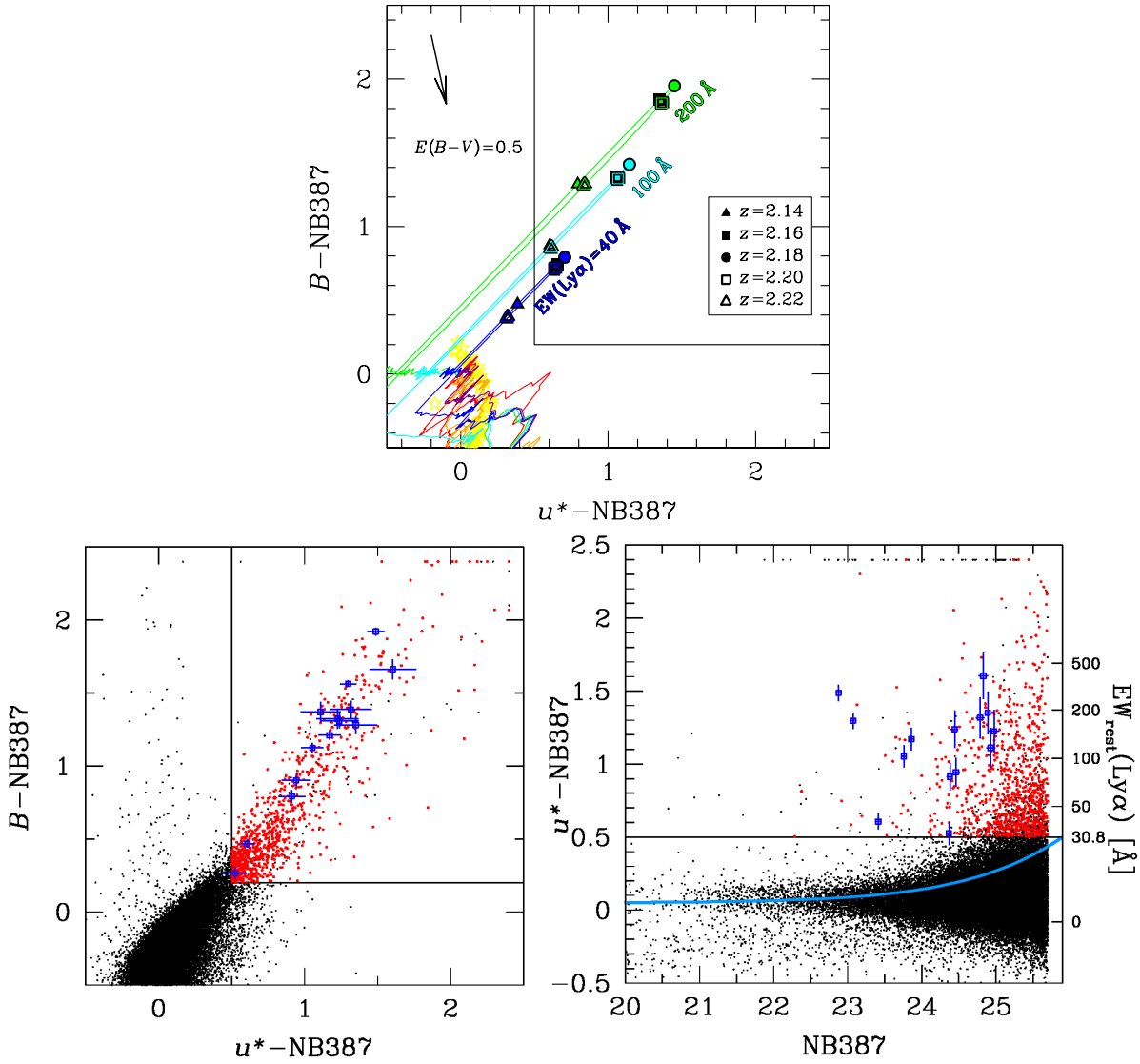

Figure A.8. *Top:* $B-$NB387 vs. u^*-NB387 plane for selection of LAEs at $z \simeq 2.2$ in SXDS. The solid lines in various colors indicate tracks of model galaxies redshifted from 0 to 3.5 with and without Lyα emission: purple: simple stellar population with an age of 0.03 Gyr; green, cyan, and blue: simple stellar population with Lyα emission of $\mathrm{EW_{rest}} = 200, 100$, and 40 Å, respectively. The symbols on the tracks of model galaxies with Lyα emission correspond to $z = 2.14$ (filled triangles), 2.16 (filled squares), 2.18 (filled circles), 2.20 (open squares), and 2.22 (open triangles). The red and orange solid lines represent tracks of elliptical and spiral galaxies from the SWIRE template library (Polletta et al. 2007), respectively. The yellow stars show Galactic stars from Gunn & Stryker (1983). The tilted arrow indicates the reddening effect in the case of $E(B-V) = 0.5$ (Calzetti et al. 2000) for $z \sim 2$ galaxies. The objects that are located in the area enclosed by the solid black lines are considered to be LAE candidates. *Bottom Left:* Distribution of NB387-detected objects in the $B-$NB387 vs. u^*-NB387 plane. The black dots indicate all the detected objects, while the red dots show LAE candidates after removing spurious objects and interlopers. The blue open squares with errorbars show spectroscopically confirmed LAEs. For the purpose of display, objects whose u^*-NB387 colors exceed 2.4 are plotted at $u^*-\mathrm{NB387} = 2.4$. *Bottom Right:* Distribution of NB387-detected objects in the u^*-NB387 vs. NB387 plane. The symbols and colors are the same as those in the left panel. The horizontal solid line shows the selection threshold of u^*-NB387 and the blue curve indicates the 2σ photometric error in u^*-NB387 for sources with $u^*-\mathrm{NB387} = 0.05$, which is the average u^*-NB387 color of all the objects. The right y axis shows the rest-frame Lyα equivalent width of $z = 2.18$ LAEs with u^*-NB387 color corresponding to the left y axis. For the purpose of display, objects whose u^*-NB387 colors exceed 2.4 are plotted at $u^*-\mathrm{NB387}= 2.4$.

Table A.3. Properties of the IMACS spectroscopic sample

ID	RA (1)	Dec. (1)	mag(NB387) (2)	$\lambda_{\rm obs}$ (3)	z (4)	flag (5)
SXDS1-04640	02:18:48.968	−05:09:00.32	23.07 ± 0.02	3862.83	2.1767	b
SXDS1-07673	02:18:56.532	−05:05:48.41	24.98 ± 0.07	3853.55	2.1690	c
SXDS1-08099	02:19:05.729	−05:05:23.86	24.79 ± 0.05	3889.02	2.1982	c
SXDS1-08204	02:18:57.385	−05:05:18.82	24.46 ± 0.05	3895.63	2.2036	b
SXDS1-08321	02:19:05.279	−05:05:11.22	24.89 ± 0.06	3891.62	2.2003	b
SXDS1-09219	02:19:02.396	−05:04:19.27	24.37 ± 0.04	3890.03	2.1990	c
SXDS1-09951	02:18:50.038	−05:03:34.09	24.38 ± 0.04	3901.78	2.2087	b
SXDS1-11135	02:18:37.381	−05:02:24.61	23.86 ± 0.03	3882.13	2.1925	b
SXDS1-12596	02:18:55.071	−05:00:58.82	24.83 ± 0.06	3886.29	2.1960	c
SXDS1-16564	02:19:09.542	−04:57:13.32	22.88 ± 0.03	3861.44	2.1755	a

Note: (1) Coordinates are in J2000. (2) NB387 magnitudes with $2''$ diameter apertures. (3) Central wavelengths of observed Lyα lines (Å). We perform a Gaussian fitting to each detected line using MPFIT, and derive the central wavelengths. (4) Redshifts of Lyα lines estimated from the central wavelengths. (5) Flags of reliability of the lines by inspecting the 2D spectra by eye: "a" secure, "b" likely, "c" tentative.

emitters. Although some studies have shown that ionizing photons are more likely to escape from Lyα selected galaxies than from UV-selected galaxies (e.g., Iwata et al. 2009; Nestor et al. 2011, 2013), the estimated UV-to-Ly-continuum flux density ratio is $\gtrsim 2$ even for LAEs (Nestor et al. 2011), therefore the Ly-continuum of $z \sim 2$ LAEs is expected to be fainter than the UV continuum by ~ 1 mag or more. Since the detection limit of the GALEX images is ~ 24 (3σ) both in NUV and FUV, LAEs fainter than $V \sim 23$ should be invisible in the GALEX images. We find 12 objects which have a counterpart in either of the NUV or FUV image within $3''$ from the NB387 position. Among them, 4 are fainter than $V = 23$, thus to be inferred to be interlopers. The remaining eight are brighter than $V = 23$, and their GALEX magnitudes are also bright enough to be consistent with them being interlopers. Indeed, all eight are also detected as an X-ray or radio source as described in the next paragraph. We thus remove these 12 objects from the sample.

For Mg II and C IV emitters, we use X-ray and radio imaging data, since both emitters selected by Equation (A.1) should have large EWs ($\mathrm{EW_{rest}} \gtrsim 30$ Å) and thus they are likely to be AGNs. For X-ray data, we use the *XMM-Newton* $0.2 - 10.0$ keV band source catalog by Ueda et al. (2008). For radio data, we use the Very Large Array (VLA) 1.4 GHz source catalog by Simpson et al. (2006). After removing some confused objects by visual inspection, we find 11 (1) LAE candidates with an X-ray (radio) counterpart. The number of likely Mg II or C IV emitters is thus 12. Note that 10 out of the 12 are also detected in the GALEX data.

After removing spurious objects and obvious [O II] and C IV emitters, we have 919 $(= 1,044 - (21 + 90) - (12 + 12 - 10))$ LAE candidates. We plot all the candidates on the u^*-NB387 vs. $B-$NB387 two color plane in the bottom left panel of Figure A.8 and on the u^*-NB387 vs. NB387 color-magnitude plane in the bottom right panel of Figure A.8. These plots show that the candidates (red dots) are placed

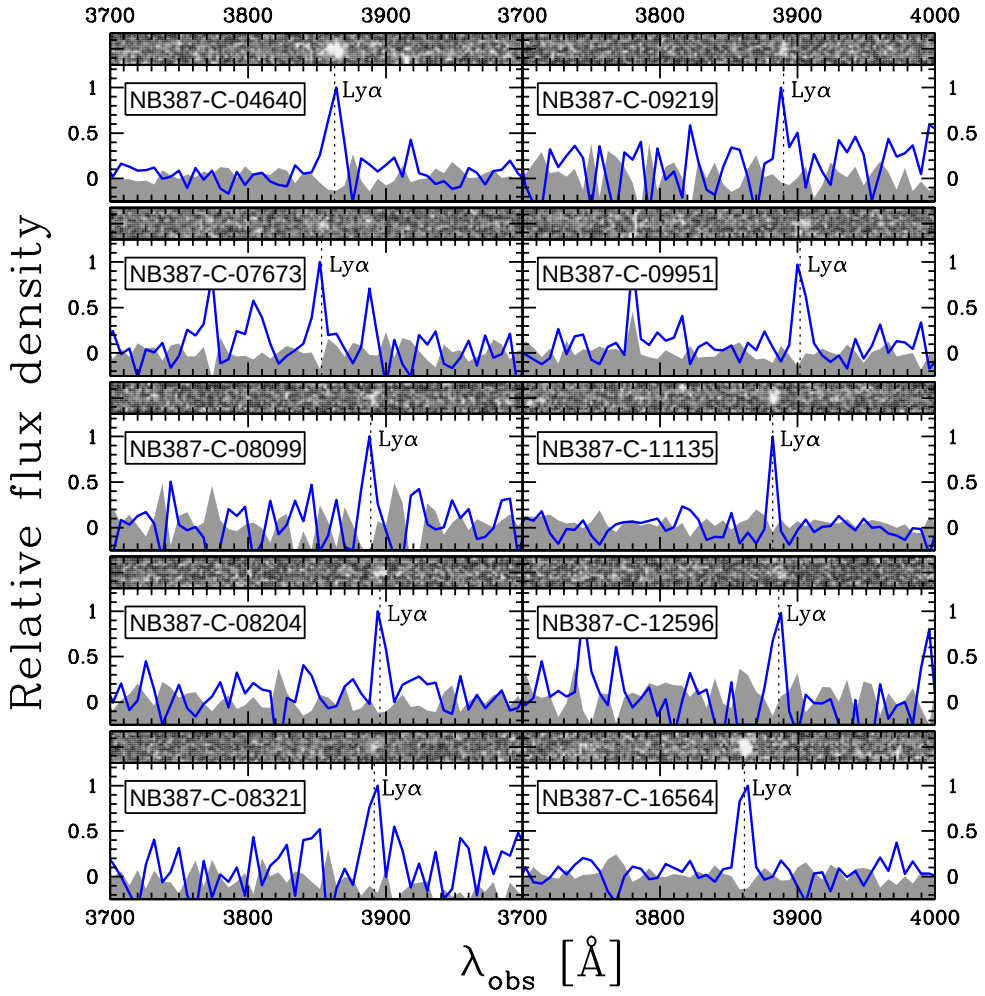

Figure A.9. IMACS spectra of ten confirmed LAEs. For each object, the top panel shows the 2*D* spectrum, while the bottom panel showing the 1D spectrum (blue line) and the sky background (gray shaded area), both of which have been smoothed with a 3 pixel boxcar filter and arbitrarily normalized.

in the isolated region away from the locus of other galaxies and Galactic stars.

A.2.1.5. Follow-up Spectroscopy Data

We carried out follow-up spectroscopy of 30 objects selected from the whole sample ($N = 919$) so that they are distributed in wide ranges of NB387 magnitudes and u^*-NB387 colors. The observations were made with the Inamori Magellan Areal Camera and Spectrograph (IMACS; Dressler et al. 2006) on the Magellan telescope using the 300 lines mm^{-1} grism and the WB3600 – 5700 filter on 2010 July 9-10 under photometric conditions. We used the $f/4$ camera, which has a better sensitivity than the $f/2$ camera at short wavelengths. The total throughput of the $f/4$ camera with the 300 lines mm^{-1} grism at 3870Å is 6.2 %, while that of the $f/2$ camera is 2.6 %. The on-source exposure time was 13,700 seconds, with a seeing size of $0\farcs48 - 0\farcs63$. We chose a $0\farcs8$ slit width, which gives a resolving power of $R \sim 700$ around 4000 Å. The COSMOS pipeline was used for data reduction.

By inspecting the reduced spectra by eye, we detected an emission line around 3870 Å for ten objects, while the remaining 20 had no visible emission line. The main reason for this low detection rate is the

Table A.4. Properties of the LRIS spectroscopic sample in the SXDS field (Shibuya et al. 2014a)

ID	RA	Dec.	mag(NB387)	$\lambda_{\rm obs}$	z
	(1)	(1)	(2)	(3)	(4)
SXDS1-06713	02:17:41.397	−05:06:49.08	23.76 ± 0.03	3894.18	2.2033
SXDS1-10535	02:17:41.922	−05:02:55.87	24.93 ± 0.06	3903.62	2.2111
SXDS1-10600	02:17:46.092	−05:02:54.97	23.41 ± 0.03	3887.51	2.1978
SXDS1-10942	02:17:59.542	−05:02:34.36	24.44 ± 0.05	3905.50	2.2126

Note: (1) Coordinates are in J2000. (2) NB387 magnitudes with $2''$ diameter apertures. (3) Central wavelengths of observed Lyα lines (Å). (4) Redshifts of Lyα lines estimated from the central wavelengths.

bright limiting flux of our observation due to the low sensitivity below 4000 Å and the relatively short exposure time. Indeed, all ten objects with line emission are brighter than NB387 = 25.0, and the success rate limited to NB387 < 25.0 (13 objects in total) is found to be $10/13 = 77\,\%$. Among the remaining three bright objects, two have NB387$\simeq 25.0$ and may be marginally undetected. The other one object has NB387 $= 24.4$, but smaller Lyα flux expected from its u^*-NB387 compared with the confirmed candidates. The spectra of the ten confirmed LAEs are shown in Figure A.9, and the NB387 magnitudes and Lyα-based redshifts are given in Table A.3.

The ten objects are not [O II] emitters at $z \simeq 0.04$ because of the lack of [O III]λ5007 line at the corresponding wavelength, $\simeq 5200$ Å. They are not AGNs either, with Mg II emission at $z \simeq 0.4$ or CIV emission at $z \simeq 1.5$, because of the absence of emission lines at $3600 - 5700$ Å (e.g., Mg II: [O II] line at $\simeq 5150$ Å, CIV: He IIλ1640 line at $\simeq 4100$ Å and C III]λ1909 line at $\simeq 4770$ Å) and because we have removed AGN candidates from the sample in advance (see §A.2.1.4). Therefore, we conclude that all ten objects are LAEs at $z \simeq 2.2$. This demonstrates that the contamination in our LAE sample is very low, at least for bright objects.

In addition to the IMACS observation, we performed a follow-up spectroscopy observation with Low Resolution Imaging Spectrometer (LRIS; Oke et al. 1995) on Keck I. The observation was made on 2012 March 19–21 and November 14–15. The SXDS mask observation was performed in November 14–15. We used the blue channel of LRIS with the 600 groove mm^{-1} grism blazed at 4000 Å for the SXDS mask. With the $1\farcs0$ slits used in the mask, the spectral resolution in the blue was ~ 4 Å FWHM, corresponding to $R \sim 1000$ for the wavelengths of Lyα emission of $z = 2.2$ LAEs. The on-source exposure time was 40,854 seconds, with a seeing size of $\sim 1\farcs0$. The bulk of the LRIS data reduction was done with the XIDL/Low-Redux package[A.2]. By inspecting the reduced spectra, we detected Lyα emission line for additional four objects. Table A.4 summarizes the LAEs with NB387 magnitude and Lyα-based redshift. They are also plotted as the spectroscopically confirmed LAEs in Figure A.8 (blue open squares). More detailed analysis regarding the LRIS spectra are given in Shibuya et al. (2014a).

[A.2] `http://www.ucolick.org/~xavier/LowRedux/`

Table A.5. Summary of Optical and NIR Broadband Imaging Data in the COSMOS Field

Band	Observatory	PSF (1)	Limit Mag (2)	Reference (3)
u^*	CFHT	0.90	27.2	(a)
B	Subaru	0.95	27.5	(b)
V	Subaru	1.32	26.8	(b)
r'	Subaru	1.04	26.8	(b)
i'	Subaru	0.95	26.3	(b)
z'	Subaru	1.14	25.4	(b)
J	UKIRT	1.74	22.7	(c)
H	CFHT	0.75	22.1	(a)
K_S	CFHT	0.68	23.2	(a)

Note: (1) PSF size is defined as an FWHM of point sources (arcsec). (2) The limiting magnitude (5σ) estimated by $2''$ diameter random aperture photometry. (3) (a) `http://irsa.ipac.caltech.edu/data/COSMOS/images/cfht/`; (b) `http://irsa.ipac.caltech.edu/data/COSMOS/images/subaru/`; (c) `http://irsa.ipac.caltech.edu/data/COSMOS/images/ukirt/`.

A.2.2. COSMOS

A.2.2.1. Broadband Images

We use the publicly available u^* data taken with CFHT/MegaCam, B, V, r', i', and z' data with Subaru/Suprime-Cam, J data with UKIRT/WFCAM, H and K_S data with CFHT/WIRCAM. We also use Spitzer/IRAC 3.6, 4.5, 5.8, and 8.0 μm data. All data are collected from the COSMOS Archive[A.3]. Table A.5 summarizes the details of the broadband data. The passbands of optical and NIR broadband images are shown in Figure A.10.

A.2.2.2. Candidate Selection

We select LAE candidates in the same manner as done in the SXDS field (Section A.2.1). We perform source detection and photometry with $2''$ diameter apertures. All magnitudes are corrected for Galactic extinction of $E(B-V) = 0.018$ (Schlegel et al. 1998). The NB387-detection catalog contains 31,401 objects with aperture magnitudes brighter than the 5σ sky noise.

Since the u^* and B-band are the same as used in the SXDS field, we adopt the the same criteria for the LAE selection of Equation (A.1; see also the top panel of Figure A.8). After removing spurious objects and obvious [O II] and CIV emitters[A.4] in the same manner as in Sections A.2.1.3 and A.2.1.4, we have 619 LAE candidates. We plot the candidates on the u^*-NB387 vs. $B-$NB387 two color plane and on the u^*-NB387 vs. NB387 color-magnitude plane in the left and right panels of Figure A.11, respectively.

[A.3] `http://irsa.ipac.caltech.edu/data/COSMOS/`

[A.4] We have 23 emitters with GALEX, X-ray, and/or 1.4 GHz radio detections.

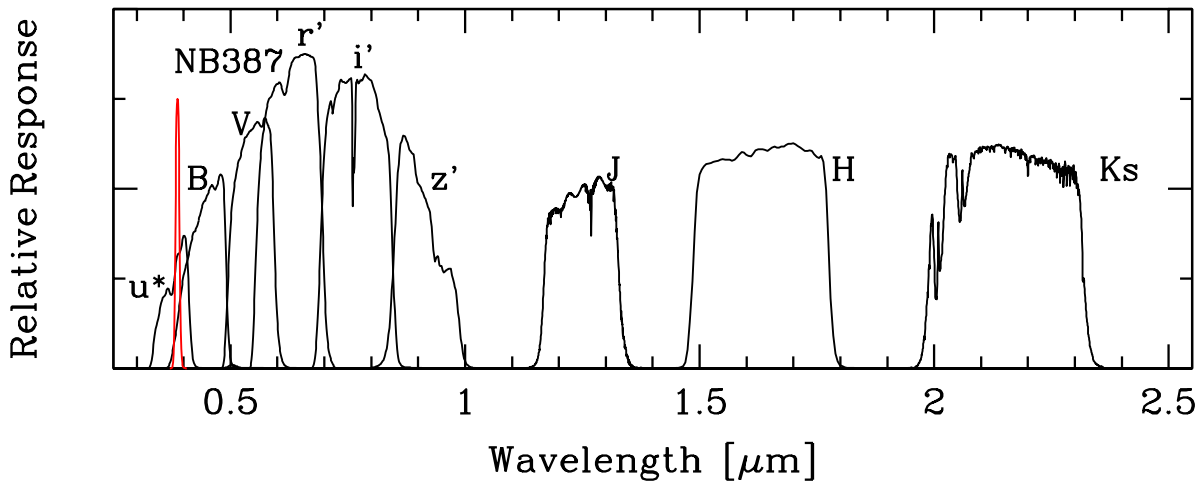

Figure A.10. Relative response curves of the optical and NIR broadband filters in the COSMOS field. The responses include the throughputs of the instrument and the telescope as well as atmospheric absorption.

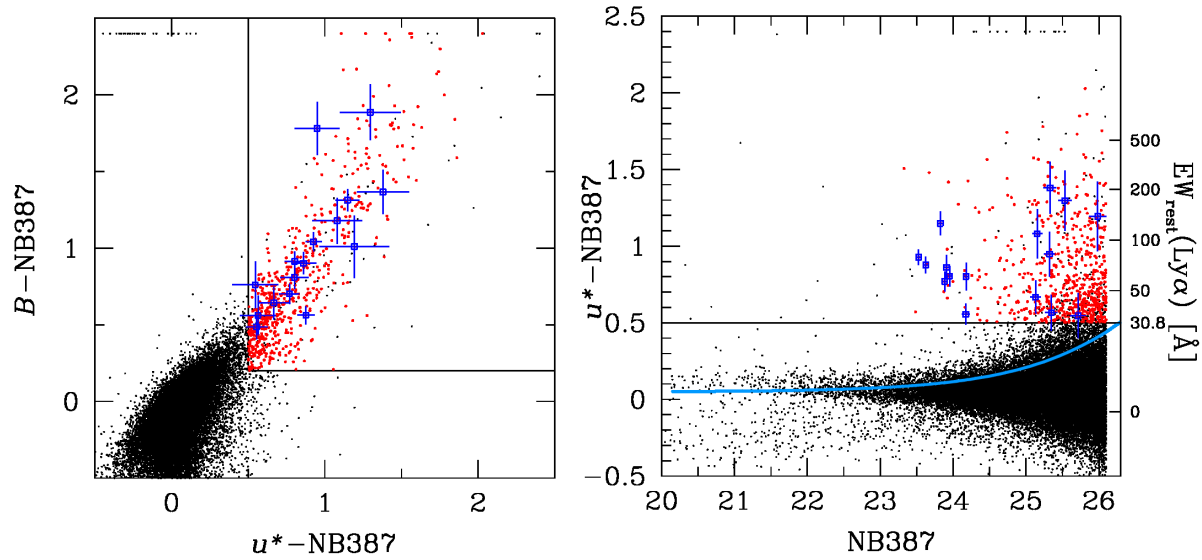

Figure A.11. *Left:* Distribution of NB387-detected objects in the $B-$NB387 vs. u^*-NB387 plane in COSMOS. The black dots indicate all the detected objects, while the red dots show LAE candidates after removing spurious objects and interlopers. The blue open squares with errorbars show spectroscopically confirmed LAEs. For the purpose of display, objects whose $u^* - NB387$ colors exceed 2.4 are plotted at $u^*-\mathrm{NB387} = 2.4$. *Right:* Distribution of NB387-detected objects in the u^*-NB387 vs. NB387 plane. The symbols and colors are the same as those in the left panel. The horizontal solid line shows the selection threshold of u^*-NB387 and the blue curve indicates the 2σ photometric error in u^*-NB387 for sources with $u^*-\mathrm{NB387} = 0.05$, which is the average u^*-NB387 color of all the objects. The right y axis shows the rest-frame Lyα equivalent width of $z = 2.18$ LAEs with u^*-NB387 color corresponding to the left y axis. For the purpose of display, objects whose u^*-NB387 colors exceed 2.4 are plotted at $u^*-\mathrm{NB387}= 2.4$.

Table A.6. Properties of the spectroscopic sample in the COSMOS field with LRIS (Shibuya et al. 2014a) and MagE (Hashimoto et al. 2013; M. Rauch et al. in preparation)

ID	RA (1)	Dec. (1)	mag(NB387) (2)	$\lambda_{\rm obs}$ (3)	z (4)
LRIS March run					
COSMOS-08357	09:59:59.073	+02:05:31.58	25.13 ± 0.07	3868.79	2.1824
COSMOS-12027	09:59:44.255	+02:07:42.71	23.95 ± 0.04	3878.72	2.1906
COSMOS-12805	10:00:15.288	+02:08:07.48	24.18 ± 0.05	3843.27	2.1614
COSMOS-13138	10:00:02.606	+02:08:24.49	25.35 ± 0.08	3866.73	2.1807
COSMOS-13636	09:59:59.387	+02:08:38.36	23.53 ± 0.03	3844.68	2.1626
COSMOS-13820	09:59:49.300	+02:08:49.42	25.71 ± 0.11	3820.20	2.1425
COSMOS-14135	09:59:54.494	+02:09:03.02	25.98 ± 0.12	3893.06	2.2024
COSMOS-14212	09:59:50.057	+02:08:53.81	23.88 ± 0.04	3879.99	2.1917
LRIS November run					
COSMOS-38019	09:59:36.490	+02:22:53.53	25.15 ± 0.07	3900.36	2.2084
COSMOS-38380	09:59:40.940	+02:23:04.18	23.91 ± 0.04	3909.79	2.2162
COSMOS-40792	09:59:46.662	+02:24:34.19	25.53 ± 0.09	3901.43	2.2093
COSMOS-41547	09:59:41.909	+02:25:00.01	25.32 ± 0.08	3832.08	2.1522
COSMOS-43982	09:59:54.394	+02:26:29.96	23.83 ± 0.04	3883.01	2.1941
COSMOS-44993	09:59:53.874	+02:27:10.99	25.33 ± 0.09	3907.65	2.2144
COSMOS-46597	09:59:45.975	+02:28:08.00	24.18 ± 0.05	3857.99	2.1736
MagE					
COSMOS-13636(†)	09:59:59.387	+02:08:38.36	23.53 ± 0.03	···	2.1623
COSMOS-30679	10:00:29.819	+02:18:49.00	23.63 ± 0.04	···	2.2005
COSMOS-43982(†)	09:59:54.394	+02:26:29.96	23.83 ± 0.04	···	2.1940

Note: (1) Coordinates are in J2000. (2) NB387 magnitudes with $2''$ diameter apertures. (3) Central wavelengths of observed Lyα lines (Å). (4) Redshifts of Lyα lines estimated from the central wavelengths. (†) These LAEs are also observed with LRIS. The redshifts of Lyα emission obtained from the two observations agree well each other.

A.2.2.3. Follow-up Spectroscopy Data

In the COSMOS field, we performed follow-up spectroscopy observation with LRIS in 2012 March 19–21 and November 15. We used two masks, targeting two different pointings. We chose the same grism and slit widths as for the SXDS mask (Section A.2.1.5). The on-source exposure time was 24,000 and 9,000 seconds for the March and the November runs, respectively, with a seeing size of $\sim 1\farcs0$. The bulk of the LRIS data reduction was done with the XIDL/Low-Redux package[A.5]. By inspecting the reduced spectra, we detected Lyα emission line for 15 objects. Table A.6 summarizes the LAEs with

[A.5] `http://www.ucolick.org/~xavier/LowRedux/`

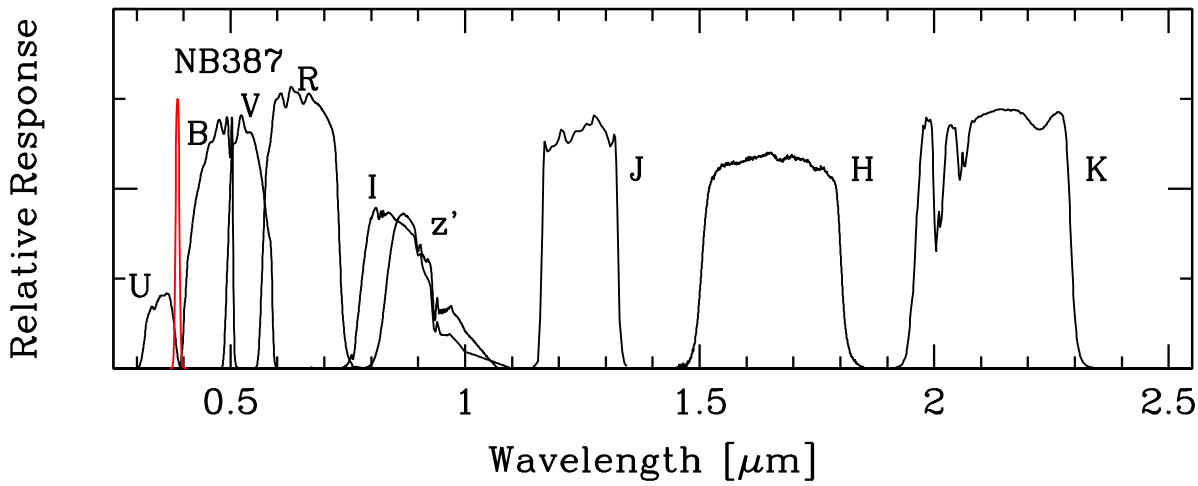

Figure A.12. Relative response curves of the optical and NIR broadband filters in the CDFS field. The responses include the throughputs of the instrument and the telescope as well as atmospheric absorption.

NB387 magnitude and Lyα-based redshift. More detailed analysis regarding the LRIS spectra are given in Shibuya et al. (2014a).

In addition to the LRIS observation, three LAEs (COSMOS-13636, -30679, -43982) have a high-quality Magellan/MagE (Marshall et al. 2008) spectrum of Lyα (Hashimoto et al. 2013; M. Rauch et al. in preparation). Details of the observation and analysis are given in M. Rauch et al. (in preparation). We note that two of the three LAEs are also observed with LRIS. We have confirmed that both instruments provide almost the same redshifts of Lyα (Table A.6).

We have in total 16 LAEs with confirmed Lyα emission. They are also plotted as the spectroscopically confirmed LAEs in Figure A.11 (blue open squares).

A.2.3. CDFS

A.2.3.1. Broadband Images

We use the publicly available U, B, V, R, and I data obtained by combining public images taken with ESO 2.2m and WFI by the ESO Deep Public Survey and COMBO-17 teams, z' data taken with CTIO/MOSAIC II, J and K data with CTIO/ISPI, and H data with NTT/SOFI. We also use Spitzer/IRAC 3.6, 4.5, 5.8, and 8.0 μm data. All data are collected from the MUSYC Public Data Release[A.6], and are summarized in Gawiser et al. (2006). Table A.7 summarizes the details of the broadband data. The passbands of optical and NIR broadband images are shown in Figure A.12.

A.2.3.2. Candidate Selection

We select LAE candidates in the same manner as done in the SXDS field (Section A.2.1). We perform source detection and photometry with $2''$ diameter apertures. All magnitudes are corrected for Galactic extinction of $E(B-V) = 0.008$ (Schlegel et al. 1998). The NB387-detection catalog contains 36,998 objects with aperture magnitudes brighter than the 5σ sky noise.

[A.6] http://www.astro.yale.edu/MUSYC/

Table A.7. Summary of Optical and NIR Broadband Imaging Data in the CDFS Field

Band	Observatory	PSF (1)	Limit Mag (2)	Reference (3)
U	MPG/ESO 2.2m	1.02	26.2	(a), (b)
B	MPG/ESO 2.2m	0.97	26.9	(a), (b)
V	MPG/ESO 2.2m	0.92	26.4	(a), (b)
R	MPG/ESO 2.2m	0.80	26.4	(a), (b)
I	MPG/ESO 2.2m	0.91	24.7	(a), (b)
z'	CTIO	1.02	24.2	(a), (b)
J	CTIO	1.5–1.6	23.4	(b), (c)
H	NTT	1.5–1.6	23.4	(b), (c)
K	CTIO	1.5–1.6	22.8	(b), (c)

Note: (1) PSF size is defined as an FWHM of point sources (arcsec). (2) The limiting magnitude (5σ) estimated by $2''$ diameter random aperture photometry. (3) (a) Gawiser et al. (2006); (b) Cardamone et al. (2010); (c) Taylor et al. (2009); see also `http://www.astro.yale.edu/MUSYC/`.

The color criteria for selecting LAEs in the CDFS is defined as:

$$U - \mathrm{NB387} > 0.8 \;\&\&\; B - \mathrm{NB387} > 0.2, \tag{A.2}$$

which select LAEs with $\mathrm{EW_{rest}} \gtrsim 30$ Å. This criteria is determined based on model galaxies and Galactic stars on the $U-$NB387 vs. $B-$NB387 color plane (top panel of Figure A.13). Using Equation (A.2), we have 1,108 LAE candidates after removing spurious objects and obvious [O II] and C IV emitters[A.7]. However, due to the relative shallowness of the U-band data, $U-$NB387 values for the faintest LAE candidates are not significantly large compared with the 2σ photometric errors in $U-$NB387. If we constrain galaxies to have $U-$NB387 colors larger than the 2σ photometric error at a given NB387 brightness, the number of LAE candidates decreases to 747. We mainly focused on the latter sample, which is considered to have less contamination in the faint end of NB387 magnitude. We plot the candidates on the $U-$NB387 vs. $B-$NB387 two color plane and on the $U-$NB387 vs. NB387 color-magnitude plane in the bottom left and right panels of Figure A.13, respectively. Candidates in the clean sample are plotted with red, while the other 361 ($= 1108 - 747$) candidates in the full sample are shown with light red.

A.2.3.3. Follow-up Spectroscopy Data

In the CDFS field, two LAEs (CDFS-3865 and CDFS-6482) have been observed by MagE and identified by their strong Lyα emission (Hashimoto et al. 2013; see also Table A.8). Details of the observation and analysis are given in M. Rauch et al. (in preparation).

[A.7] We have 5 emitters with GALEX detection.

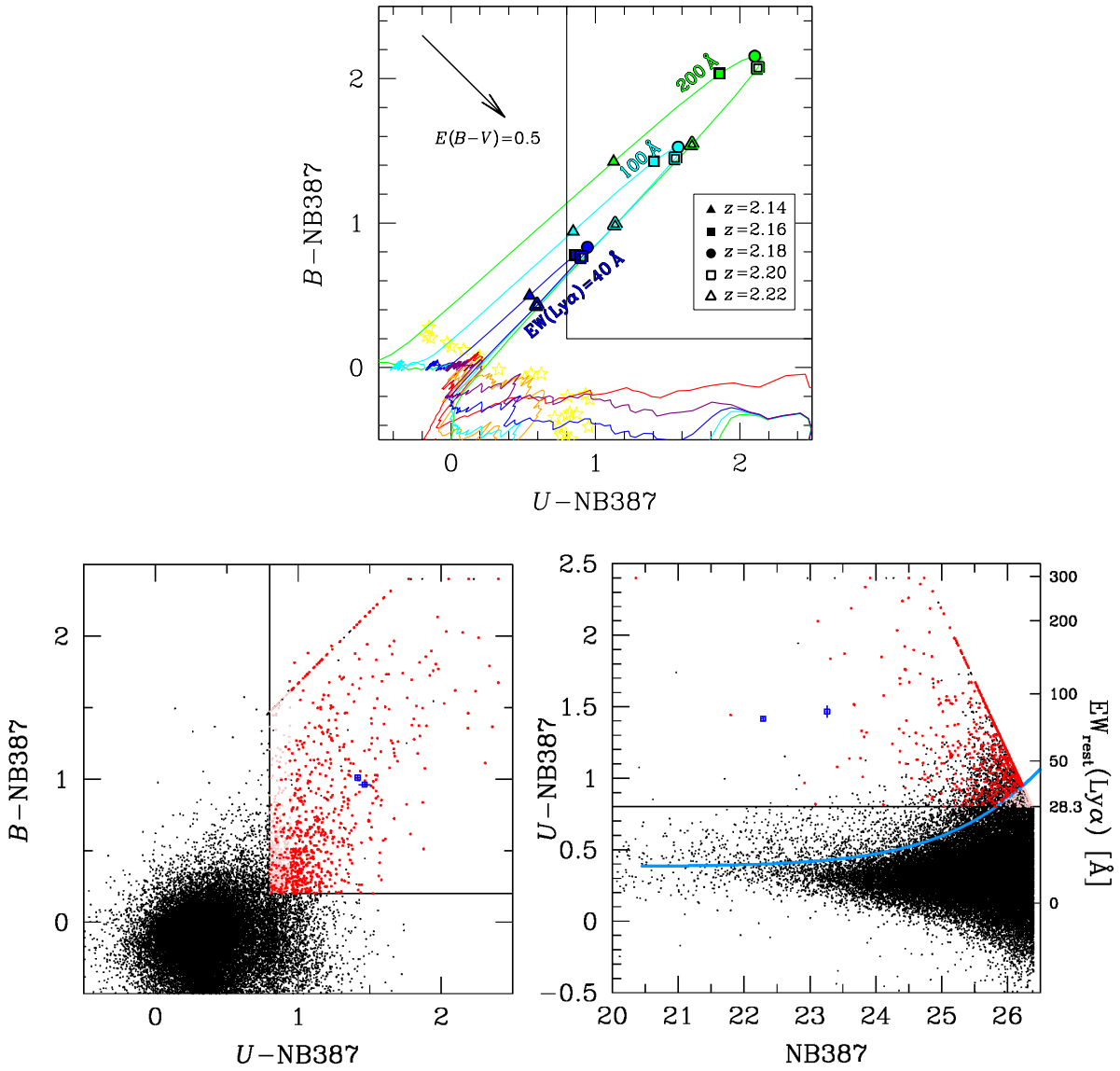

Figure A.13. *Top:* $B-$NB387 vs. $U-$NB387 plane for selection of LAEs at $z \simeq 2.2$ in CDFS. The colors and symbols are the same as those used in the top panel of Figure A.8. *Bottom Left:* Distribution of NB387-detected objects in the $B-$NB387 vs. $U-$NB387 plane. The black dots indicate all the detected objects. The red dots show LAE candidates in the clean sample, while the light red dots are the rest of LAEs in the full sample after the removal of spurious objects and interlopers. The blue open squares with errorbars show spectroscopically confirmed LAEs. For the purpose of display, objects whose $U-$NB387 colors exceed 2.4 are plotted at $U-$NB387 $= 2.4$. *Bottom Right:* Distribution of NB387-detected objects in the $U-$NB387 vs. NB387 plane. The symbols and colors are the same as those in the left panel. The horizontal solid line shows the selection threshold of $U-$NB387 and the blue curve indicates the 2σ photometric error in $U-$NB387 for sources with $U-$NB387 $= 0.38$, which is the average $U-$NB387 color of all the objects. The right y axis shows the rest-frame Lyα equivalent width of $z = 2.18$ LAEs with $U-$NB387 color corresponding to the left y axis. For the purpose of display, objects whose $U-$NB387 colors exceed 2.4 are plotted at $U-$NB387$= 2.4$.

Table A.8. Properties of the spectroscopic sample in the CDFS field with MagE (Hashimoto et al. 2013; M. Rauch et al. in preparation)

ID	RA (1)	Dec. (1)	mag(NB387) (2)	λ_{obs} (3)	z (4)
LRIS March run					
CDFS-3867	03:32:32.312	−28:00:52.19	22.29 ± 0.01	···	2.1751
CDFS-6482	03:32:49.336	−27:59:52.35	23.26 ± 0.02	···	2.2061

Note: (1) Coordinates are in J2000. (2) NB387 magnitudes with $2''$ diameter apertures. (3) Central wavelengths of observed Lyα lines (Å). (4) Redshifts of Lyα lines estimated from the central wavelengths.

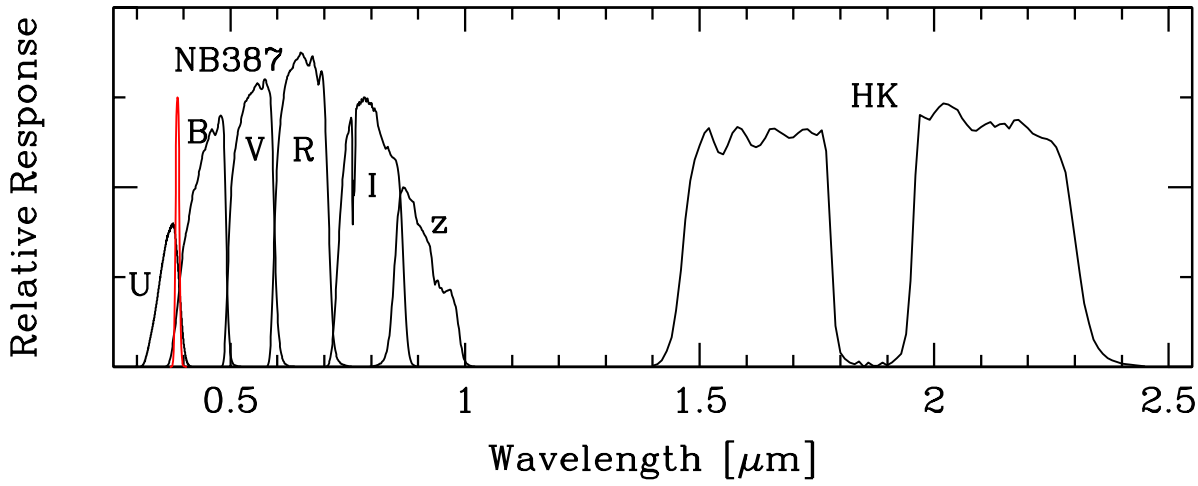

Figure A.14. Relative response curves of the optical and NIR broadband filters in the HDFN field. The responses include the throughputs of the instrument and the telescope as well as atmospheric absorption.

A.2.4. HDFN

A.2.4.1. Broadband Images

We use the publicly available U data taken with KPNO, B, V, R, I, and z' data with Subaru, and HK data with UH 2.2m. We also use Spitzer/IRAC 3.6, 4.5, 5.8, and 8.0 μm data. All data are collected from the Hawaii Hubble Deep Field North Survey[A.8], and are summarized in Capak et al. (2004). Table A.9 summarizes the details of the broadband data. The passbands of optical and NIR broadband images are shown in Figure A.14.

A.2.4.2. Candidate Selection

We select LAE candidates in the same manner as done in the SXDS field (Section A.2.1). We perform source detection and photometry with $3''$ diameter apertures, since the PSF size of U band image is relatively large ($\sim 1\farcs3$). All magnitudes are corrected for Galactic extinction of $E(B-V) = 0.012$

[A.8] http://www.astro.caltech.edu/~capak/hdf/index.html

Table A.9. Summary of Optical and NIR Broadband Imaging Data in the HDFN Field

Band	Observatory	PSF (1)	Limit Mag (2)	Reference (3)
U	KPNO	1.29	26.4	(a)
B	Subaru	0.77	26.3	(a)
V	Subaru	1.25	25.7	(a)
R	Subaru	1.19	26.0	(a)
I	Subaru	0.80	25.2	(a)
z'	Subaru	0.80	24.9	(a)
HK	UH 2.2m	0.87	21.4–21.6	(b)

Note: (1) PSF size is defined as an FWHM of point sources (arcsec). (2) The limiting magnitude (5σ) estimated by $3''$ diameter random aperture photometry. (3) (a) Capak et al. (2004); see also `http://www.astro.caltech.edu/~capak/hdf/index.html`.

(Schlegel et al. 1998). The NB387-detection catalog contains 36,236 objects with aperture magnitudes brighter than the 5σ sky noise.

The color criteria for selecting LAEs in the CDFS is defined as:

$$U - \mathrm{NB387} > 0.5 \;\&\&\; B - \mathrm{NB387} > 0.2, \tag{A.3}$$

which select LAEs with $\mathrm{EW_{rest}} \gtrsim 20$ Å. This criteria is determined based on model galaxies and Galactic stars on the $U-$NB387 vs. $B-$NB387 color plane (top panel of Figure A.15). Using Equation (A.3), we have 950 LAE candidates after removing spurious objects and obvious [O II] and CIV emitters[A.9]. We have confirmed that the 2σ photometric errors in $U-$NB387 for the faintest objects in the sample of HDFN is smaller than the criterion of $U-$NB387$= 0.5$. We plot the candidates on the $U-$NB387 vs. $B-$NB387 two color plane and on the $U-$NB387 vs. NB387 color-magnitude plane in the bottom left and right panels of Figure A.15, respectively.

A.2.4.3. Follow-up Spectroscopy Data

In the HDFN field, we performed follow-up spectroscopy observation with LRIS in 2012 March 19–20. We used two masks, targeting two different pointings. For one mask, we chose the same grism and slit widths as for the SXDS mask (Section A.2.1.5). For the other mask, we used the blue channel of LRIS with the 1200 groove mm^{-1} grism blazed at 3400 Å. With the $1\farcs0$ slits used in the mask, the spectral resolution in the blue was ~ 1.6 Å FWHM, corresponding to $R \sim 2500$ for the wavelengths of Lyα emission of $z = 2.2$ LAEs. The on-source exposure time was 18,000 and 17,800 seconds for the first and second masks, respectively, with a seeing size of $\sim 1\farcs0$. The bulk of the LRIS data reduction was done with the XIDL/Low-Redux package[A.10]. By inspecting the reduced spectra, we detected Lyα emission line for 5 objects. Table A.10 summarizes the LAEs with NB387 magnitude and Lyα-based

[A.9] We have 17 emitters with either GALEX of X-ray detection.

[A.10] `http://www.ucolick.org/~xavier/LowRedux/`

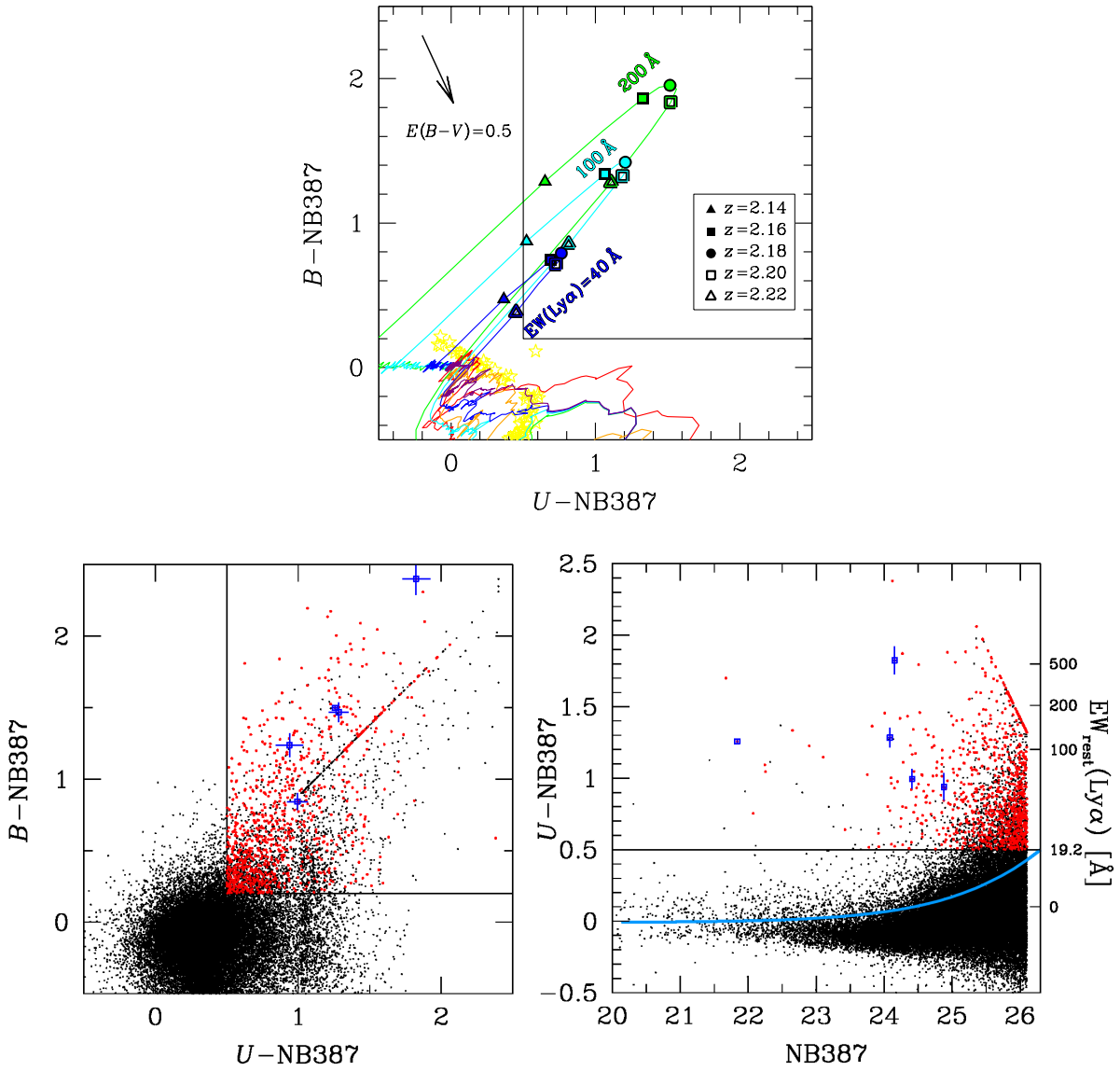

Figure A.15. *Top:* $B-$NB387 vs. $U-$NB387 plane for selection of LAEs at $z \simeq 2.2$ in HDFN. The colors and symbols are the same as those used in the top panel of Figure A.8. *Bottom Left:* Distribution of NB387-detected objects in the $B-$NB387 vs. $U-$NB387 plane. The black dots indicate all the detected objects. The red dots show LAE candidates in the clean sample, while the light red dots are the rest of LAEs in the full sample after the removal of spurious objects and interlopers. The blue open squares with errorbars show spectroscopically confirmed LAEs. For the purpose of display, objects whose $U-$NB387 colors exceed 2.4 are plotted at $U-$NB387 $= 2.4$. *Bottom Right:* Distribution of NB387-detected objects in the $U-$NB387 vs. NB387 plane. The symbols and colors are the same as those in the left panel. The horizontal solid line shows the selection threshold of $U-$NB387 and the blue curve indicates the 2σ photometric error in $U-$NB387 for sources with $U-$NB387 $= 0.38$, which is the average $U-$NB387 color of all the objects. The right y axis shows the rest-frame Lyα equivalent width of $z = 2.18$ LAEs with $U-$NB387 color corresponding to the left y axis. For the purpose of display, objects whose $U-$NB387 colors exceed 2.4 are plotted at $U-$NB387$= 2.4$.

Table A.10. Properties of the spectroscopic sample in the HDFN field with LRIS (Shibuya et al. 2014a)

ID	RA (1)	Dec. (1)	mag(NB387) (2)	$\lambda_{\rm obs}$ (3)	z (4)
LRIS March run					
HDFN-18325	12:36:23.361	+62:06:05.10	21.84 ± 0.01	3858.78	2.1742
HDFN-20042	12:36:07.055	+62:07:03.54	24.88 ± 0.04	3864.87	2.1792
HDFN-31902	12:37:15.064	+62:12:32.95	24.09 ± 0.03	3865.31	2.1796
HDFN-42659	12:37:49.814	+62:17:30.43	24.15 ± 0.03	3882.07	2.1934
HDFN-43408	12:37:39.031	+62:17:54.29	24.41 ± 0.03	3886.59	2.1971

Note: (1) Coordinates are in J2000. (2) NB387 magnitudes with $2''$ diameter apertures. (3) Central wavelengths of observed Lyα lines (Å). (4) Redshifts of Lyα lines estimated from the central wavelengths. (†) These LAEs are also observed with LRIS. The redshifts of Lyα emission obtained from the two observations agree well each other.

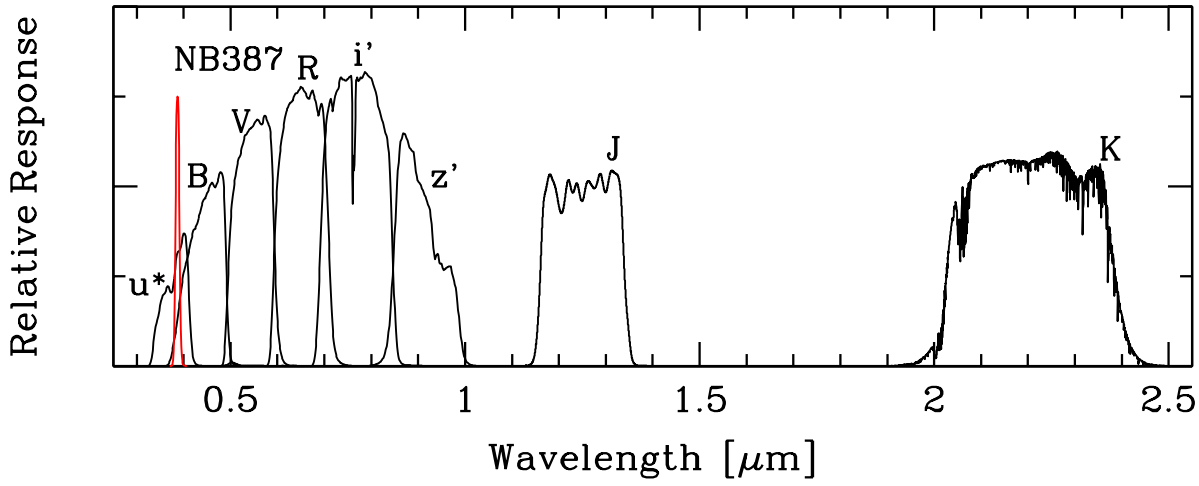

Figure A.16. Relative response curves of the optical and NIR broadband filters in the SSA22 field. The responses include the throughputs of the instrument and the telescope as well as atmospheric absorption.

redshift. They are also plotted as the spectroscopically confirmed LAEs in Figure A.15 (blue open squares). More detailed analysis regarding the LRIS spectra are given in Shibuya et al. (2014a).

A.2.5. SSA22

A.2.5.1. Broadband Images

We use the u^* data taken with CFHT/MegaCam, B, V, R, i', and z' data with Subaru/Suprime-Cam, J data with KPNO/NEWFIRM, and K data with UKIRT/WFCAM. The optical imaging data are provided by T. Hayashino (see also Hayashino et al. 2004). The J data are obtained from the NewHα Survey (Ly et al. 2011; Lee et al. 2012). The K data are collected from the WFCAM data access page. We also use Spitzer/IRAC 3.6, 4.5, 5.8, and 8.0 μm data. Table A.11 summarizes the details of the broadband data. The passbands of optical and NIR broadband images are shown in Figure A.16.

Table A.11. Summary of Optical and NIR Broadband Imaging Data in the SSA22 Field

Band	Observatory	PSF (1)	Limit Mag (2)	Reference (3)
u^*	CFHT	1.00	26.3	(a)
B	Subaru	1.02	26.7	(a)
V	Subaru	1.05	26.8	(a)
R	Subaru	1.06	26.7	(a)
i'	Subaru	1.04	26.4	(a)
z'	Subaru	1.03	25.7	(a)
J	KPNO	1.37	23.5	(b), (c)
K	UKIRT	0.84	21.2	(d)

Note: (1) PSF size is defined as an FWHM of point sources (arcsec). (2) The limiting magnitude (5σ) estimated by $2''$ diameter random aperture photometry. (3) (a) Hayashino et al. (2004); (b) Ly et al. (2011) (c) Lee et al. (2012) (d) `http://surveys.roe.ac.uk/wsa/`

A.2.5.2. Candidate Selection

We select LAE candidates in the same manner as done in the SXDS field (Section A.2.1). We perform source detection and photometry with $2''$ diameter apertures. All magnitudes are corrected for Galactic extinction of $E(B-V) = 0.08$ (Schlegel et al. 1998). The NB387-detection catalog contains 8942 objects with aperture magnitudes brighter than the 5σ sky noise.

Since the u^* and B-band are the same as used in the SXDS field, we adopt the the same criteria for the LAE selection of Equation (A.1; see also the top panel of Figure A.8). After removing spurious objects and obvious [O II] and CIV emitters[A.11] in the same manner as in Sections A.2.1.3 and A.2.1.4, we have 168 LAE candidates. We plot the candidates on the u^*-NB387 vs. $B-$NB387 two color plane and on the u^*-NB387 vs. NB387 color-magnitude plane in the left and right panels of Figure A.17, respectively.

To summarize, we have constructed the $z = 2.2$ LAE sample, which contains in total $3,403$ candidates in the SXDS, COSMOS, CDFS, HDFN, and SSA22 fields, covering $\sim 1.5\,\mathrm{deg}^2$ under the constraint of 2σ excess of NB387 brightness over U (Table A.12). These LAEs provide us with great opportunities to investigate LAEs' rest-frame optical spectroscopic properties such as metallicity and ionization parameter at relatively high-z. In the following two Chapters, we present estimations of these quantities for the LAEs by using NIR narrowband imaging and spectroscopy data.

[A.11] We have 3 emitters with GALEX detection.

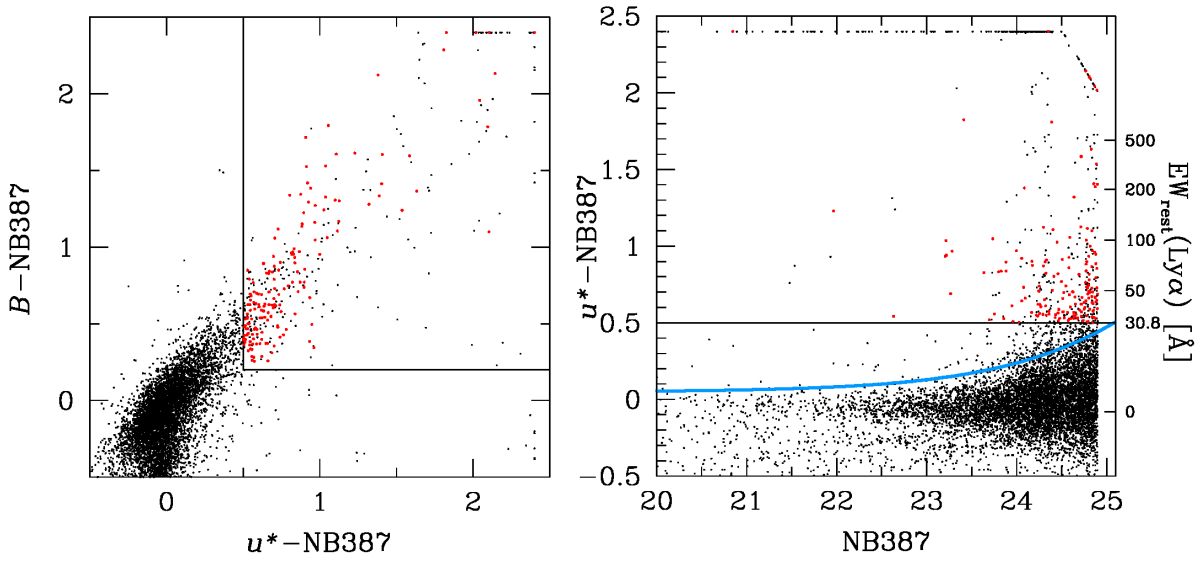

Figure A.17. *Left:* Distribution of NB387-detected objects in the $B-$NB387 vs. u^*-NB387 plane in SSA22. The black dots indicate all the detected objects, while the red dots show LAE candidates after removing spurious objects and interlopers. The blue open squares with errorbars show spectroscopically confirmed LAEs. For the purpose of display, objects whose $u^* - NB387$ colors exceed 2.4 are plotted at $u^*-\mathrm{NB387} = 2.4$. *Right:* Distribution of NB387-detected objects in the u^*-NB387 vs. NB387 plane. The symbols and colors are the same as those in the left panel. The horizontal solid line shows the selection threshold of u^*-NB387 and the blue curve indicates the 2σ photometric error in u^*-NB387 for sources with $u^*-\mathrm{NB387} = 0.05$, which is the average u^*-NB387 color of all the objects. The right y axis shows the rest-frame Lyα equivalent width of $z = 2.18$ LAEs with u^*-NB387 color corresponding to the left y axis. For the purpose of display, objects whose u^*-NB387 colors exceed 2.4 are plotted at $u^*-\mathrm{NB387}= 2.4$.

Table A.12. The $z = 2.2$ LAE sample

Field	Area (deg^2)	No. of LAEs
SXDS	0.56	919
COSMOS	0.23	619
CDFS	0.25	747 (1108)[(1)]
HDFN	0.25	950
SSA22	0.22	168
in total	1.51	3,403 (3764)[(1)]

Note: (1) The value in the round brackets shows the number of LAE candidates without the constraint of $> 2\sigma$ excess of NB387 brightness over U (see, e.g., Section A.2.3.2).

B Physical Properties of LAEs from NIR Spectroscopy

In this appendix, we present full results of the Keck/NIRSPEC and Magellan/MMIRS follow-up spectroscopy of LAEs (Section 3.1). We successfully detect Hα emission from seven LAEs, and perform a detailed analysis of six LAEs, free from active galactic nucleus activity, two out of which, CDFS-3865 and COSMOS-30679, have [O II] and [O III] line detections. They are the first [O II]-detected LAEs at high-z, and their [O III]/[O II] ratios and $R23$-index provide the first simultaneous determinations of ionization parameter and metallicity for LAEs.

We describe the spectroscopic sample in Section B.1, which includes supplementary Table and Figure. The detection and measurement of emission lines in the NIR spectroscopy is summarized in Section B.2. In Section B.3, we derive properties of LAEs including estimates of ionization parameter, metallicity, SFR, from the rest-frame optical nebular lines. We check for the presence of active galactic nuclei (AGNs) in the LAEs. The stellar populations inferred from SED fitting to the broadband photometry of the LAE are also presented.

B.1. NIR spectroscopic Sample

Table B.1 summarizes the details of the sample of our NIR follow-up spectroscopy with Keck/NIRSPEC and Magellan/MMIRS. Figure B.1 shows the distributions of the LAEs presented in this appendix on the $U-$NB387 versus NB387 color magnitude diagram.

B.2. Emission Line Detections

B.2.1. Hα Detection

Figure B.2 presents the 1D and 2D spectra, and Table B.2 summarizes the line flues and their 1σ errors. We detect significant Hα emission in K band 2D spectra for COSMOS-08501, COSMOS-13636, COSMOS-30679, COSMOS-43982, CDFS-3865, CDFS-6482, and SSA22-8043, but we do not identify any emission lines for the other two LAEs, HDFN-18325 and HDFN-18431. Both LAEs are expected to have strong Lyα, hence strong Hα. Especially, a recent follow-up observation has identified a Lyα emission from HDFN-18325 (Appendix A.2.4.3). A possible reason why we do not detect lines for HDFN-18431 is that no alignment star was observed simultaneously, and the object may have drifted significantly out of the slit. The same issue may explain the non-detection of Hα for HDFN-18325, since half of the observation was done without an alignment star (Section 3.1.1.2). Since we have not

Table B.1. Summary of the LAE sample with NIR spectroscopy

Object	RA	Dec	NB387	$U-$NB387	$B-$NB387	EW(Lyα)	F(Lyα)	Exp. Time[6]			Instr.
	(1)	(1)	(2)	(3)	(3)	(4)	(5)	(J)	(H)	(K)	(7)
COSMOS-08501	10:01:16.80	+02:05:36.26	23.94	1.41 ± 0.09	2.05 ± 0.10	255 ± 26	24.0 ± 1.1	···	···	3600	N
COSMOS-13636	09:59:59.38	+02:08:38.36	23.53	0.91 ± 0.05	1.03 ± 0.06	73 ± 5	32.4 ± 1.4	···	···	5400	N
COSMOS-30679	10:00:29.81	+02:18:49.00	23.63	0.86 ± 0.05	0.55 ± 0.06	34 ± 3	19.1 ± 1.4	5400	7200	6300	N
COSMOS-30679[†]	···	···	23.73	1.20 ± 0.07	1.16 ± 0.07	87 ± 7	23.2 ± 1.8	···	···	···	···
COSMOS-43982	09:59:54.39	+02:26:29.96	23.83	1.14 ± 0.08	1.30 ± 0.07	105 ± 8	30.3 ± 1.3	···	···	3600	N
HDFN-18325	12:36:23.36	+62:06:05.10	21.84	1.26 ± 0.02	1.50 ± 0.02	122 ± 2	125 ± 1.2	···	···	3600	N
HDFN-18431	12:36:25.62	+62:05:37.43	23.20	1.15 ± 0.03	1.71 ± 0.04	156 ± 6	37.8 ± 0.7	···	···	3600	N
CDFS-3865	03:32:32.31	−28:00:52.20	22.29	1.42 ± 1.23	1.01 ± 0.42	64 ± 29	84.0 ± 13.9	5100	10800		N/M
CDFS-6482	03:32:49.34	−27:59:52.35	23.26	1.47 ± 1.92	0.96 ± 0.66	75 ± 52	41.9 ± 22.0	···	10800		M
SSA22-8043	22:17:47.33	+00:08:28.36	24.51	0.66 ± 0.06	0.52 ± 0.06	28 ± 4	6.3 ± 1.1	···	10800		M

Note: (1) Coordinates are in J2000. (2) NB387 aperture magnitude. The diameter of the aperture is $2\farcs0$, and the typical error is 0.04 mag. (3) $U-$NB387 and $B-$NB387 colors and their 1σ errors calculated from aperture magnitudes. (4) Rest-frame EW of Lyα emission line in units of Å calculated from $B-$NB387 color and redshift of Hα. For HDFN objects whose Hα are not detected, we assume $z = 2.18$, which corresponds to the wavelength of the peak of the NB387 transmission curve. (5) Flux of Lyα emission line in units of 10^{-17} erg s^{-1} cm^{-2} calculated from EW(Lyα) and B band total magnitude. (6) Exposure time with NIRSPEC J, H, and K bands in units of second. For the CDFS and SSA22 objects, their H and K bands spectra were taken with MMIRS using the HK grism. (7) Instrument used for the spectroscopy. "N" stands for NIRSPEC, and "M" for MMIRS. For CDFS-3865, its J band spectrum was obtained with NIRSPEC, and H and K bands spectra with MMIRS. (†) Values obtained after removing the contribution from an adjacent object (Section B.3.2).

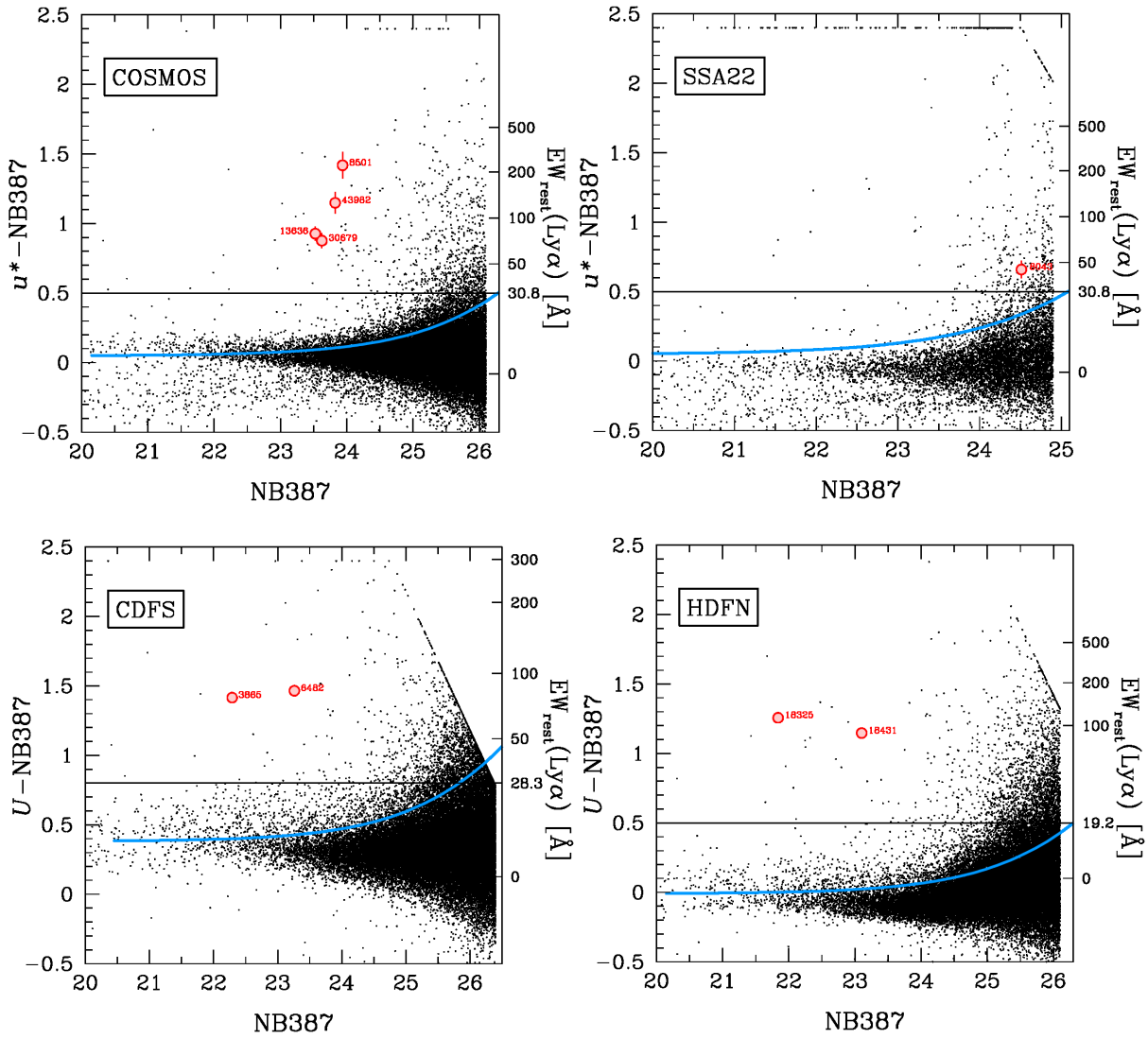

Figure B.1. Distribution of all objects in the $U-$NB387 vs. NB387 plane detected in the COSMOS (top left), SSA22 (top right), CDFS (bottom left), and HDFN fields (bottom right). The red circles show the LAEs selected for the spectroscopic follow-up observations, and the black dots show the NB387-detected objects. For the purpose of display, objects whose $U-$NB387 colors exceed 2.4 are plotted at $U-$NB387$=2.4$. The horizontal solid line in each panel shows the selection threshold of $U-$NB387 and the blue curve indicates the 2σ photometric error in $U-$NB387 for objects (Appendix A). The right y-axis in each panel shows the rest-frame Lyα equivalent width of $z=2.18$ LAEs with the $U-$NB387 color corresponding to the left y-axis.

yet obtained Lyα spectrum for HDFN-18431, the non-detection may be alternatively due to the mis-selection of LAEs. Future optical spectroscopy is needed to resolve this issue. In the following sections, we use the seven LAEs with reliable Hα detection.

B.2.2. Other Emission Line Detections

For CDFS-3865, we additionally obtain [O II]λ3727, Hβ, and [O III]$\lambda\lambda$4959, 5007 emission lines. Combined with the Hα-detection, a full suite of prominent rest-frame optical nebular lines are thus

Table B.2. Fluxes of nebular lines determined from NIR Spectroscopy

Object	[O II]λ3727	Hβ	[O III]λ4959	[O III]λ5007	Hα	[N II]λ6484
COSMOS-08501	···	···	···	···	1.91 ± 0.36	< 0.36
COSMOS-13636	···	···	···	···	2.71 ± 0.38	< 0.38
COSMOS-30679	1.04 ± 0.26	··· $^{(\star)}$	··· $^{(\star)}$	4.11 ± 0.41	3.11 ± 0.27	< 0.27
COSMOS-43982	···	···	···	···	6.63 ± 0.58	4.14 ± 0.58
Composite$^{(\dagger)}$	···	···	···	···	2.64 ± 0.20	< 0.20
CDFS-3865	2.53 ± 0.41	13.0 ± 4.1	19.0 ± 3.5	53.6 ± 3.5	38.5 ± 2.4	< 2.4
CDFS-6482	···	···	···	23.8 ± 2.7	9.38 ± 1.71	< 1.71
SSA22-8043	···	···	···	11.0 ± 4.2	14.7 ± 4.3	< 4.3

Note: Fluxes and their 1σ errors are given in unit of 10^{-17} erg s^{-1} cm^{-2}. For lines with less than the 3σ detection level, we list their 1σ upper-limits. (†) Composite spectrum of the four objects (Section B.3.1). ($\star$) These lines suffer badly from OH-lines subtraction errors.

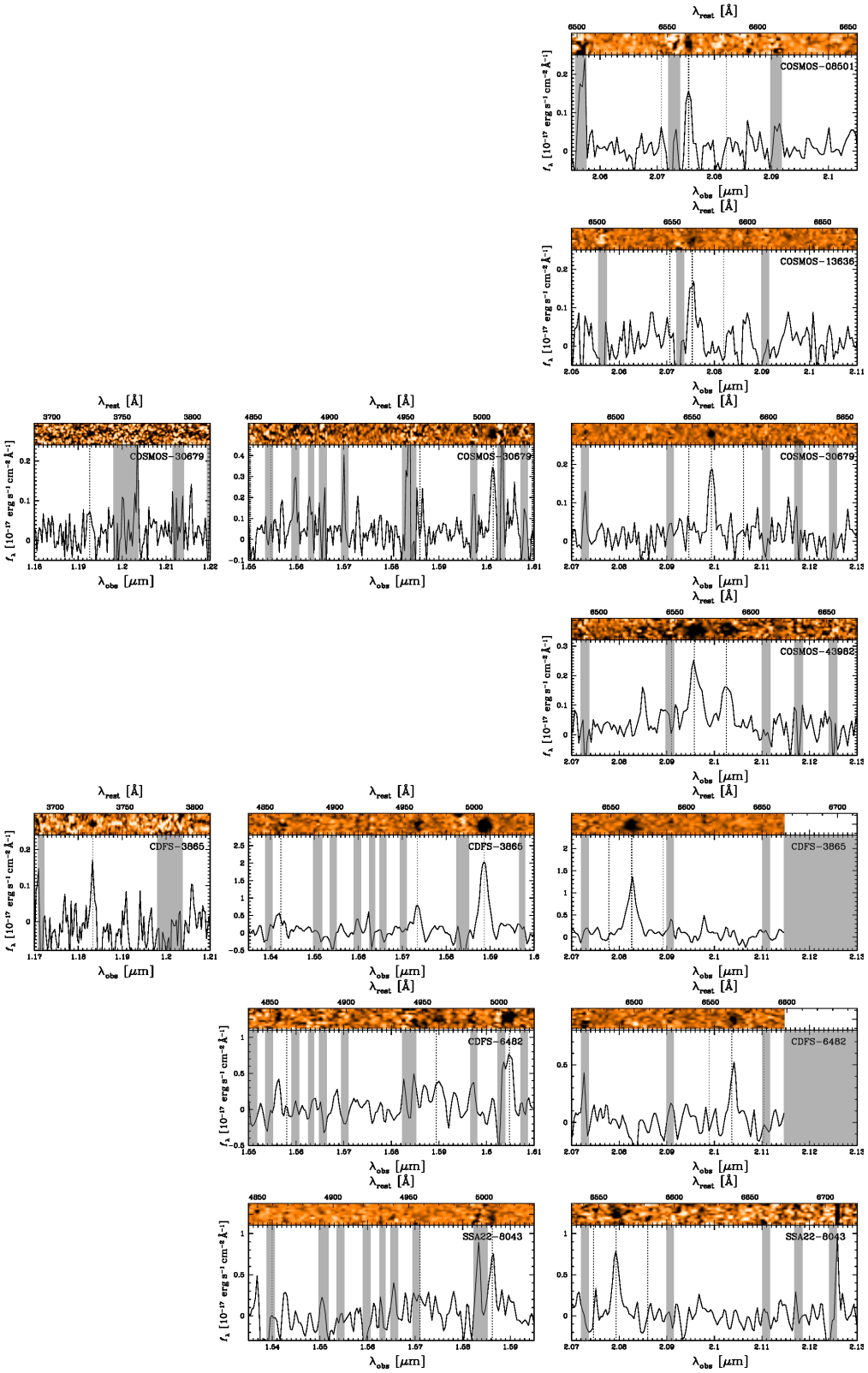

Figure B.2. From left to right, J, H, and K band spectra of the LAEs. In each panel, the 2D and 1D spectra are shown in the top and bottom, respectively. The vertical dotted lines in the 1D spectra show the expected locations of nebular emission lines; [O II]λ3727, Hβ, [O III]$\lambda\lambda$4959, 5007, [N II]λ6548, Hα, and [N II]λ6584 based on the peak of the detected Hα emission lines. The gray shaded areas overlaid on each 1D spectrum highlight spectral regions strongly affected by OH-airglow. For CDFS objects, their K band spectra at 2.115 μm and longer are not obtained due to a lack of sensitivity of MMIRS, and also shaded with gray.

obtained for this object. We note that the [O II] flux may be underestimated due to the possible flux loss caused by the guiding drift issue known to NIRSPEC. Since CDFS-3865 was observed with NIRSPEC without any alignment star simultaneously, the maximum flux loss caused by the guiding drift ($\sim 1\farcs5$ per hour; private communication with NIRSPEC support scientists) could be comparable to the observed value. However, we do not know the drift direction, and the true flux loss cannot be estimated. Therefore, we do not correct for any flux loss for [O II]. We emphasize that the possible factor$\lesssim 2$ uncertainties in [O II] flux do not change our main results (Section B.3.3). For COSMOS-30679, we obtain [O II] and [O III]λ5007 emission lines, while we do not identify Hβ and [O III]λ4959, because they fall in a dense OH-line wavelength range. We thus cannot place meaningful upper limits on their fluxes. When fluxes for these lines are required for inferring physical properties, we assume a value of 0.28 for the [O III]λ4959/5007 ratio (e.g., Richard et al. 2011) and calculate the Hβ flux based on the observed Hα flux, the intrinsic Hα/Hβ ratio assuming Case B recombination (2.86; Osterbrock 1989), and the dust extinction estimated from SED fitting. We have checked for CDFS-3865 that the Hβ flux estimated in this way is consistent with the really observed Hβ flux (see also Section B.3.2). We emphasize that the two LAEs, CDFS-3865 and COSMOS-30679, are the first [O II]-detected LAEs individually at high-z. The [O II]+[O III] lines provide the simultaneous determinations of ionization state and oxygen abundance (Section B.3.3).

For CDFS-6482 and SSA22-8043, we detect [O III]λ5007 while do not identify Hβ and [O III]λ4959, probably due to the contamination by OH-lines and the limited sensitivity of the instrument (More detailed descriptions about the MMIRS objects are provided by Hashimoto et al. 2013). For COSMOS-43982, we clearly detect [N II]λ6584 emission line, which is not identified for the other LAEs. The [N II]-detection suggests a non-negligible contribution of AGN to the emission lines for the object. Further investigations of AGN contamination are discussed in Section B.3.1.

B.3. Physical Properties of LAEs

B.3.1. Removal of Objects with AGN

AGN, as well as star-formation, can produce large amounts of ionizing photons, and show strong Lyα. Since our interest is star-forming LAEs, we need to remove LAEs with AGN activity from the sample.

During the LAE sample selection, bright LAEs with AGN signature have been removed (see Section 3.1.1.1 and Appendix A.2.1.4). Obvious AGNs are therefore excluded from the sample. However, the procedure is not always perfect, and can miss objects with relatively weak AGN activity. In order to assess possible contamination of AGN in our LAE sample, we plot our LAEs on a BPT diagram (Figure B.3; Baldwin et al. 1981) which is widely used to separate star forming galaxies from AGN. In Figure B.3, the underlying small gray points denote the spectroscopic objects from the Sloan Digital Sky Survey (SDSS; York et al. 2000)[B.1]. The two curves shown in Figure B.3 are the empirical demarcations (Kewley et al. 2001; Kauffmann et al. 2003a). Since only one LAE, CDFS-3865, has both [O III] and Hβ, all the other LAEs are shown with vertical lines. Due to the non-detection of [N II], the vertical lines show upper-limits of [N II]/Hα except for COSMOS-43982, which has an individual [N II] detection.

[B.1] We use a part of the spectroscopic data taken from the MPA-JHU DR7 release of spectrum measurements: `http://www.mpa-garching.mpg.de/SDSS/DR7/`

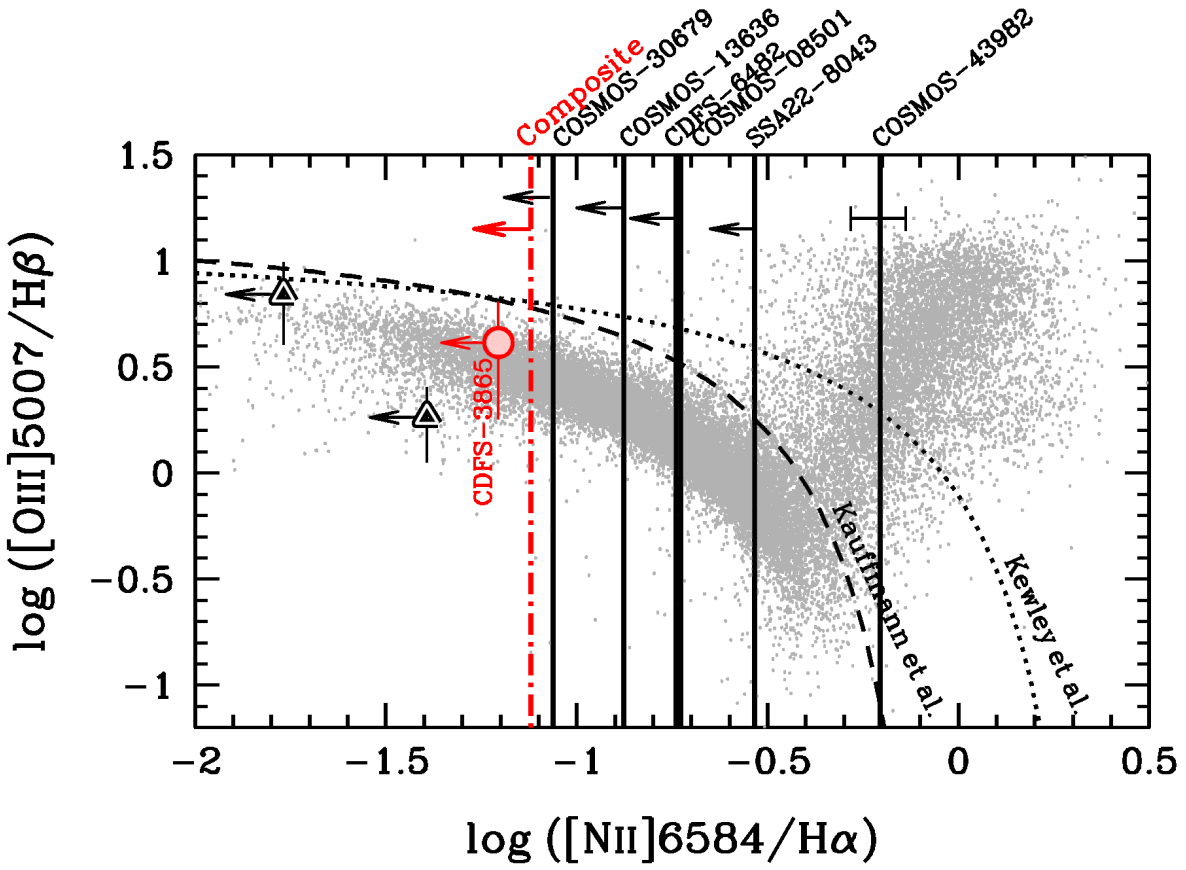

Figure B.3. BPT-diagram (Baldwin et al. 1981). The dotted and dashed curves show the dividing line between star-forming galaxies and AGNs defined by Kewley et al. (2001) and Kauffmann et al. (2003a), respectively. CDFS-3865 is shown with the red circle, while the other LAEs are shown with the vertical solid lines, due to the lacks of [O III] and/or Hβ. Since we do not identify [N II] except for COSMOS-43982, upper-limits of [N II]/Ha are given. The [N II]/Ha ratio for COSMOS-43982 is given with a horizontal error bar. The red dot-dashed vertical line indicates the upper-limit of [N II]/Hα for the composite spectrum of NIRSPEC-detected LAEs. The two triangles represent LAEs at $z \sim 2.3$ and 2.5 from Finkelstein et al. (2011). The gray small points are randomly selected objects from the SDSS spectroscopic sample.

Based on its relatively high [N II]/Hα ratio, COSMOS-43982 may be contaminated by an AGN, though there remains a possibility that this LAE may be a star-formation dominated galaxy with a very small [O III]/Hβ ratio (cf. Kewley et al. 2013b). For this analysis, we choose to be conservative and regard the object as a candidate possessing AGN activity. The properties of COSMOS-43982 are considered and interpreted carefully in the following sections.

For CDFS-3865, thanks to its relatively strong constraint on [N II]/Hα, we can see that the object is along the star forming sequence and has negligible AGN activity, similar to two other LAEs with spectroscopic follow-up at similar redshifts (Finkelstein et al. 2011). Although the other LAEs have no constraint on their y-axis values, AGN contributions to them are assumed to be minimal, since there are few AGNs in the range $\log([\mathrm{N\,II}]/\mathrm{H}\alpha) \lesssim -0.5$, as suggested from the underlying SDSS galaxies.

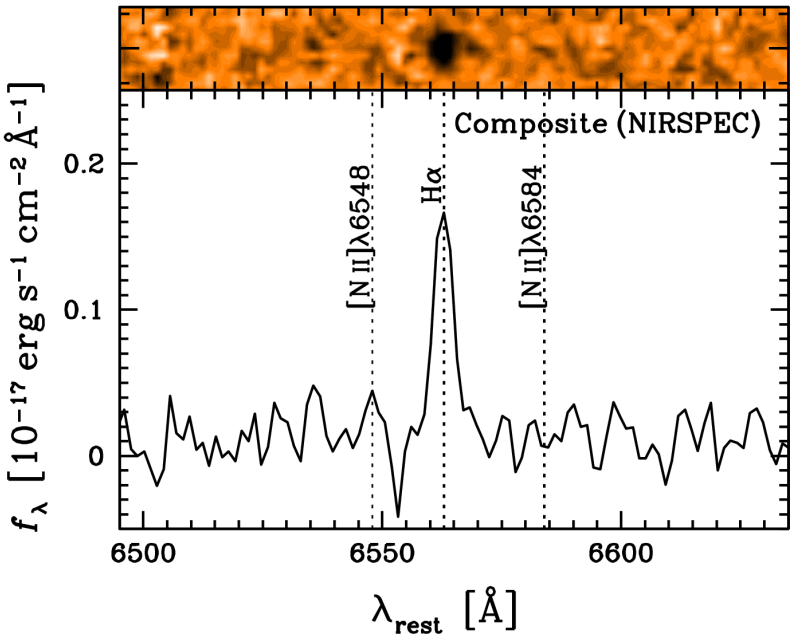

Figure B.4. *K* band composite spectrum of the NIRSPEC-detected objects.

In order to check the assumption, we stack the *K* band spectra of the four NIRSPEC-detected LAEs[B.2] with inverse-variance weights. The composite spectrum is shown in Figure B.4, and provides an average, deeper constraint on [N II]/Hα ratio for the LAEs. The red dot-dashed line in Figure B.3 shows the upper-limit of [N II]/Hα ratio constrained by the composite spectrum. The line is further away from the area occupied with AGNs. Therefore, AGN activity is on average negligible for the LAEs. In the following sections, we regard all the LAEs except for COSMOS-43982 as galaxies dominated by star-formation.

B.3.2. Stellar Mass and E(B-V) from SED Fitting

We perform SED fitting to broadband photometry to infer properties of the stellar populations. The majority of images are collected from publicly available databases (see notes in Table B.3). The optical and NIR photometry is done with a $2\farcs0$ diameter aperture using the double-image mode of SExtractor (Bertin & Arnouts 1996). The aperture magnitudes are then converted into total magnitudes using aperture correction values, which are estimated from differences between aperture magnitudes and `MAG_AUTO` values for point sources. For the IRAC imaging, we use a $3\farcs0$ diameter aperture and Yan et al. (2005)'s aperture correction values. Table B.3 summarizes the results.

The procedure of the SED fitting is the same as that of Ono et al. (2010a), except for fixed redshifts, which are derived from Hα. Briefly, we use the stellar population synthesis model GALAXEV (Bruzual & Charlot 2003) for stellar SEDs, and include nebular emission (Schaerer & de Barros 2009). We set the escape fraction of ionizing photons ($f_{\rm esc}$) as 0.05. Such low $f_{\rm esc}$ has been suggested for $z \sim 3$ LBGs (e.g., Shapley et al. 2006; see also Iwata et al. 2009). Recently, Nestor et al. (2013) suggest that faint LAEs may have a higher $f_{\rm esc}$ ($\sim$ 0.10–0.30) in contrast with bright LBGs. We have checked that even if we assume $f_{\rm esc} = 0.20$, the derived quantities do not change significantly. We adopt a Salpeter initial mass function (IMF; Salpeter 1955) with lower and upper mass cut-offs of 0.1 and 100$M_\odot$. We choose constant star-

[B.2] We do not use the MMIRS spectra due to their worse sensitivity and spectral resolution.

Table B.3. Broadband Photometry of the LAEs with NIR Spectroscopy

COSMOS sample[(1)]	B	V	r'	i'	z'	J	⋯	K_s	[3.6]	[4.5]	[5.8]	[8.0]
COSMOS-08501	25.86	25.91	26.08	25.88	25.81	98.45	⋯	25.64	99.99	99.99	99.99	99.99
COSMOS-13636	24.43	24.21	24.35	24.19	24.24	23.10	⋯	23.43	24.10	23.75	99.99	99.99
COSMOS-30679	24.05	23.12	22.91	22.46	22.33	21.15	⋯	21.82	22.12	22.57	99.99	23.06
COSMOS-30679[(†)]	24.76	23.82	24.44	24.09	23.49	22.31	⋯	23.29	⋯	⋯	⋯	⋯
COSMOS-43982	25.00	24.38	24.48	23.99	23.73	21.89	⋯	21.62	21.20	21.02	20.69	20.75
(limitmag)	(29.13)	(28.18)	(28.33)	(27.87)	(26.89)	(24.17)	⋯	(24.84)	(25.05)	(24.25)	(21.90)	(20.63)
(limitmag)[(†)]	(28.76)	(26.24)	(25.79)	(25.34)	(24.85)	(23.68)	⋯	(24.63)	⋯	⋯	⋯	⋯

CDFS sample[(2)]	B	V	R	I	z'	J	H	K	[3.6]	[4.5]	[5.8]	[8.0]
CDFS-3865	23.01	22.94	22.92	23.14	22.93	22.73	22.27	22.38	22.82	22.82	22.51	23.00
CDFS-6482	23.93	23.87	23.78	23.95	23.67	23.50	23.36	23.07	22.88	22.83	22.34	99.99
(limitmag)	(28.32)	(27.85)	(27.82)	(26.14)	(25.64)	(24.57)	(24.57)	(23.97)	(26.23)	(25.68)	(23.66)	(23.43)

SSA22 sample[(3)]	B	V	R	i'	z'	J	⋯	K	[3.6]	[4.5]	[5.8]	[8.0]
SSA22-8043	24.80	24.63	25.54	24.64	24.59	24.10	⋯	21.79	23.33	23.14	26.58	21.15
(limitmag)	(27.85)	(27.99)	(28.03)	(27.75)	(27.16)	(24.74)	⋯	(22.78)	(25.40)	(23.64)	(22.71)	(20.95)

Note: Broadband photometry of the LAEs. All magnitudes are total magnitudes. 99.99 mag means no signal detected. Magnitudes in parentheses are 1σ uncertainties adopted in SED fitting.

(1) $BVr'i'z'$ data are obtained from Subaru/Suprime-Cam, J data from UKIRT/WFCAM, K_s data from CFHT/WIRCAM, and [3.6] – [8.0] data from Spitzer/IRAC. All data are collected from the COSMOS Archive. (2) $BVRI$ data are obtained from MPG/ESO 2.2m/WFI, z' data from CTIO/MOSAIC II, JK data from CTIO/ISPI, H data from NTT/SOFI, and [3.6] – [8.0] data from Spitzer/IRAC. Optical and NIR data are collected from the MUSYC Public Data Release (Gawiser et al. 2006), and Spitzer data from the SIMPLE Legacy II project. (3) $BVRi'z'$ data are obtained from Subaru/Suprime-Cam, J data from KPNO/NEWFIRM, K data from UKIRT/WFCAM, and [3.6] – [8.0] data from Spitzer/IRAC. Optical data are provided by T. Hayashino (see also Hayashino et al. 2004), J data are obtained from the NewHα survey (Lee et al. 2012; Ly et al. 2011). K data are collected from the WFCAM data access page, and Spitzer data from the Spitzer Heritage Archive. (†) Values obtained after removing the contribution from an adjacent object (Section B.3.2). The limiting magnitudes are calculated by adding the photometric errors and additional errors (residuals after subtracting GALFIT models) in quadrature. The limiting magnitudes are thus shallower than those given above (photometric only).

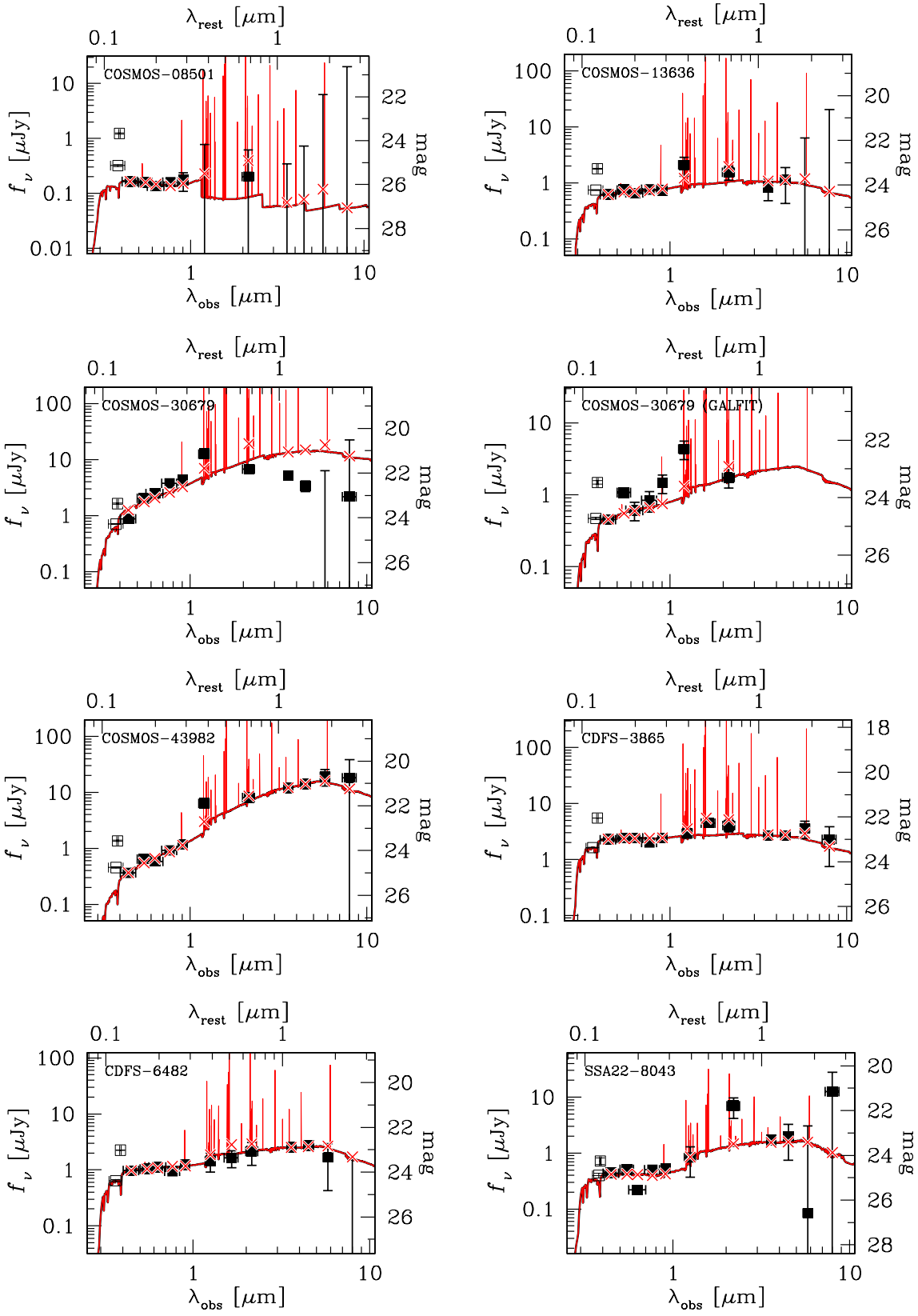

Figure B.5. Results of SED fitting. The filled squares show the observed flux densities used for the fitting (B, V, r, i, z, J, (H), K, [3.6], [4.5], [5.8], and [8.0]), while the open squares indicate those we omit for the fitting (U and NB387), due to the unknown flux contributions of IGM absorption. The red lines show the best-fit model spectra, and the red crosses correspond to the best-fit flux densities.

Table B.4. Physical Properties of the LAEs with NIR Spectroscopy from SED fitting

Object	$\log(M_\star)$ ($M_\odot$)	$E(B-V)$ (mag)	log(age) (yr)	log(SFR) ($M_\odot$/yr)	χ^2
COSMOS-08501	$7.84^{+1.21}_{-0.27}$	$0.08^{+0.04}_{-0.08}$	$6.16^{+2.75}_{-1.06}$	$1.68^{+1.24}_{-1.44}$	1.825
COSMOS-13636	$9.12^{+0.13}_{-0.14}$	$0.18^{+0.01}_{-0.01}$	$7.34^{+0.23}_{-0.22}$	$1.80^{+0.08}_{-0.09}$	22.356
COSMOS-30679	$10.34^{+0.00}_{-0.00}$	$0.40^{+0.00}_{-0.00}$	$7.26^{+0.00}_{-0.00}$	$3.10^{+0.00}_{-0.00}$	7062.297
COSMOS-30679(†)	$9.74^{+0.26}_{-0.52}$	$0.24^{+0.04}_{-0.04}$	$8.01^{+0.45}_{-0.79}$	$1.79^{+0.29}_{-0.19}$	32.068
COSMOS-43982	$10.80^{+0.01}_{-0.06}$	$0.40^{+0.02}_{-0.01}$	$8.51^{+0.05}_{-0.15}$	$2.37^{+0.08}_{-0.04}$	71.642
CDFS-3865	$9.50^{+0.01}_{-0.03}$	$0.14^{+0.00}_{-0.00}$	$7.36^{+0.02}_{-0.04}$	$2.17^{+0.01}_{-0.01}$	32.170
CDFS-6482	$9.80^{+0.06}_{-0.05}$	$0.15^{+0.02}_{-0.02}$	$8.16^{+0.15}_{-0.15}$	$1.71^{+0.09}_{-0.09}$	12.374
SSA22-8043	$10.07^{+0.06}_{-0.06}$	$0.03^{+0.02}_{-0.01}$	$9.44^{+0.00}_{-0.10}$	$0.76^{+0.07}_{-0.03}$	112.288

Note: Physical properties and their 1σ errors of LAEs from SED fitting. Stellar metallicity is fixed to $0.2Z_\odot$. Escape fraction of ionizing photons is fixed to 0.05. (†) Values obtained after removing the contribution from an adjacent object (Section B.3.2).

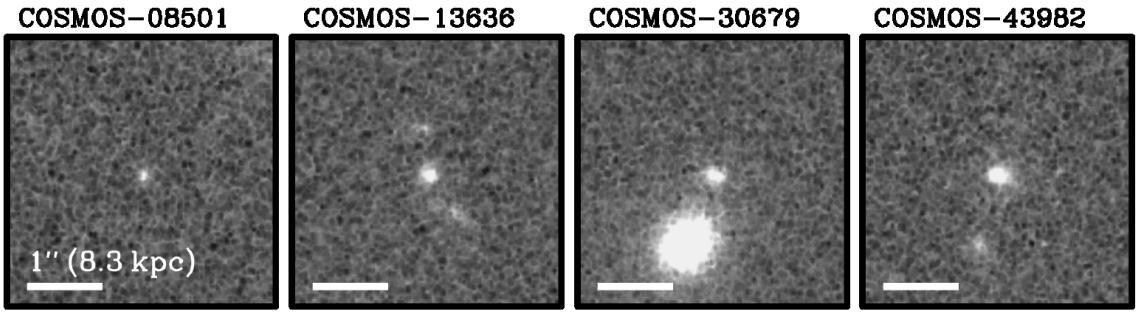

Figure B.6. HST/ACS F814W images for COSMOS objects. White tick indicates 1 arcsec, corresponding to ~ 8.3 kpc at $z = 2.2$. North is up and east is to the left.

formation history and the stellar metallicity $Z = 0.2Z_\odot$. For dust extinction, we use Calzetti's extinction law (Calzetti et al. 2000) on the assumption of $E(B-V)_{\rm gas} = E(B-V)_\star$ as proposed by Erb et al. (2006b), although this assumption is still debatable for high-z galaxies (e.g., Förster Schreiber et al. 2009; Ly et al. 2012)[B.3]. Intergalactic medium (IGM) attenuation is calculated using the prescription given by Madau (1995). These assumptions are usually used for SED fitting for high-z LAEs. E.g., Guaita et al. (2011) test three different star-formation histories when performing SED fitting to $z \sim 2.1$ stacked LAEs, and find equally good fits to the data. The authors also note that SED fitting can relatively well constrain stellar mass and dust extinction among the free parameters. The derived properties are given in Table B.4, and the best-fit SEDs are shown in Figure B.5.

One problem is that COSMOS-30679 was found to be blended with another brighter adjacent object via examination of the COSMOS HST/ACS F814W imaging data (Figure B.6). In order to deblend this object, we use the galaxy profile fitting software GALFIT (v3.0; Peng et al. 2010). We first run GALFIT in the B band and fit both objects simultaneously. Then, we perform fittings in other bands by

[B.3] Adopting $E(B-V)_{\rm gas} = E(B-V)_\star/0.44$ (Calzetti et al. 2000) decreases ionization parameters (Section B.3.3) by a factor of $\lesssim 2$, but the changes are smaller than their 1σ errors. Changes in metallicities are also small compared with the errors.

Table B.5. Physical Properties of the LAEs with NIR Spectroscopy from Nebular lines

Object	$12+\log(\mathrm{O/H})$		$q_{\rm ion}$	SFR	$\mathrm{SFR_{cor}}$	EW(Hα)	L(Hα)	EW(Lyα)	L(Lyα)	AGN
	$N2$	$R23$	(10^7 cm s^{-1})	($M_\odot$ yr^{-1})	($M_\odot$ yr^{-1})	(Å)	(10^{42} erg s^{-1})	(Å)	(10^{42} erg s^{-1})	(10)
	(1)	(2)	(3)	(4)	(5)	(6)	(7)	(8)	(9)	
COSMOS-08501	<8.73	···	···	$5.3^{+1.0}_{-1.0}$	$6.7^{+1.6}_{-2.1}$	>280	0.67 ± 0.13	255 ± 26	8.41 ± 0.40	0
COSMOS-13636	<8.61	···	···	$7.5^{+1.1}_{-1.1}$	$13.2^{+1.9}_{-1.9}$	93^{+26}_{-32}	0.95 ± 0.13	73 ± 5	11.35 ± 0.50	0
COSMOS-30679$^{(\dagger)}$	<8.46	$8.18^{+0.28}_{-0.28}$	8^{+10}_{-4}	$9.0^{+0.8}_{-0.8}$	$18.6^{+2.6}_{-2.6}$	93^{+25}_{-33}	1.14 ± 0.10	87 ± 7	8.47 ± 0.65	0
COSMOS-43982	···	···	···	$19.0^{+1.7}_{-1.7}$	$65.7^{+6.7}_{-6.0}$	41^{+4}_{-4}	2.41 ± 0.21	105 ± 8	11.00 ± 0.47	1
CDFS-3865	<8.35	$7.84^{+0.24}_{-0.25}$	25^{+17}_{-8}	$107.9^{+6.7}_{-6.7}$	$166.0^{+10.3}_{-10.3}$	813^{+175}_{-216}	13.65 ± 0.85	64 ± 29	29.79 ± 4.93	0
CDFS-6482	<8.72	···	···	$27.2^{+5.0}_{-5.0}$	$43.1^{+8.2}_{-8.2}$	261^{+103}_{-149}	3.45 ± 0.63	75 ± 52	15.40 ± 8.09	0
SSA22-8043	<8.90	···	···	$41.0^{+12.0}_{-12.0}$	$44.4^{+13.2}_{-13.1}$	120^{+53}_{-69}	5.19 ± 1.52	28 ± 4	2.22 ± 0.38	0

Note: (1) Oxygen abundance derived from $N2$-index (Section B.3.3). If [N II] is undetected, 1σ upper-limit is given. (2) Oxygen abundance derived from $R23$-index (Section B.3.3). Ionization parameter is derived simultaneously. (3) Ionization parameter (10^7 cm s^{-1}) estimated from the [O III]/[O II] ratio and $Z(R23)$ (Section B.3.3). (4) Star formation rate ($M_\odot$ yr^{-1}) derived from uncorrected Hα luminosity (Section B.3.4). (5) Star formation rate ($M_\odot$ yr^{-1}) derived from Hα luminosity after correcting for extinction derived from SED fitting (Section B.3.4). (6) Rest-frame equivalent width of Hα (Å; Section B.3.5). (7) Observed luminosity of Hα (10^{42} erg s^{-1}). (8) Rest-frame equivalent width of Lyα (Å; see Table Section B.1). (9) Observed luminosity of Lyα (10^{42} erg s^{-1}). (10) Flag of AGN (Section B.3.1): AGN candidates are flagged with "1". (†) Values obtained after removing the contribution from an adjacent object (Section B.3.2).

fixing parameters (except for brightnesses) to those derived in the B band fitting and derive the deblended photometry, which is listed in Table B.4. We confirm that the i' band brightness estimated from the deblended object is consistent with the photometry in the HST/ACS F814W high-resolution image within their errors. We add residuals after subtracting the fitted profiles into the photometric errors in quadrature, so that those errors are used in the SED fitting. Since the adjacent object appears dominant at longer wavelengths and deblending gets less reliable, we do not perform the deblending for the IRAC images. We therefore fit the SED of COSMOS-30679 after deblending without the IRAC data. The best fit SEDs of COSMOS-30679 after and before deblending are shown in two panels in the second row of Figure B.5. Although the bumpy shape of the SED after the deblending suggests additional contamination from the adjacent object, the fitting is acceptable (relatively small χ^2 value) compared with that obtained before deblending. In the following sections, we use the quantities after deblending.

We obtain from our sample stellar masses ranging from $7\times10^7\,M_\odot$ to $1\times10^{10}\,M_\odot$ and dust extinction $E(B-V)=0.03$ to 0.24 (except for the AGN LAE). These results are consistent with the previously recognized trend that LAEs at $z\sim2$ are diverse, unlike higher redshift counterparts (e.g., Nilsson et al. 2011). We also find that dust extinctions estimated from the Hα/Hβ ratio and SED fitting are consistent with each other for CDFS-3865 (Hashimoto et al. 2013). This supports our assumption that the dust extinction from SED fitting under the assumption of $E(B-V)_{\rm gas}=E(B-V)_\star$ can be reasonably applied for the extinction correction of nebular lines.

B.3.3. Ionization Parameter and Metallicity

The ionization state in an HII region is often characterized by the ionization parameter, $q_{\rm ion}$, which is the ratio of the mean ionizing photon flux to the mean hydrogen atom density. Larger $q_{\rm ion}$ means the HII region is more highly ionized, probably achieved by a harder ionizing spectrum. Consequently, emission lines with higher ionization potentials are expected to be observed more strongly with increasing $q_{\rm ion}$. In this sense, the ionization parameter is well determined using ratios of emission lines of different ionization stages of the same element, such as the [O III]/[O II] ratio (e.g., Kewley & Dopita 2002; Section 2.3.2). However, the [O III]/[O II] ratio depends not only on ionization state but also on gas metallicity (Fig. 1 of Kewley & Dopita 2002; Section 2.3.2). Since the gas temperature decreases as gas metallicity increases, the far infrared fine-structure cooling by doubly ionized species (i.e., O^{2+}) becomes efficient when the gas metallicity is high (e.g., Charlot & Longhetti 2001; Dopita et al. 2000), resulting in a decrease of [O III] line in optical. Conversely, metallicity estimates using $R23$-index are affected by the ionization parameter to some extent (e.g., Kewley & Dopita 2002; Nagao et al. 2006). Therefore, we combine the [O III]/[O II] ratio and $R23$-index (both corrected for dust extinction estimated from SED fitting) to estimate its ionization parameter and metallicity at the same time iteratively (see also Section 2.3.3). We assume in this chapter $f_{\rm esc}=0$ for simplicity. Possible effects of non-zero escape fractions are discussed in Section 5.1.5.

We describe the procedure for CDFS-3865 as an example. As an initial guess of metallicity, we use the empirical $R23$ indicator determined by local galaxies (Maiolino et al. 2008). We obtain two solutions $12+\log({\rm O/H})=7.45^{+0.24}_{-0.19}$ and $8.66^{+0.20}_{-0.26}$. We then use another alternative indicator, $N2$-index defined as [N II]λ6584/Hα (Maiolino et al. 2008). The upper-limit of $N2$-index provides an upper-limit of metallicity $12+\log({\rm O/H})=8.35$ (1σ), which removes the high-metallicity solution by $R23$-index at the 2.5σ level. Therefore, the empirical relation yields the metallicity $12+\log({\rm O/H})=7.45^{+0.24}_{-0.19}$. As the second step, we use this metallicity and the [O III]/[O II] ratio to estimate its ionization parameter.

Kewley & Dopita (2002) calculate the relations between [O III]/[O II] ratio and ionization parameter with discrete values of metallicity. Among them, our initial guess of metallicity corresponds to their lowest metallicity ($\sim 0.09\,Z_\odot$; Asplund et al. 2009). By using the relation, we find that the high [O III]/[O II] ratio can only be reproduced with ionization parameters as high as several times $10^8\,\mathrm{cm\,s^{-1}}$. As the third step, we recalculate its metallicity from the Kewley & Dopita (2002)'s relation ($R23$-index) for the ionization parameter $3\times10^8\,\mathrm{cm\,s^{-1}}$, and obtain $12+\log(\mathrm{O/H}) = 7.84^{+0.24}_{-0.25}$[B.4]. Finally, we recalculate its ionization parameter based on the metallicity and Eq. (12) of Kewley & Dopita (2002)[B.5], and obtain $q_\mathrm{ion} = 2.5^{+1.7}_{-0.8}\times10^8\,\mathrm{cm\,s^{-1}}$. This is consistent with the assumed ionization parameter in the third step ($3\times10^8\,\mathrm{cm\,s^{-1}}$). We check that further iterations do not change our final solutions. To summarize, CDFS-3865 has the ionization parameter $q_\mathrm{ion} = 2.5^{+1.7}_{-0.8}\times10^8\,\mathrm{cm\,s^{-1}}$ and the metallicity $12+\log(\mathrm{O/H}) = 7.84^{+0.24}_{-0.25}$.

In the same manner, we estimate COSMOS-30679's ionization parameter and metallicity to be $q_\mathrm{ion} = 8^{+10}_{-4}\times10^7\,\mathrm{cm\,s^{-1}}$ and $12+\log(\mathrm{O/H}) = 8.18^{+0.28}_{-0.28}$, respectively. Since COSMOS-30679 does not have Hβ, its strength is inferred from Hα assuming the Case B and the dust extinction. In addition, its broadband SED is fitted after being deblended with the adjacent object (Section B.3.2). Therefore, the object may possess larger uncertainties.

For the LAEs without [O II], we estimate their metallicities by using the empirical $N2$-index relation, and no constraint on ionization parameters is provided for them.

The metallicities and the ionization parameters are summarized in Table B.5.

B.3.4. Star Formation Rate

The Hα luminosity is thought to be the most reliable SFR indicator relative to those based on the rest-frame UV and optical spectral features. Indeed, it is proportional to the birth rate of massive stars as well as being relatively insensitive to dust extinction as compared with UV-continuum. We measure the SFR of the LAEs from the Hα luminosity using the relation (Kennicutt 1998):

$$\mathrm{SFR}\,[M_\odot\,\mathrm{yr^{-1}}] = 7.9\times10^{-42}L(\mathrm{H}\alpha)\,\mathrm{erg\,s^{-1}}. \tag{B.1}$$

In Table B.5, we summarize the derived SFRs.

B.3.5. Hα Equivalent Width

We calculate the Hα equivalent width of an object from the Hα flux divided by its continuum flux density derived from K band photometry. To estimate the proper continuum, however, we have to remove the contribution of the Hα emission on the K band photometry. We follow the prescription given in the appendix of Guaita et al. (2010) (see also Finkelstein et al. 2011):

$$f_\nu(\mathrm{H}\alpha) = R_T\times\frac{F(\mathrm{H}\alpha)}{\int T_K(\lambda)\frac{c}{\lambda^2}\,d\lambda}, \tag{B.2}$$

where $f_\nu(\mathrm{H}\alpha)$ is the amount of flux that Hα line contributes to the K band photometry, $F(\mathrm{H}\alpha)$ is the observed Hα flux, R_T is the ratio between the filter transmission at $\lambda_{\mathrm{H}\alpha}$ and the maximum of the K band transmission function, and $T_K(\lambda)$ is the K band filter transmission at a given wavelength. The flux

[B.4] Using the $1.5\times10^8\,\mathrm{cm\,s^{-1}}$ relation does not change the metallicity estimate significantly (~ 0.02 dex lower).

[B.5] Although the original relations are suspended at $q_\mathrm{ion} = 3\times10^8\,\mathrm{cm\,s^{-1}}$, we extend their polynomials toward higher q_ion values.

estimated from the calculation is subtracted from the K band photometry. The corrections span from 0.05 (COSMOS-43982) to as much as 0.63 mag (CDFS-3865). Since COSMOS-08501 is not detected in the K band, we use the 1σ lower-limit of the K band photometry. We thus obtain an upper-limit of the continuum (correction > 0.26 mag), hence a lower-limit of the EW(Hα) for COSMOS-08501. The derived EWs(Hα) are listed in Table B.5.

C Physical Properties of LAEs from NIR Narrowband Imaging

In this appendix, we present the full description of the triple narrowband survey (Section 3.2). We report the average metallicity and SFR of $z \simeq 2.2$ LAEs measured from [O II]λ3727, and Hα (+[N II]$\lambda\lambda$6584, 6548), which are obtained by the two NIR narrowband filters NB118 ($\lambda_c = 11866$Å, FWHM= 111Å) and NB209 ($\lambda_c = 20958$Å, FWHM= 205Å), respectively, developed by J. Lee et al. (Lee et al. in preparation; see also Ly et al. 2011; Lee et al. 2012). By stacking NIR narrowband images of the LAEs, we successfully obtain average nebular-line fluxes of LAEs, the majority of which are too faint to be identified individually by narrowband imaging or spectroscopy. The stacked objects have a stellar mass of $\lesssim 10^9 M_\odot$, enabling us to investigate properties of low-mass galaxies at high-z. Previous high-z spectroscopic samples are biased for high-mass galaxies ($\gtrsim 10^{9.5} M_\odot$). The stacked LAEs thus provide the opportunity for us to examine the relation between stellar mass, SFR, and metallicity in the lowest mass range at high-z.

We describe the triple narrowband survey in Section C.1. In Section C.2, we show the stacking analysis to detect [O II] and Hα+[N II] emission. Objects with individual detections of these lines are also briefly mentioned. In Section C.3, we derive metallicity and SFR for the stacked LAEs. The stellar populations inferred from SED fitting to the broadband photometry of the stacked LAEs are also presented.

C.1. Triple Narrowband Survey

C.1.1. Overview

The redshift $z \simeq 2.2$ is unique because [O II]λ3727 and Hydrogen Hα lines fall into wavelength ranges where OH airglow is very weak (Figure 1.5), thus enabling one to study SFRs and metallicities of LAEs using these lines from the ground. As described in Appendix A, we developed a new NB filter, NB387, to select LAEs over $z = 2.14$–2.22. Two emission lines of [O II] and Hα in this redshift range are then observed through NIR narrowband filters, NB118 ($\lambda_c = 11866$ Å and FWHM= 111 Å) and NB209 ($\lambda_c = 20958$ Å and FWHM= 205 Å), respectively, developed by the NewHα Survey (Lee et al. 2012; J. Lee et al. in preparation). The response curves of these two narrowband filters are shown in Figure C.1. In this chapter, we present the results from data of the Subaru/XMM-Newton Deep Survey (SXDS) field, which are the first results of this triple-narrowband survey.

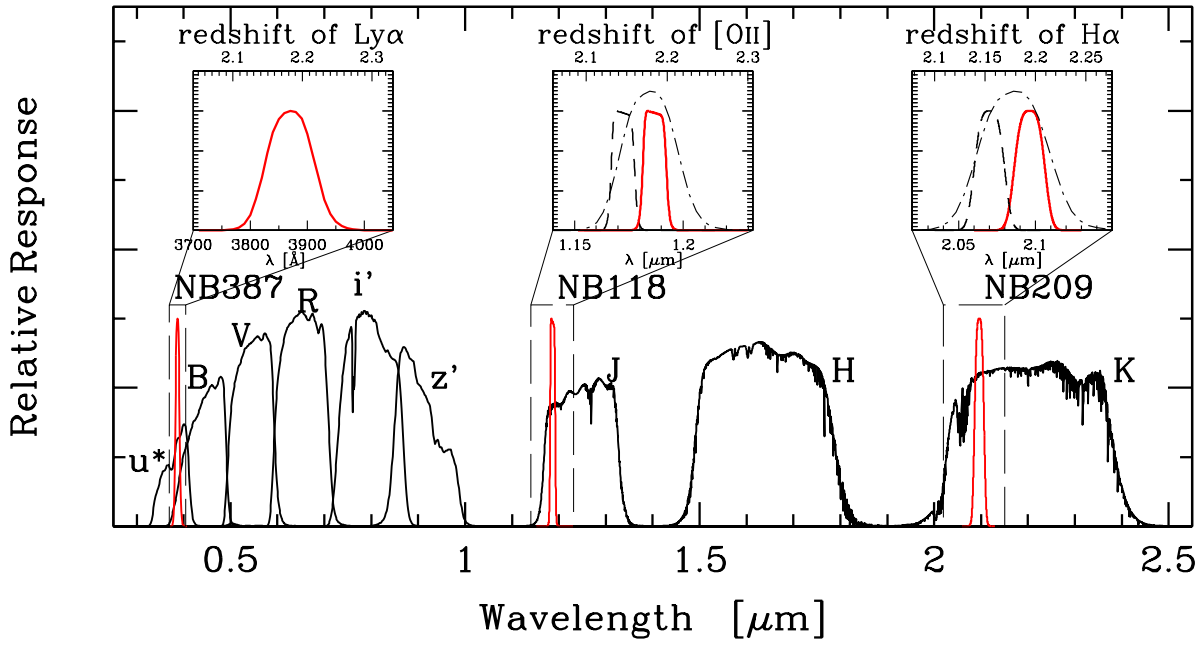

Figure C.1. Relative response curves of the triple narrowband filters, NB387 at Subaru and NB118 and NB209 at KPNO/NEWFIRM (red), superimposed on those of the optical and NIR broadband filters (Figure A.6). The responses include the throughputs of the instrument and the telescope as well as atmospheric absorption. The inner panels are a zoom-in around NB387, NB118, and NB209, whose upper x-axis shows the redshifts of Lyα, [O II], and Hα, respectively. In the NB118 and NB209 zoom-in panels, the dashed curves indicate the response curves of NB118 and NB209 at the corner of the filter (see the text for details; Equation (C.1)), while the dot-dashed lines are re-scaled response curves of NB387 along the wavelength axis to sample [O II] and Hα after correction for a velocity offset between Lyα and nebular lines of 400 km s^{-1}.

C.1.2. NB118 and NB209 Imaging Data

The SXDS field has been partly imaged in the NIR NB118 and NB209 narrowbands with KPNO/NEWFIRM by the NewHα Survey (Lee et al. 2012; J. Lee et al. in preparation). Details on the NB118 observations are also given in Ly et al. (2011). The regions imaged are shown in Figure C.2. Exposure times were 8.47–12.67 hr for NB118 and 11.75 hr for NB209. Both images were registered to the Suprime-Cam z' band images using common bright stars. The 5σ limiting magnitudes in a 2″ diameter aperture are estimated to be $\simeq$ 23.6 mag for the NB118 and $\simeq$ 22.6 mag for the NB209[C.1]. Errors in photometric zero points of the NB118 and NB209 images are less than 0.05 mag, which are inferred following the same manner as the NB387 images.

In NEWFIRM the incident angle to the filter surface is not exactly normal but varies as a function of the distance from the field center (J. Lee et al. in preparation; see also Tanaka et al. (2011) for Subaru/MOIRCS). Accordingly, the central wavelength of NB118 and NB209 also varies over the FoV, since both filters are interference filters. The central wavelength at an incident angle θ (angle from

[C.1] Our effective limiting magnitudes of NB118 and NB209 are 0.2 – 0.3 mag deeper than the magnitudes listed here owing to smoothing procedures (see Section C.2.1). The limiting magnitudes after the smoothing are described in Section C.2.2.

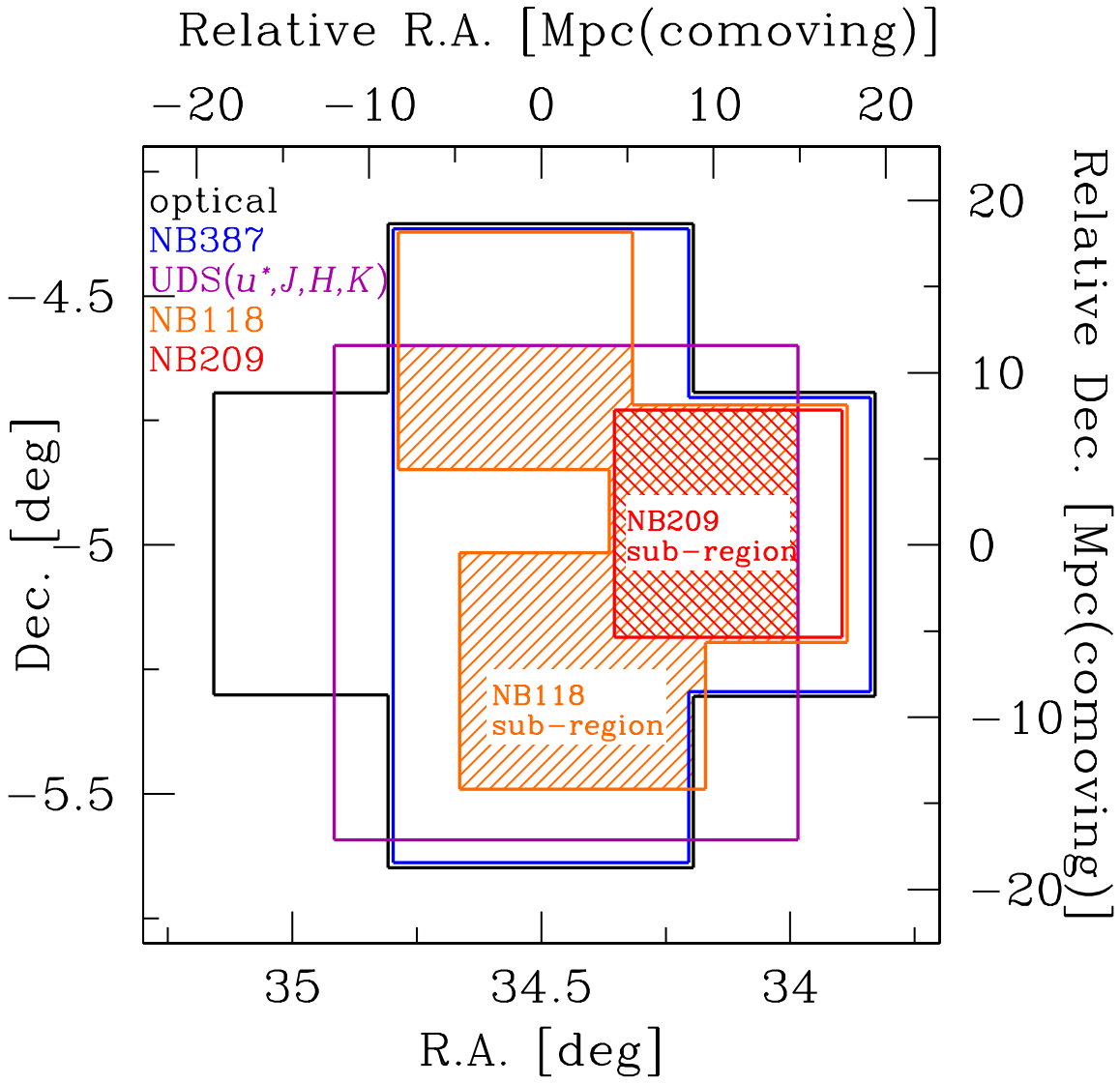

Figure C.2. Areas covered by respective imaging data in the SXDS. Lines in different colors outline areas covered in different passbands: blue: NB387; magenta: u^* and J, H, K; orange: NB118; red: NB209; black: optical (B, V, R, i', z'). The orange-shaded and red-shaded regions correspond to the NB118 sub-region and the NB209 sub-region, respectively. Note that the NB209 sub-region is embedded in the the NB118 sub-region (see Section C.1.2).

normal incidence) is given by

$$\lambda(\theta) = \lambda_0 \cos(\theta/n), \tag{C.1}$$

where λ_0 is the wavelength at normal incidence and n is the index of refraction of the material on which interference film is coated. We adopt $n = 1.50$ for NB118 and $n = 1.49$ for NB209 (J. Lee et al. in preparation). At the corner of the filter θ has the maximum value of 13.5 degree. Thus, the maximum wavelength shifts are $\simeq -150$ Å and $\simeq -260$ Å for NB118 and NB209, respectively. The passband of NB387 is broad enough to cover Lyα lines at the redshifts of [O II] and Hα lines corresponding to these shifted wavelengths (see also inner panels of Figure C.1). However, as seen in §C.2.1.2, we have to take

into account the passband shift over the FoV when calculating the equivalent widths and fluxes of [O II] and Hα lines of stacked objects.

We select LAEs in a $2,003\,\mathrm{arcmin}^2$ region which is covered by all the three passbands for selecting LAES: NB387, u^*, and B (the region enclosed by both the blue and magenta lines in Figure C.2; see also Section A.2.1). In this chapter, however, we use only LAEs in a sub-region of $1,283\,\mathrm{arcmin}^2$ which is covered by NB118 (orange-shaded area in Figure C.2). In this "NB118 sub-region," a $353\,\mathrm{arcmin}^2$ region is covered by NB209 as well ("NB209 sub-region"; red-shaded area in Figure C.2). Note that the J, H, K data are available for the NB118 sub-region. Among the 919 LAE candidates found in the entire SXDS field (Section A.2.1), 561 are in the NB118 sub-region and 105 in the NB209 sub-region.

C.2. [O II] and Hα Emission Lines

Our NIR images are not deep enough to study [O II] and Hα properties of LAEs based on individual detections. Indeed, only 10 objects have detection of [O II] emission and only 3 have detection of Hα+[N II] emission, as described in §C.2.2. We therefore carry out a stacking analysis of the whole LAE sample in the NB118 sub-region, and discuss average emission-line properties of $z \simeq 2.2$ LAEs. The individually detected objects are discussed below and compared with the stacked objects.

C.2.1. Stacking Analysis

Stacking is done separately for the NB118 sub-region and the NB209 sub-region. For the NB118 sub-region, we stack the NB118 and J images at the positions of 561 LAE candidates. Similarly, for the NB209 sub-region, the NB118, J, NB209, and K images are stacked at the positions of the 105 LAE candidates. Before stacking, we mask regions affected by a ghost, a stellar halo, and bad pixels, as well as regions with relatively large noise. The stacked image in the NB118 sub-region are used to detect the [O II] flux at the highest S/N ratio, while the stacked image in the NB209 sub-region are used to compare [O II] and Hα fluxes in a common sample. To derive the average Lyα flux, we also stack NB387 and u^* images for each sub-region. All stackings are done by median-stacking. Before the stacking, we smooth the images with gaussian filters so that both narrowband and broadband images have the same PSF sizes. This enables us to measure the colors of the stacked objects by aperture photometry (Section C.2.1.1). The PSF size before smoothing is $1\farcs6$ for NB118 and J, $1\farcs2$ for NB209 and K, and $1\farcs2$ for NB387 and u^*. We do not remove the individually detected objects from the stacking analysis in order to increase the number of candidates for stackings. In fact, results after removing the individually detected objects are consistent with the results in Equation (C.2) owing to the median-stacking.

The stacked images are shown in Figure C.3. A signal is clearly visible in all the passbands including NB118 and NB209. We measure the magnitudes and colors of the stacked images in Section C.2.1.1, and convert them into line fluxes using Monte Carlo simulations in Section C.2.1.2.

C.2.1.1. Photometry

We measure aperture magnitudes of the stacked objects using the IRAF task `phot`. The aperture diameter is set to be $2\farcs5 - 3\farcs2$ (about twice the PSF size) to calculate colors, while larger apertures of $4\farcs8 - 6\farcs1$ (depending on the passband) are adopted to obtain total magnitudes. Errors in the magnitudes are estimated in the same manner as in Ono et el. (2010b); we create 1,000 median-stacked sky noise

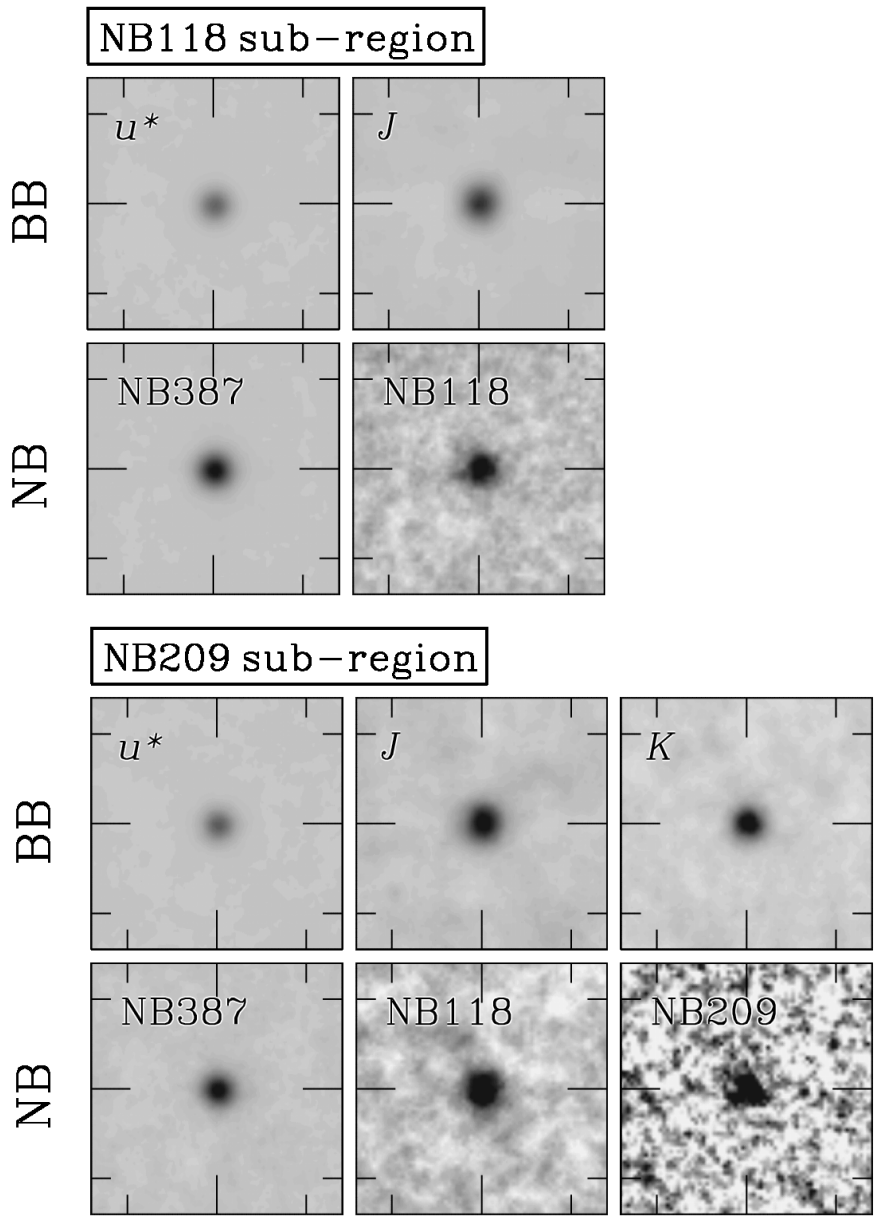

Figure C.3. *Top:* Snapshots of the stacked LAE in u^* (top left), NB387 (bottom left), J (top right), and NB118 (bottom right) in the NB118 sub-region. *Bottom:* Snapshots of the stacked LAE in u^* (top left), NB387 (bottom left), J (top center), NB118 (bottom center), K (top right), and NB209 (bottom right) in the NB209 sub-region. Each image is $15'' \times 15''$ in size.

images, each of which is made of 561 (105) randomly-selected sky noise images in the NB118 (NB209) sub-regions. We then fit the negative part of histograms with a Gaussian, whose FWHMs are used to estimate the limiting magnitudes. The magnitudes and errors obtained are summarized in Table C.1. The uncertainties of zero points are not included in the errors.

C.2.1.2. Equivalent Widths and Fluxes of the Lines

The $J-$NB118 and $K-$NB209 colors for the stacked objects are calculated to be:

$$\begin{aligned} J-\mathrm{NB118}\,(\mathrm{NB118sub}) &= 0.43\pm0.05 \\ J-\mathrm{NB118}\,(\mathrm{NB209sub}) &= 0.39\pm0.08 \\ K-\mathrm{NB209}\,(\mathrm{NB209sub}) &= 0.65\pm0.11, \end{aligned} \tag{C.2}$$

where the color with 'NB118sub' and 'NB209sub' in round brackets is derived from the stacked object in the NB118 sub-region and that in the NB209 sub-region, respectively. These large, positive values with the small errors indicate significant detection of the lines. In order to estimate the [O II] and Hα+[N II] equivalent widths and fluxes with the best accuracy, we used Monte Carlo simulations. If both a narrowband and a broadband (which brackets the narrowband) filters have ideal top-hat response functions, an EW of an emission line falling in the narrowband can be calculated as:

$$\mathrm{EW_{rest}} = \frac{\left(f_\lambda^N - f_\lambda^B\right)\Delta\lambda^N\Delta\lambda^B}{\Delta\lambda^B f_\lambda^B - \Delta\lambda^N f_\lambda^N}\frac{1}{1+z}, \tag{C.3}$$

where f_λ is the flux density per unit wavelength, $\Delta\lambda$ is the width of a given filter, z is redshift, and superscripts N and B indicate narrowband and broadband, respectively. To derive this formula, we have assumed that the flux density of the continuum emission is constant over the whole wavelength range. If this formula is used, the colors obtained above are converted into $\mathrm{EW_{rest,NB118sub}}$ ([O II])$=25$ Å, $\mathrm{EW_{rest,NB209sub}}$ ([O II])$=23$ Å, and $\mathrm{EW_{rest,NB209sub}}$ (Hα+[N II])$=58$ Å, respectively.

Although these values are useful as zero-order estimates, their accuracy is not sufficient for our purpose. In fact the assumption on the shape of the passband used to derive Equation (C.3) is over simplified in two aspects: the actual NB118 and NB209 passbands are not top-hat but rather close to a triangle shape and the central wavelengths of these passbands vary over the FoV (Equation (C.1); see §C.1.2). These issues must be considered to obtain correct EW values, since the objects used for stacking have different redshifts (corresponding to the different locations within the band width of NB387) and they are distributed across the FoV. In general, Equation (C.3) is correct only when a line is located where the response function of the narrowband peaks. In reality, however, a large fraction of the LAEs are expected to have [O II] and Hα+[N II] lines off the peak responses of NB118 and NB209 based on the re-scaled shapes of NB387 (see Figure C.1). This means that the EWs of stacked objects calculated by Equation (C.3) are always underestimated.

We carry out Monte Carlo simulations taking into account of the above two points more accurately to estimate the EWs from the observed colors of the stacked objects. As an example, we describe below the simulations for the [O II] line of the objects in the NB118 sub-region. The simulations for [O II] and Hα+[N II] lines in the NB209 sub-region are essentially the same.

The simulations are carried out under the assumption that all 561 objects have identical spectra, i.e., the same EW and the same underlying continuum spectra. For the continuum spectra, we use the best-fit spectrum from the SED fitting to the stacked LAE (see Section C.3.1)[C.2]. We then vary $\mathrm{EW_{rest}}$

[C.2] We also try two independent SEDs for the simulation; the best-fit SED of spectroscopically confirmed BX galaxies at $2.0 < z < 2.2$ with constant star formation history (Guaita et al. 2011) and the best-fit spectrum from the SED fitting to the $z = 3.1$ stacked LAE (Ono et al. 2010a), and find that the results are consistent with each other well within their 1σ errors.

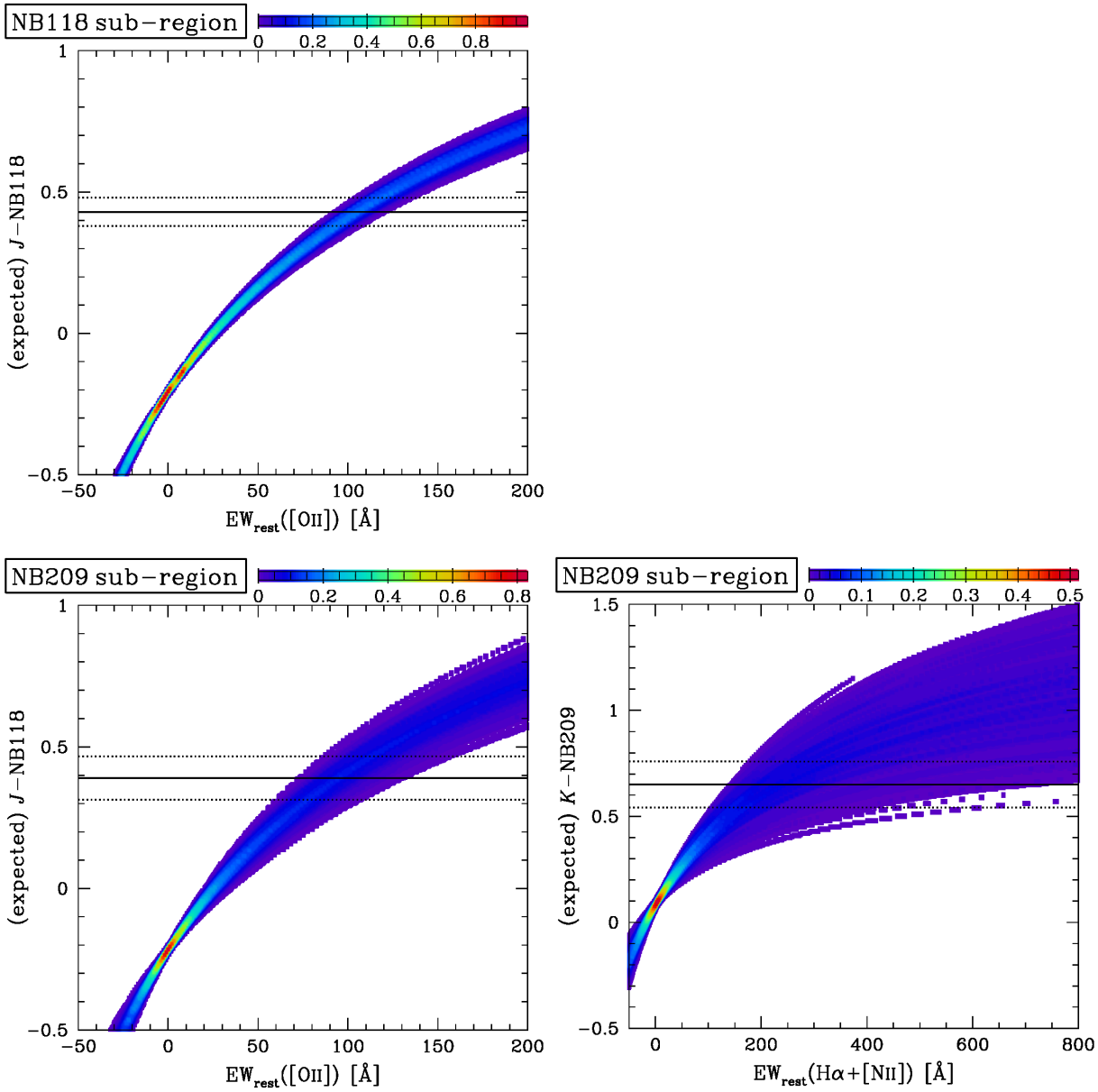

Figure C.4. Relation between EW_{rest} and expected $J-$NB118 and $K-$NB209 colors from the Monte Carlo simulations: *(top left)* EW_{rest} ([O II]) vs. $J-$NB118 in the NB118 sub-region; *(bottom left)* EW_{rest} ([O II]) vs. $J-$NB118 in the NB209 sub-region; *(bottom right)* EW_{rest} (Hα+[N II]) vs. $K-$NB209 in the NB209 sub-region. The color contours indicate the probability of $J-$NB118 or $K-$NB209 at given EW_{rest}; redder colors mean higher possibilities as shown in the color bars in the top. The solid black lines correspond to the measured $J-$NB118 or $K-$NB209 colors and the dotted black lines are their 1σ errors.

over -100 Å and 300 Å with 1 Å interval, and for each value we carry out a Monte Carlo simulation described by steps 1 – 4 below to derive the probability distribution of $J-$NB118 color for that EW. We thus simulate the relation between EW and $J-$NB118. The EW of the real, stacked object is calculated by substituting the observed $J-$NB118 color into the relation.

1. We first generate 561 LAEs with a given EW value, and assign to each one of the 561 positions on the FoV of the real objects without duplication. Then, assuming that the (Lyα) redshift distribution of our LAEs is same as the shape of the NB387 response function, with a peak at $z = 2.18$ and an FWHM of $\Delta z = 0.075$, we randomly select a redshift for each of the 561 objects from this distribution.

2. Spectroscopic observations of high-redshift star-forming galaxies have found that the redshift measured from Lyα line is offset from the nebular-line redshift by a few hundred km s^{-1}, due to radial acceleration of the circumgalactic gas emitting the line (e.g., Pettini et al. 2001; Steidel et al. 2010; McLinden et al. 2011; Finkelstein et al. 2011). We randomly assign a redshift offset to each of the 561 objects simulated in step 1, assuming that the offsets obey the distribution function obtained by Steidel et al. (2010) for $z \sim 2$ galaxies[C.3]. Each object is thus given an [O II] redshift.

3. For each object we calculate f_λ^J and $f_\lambda^{\mathrm{NB118}}$ using the EW, continuum spectrum, [O II] redshift, and the NB118 response function at the position of the object on the FoV. We then sum the 561 objects' f_λ^J and $f_\lambda^{\mathrm{NB118}}$, and divide the former by the latter to obtain the $J-$NB118 color of the stacked object.

4. We repeat steps 1 – 3 500 times to obtain the probability distribution of $J-$NB118 color for the given EW.

Figure C.4 shows the results of the simulations, i.e., the distribution of $J-$NB118 and $K-$NB209 color as a function of EW. In each panel, the color contour indicates the probability of $J-$NB118 or $K-$NB209 at given EWs, and the solid line and two dotted lines indicate the central value and the 1σ lower and upper limits, respectively, of the observed color. We translate the observed colors and their errors into EWs in the following manner. First, we assume that for each of $J-$NB118 and $K-$NB209, the probability distribution of the true value is a Gaussian with its σ equal to the observed 1σ error in that color. Next, we randomly select a color following this Gaussian probability distribution, and assign to it an EW based on the EW probability distribution against color shown in Figure C.4. We repeat this procedure 10,000 times. Finally, we sort the 10,000 EWs in ascending order, and regard the 50 %-tile, 16%-tile, and 84 %-tile as the central value, 1σ lower limit, and 1σ upper limit, respectively. From the translation procedures, we obtain $\mathrm{EW_{rest}}$ for [O II] and Hα+[N II]:

$$\begin{aligned} \mathrm{EW_{rest,NB118sub}}(\mathrm{[O\,II]}) &= 106^{+14}_{-12}\,\text{Å} \\ \mathrm{EW_{rest,NB209sub}}(\mathrm{[O\,II]}) &= 96^{+23}_{-19}\,\text{Å} \\ \mathrm{EW_{rest,NB209sub}}(\mathrm{H\alpha{+}[N\,II]}) &= 271^{+242}_{-104}\,\text{Å}. \end{aligned} \tag{C.4}$$

[C.3] Although LAEs are so far found to have systematically smaller velocity offsets than LBGs, ~ 200 km s^{-1} for LAEs (Hashimoto et al. 2013; see also McLinden et al. 2011; Finkelstein et al. 2011) while ~ 400 km s^{-1} for LBGs (Steidel et al. 2010), we use the data of Steidel et al. (2010) since it is based on much a larger number of measurements (> 40 LBGs while 4 LAEs) and thus statistically more reliable. In any case, the wavelength shift caused by velocity offset is much smaller than that due to the variation of the response curve over the FoV (~ 15Å by a velocity offset of ~ 400 km s^{-1} while up to ~ 150Å by the positional variation for NB118).

Table C.1. Color and Emission Line Properties of the stacked LAEs in the two sub samples

sub-sample $\cdots[N]^{(1)}$	Line	$m^{\rm BB}_{\rm aper}$ (2)	$m^{\rm NB}_{\rm aper}$ (3)	$m^{\rm NB}_{\rm total}$ (4)	EW$_{\rm rest}$ (5)	Flux (6)	Luminosity (7)
NB118	[O II]	25.18 ± 0.02	24.74 ± 0.05	24.57	106^{+14}_{-12}	$9.65^{+0.39}_{-0.39}\times10^{-18}$	$3.54^{+0.14}_{-0.14}\times10^{41}$
$\cdots[561]$	Lyα	25.83 ± 0.01	25.05 ± 0.01	24.87	86^{+3}_{-2}	$5.76^{+0.11}_{-0.09}\times10^{-17}$	$2.11^{+0.04}_{-0.03}\times10^{42}$
NB209	[O II]	24.72 ± 0.03	24.33 ± 0.07	24.11	96^{+23}_{-19}	$1.44^{+0.09}_{-0.10}\times10^{-17}$	$5.26^{+0.35}_{-0.38}\times10^{41}$
$\cdots[105]$	Hα+[N II]	24.72 ± 0.03	24.07 ± 0.10	23.62	271^{+242}_{-104}	$2.18^{+0.34}_{-0.33}\times10^{-17}$	$7.98^{+1.25}_{-1.21}\times10^{41}$
	H$\alpha^{(8)}$	$\cdots$	$\cdots$	$\cdots$	256^{+229}_{-98}	$2.06^{+0.32}_{-0.31}\times10^{-17}$	$7.55^{+1.19}_{-1.15}\times10^{41}$
	Lyα	25.75 ± 0.02	25.09 ± 0.02	24.94	63^{+3}_{-5}	$4.90^{+0.12}_{-0.19}\times10^{-17}$	$1.80^{+0.05}_{-0.07}\times10^{42}$

Note: (1) Numbers of stacked objects in square brackets. (2) Broadband aperture magnitudes and their 1σ errors. Broadbands are J for [O II], K for Hα+[N II], and u^* for Lyα. The diameter of the aperture is $2\farcs5-3\farcs2$. Aperture sizes are chosen to have twice the PSF sizes. (3) Narrowband aperture magnitudes and their 1σ errors. Narrowbands are NB118 for [O II], NB209 for Hα+[N II], and NB387 for Lyα. The diameter of the aperture is $2\farcs5-3\farcs2$. Aperture sizes are chosen to have twice the PSF sizes. (4) Narrowband total magnitudes. The diameters of the aperture are $4\farcs8$ and $6\farcs1$ for [O II] and Lyα line in the NB118 sub-region, respectively, and $5\farcs7$, $5\farcs7$, and $6\farcs1$ for [O II], Hα+[N II], and Lyα line in the NB209 sub-region, respectively. Aperture sizes are chosen to include close to 100 % of the flux. (5) Rest-frame equivalent width of the lines (Å). For [O II] and Hα+[N II], EWs are estimated by Monte Carlo simulations (see §C.2.1.2 in details), and for Lyα, the colors of u^*-NB387 are used for the estimates of EWs. (6) Line fluxes in unit of erg s^{-1} cm^{-2}. (7) Line luminosities in unit of erg s^{-1}. (8) The contribution from [N II]$\lambda\lambda6584,6548$ lines is subtracted from the observed Hα+[N II] luminosity using the metallicity estimated in Section C.3.2 (see also Section C.3.3).

The errors in EW correspond to 1σ. The large scatter in $\mathrm{EW_{rest,\,NB209sub}}(\mathrm{H}\alpha+[\mathrm{N\,II}])$ is due to the large photometric error of $K-\mathrm{NB209}$ (see Equation (C.2)) and the large variance of the NB209 passband over the FoV.

We calculate the [O II] and Hα fluxes from the EWs obtained here combined with the total magnitudes derived in §C.2.1.1, and convert them into luminosities. These values are summarized in Table C.1.

We estimate the Lyα EW in a similar manner to what we explain above; we run the same Monte Carlo simulation skipping step 2, and then translate the $u^*-\mathrm{NB387}$ color into the Lyα EW. The Lyα $\mathrm{EW_{rest}}$ derived for the NB118 (NB209) sub-region is 86^{+3}_{-2} (63^{+3}_{-5}) Å, from which we obtain the observed Lyα luminosity to be $2.11^{+0.04}_{-0.03}\times10^{42}$ ($1.80^{+0.05}_{-0.07}\times10^{42}$) erg s^{-1} (Table C.1).

From previous narrowband surveys, LAEs with $L(\mathrm{Ly}\alpha)=10^{42}-10^{44}$ erg s^{-1} are referred to as typical LAEs (e.g., Gronwall et al. 2007; Ouchi et al. 2008) Therefore, the stacked LAEs we obtain are expected to have average properties of LAEs with $L(\mathrm{Ly}\alpha)>10^{42}$.

C.2.2. Individual Objects

Seventeen out of the 561 LAE candidates in the NB118 sub-region are detected in NB118 at $\geq 5\sigma$ levels, among which ten have $J-\mathrm{NB118}\geq0.0$ and $\mathrm{NB118}<\mathrm{NB118}\,(5\sigma)$[C.4], indicative of the presence of [O II] emission. A detailed calculation using the continuum spectrum from the SED fitting shows that these detection criteria correspond to $\mathrm{EW_{rest}}([\mathrm{O\,II}])\gtrsim7$ Å and $f([\mathrm{O\,II}])\gtrsim1.2\times10^{-17}$ erg s^{-1} cm^{-2}. Similarly, seven out of the 105 objects in the NB209 sub-region are detected in NB209 at $\geq5\sigma$ levels, among which three has $K-\mathrm{NB209}>0.3$ and $\mathrm{NB209}<\mathrm{NB209}\,(5\sigma)$, indicative of the presence of Hα+[N II] emission at more than the 5σ level. These detection criteria correspond to $\mathrm{EW_{rest}}(\mathrm{H}\alpha+[\mathrm{N\,II}])\gtrsim22$ Å and $f(\mathrm{H}\alpha+[\mathrm{N\,II}])\gtrsim2.1\times10^{-17}$ erg s^{-1} cm^{-2}. Two of the Hα+[N II] detected objects (SXDS5-04041 and SXDS5-04492) are also detected in [O II], while one (SXDS1-22326) is not detected in [O II], probably due to a variation of dust extinction and the complicated origin of the [O II] luminosity (see Section C.3.3.2). The EWs and line luminosities of these objects are summarized in Table C.2.

C.2.3. Average EWs and Luminosities of [O II] and Hα

Before presenting the physical properties derived from [O II] and Hα emission lines, we summarize the strengths of these lines of the stacked LAEs.

The stacked object from the NB118 sub-region has $\mathrm{EW}([\mathrm{O\,II}])=106^{+14}_{-12}$ Å and $L([\mathrm{O\,II}])=3.54^{+0.11}_{-0.11}\times10^{41}$ erg s^{-1}. This EW([O II]) is much larger than those obtained for typical high-z galaxies (e.g., $z\sim1$ galaxies from the DEEP2 survey; Cooper et al. 2006).

The stacked object from the NB209 sub-region has $\mathrm{EW}(\mathrm{H}\alpha+[\mathrm{N\,II}])=271^{+242}_{-104}$ Å and $L(\mathrm{H}\alpha+[\mathrm{N\,II}])=7.98^{+1.17}_{-1.15}\times10^{41}$ erg s^{-1}, which correspond to $\mathrm{EW}(\mathrm{H}\alpha)=256^{+229}_{-98}$ Å and $L(\mathrm{H}\alpha)=7.55^{+1.11}_{-1.10}\times10^{41}$ erg s^{-1} after subtraction of [N II] emission (see Section C.3.3). This EW(Hα) is larger than those obtained for other high-z galaxies; e.g., Erb et al. (2006b) performed Hα spectroscopy of $z\sim2$ UV-selected galaxies to find the median EW(Hα) $\sim$ 170Å (note that EW(Hα) of UV-selected galaxies from Hα spectroscopy may be biased high, since objects with stronger Hα emission can be observed more easily). Recently,

[C.4]The 5σ limiting magnitude here is defined with aperture sizes of $3\farcs2$ diameter for NB118 and $2\farcs5$ diameter for NB209, and estimated to be $\simeq22.9$ and $\simeq22.4$, respectively.

Table C.2. Emission Line Properties of the individually detected objects

ID	RA[(1)]	Dec.[(1)]	$EW_{Ly\alpha}$ (2)	$L_{Ly\alpha}$ (3)	$EW_{[O\,II]}$ (4)	$L_{[O\,II]}$ (5)	$EW_{H\alpha+[N\,II]}$ (6)	$L_{H\alpha+[N\,II]}$ (7)
SXDS1-06908	02:17:57.113	-05:06:37.06	45^{+9}_{-7}	$4.58^{+0.71}_{-0.65}$	277^{+154}_{-93}	$3.90^{+0.17}_{-0.22}$	···	···
SXDS1-22326	02:17:11.390	-04:51:14.10	54^{+23}_{-17}	$1.56^{+0.49}_{-0.42}$	···	···	198^{+67}_{-55}	$2.93^{+0.28}_{-0.34}$
SXDS1-26967	02:17:19.875	-04:46:54.76	31^{+13}_{-10}	$0.96^{+0.33}_{-0.28}$	22^{+10}_{-8}	$2.27^{+0.56}_{-0.65}$	···	···
SXDS2-01923	02:17:55.840	-04:47:40.11	121^{+32}_{-24}	$4.87^{+0.75}_{-0.68}$	127^{+32}_{-26}	$3.81^{+0.18}_{-0.21}$	···	···
SXDS3-25047	02:17:32.417	-05:12:51.09	31^{+3}_{-2}	$19.43^{+1.39}_{-1.35}$	18^{+2}_{-2}	$6.90^{+0.48}_{-0.50}$	···	···
SXDS5-00165	02:17:07.486	-04:53:53.75	59^{+16}_{-13}	$3.45^{+0.72}_{-0.64}$	35^{+19}_{-15}	$1.40^{+0.32}_{-0.39}$	···	···
SXDS5-00372	02:17:04.957	-04:45:35.62	32^{+7}_{-6}	$4.94^{+0.95}_{-0.87}$	20^{+9}_{-7}	$1.63^{+0.40}_{-0.45}$	···	···
SXDS5-02225	02:16:46.049	-04:59:05.44	39^{+12}_{-10}	$1.82^{+0.44}_{-0.40}$	10^{+8}_{-7}	$0.86^{+0.45}_{-0.53}$	···	···
SXDS5-04041	02:16:28.164	-04:45:17.72	63^{+18}_{-14}	$2.99^{+0.62}_{-0.55}$	75^{+19}_{-16}	$3.87^{+0.27}_{-0.31}$	406^{+66}_{-58}	$6.80^{+0.20}_{-0.22}$
SXDS5-04492	02:16:23.751	-04:57:57.92	43^{+13}_{-11}	$2.31^{+0.55}_{-0.49}$	92^{+37}_{-28}	$2.98^{+0.26}_{-0.32}$	68^{+27}_{-24}	$2.08^{+0.43}_{-0.51}$
SXDS5-06136	02:16:07.936	-05:00:07.96	40^{+8}_{-7}	$5.50^{+0.94}_{-0.87}$	12^{+3}_{-3}	$2.44^{+0.47}_{-0.50}$	···	···

Note: (1) Coordinates are in J2000. (2) Rest-frame equivalent width of Lyα in unit of Å. (3) Lyα luminosity in unit of 10^{42} erg s^{-1}. (4) Rest-frame equivalent width of [O II] in unit of Å. (5) [O II] luminosity in unit of 10^{42} erg s^{-1}. (6) Rest-frame equivalent width of Hα+[N II] in unit of Å. (7) Hα+[N II] luminosity in unit of 10^{42} erg s^{-1}.

Cowie et al. (2011) have found that the bulk ($\sim 75\,\%$) of the local LAEs have EW(Hα) > 100 Å. Thus, it seems that a large Hα EW is a common character of LAEs irrespective of redshift.

C.3. Physical Properties of the Stacked LAE

C.3.1. Stellar Mass and $E(B-V)$ from SED Fitting

We perform SED fitting for the stacked objects in the NB118 sub-region and the NB209 sub-region to infer their stellar populations. We note that the stacked objects used for the SED fitting are not exactly the same as those presented in Section C.2.1, but the stacking is performed only for objects with Spitzer/IRAC 3.6, 4.5, 5.8, and 8.0μm photometry so that stellar population parameters be well constrained[C.5]. After removing objects with any confusion from neighboring objects in the IRAC images by eye, we stack 304 and 55 LAE candidates in the NB118 sub-region and the NB209 sub-region, respectively.

The procedure of the SED fitting is the same as that of Ono et el. (2010b) and Section B.3.2, except for a fixed redshift ($z = 2.18$). We use the stellar population synthesis model GALAXEV (Bruzual & Charlot 2003) for stellar SEDs, and include nebular emission (Schaerer & de Barros 2009). A Salpeter initial mass function (IMF; Salpeter 1955) is assumed. We choose constant star formation history and the stellar metallicity $Z = 0.2\,Z_{\odot}$ since previous studies have shown that most LAEs are young, and that constant star formation history and sub-solar stellar metallicities are reasonable assumptions. Since we include nebular emission in the fitting, varying star formation history and stellar metallicity makes the fitting too complicated. Guaita et al. (2011) performed SED fitting to $z \sim 2.1$ stacked LAEs with three scenarios of star formation histories, exponentially increasing, decreasing, and constant star formation, to find equally good fits to the data. They also note that among the free parameters SED fitting can relatively well constrain stellar mass and dust extinction, which are of particular interest in this thesis. We also note that the assumption of sub-solar metallicity is consistent with the gas-phase metallicity derived for our stacked LAE (see Section C.3.2). For dust extinction, we use Calzetti's extinction law (Calzetti et al. 2000) on the assumption of $E(B-V)_{\rm gas} = E(B-V)_{\star}$ as proposed by Erb et al. (2006b). IGM attenuation is calculated using the prescription given by Madau (1995). We do not use u^* and NB387 data since they are significantly contaminated by strong Lyα emission. Table C.3 summarizes the broadband photometry of the stacked objects that are used for SED fitting. The limiting magnitudes listed in Table C.3 are estimated in the same manner as explained in Section C.2.1.1. In SED fitting to the stacked objects, we include only photometric errors. We do not include any possible systematic errors such as uncertainties in photometric zero points.

We obtain $M_{\star} = 2.88^{+0.43}_{-0.13} \times 10^8\,M_{\odot}$, $E(B-V) = 0.21^{+0.02}_{-0.04}$, and age $= 1.26^{+1.76}_{-0.26} \times 10^7$ yr for the stacked object in the NB118 sub-region, with a chi-squares of $\chi^2 = 13.4$, and $M_{\star} = 4.79^{+0.22}_{-0.81} \times 10^8\,M_{\odot}$, $E(B-V) = 0.27^{+0.01}_{-0.03}$, and age $= 8.32^{+1.68}_{-1.40} \times 10^6$ yr for the stacked object in the NB209 sub-region, with $\chi^2 = 13.3$. Table C.4 summarizes the physical properties derived from SED fitting, and Figure C.5 shows the best-fit model spectra with the observed flux densities.

Although the dust extinction of our LAEs is rather high compared with those of higher-z LAEs ($E(B-V) = 0.00 - 0.07$ at $z \sim 3$; e.g., Nilsson et al. 2007; Ono et al. 2010a), such an increasing trend of $E(B-V)$ in LAEs down to $z \sim 2$ is also seen in other studies (Nilsson et al. 2011; Guaita et al. 2011).

[C.5] We demand only IRAC coverage, not IRAC detection.

Table C.3. Broadband Photometry of the stacked LAEs

sample	B	V	R	i'	z'	J	H	K	[3.6]	[4.5]	[5.8]	[8.0]
NB118 sub-region	25.96	25.93	25.95	25.85	25.82	25.44	25.12	25.30	25.38	25.56	26.90	99.99
	(29.31)	(29.28)	(29.29)	(29.20)	(29.13)	(28.60)	(28.06)	(28.41)	(28.56)	(28.08)	(26.26)	(26.00)
NB209 sub-region	25.87	25.80	25.75	25.60	25.48	25.09	24.72	24.96	25.13	25.11	25.51	26.19
	(29.20)	(29.11)	(29.07)	(28.93)	(28.73)	(28.06)	(27.38)	(27.86)	(27.62)	(27.28)	(25.35)	(25.04)

Note: Broadband photometry of the stacked objects whose stackings are performed for objects with IRAC coverage (Section C.3.1). All magnitudes are total magnitudes. 99.99 mag means negative flux densities. Magnitudes in parentheses are 1σ limiting magnitudes.

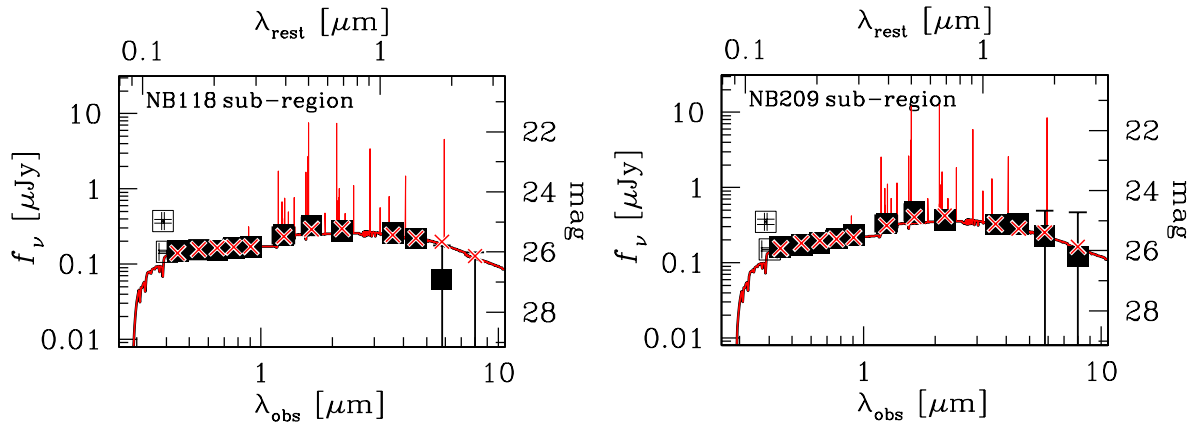

Figure C.5. Results of SED fitting for the stacked objects in the NB118 sub-region (left) and the NB209 sub-region (right). The filled squares show the observed flux densities used for the fitting (B, V, R, i', z', J, H, K, [3.6], [4.5], [5.8], and [8.0]), while the open squares indicate those not used for the fitting (u^* and NB387). The red lines show the best-fit model spectra, and the red crosses correspond to the best-fit flux densities.

Table C.4. Physical Properties of the stacked objects from SED fitting

sample	$M_\star$ $[10^8 M_\odot]$	$E(B-V)_\star$ [mag]	Age [Myr]	$f_{\rm esc}$	χ^2
NB118 sub-region	$2.88^{+0.43}_{-0.13}$	$0.21^{+0.02}_{-0.04}$	$12.6^{+17.6}_{-2.6}$	$0.7^{+0.1}_{-0.3}$	13.425
NB209 sub-region	$4.79^{+0.22}_{-0.81}$	$0.27^{+0.01}_{-0.03}$	$8.32^{+1.68}_{-1.40}$	$0.8^{+0.0}_{-0.1}$	13.290

Note: Physical properties of the stacked objects from SED fitting. Stellar metallicity is fixed to $0.2 Z_\odot$.

Nilsson et al. (2011) performed SED fitting to $z \sim 2.3$ LAEs to find that A_V ($E(B-V)$) varies over $0.0-2.5$ ($0.00-0.61$) with an average of $A_V = 0.6$ ($E(B-V) = 0.15$) and $A_V = 1.5$ ($E(B-V) = 0.37$) for old and young population models, respectively. Guaita et al. (2011) obtained $E(B-V) = 0.22^{+0.06}_{-0.13}$ for stacked $z \sim 2.1$ LAEs assuming constant star formation history. These findings combined with our result may indicate a strong evolution of dust extinction in LAEs from $z > 3$ to $z \sim 2$. More details of results and discussions of the SED fitting will be reported elsewhere (Y. Ono et al. in preparation). We note that the results from the SED fitting may suffer from additional errors due to degeneracy with age or stellar metallicity, and due to possible systematic uncertainties in photometry.

C.3.2. Metallicity

An accurate estimate of gas phase metallicity requires knowledge of the electron temperature which is provided by comparing auroral lines to nebular emission lines (e.g., [O III]λ4363/λ5007; *direct* T_e method; e.g., Kennicutt et al. 2003; Izotov et al. 2006). However, auroral lines are generally weak and it is difficult to observe them in distant galaxies. A number of empirical relations between the ratio of nebular lines and metallicity have been proposed to measure gas-phase metallicities of distant galaxies. Among them, we combine the [N II]λ6584/Hα indicator ($N2$-index: e.g., Pettini & Pagel 2004; Maiolino et al.

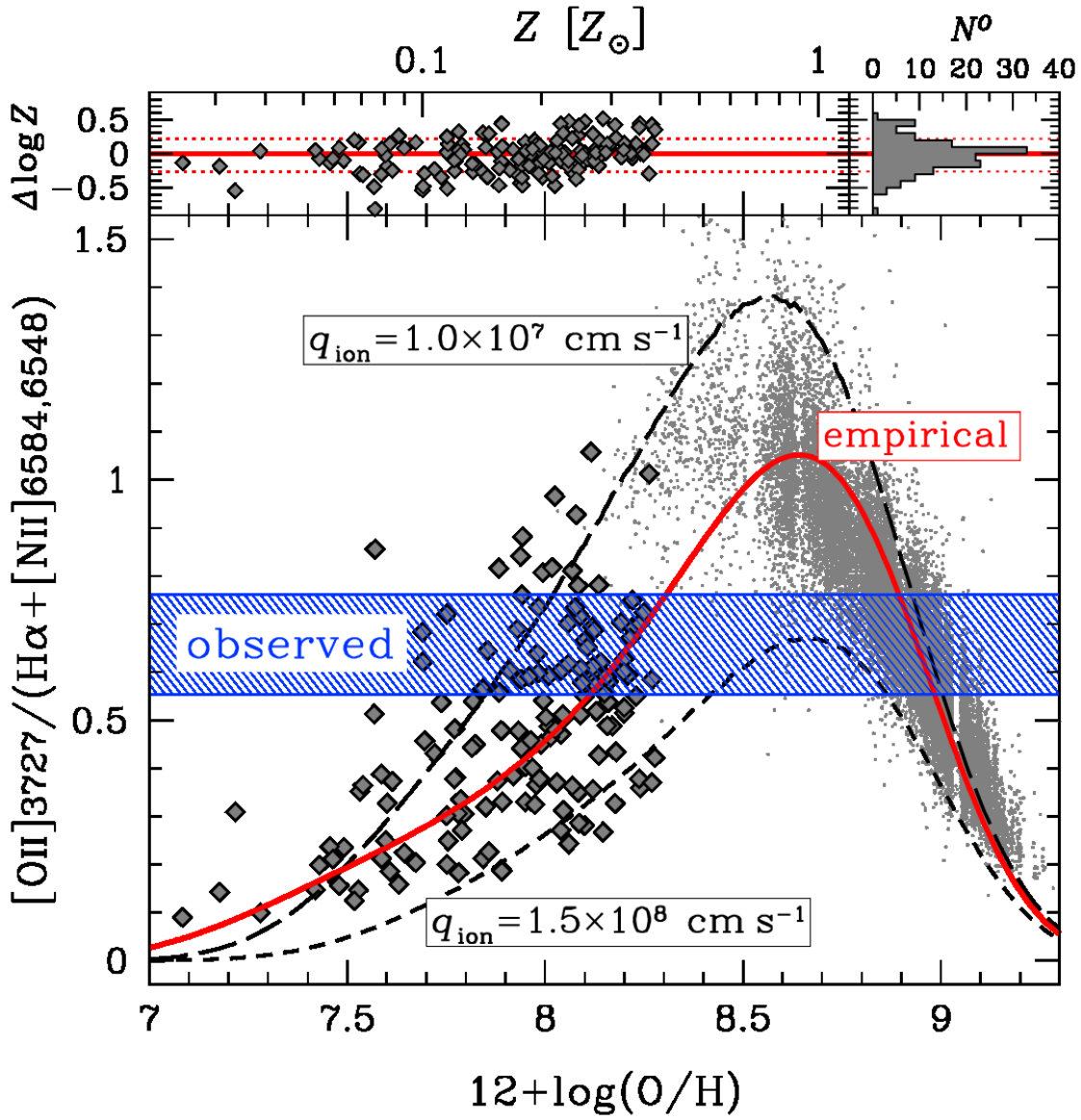

Figure C.6. *Bottom:* Relation between [O II]λ3727/(Hα+[N II]$\lambda\lambda$6584,6548) and gas-phase metallicity. The red solid line corresponds to the empirical relation given by Equation (C.5) combined with Equation (C.6). The gray diamonds represent low-metallicity galaxies compiled by Nagao et al. (2006) whose metallicities are inferred through the *direct* T_e method and then used in Maiolino et al. (2008) to fit the polynomials in Equation (C.6) in the range $12+\log Z < 8.3$; they are distributed around the best-fit line with a large scatter ($\Delta\log Z \sim 0.2$). The gray dots are SDSS galaxies (Kewley & Dopita 2002) used for the fit in the range of $12+\log Z > 8.3$ whose metallicities are inferred through photoionization models. The dashed and long-dashed lines correspond to the relations derived from a combination of stellar population synthesis and photoionization models with an ionization parameter of $q_{\rm ion}= 1.5\times10^8$ and 1.0×10^7 cm s^{-1}, respectively (Kewley & Dopita 2002). We ignore the range $Z > Z_\odot$ in this paper, because LAEs are found to be metal-poor in previous studies (Section C.3.2). The blue shaded area is the range of [O II]λ3727/(Hα+[N II]$\lambda\lambda$6584,6548) for the stacked object assuming $E(B-V)=0$. *Top:* Residuals from the best-fit polynomials for the low-metallicity galaxies (left) and their histogram (right). The two dotted lines show the rms of the residuals for $\Delta\log Z > 0$ objects (rms= 0.22) and $\Delta\log Z < 0$ objects (0.26), respectively.

Table C.5. Coefficients for metallicity indicators in Equation (C.6)

Flux ratio ($\log R$)	c_0	c_1	c_2	c_3	c_4
$\log([\mathrm{N\,II}]_{6584}/\mathrm{H}\alpha)^{(1)}$	−0.7732	1.2357	−0.2811	−0.7201	−0.3330
$\log([\mathrm{O\,II}]_{3727}/\mathrm{H}\beta)^{(1)}$	0.5603	0.0450	−1.8017	−1.8434	−0.6549
$\log([\mathrm{O\,II}]_{3727}/(\mathrm{H}\alpha+[\mathrm{N\,II}]_{6584,6548}))^{(2)}$	0.0164	−0.1673	−1.9484	−1.8158	−0.6148

Note: (1) The coefficients are taken from Table 4 of Maiolino et al. (2008). (2) The coefficients are determined by a best fit polynomial of the combined equation described in Equation (C.5).

2008) and the [O II]/Hβ indicator (e.g., Nagao et al. 2006; Maiolino et al. 2008) to derive the metallicity of our object. Even for the same metallicity index, however, calibrations are often different among the authors, leading to different metallicity measures as discussed in e.g., Nagao et al. (2006) and Kewley & Ellison (2008). As for the $N2$-index, Nagao et al. (2006)'s calibration and Pettini & Pagel (2004)'s agree well ($\Delta Z < 0.2$ dex) with each other over $7.7 < 12+\log(\mathrm{O/H}) < 8.5$, while out of this range a large difference is seen probably due to the lack of objects for calibration in Pettini & Pagel (2004) sample. We use the calibration by Maiolino et al. (2008), which is an update of Nagao et al. (2006), based on a low-Z sample ($7.7 < 12+\log(\mathrm{O/H}) < 8.3$).

We cannot, however, apply these indicators directly to our object, because we have only [O II] and Hα+[N II] fluxes. Instead, we make use the fact that [O II]/(Hα+[N II]) ratio can be expressed as a combination of the two indicators:

$$\begin{aligned}\frac{[\mathrm{O\,II}]}{(\mathrm{H}\alpha+[\mathrm{N\,II}]\lambda\lambda 6584,6548)} &= \frac{[\mathrm{O\,II}]/\mathrm{H}\alpha}{(1+[\mathrm{N\,II}]\lambda\lambda 6584,6548/\mathrm{H}\alpha)} \\ &= \frac{1}{2.86}\frac{[\mathrm{O\,II}]/\mathrm{H}\beta}{(1+1.33\times[\mathrm{N\,II}]\lambda 6584/\mathrm{H}\alpha)},\end{aligned} \tag{C.5}$$

where we assume that all lines are dust free and adopt an intrinsic Hα/Hβ ratio of 2.86 and an intrinsic [N II]λ6584/λ6548 ratio of 3.0 (Osterbrock 1989). The effect of dust extinction will be discussed later. The metallicity dependence of the two indicators is empirically approximated by the polynomial:

$$\log R = c_0 + c_1 x + c_2 x^2 + c_3 x^3 + c_4 x^4, \tag{C.6}$$

where $R =$ [O II]/Hβ or [N II]/Hα, x is the metallicity relative to solar (i.e., $x = \log(Z/Z_\odot) = 12 + \log(\mathrm{O/H}) - 8.69$; Asplund et al. 2009), and the coefficients c_0 to c_4 are taken from Table 4 of Maiolino et al. (2008). Thus, [O II]/(Hα+[N II]) ratio is expressed as a function of metallicity, as shown in Figure C.6 by the solid curve. In this figure, the gray diamonds and gray dots indicate, respectively, local low-metallicity galaxies with $12+\log(\mathrm{O/H}) < 8.3$ (Nagao et al. 2006) and SDSS galaxies with $12+\log(\mathrm{O/H}) > 8.3$ (Tremonti et al. 2004; Kewley & Dopita 2002) used to calibrate Equation (C.6); the metallicities of the former are measured with the *direct* T_e method (Nagao et al. 2006), while those of the latter are derived by applying photoionization models to the most prominent optical emission lines ([O II], Hβ, [O III], Hα, [N II], [S II]). The ratio has a peak at around solar metallicity and for any given value of [O II]/(Hα+[N II]) (except for the peak), there are two solutions of metallicity, one being sub-solar and the other being super-solar. The blue shaded region in Figure C.6 corresponds to the observed [O II]/(Hα+[N II]$\lambda\lambda$6584,6548) ratio including the 1σ photometric error: $0.66^{+0.11}_{-0.11}$. Two metallicity ranges are found to meet the observation: $12+\log(\mathrm{O/H}) = 8.21^{+0.10}_{-0.11}$ and $8.94^{+0.05}_{-0.05}$. The latter range,

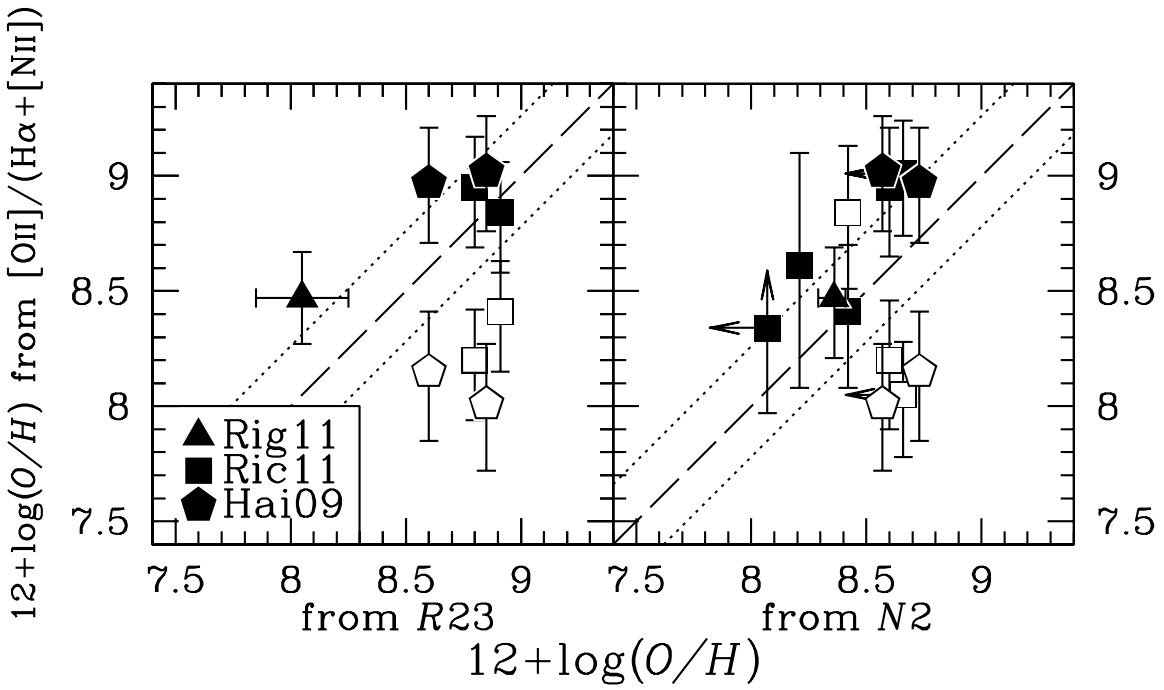

Figure C.7. Comparison of the metallicity calculated from our [O II]/(Hα+[N II]) indicator with those from two frequently used indicators, the $R23$ index (left panel) and the $N2$ index (right panel), for $z \sim 2$ lensed galaxies taken from the literature (Rigby et al. 2011 with triangle; Richard et al. 2011 with squares; Hainline et al. 2009 with pentagons). At each panel, the dashed line is the line of equality, and the dotted lines show the 1σ errors associated with our indicator including the calibration errors ($\Delta \log Z = +0.22/-0.26$). Our indicator has in principle two solutions), and for galaxies with two solutions over their 1σ errors both metallicities are plotted; solutions with the smaller differences from Z_{R23} or Z_{N2} in black, while those with the larger differences in white.

however, appears to be unlikely, since it is not consistent with recent spectroscopic observations that LAEs have much lower metallicities than the solar value (Finkelstein et al. 2011; Cowie et al. 2011). Modest dust extinction inferred from SED fitting also favors low metallicities (e.g., Gawiser et al. 2006, 2007; Pirzkal et al. 2007; Lai et al. 2008; Ono et al. 2010a). If we rule out the super-solar solution, the metallicity of our object is estimated to be $12+\log(\mathrm{O/H}) = 8.21^{+0.10}_{-0.11}$, or $Z/Z_{\odot} = 0.33^{+0.09}_{-0.07}$.

This metallicity estimate, however, involves two systematic uncertainties. First is the uncertainty in the polynomial fit given by Equation (C.6) for low-metallicity galaxies. The gray diamonds plotted in Figure C.6 represent galaxies with $12+\log(\mathrm{O/H}) < 8.3$ used in Maiolino et al. (2008) to fit the polynomials. The galaxies are distributed around the solid line (as expected), but with a large scatter of $\Delta \log Z = +0.22/-0.26$ (1σ). This may suggest that there are large errors in measurements of line ratios and/or metallicities, since these measurements collected from the literature are based on different methods to measure line ratios (Nagao et al. 2006). Alternatively, such a large scatter may be intrinsic. Dashed lines in Figure C.6 represent relations of metallicity and [O II]/(Hα+[N II]) from a combination of stellar population synthesis and photoionization models with a set of ionization parameter ($q_{\rm ion}$; Kewley & Dopita 2002). From Figure C.6, the large scatter could be explained by a diversity of ionization parameters ($q_{\rm ion} \sim (1-10) \times 10^7$ cm s^{-1}). Note that the empirical line can be reproduced by the Kewley & Dopita's photoionization model with $q_{\rm ion} \sim (4-8) \times 10^7$ cm s^{-1}. In any case, we estimate that the calibration error

in our metallicity estimate due to the uncertainty in the polynomial fit is $\Delta\log Z = +0.22/-0.26$ (1σ). In Figure C.7, we compare metallicities derived from our original indicator with those from more commonly used indicators: $R23$-index (([O II]λ3727+[O III]$\lambda\lambda$4959, 5007)/Hβ) and $N2$-index to check robustness of the indicator. We compare the indicators using spectroscopic data of $z \sim 2$ lensed galaxies (Hainline et al. 2009; Richard et al. 2011; Rigby et al. 2011). From the comparison, we see that metallicities from our indicator are roughly consistent with those from other indicators within $\Delta\log Z = +0.22/-0.26$ (1σ).

Second is the uncertainty in dust extinction. While we have assumed $E(B-V) = 0$ to derive Equation (C.5), the SED fit suggests that the stacked object may have $E(B-V)$ up to $\simeq 0.27$ (see Section C.3.1). We find that adopting $E(B-V) = 0.27$ instead of $E(B-V) = 0$ increases the metallicity estimate by $\Delta\log Z \simeq 0.3$.

When these two systematic errors are taken into account, the metallicity range of our object is estimated to be $12+\log(\mathrm{O/H}) = 8.21^{+0.10}_{-0.11}\,(\mathrm{random})\,^{+0.22}_{-0.26}\,(\mathrm{calib}) = 8.21^{+0.24}_{-0.28}$, or $Z/Z_\odot = 0.33^{+0.25}_{-0.16}$, assuming $E(B-V) = 0$. If $E(B-V) = 0.27$ is adopted, the metallicity increases to $12+\log(\mathrm{O/H}) \sim 8.5^{+0.24}_{-0.28}$, or $Z/Z_\odot = 0.7^{+0.5}_{-0.3}$. Recall, however, that our method logically permits the possibility of a super-solar metallicity and that in order to rule out such a possibility, we will require independent data favoring metal-poor LAEs. In this sense, the upper limit of the metallicity obtained above is not as strict as the lower limit. Considering this, we adopt a conservative conclusion that the metallicity of the stacked object is no less than $0.17\,Z_\odot$ (1σ), or $0.09\,Z_\odot$ (2σ). This 2σ lower limit is obtained in the following manner. The observed [O II]/(Hα+[N II]) ratio and its 2σ negative photometric error are 0.66 and -0.23, respectively, thus the 2σ lower limit of the observed [O II]/(Hα+[N II]) ratio is 0.43, which corresponds to $12+\log(\mathrm{O/H}) = 7.96$. Therefore, the 2σ negative statistical error in terms of metallicity is $(\Delta\log Z)_{\mathrm{calib}} = -(8.21-7.96) = -0.25$. On the other hand, the 2σ negative systematic error is just twice the 1σ value (-0.26), hence $(\Delta\log Z)_{\mathrm{sys}} = -0.52$ (2σ). Therefore, we obtain the 2σ negative error in terms of metallicity as $(\Delta\log Z) = -\sqrt{0.25^2+0.52^2} = -0.58$, and the 2σ lower limit of the metallicity as $12+\log(\mathrm{O/H}) = 8.21-058 = 7.63$, corresponding to $Z = 0.09\,Z_\odot$. We calculate the 3σ, 4σ, and 5σ lower limits of metallicity in the same manner to obtain $12+\log(\mathrm{O/H}) = 7.32$, 6.97, and 6.58, or $Z = 0.04\,Z_\odot$, $0.02\,Z_\odot$, and $0.008\,Z_\odot$, respectively. Although a recent spectroscopic study has placed a weak upper limit on the metallicity of bright LAEs ($Z < 0.56\,Z_\odot$ (2σ)[C.6]; Finkelstein et al. 2011), this is the first lower limit on the metallicity for typical LAEs at high-z. Scannapieco et al. (2003) proposed that LAEs may be extremely metal poor primordial galaxies, and Schaerer (2003) also found that large Lyα EWs can be observed from extremely metal poor galaxies ($Z/Z_\odot \lesssim 10^{-5}$). However, our firm lower limits, e.g., $Z > 2\times10^{-2}\,Z_\odot$ at the 4σ level, do not support this idea at least for $z = 2.2$ LAEs.

C.3.3. Star Formation Rate

C.3.3.1. Deriving SFR from Hα Luminosity

The Hα luminosity is believed to be the most reliable SFR indicator of galaxies among those based on the rest-frame UV and optical spectral features. Indeed it is proportional to the birth rate of massive stars as well as being relatively insensitive to dust extinction as compared with UV-continuum. We measure the SFR of the stacked object in the NB209 sub-region from its Hα luminosity using the relation (Kennicutt 1998) of Equation B.1.

[C.6] We have recalibrated the metallicity given in Finkelstein et al. (2011) using Equation (C.6). The original metallicity upper limit is $Z < 0.41\,Z_\odot$ (2σ).

Before applying this relation, however, we have to subtract the contribution from [N II]$\lambda\lambda$6584, 6548 lines from the observed Hα+[N II] luminosity. It is known that the [N II]/Hα ratio varies with metallicity; indeed, this ratio is used as a metallicity indicator of galaxies, called the $N2$-index (e.g., Pettini & Pagel 2004; Maiolino et al. 2008). In Table C.1, we derive L(Hα+[N II]) to be $8.0^{+1.3}_{-1.2} \times 10^{41}$ erg s^{-1}. We use the metallicity estimated in Section C.3.2 to infer L([N II])/L(Hα) $= 5.7^{+1.7}_{-1.3} \times 10^{-2}$ (Maiolino et al. 2008). The Hα luminosity is then $8.0^{+1.3}_{-1.2} \times 10^{41}/(1 + 5.7^{+1.7}_{-1.3} \times 10^{-2}) = 7.6^{+1.2}_{-1.2} \times 10^{41}$ erg s^{-1}, from which we obtain SFR $= 6^{+1}_{-1} M_\odot$ yr^{-1}.

With $E(B-V) = 0.27^{+0.01}_{-0.03}$ combined with Calzetti et al. (2000)'s extinction law, we obtain the dust-corrected Hα luminosity to be $1.7^{+0.3}_{-0.3} \times 10^{42}$ erg s^{-1}, which is translated into SFR $= 14^{+2}_{-3} M_\odot$ yr^{-1}. This SFR is the first unbiased SFR estimate from Hα luminosity for typical $z \sim 2$ LAEs of L(Lyα) $> 1 \times 10^{42}$ erg s^{-1}. Although Finkelstein et al. (2011) have derived SFRs for two $z \sim 2.3-2.5$ LAEs from Hα spectroscopy, both objects have L(Lyα) $\sim 2 \times 10^{43}$ erg s^{-1}, which is about one order of magnitude brighter than typical Lyα luminosities of LAEs from narrowband surveys (e.g., Ouchi et al. 2008), due to pre-selection of bright objects for NIR spectroscopy. Hayes et al. (2010) have measured L(Hα) for six LAEs with L(Lyα) $= (0.3-4.5) \times 10^{42}$ erg s^{-1} for which Hα emission is detected. In contrast to these studies, our study is based on a large number ($N = 105$) of purely Lyα-selected galaxies.

SED fitting of the stacked object in the NB209 sub-region gives a stellar mass of $5 \times 10^8 M_\odot$. Therefore, the stacked object has the SFR and the stellar mass of the same order of magnitudes of those of LAEs studied earlier from SED fitting ($z \sim 2$: Guaita et al. 2011, $z \sim 3$: Gawiser et al. 2006, 2007; Lai et al. 2008; Nilsson et al. 2007; Ono et al. 2010a). Some studies have derived SFRs of LAEs from (dust-uncorrected) UV-continuum (e.g., Gronwall et al. 2007; Ouchi et al. 2008, 2010; Nilsson et al. 2009, 2011; Guaita et al. 2010) which are roughly in the range $1-10 M_\odot$ yr^{-1}, comparable to our dust-uncorrected SFR.

We also estimate in a similar manner the SFRs of the (Hα+[N II])-detected objects, SXDS1-22326, SXDS5-04041, and SXDS5-04492 to be 23^{+2}_{-3}, 51^{+2}_{-2}, and 13^{+3}_{-3} $M_\odot$ yr^{-1}, respectively[C.7]. These SFRs are much larger than that of a typical LAE at $z \sim 2$, but similar to some bright LAEs at similar redshifts (Nilsson et al. 2011; Finkelstein et al. 2011). This is because our NIR narrowband images are relatively shallow, and only bright, massive LAEs with high SFR are likely to be detected. Indeed, Nilsson et al.'s and Finkelstein et al.'s LAEs are much more massive than a typical LAE ($\gtrsim 10^{10} M_\odot$) with some exceptions like HPS256 (Finkelstein et al. 2011) whose mass can be as small as $6 \times 10^8 M_\odot$. Although the (Hα+[N II])-detected objects lack Spitzer/IRAC data and their stellar masses are poorly constrained by SED fitting, rough estimate is possible from their K-band magnitudes. Daddi et al. (2004), for instance, derived a relation between K magnitude and mass for $z \sim 2$ BzK galaxies. The K-band total magnitudes of SXDS1-22326, SXDS5-04041, and SXDS5-04492 are 23.28, 23.02, and 22.39, which correspond to a stellar mass of (2–3) $\times 10^{10}$, (2–4) $\times 10^{10}$, and (4–7) $\times 10^{10} M_\odot$, respectively, following Daddi et al.'s simple relation. Although this is just a rough estimate and the relation itself involves a certain uncertainty ($\sigma(\Delta \log M_*) \sim 0.2$; Daddi et al. 2004), the individually (Hα+[N II])-detected objects are likely to be massive LAEs.

[C.7] For SXDS1-22326, we assume L(Hα+[N II]) $= L$(Hα), since its [O II] is not detected and therefore its metallicity is low enough that the contribution of [N II] to L(Hα+[N II]) is considered to be negligible. For SXDS5-04492, we adopt solar metallicity from the empirical [O II]/(Hα+[N II])-metallicity relation to correct for [N II] emission. For SXDS5-04041, the metallicity is estimated to be $12 + \log(\mathrm{O/H}) \sim 8.1$ with Equation (C.5). All SFRs are calculated assuming dust free.

C.3.3.2. Deriving SFR from [O II] Luminosity

The [O II] luminosity is also known to be a useful SFR indicator (e.g., Gallagher et al. 1989; Kennicutt 1992, 1998; Kewley et al. 2004; Moustakas et al. 2006) and frequently used to derive SFRs of galaxies at high-z, where Hα cannot be accessed from the ground (e.g., Teplitz et al. 2003; Hopkins 2004; Takahashi et al. 2007). The SFR is derived from the [O II] luminosity using the relation (Kennicutt 1998):

$$\mathrm{SFR}\,(M_\odot\ \mathrm{yr}^{-1}) = (1.4 \pm 0.4) \times 10^{-41}\, L([\mathrm{O\,II}])\ \mathrm{erg\ s}^{-1}. \tag{C.7}$$

In Table C.1, we derive $L([\mathrm{O\,II}])$ in the NB209 sub-region to be $5.3^{+0.4}_{-0.4} \times 10^{41}$ erg s^{-1}, which corresponds to SFR $= 7^{+2}_{-2}\,M_\odot\ \mathrm{yr}^{-1}$. This is consistent with the SFR derived from the Hα luminosity when dust free is assumed. However, if we take into account the dust extinction of $E(B-V) = 0.27^{+0.01}_{-0.03}$, we find that the SFR derived from the [O II] luminosity could be more than twice the SFR derived from the Hα luminosity, and they are not consistent within 1σ errors: $\mathrm{SFR_{cor}(H\alpha)} = 14^{+2}_{-3}\,M_\odot\ \mathrm{yr}^{-1}$, and $\mathrm{SFR_{cor}([O\,II])} = 32^{+9}_{-11}\,M_\odot\ \mathrm{yr}^{-1}$. Such differences have also been reported for present-day galaxies (e.g., Gilbank et al. 2010) and for high-z galaxies (e.g., Charlot et al. 2002; Tresse et al. 2002). The difference can be due to the complicated origin of the [O II] luminosity. The [O II] luminosity is not directly proportional to the ionizing luminosity, and also depends on the chemical abundance and ionization state of the ionized gas (e.g., Kennicutt 1998; Kewley et al. 2004; Moustakas et al. 2006). Indeed, the ratio of [O II]/Hβ can be used as a metallicity indicator (e.g., Nagao et al. 2006; see also Section C.3.2). Alternatively, the uncertainty of the dust correction may cause the difference of the SFRs. The relatively large dust correction for the [O II] luminosity makes it difficult to derive the SFR accurately (e.g., Jansen et al. 2001). The difference of the SFRs of our result may be also due to the overestimates of the dust extinction inferred from the SED fitting. In any case, we use the SFR derived from the Hα luminosity, which is more directly proportional to the SFR and less affected by the dust attenuation or other factors (e.g., metallicity), in the following analysis.